COMPUTATIONAL MODELING OF ADSORPTION OF COMPLEX MOLECULES IN METAL-ORGANIC FRAMEWORKS

A Dissertation
Presented to
The Academic Faculty

by

Mayank Agrawal

In Partial Fulfillment
of the Requirements for the Degree
Doctor of Philosophy in the
School of Chemical & Biomolecular Engineering

Georgia Institute of Technology
December 2019

Copyright © 2019 by Mayank Agrawal

COMPUTATIONAL MODELING OF ADSORPTION OF COMPLEX MOLECULES IN METAL-ORGANIC FRAMEWORKS

Approved by:

Dr. David S. Sholl, Advisor
School of Chemical & Biomolecular Engineering
Georgia Institute of Technology

Dr. Martin Maldovan
School of Chemical & Biomolecular Engineering
Georgia Institute of Technology

Dr. Sankar Nair
School of Chemical & Biomolecular Engineering
Georgia Institute of Technology

Dr. Seung Soon Jang
School of Material Science and Engineering
Georgia Institute of Technology

Dr. Krista Walton
School of Chemical & Biomolecular Engineering
Georgia Institute of Technology

Date Approved: October 24, 2019

To my parents, who have always supported my unconventional decisions in the family.

ACKNOWLEDGEMENTS

Throughout my Ph.D. I have received a great deal of support and assistance. First and foremost, I would like to thank my thesis advisor, Dr. David Sholl, for his continuous support of my research, his patience, motivation and immense knowledge. When I joined Georgia Tech in Spring 2015, I didn't have many project offers. Dr. Sholl, however, welcomed me to his group. Later when my original funding from ExxonMobil ended, he provided me with the stability to do research by finding other sources of funding. I am forever grateful for his help and guidance throughout my five years at Georgia Tech. I could not have hoped for a better Ph.D. experience than the one I have had in his group.

I would like to express my deepest gratitude to my thesis committee members: Dr. Sankar Nair, Dr. Krista Walton, Dr. Martin Maldovan, and Dr. Seung Soon Jang, for their insightful comments and encouragement as well as their feedback about my research. I would also like to thank Dr. Andrew Medford for his help and guidance in deciding my future career path.

I would like to convey my gratitude to ExxonMobil Chemical Company and Sandia National Labs for funding my research. It was a privilege to work with a diverse network of colleagues. I especially thank Dr. Jeffery Greathouse at Sandia National Labs for all his inputs to the projects and for being a patient collaborator for the past two years.

My fellow group members played a critical role in my success/time here at Georgia Tech. I would like to thank Dr. Salah Boulfelfel, Dr. Hanjun Fang, Dr. Ross Verploegh, Dr. Joshua Howe and Dr. Dai Tang from whom I have learned a tremendous amount about

atomistic simulations. I would like to thank Wenqin You for being a great friend and a very diligent officemate who has inspired me to continuously work harder. I am thankful to Dr. Ambarish Kulkarni, Dr. Jason Gee, Dr. Dalar Nazarian, Dr Rohan Awati, Dr. Souryadeep Bhattacharyya, Dr. Chu Han, Dr. Raghu Thyagarajan, Dr. Anny Liu, Dr. Rebecca Han, John Findley, Omar I Knio and Jongwoo Park for their help in various academic activities, thought-provoking discussions and for sharing fun times together at Georgia Tech.

I acknowledge the contribution of my mentors at IIT Delhi, Dr. Kamal Pant, Dr. Sanat Mohanty and Dr. Ali Haider who motivated and helped me to pursue a career in research.

I have had an amazing time with my closest friends in the USA: Aditya Anupam, Kalki Kukreja, Abhinav Malhotra, Akanksha Mahajan, Anshuman Sinha, and Akshay Korde. During my time as a graduate student, I was blessed to meet Aditi Gupta. She has been my best friend and a never-ending source of support throughout this process. Her positive outlook has helped me sail through the most challenging times of this journey.

Finally, I cannot fully express my thanks to my parents who have always supported and encouraged my decisions. I am fortunate to have two younger sisters, Priyanka Agrawal and Neha Agrawal, whose presence have encouraged me to become more mature and responsible. These traits have helped me tackle the challenges of my personal and professional life and for that I am forever grateful to my beloved little siblings.

Mayank Agrawal, Atlanta, October 2019

TABLE OF CONTENTS

LIST OF TABLES

LIST OF FIGURES

SUMMARY

Metal-organic frameworks (MOFs) are nanoporous materials that have organic parts connected to metal nodes constructing a crystalline structures. MOFs are intrinsically flexible in nature, however, general practices in computational studies of MOFs assume the structure to be rigid during simulations. In this thesis, we focus on the effects of framework flexibility in MOFs on their adsorption properties. We first divided the flexibility in MOFs into two categories: flexibility with constant volume ($\Delta V=0$) and flexibility with volume change ($\Delta V\neq0$). We then demonstrated that flexibility with $\Delta V=0$ in MOFs can affect their adsorption at dilute loadings and multicomponent adsorption significantly but have negligible effects on the single component adsorption at high loadings. Following this work, we studied MIL-53, a MOF that show the flexibility $\Delta V\neq0$ and concluded that the flexibility with $\Delta V\neq0$ can significantly affect even the single component adsorption in MOFs.

In the second half of the thesis, we focused on the adsorption and diffusion properties of chemical warfare agents (CWAs) and their simulants in MOFs. We compared the Henry constants of two CWAs, sarin and soman, with their simulants to study whether the available simulants are accurately able to mimic the CWAs' adsorption properties. We then extended this study to calculate diffusion coefficients of CWAs and simulants. Our results showed that dimethyl-methylphosphonate (DMMP) is the best simulant available to mimic adsorption and diffusion properties of sarin while dimethyl-nitrophenylphosphonate (DMNP) is the closest simulant to predit soman's adsorption properties. Finally, we performed a literature meta-analysis to assess the frequency of

replicate materials synthesis and found that less than 12% of MOFs have been replicated in a published report. The methodology and the findings of this thesis advance the scientific knowledge on adsorption and diffusion in nanoporous materials and suggest ways how the research community can improve replicability of these materials.

CHAPTER 1. INTRODUCTION

1.1 Metal-Organic Frameworks

Over the past 70 years, research into porous materials has resulted in a number of applications which have had a direct impact on industrial processes as well as domestic life.[1] Discovered in the late 1990's, metal-organic frameworks (MOFs) are relatively new compared to traditional porous frameworks like zeolites and activated carbon. MOFs are crystalline nanoporous materials consisting of organic linkers connected with inorganic clusters. These frameworks have shown their advantages over other porous materials due to their high surface area (extending beyond 6000 m^2/g), high porosity (up to 90% free volume) and thermal stability[1–3] in clean energy applications such as gas storage, catalysis, drug delivery, membranes, biomedical imaging, sensors etc. The combination of the two components of a MOF, the metal center and the organic linker, provides many synthetic possibilities compared to other porous materials. While more than 37000 MOFs[4] have been reported in last 20 years, only 230 zeolites[5] have been synthesized since the late 1940's.

1.2 Flexibility in MOFs

The presence of inorganic centers connected with organic linkers introduces flexibility in MOFs that makes it complex to study these systems computationally. Accurate prediction of MOF properties requires the fundamental understanding of flexibility in the frameworks. Structural flexibility in MOFs can cause these framework to respond to temperature, pressure, adsorption or other physical stimuli.[6,7] For a thorough discussion of flexibility in MOFs, a classification of the modes of framework flexibility is

required. One widely accepted description of this type was presented by Bousquet *et al.*[8] and Coudert *et al.*[9] as shown in **Figure 1.1**. One class of flexibility is characterized by the change in unit cell volume ($\Delta V \neq 0$), e.g. breathing, swelling and subnetwork displacement. *Breathing* modes of flexibility correspond to a drastic change in unit cell volume upon guest molecule adsorption/desorption. This is a reversible transition in which characteristic distance and angles of the unit cell change and the crystallographic space groups of the two or more distinct phases may be different. An example of this kind of flexibility is MIL-53(M) series.[10,11] A *swelling* mode of flexibility is characterized by a gradual enlargement of the MOF unit cell without change in its shape due to guest adsorption. MIL-88[12] shows a change in volume from 1135 $Å^3$ to 1840 $Å^3$ upon n-butanol adsorption and to 2110 $Å^3$ after soaking in water. Thermal expansion or shrinking in the absence of guest molecules is another flexibility mode related to swelling. *Subnetwork displacement* is a phenomenon specific to systems having individual frameworks not connected to each other by chemical bonds. In these frameworks, subnets can drift, relocate or shift in relation to each other. For instance, the 2D MOF [$Cu(dhbc)_2(bipy)$] shows a gate-opening/closing after a certain threshold pressure of nitrogen, oxygen or methane is applied.[13]

Framework flexibility can also occur without change in unit cell volume ($\Delta V = 0$). *Linker rotation*, described as a continuous transition where spatial alignment of linker is changed around a rotational axis, is an example of this kind of flexibility. Other degrees of freedom can also be affected. Recent studies[14–16] used molecular simulations to show that constant volume flexibility can have a significant impact on adsorption properties of MOFs. It is important to note that all MOFs are subject to constant volume flexibility, while only a subset of MOFs are affected by flexibility with $\Delta V \neq 0$.

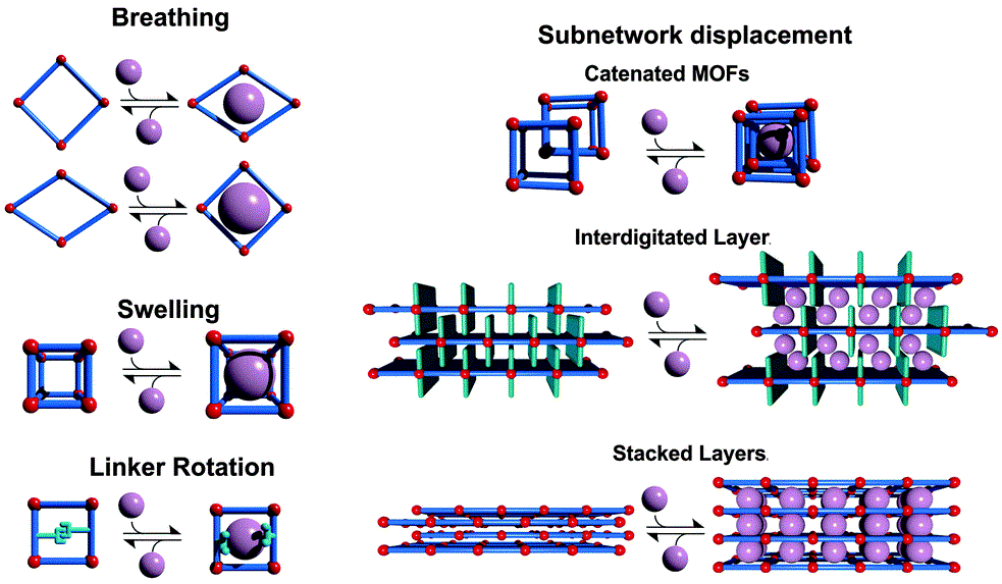

Figure 1.1: Classification of different flexibility modes in MOFs. This figure is taken from the work of Schneemann et al.[7] Copyright The Royal Society of Chemistry 2014.

It is obviously preferable that the modes of flexibility just discussed should be included when modeling MOFs to quantitatively describe these materials. Said differently, calculations based on a rigid structure approximation may not be appropriate for many of these materials. In this doctoral thesis, we aim to study the impact of flexibility in MOFs on adsorption properties for a range of molecular mixtures at different operating conditions. We use quantum mechanical models to obtained energy minimized geometries, molecular dynamics (MD) to describe the flexibility in MOFs and Monte Carlo simulations to predict their adsorption properties.

1.3 Chemical Warfare Agents

Chemical warfare agents (CWAs) comprise a diverse group of extremely hazardous materials.[17] As potential weapon for mass destruction, CWAs are capable of causing catastrophic medical disasters that could overwhelm any healthcare system. CWAs possess

different characteristics and are classified into several groups. Nerve agents are considered one of the most dangerous category that acquired their name because they affect the functioning of the nervous system. The first known nerve agent, Tabun (GA), was developd by the German chemist, Gerhard Schrader, in the 1930s during his research in the development of new OP insecticides. Following this, a series of nerve agents known as G-agents, which include sarin (GB) and soman (GD), were developed. The most critical effect of nerve agents are paralysis of the respiratory muscles and inhibition of the respiratory center which results in immediate death if the concentration of the nerve agent is high. To avoid harm, it is crucial to capture these compounds quickly and efficiently from the air rather than rely on medical treatment later. In the past couple of decades, extensive research has been done to find new materials to capture these compounds effectively. MOFs have shown their potential as catalysts to degrade CWAs and as adsorbent materials to capture them.[18–21] We use molecular simulations to study the adsorption of CWAs in thousands of MOFs from CoRE MOF database.[22] Further, we extend this work to study diffusion of CWAs in selected MOFs to provide insights into the kinetics of these molecules inside nanoporous materials.

1.4 Computational Theory

1.4.1 Molecular dynamics (MD)

Molecular dynamics (MD) is a classical simulation method for studying the physical movements of atoms and molecules by solving Newton's equations of motions for many-particle system where forces between the particles are often calculated using interatomic potentials or molecular force fields.[23] The initial state of the system is defined

by positions and velocities for each particle in three dimensions. We calculate the force on each particle after small time step and update the position and velocity. This process is repeated until the system reaches equilibrium, where the average properties of the system don't change with time. We can calculate system properties such as energy, temperature and pressure by taking ensemble averages at any moment in time.

The Lennard-Jones (LJ) potential is a mathematically simple model that approximates the interactions between a pair of atoms of molecules[24]

$$V_{LJ}(r) = 4\varepsilon\left[\left(\frac{\sigma}{r}\right)^{12} - \left(\frac{\sigma}{r}\right)^{6}\right] \tag{1.1}$$

where ε is the depth of the potential well, σ is the distance at which the interparticle potential is zero, and r is the distance between the particles. The corresponding force for this potential in *x* direction would be

$$f_x(r) = \frac{48\epsilon x}{r^2}\left[\left(\frac{\sigma}{r}\right)^{12} - \frac{1}{2}\left(\frac{\sigma}{r}\right)^{6}\right] \tag{1.2}$$

The most time consuming part of MD simulations is to calculate forces on each atom at each time step. To reduce the number of force pairs evaluated, the interaction potential between particles is typically truncated at a radial cutoff distance where the force decayed sufficiently to not influence the properties of interest. A neighbor list storing a list of particles that are within the cutoff is then created for each particle. The pair forces only need to be computed for the particles in the neighbor list.[23] This neighbor list is rebuilt less frequently than every MD step which reduces the computational time significantly.

1.4.2 Monte Carlo simulations

The main idea behind this method is that the results are computed based on repeated random sampling and statistical analysis.[23,25] MC simulations can be applied to different ensembles such as canonical (NVT), isobaric-isothermal (NPT), grand canonical (μVT) etc.[26] For adsorption calculations, Grand Canonical Monte Carlo (GCMC) simulations are used to model grand canonical ensembles (constant μVT), in which MC sampling drives the system to reach an equilibrium based on chemical potential at constant volume and temperature. The trial moves used in a GCMC simulation are translational, rotational, insertion/deletion and swap with another molecule to obtain a new configuration. The moves are accepted with a probability,

$$p(old \rightarrow new) = \min(1, e^{-\beta(U_{new} - U_{old})}) \quad (1.3)$$

where $\beta = 1/k_B T$ and U is the energy of the system. Energy of the system is calculated based on force fields as described above. In a case where the new configuration has lower energy than old configuration, it will be accepted with the probably of 1, otherwise with a probability less than 1. If the move is rejected then the old configuration is kept. At equilibrium, the number of molecules inside the system don't change with time which is considered the adsorption amount at that temperature and pressure.

1.4.3 Density functional theory (DFT)

Density functional theory (DFT) is a quantum mechanical method that approximates a solution to the time-dependent many-body Schrödinger equation.[27] The root of DFT go back to 1920's when Erwin Schrödinger introduced Schrödinger equation

which is the foundation of quantum chemical calculations.[28] The Schrödinger equation can be solved exactly for simple systems like particles in a box, harmonic oscillator etc. However, it becomes more challenging as the system gets more complex. For such systems, the time-dependent Schrödinger equation is described as

$$\hat{H}\,\Psi = E\Psi \tag{1.4}$$

where Ψ is the wavefunction describing the state, $\hat{H}$ is Hamiltonian operator and E is the energy level of the state. For a many-body system, ψ describes the spatial positions of all the atomic nuclei and electrons in 3D space. Given m nuclei and n electrons, this wavefunction has 3(n+m) variables which makes it exponentially difficult to find a solution for larger systems. Each proton or neutron in the nucleus is more than 1800 times heavier than the electron, so first simplification to solve this equation is to assume that the electronic movements are nearly instantaneous compared to changes in nuclear positions. The Born-Oppenheimer approximation allows motion of the nuclei and electrons to be separated,

$$\Psi_{\text{total}} = \psi_{electronic} \times \psi_{nuclear} \tag{1.5}$$

So, the Schrödinger equation becomes,

$$H\,\psi_e = \left[-\frac{h^2}{2m}\sum_{i=1}^{N}\nabla_i^2 + \sum_{i=1}^{N}V(\vec{r_i}) + \sum_{i=1}^{N}\sum_{j<i}U(\vec{r_i},\vec{r_j})\right]\psi_e = E\,\psi_e \tag{1.6}$$

where the three terms in the bracket are kinetic energy of each electron, interaction energy between each electron and all the nuclei, and the interaction energy between different electrons respectively.[28]

Although the electron wave function can be approximated as the product of individual wave function of N electrons, the challenging part of solving this equation is the fact that an individual electron wave function can't be obtained without considering others as well. Therefore, approximations are required to solve this equation for many body problem. DFT provides a solution to this problem based on two theorems which are established in 1960's. The first theorem, which was established by Hohenberg and Kohn, postulates that the ground state energy is a unique functional of the electron density. So the equation can be solved by determining a function with three variables electron density rather than using wave functions with 3N variables. The second theorem states that the true electron density is the one minimizing the energy of the overall functional. However, the true functional is unknown which motivated Kohn and Sham to convert the Schrödinger equation into a set of equations, the Kohn-Sham equations, describing interactions of single electrons as

$$\left[-\frac{h^2}{2m}\nabla^2 + V(r) + V_H(r) + V_{XC}(r)\right]\psi_i(r) = \varepsilon_i(r)\,\psi_i(r) \tag{1.7}$$

where $V(r)$, $V_H(r)$ and $V_{XC}(r)$ denote the electron-nuclei interaction potential, Hartree potential and exchange-correlation contribution respectively. Still, V_{XC} is unknown and must be approximated. Two key approximations used in DFT calculations are the local density approximation (LDA) and generalized gradient approximation (GGA). LDA utilizes solely the local electron density to determine the unknown V_{XC}. GGA approach involves the knowledge of the local electron density and the local electron density gradient to define V_{XC}. There are different GGA functionals derived based on different approaches

to define the density functional gradient such as Perdew-Wang functional (PW91)[29] and Perdew-Burke-Ernzerhof (PBE)[30] etc.

One of the limitations of DFT with standard XC functionals is that this method does correctly account for long-range interactions. To account for such interactions, dispersion corrected DFT functionals e.g. semi-empirical DFT-D[31] and non-empirical vdW-DF[32,33] have been proposed. In our calculations, we use PBE functional with DFT-D2 dispersion corrections.

1.5 Dissertation Scope

The work in this thesis advances the current understanding of the effects of flexibility in MOFs on their adsorption properties. We also study the adsorption and diffusion of CWAs and simulants in MOFs and compare their properties. Finally, we discuss the replicability of MOFs synthesis by literature-analysis and discuss the accuracy of a simple power-law model for the frequency of repeat syntheses.

Chapter 2 presents a detailed and systematic study on the effects of constant volume flexibility in 100 randomly selected MOFs for a variety of adsorbates and mixtures. These results quantify the significance of the effect of flexibility with $\Delta V=0$ on adsorption at dilute and non-dilute loadings and examine whether there is any correlation between the effects of flexibility at different loadings.

Chapter 3 extends the study of flexibility with $\Delta V=0$ to flexibility with $\Delta V\neq0$ in MIL-53 series for xylene adsorption. This work considers the flexibility effects on single component and multi-component adsorption of xylene isomers in MIL-53 and discusses whether the flexibility effects are dependent on the metal-center in MIL-53 series.

Chapter 4 is motivated by the lack of knowledge regarding the accuracy of simulants in predicting the adsorption properties of CWAs in nanoporous materials. This chapter explores how useful common simulants of CWAs are at predicting adsorption behavior in nanoporous materials.

Chapter 5 determine diffusion coefficients of CWAs and simulants. We compare the diffusion properties to evaluate which simulant could better represent the kinetics of CWA diffusion in adsorbents.

Chapter 6 assess how often synthesis of a newly reported material is repeated in the scientific literature. We also present a simple power law model for the frequency of repeat syntheses and assess the validity of this model using MOFs.

1.6 References

(1) James, S. L. Metal-organic frameworks. *Chem. Soc. Rev.* **2003**, *32* (8), 276–288.

(2) Zhou, H. C.; Long, J. R.; Yaghi, O. M. Introduction to metal-organic frameworks. *Chem. Rev.* **2012**, *112* (2), 673–674.

(3) Zhou, H. C.; Kitagawa, S. Metal-Organic Frameworks (MOFs). *Chem. Soc. Rev.* **2014**, *43* (16), 5415–5418.

(4) Groom, C. R.; Bruno, I. J.; Lightfoot, M. P.; Ward, S. C. The Cambridge Structural Database. *Acta Cryst.* **2016**, *B72*, 171–179.

(5) Baerlocher, C.; McCusker, L. B. Database of Zeolite Structures: http://www.izastructure.org/databases/. *Struct. Comm. Int. Zeolite Assoc.* **1996**.

(6) Zhang, J.-P.; Zhou, H.-L.; Zhou, D.-D.; Liao, P.-Q.; Chen, X.-M. Controlling flexibility of metal–organic frameworks. *Natl. Sci. Rev.* **2017**, 907–919.

(7) Schneemann, A.; Bon, V.; Schwedler, I.; Senkovska, I.; Kaskel, S.; Fischer, R. A. Flexible metal-organic frameworks. *Chem. Soc. Rev.* **2014**, *43* (16), 6062–6096.

(8) Bousquet, D.; Coudert, F. X.; Fossati, A. G. J.; Neimark, A. V.; Fuchs, A. H.; Boutin, A. Adsorption induced transitions in soft porous crystals: An osmotic potential approach to multistability and intermediate structures. *J. Chem. Phys.* **2013**, *138* (17).

(9) Coudert, F. X.; Boutin, A.; Fuchs, A. H.; Neimark, A. V. Adsorption deformation and structural transitions in metal-organic frameworks: From the unit cell to the crystal. *J. Phys. Chem. Lett.* **2013**, *4* (19), 3198–3205.

(10) Agrawal, M.; Bhattacharyya, S.; Huang, Y.; Jayachandrababu, K. C.; Murdock, C. R.; Bentley, J. A.; Rivas-Cardona, A.; Mertens, M. M.; Walton, K. S.; Sholl, D. S.; et al. Liquid-Phase Multicomponent Adsorption and Separation of Xylene Mixtures by Flexible MIL-53 Adsorbents. *J. Phys. Chem. C* **2018**, *122* (1), 386–397.

(11) Triguero, C.; Coudert, F. X.; Boutin, A.; Fuchs, A. H.; Neimark, A. V. Mechanism of breathing transitions in metal-organic frameworks. *J. Phys. Chem. Lett.* **2011**, *2* (16), 2033–2037.

(12) Mellot-Draznieks, C.; Serre, C.; Surblé, S.; Audebrand, N.; Férey, G. Very large swelling in hybrid frameworks: A combined computational and powder diffraction study. *J. Am. Chem. Soc.* **2005**, *127* (46), 16273–16278.

(13) Kitaura, R.; Seki, K.; Akiyama, G.; Kitagawa, S. Porous coordination-polymer crystals with gated channels specific for supercritical gases. *Angew. Chemie - Int. Ed.* **2003**, *42* (4), 428–431.

(14) Gee, J. A.; Sholl, D. S. Effect of Framework Flexibility on C_8 Aromatic Adsorption at High Loadings in Metal-Organic Frameworks. *J. Phys. Chem. C* **2016**, *120* (1), 370–376.

(15) Agrawal, M.; Sholl, D. S. Effect of intrinsic flexibility on adsorption properties of metal-organic frameworks at dilute and non-dilute loadings. *ACS Appl. Mater. Interfaces* **2019**, *11*, 31060–31068.

(16) Witman, M.; Ling, S.; Jawahery, S.; Boyd, P. G.; Haranczyk, M.; Slater, B.; Smit, B. The Influence of Intrinsic Framework Flexibility on Adsorption in Nanoporous Materials. *J. Am. Chem. Soc.* **2017**, *139* (15), 5547–5557.

(17) Geoghegan, J.; Tong, J. L. Chemical warfare agents. *Contin. Educ. Anaesthesia, Crit. Care Pain* **2006**, *6* (6), 230–234.

(18) Momenitaheri, M.; Cramer, C. J.; Momeni, M. R.; Cramer, C. J. Computational Screening of Roles of Defects and Metal Substitution on Reactivity of Different Single- vs Double-Node Metal – Organic Frameworks for Sarin Decomposition Computational Screening of Roles of Defects and Metal Substitution on Reactivity of Dif. **2019**, No. 1.

(19) Momeni, M. R.; Cramer, C. J. Dual Role of Water in Heterogeneous Catalytic Hydrolysis of Sarin by Zirconium-Based Metal-Organic Frameworks. *ACS Appl. Mater. Interfaces* **2018**, *10* (22), 18435–18439.

(20) Darunte, L. A.; Oetomo, A. D.; Walton, K. S.; Sholl, D. S.; Jones, C. W. Direct Air Capture of CO_2 Using Amine Functionalized MIL-101(Cr). *ACS Sustain. Chem. Eng.* **2016**, *4*, 5761–5768.

(21) Matito-Martos, I.; Moghadam, P. Z.; Li, A.; Colombo, V.; R Navarro, J. A.; Calero, S.; Fairen-Jimenez, D. Discovery of an Optimal Porous Crystalline Material for the Capture of Chemical Warfare Agents. *Chem. Mater.* **2018**, *30*, 4571–4579.

(22) Chung, Y. G.; Camp, J.; Haranczyk, M.; Sikora, B. J.; Bury, W.; Krungleviciute, V.; Farha, O. K.; Sholl, D. S.; Snurr, R. Q. Computation-Ready, Experimental Metal−Organic Frameworks: A tool to enable high-throughput screening of nanoporous crystals. *Chem. Mater.* **2014**, *26*, 6185–6192.

(23) Frenkel, D.; Smit, B. *Understanding Molecular Simulations: From Algorithms to Applications*, 2nd ed.; Academic Press, Inc., 2001.

(24) Jones, J. E. On the Determination of Molecular Fields.—II. From the Equation of State of a Gas. *Proc. R. Soc. a* **1924**, *106*, 463–477.

(25) Rubinstein, R. Y.; Kroese, D. P. *Simulation and the Monte Carlo Method*; Wiley, 1981.

(26) Binder, K. *Monte Carlo Methods in Statistical Physics*; Springer Science &

Business Media, 2012.

(27) Sholl, D. S.; Steckel, J. A. *Density Functional Theory: A Practical Introduction*; 2011.

(28) Schrödinger, E. An undulatory theory of the mechanics of atoms and molecules. *Phys. Rev.* **1926**, *28* (6), 1049–1070.

(29) Perdew, J. P.; Chevary, J. A.; Vosko, S. H.; Jackson, K. A.; Pederson, M. R.; Singh, D. J.; Fiolhais, C. Atoms, molecules, solids, and surfaces: Applications of the generalized gradient approximation for exchange and correlation. *Phys. Rev. B* **1993**, *48* (7), 4978.

(30) Perdew, J. P.; Burke, K.; Ernzerhof, M. Generalized gradient approximation made simple. *Phys. Rev. Lett.* **1996**, *77* (18), 3865–3868.

(31) Fias, S.; Damme, S. Van; Bultinck, P. Semiempirical GGA-Type Density Functional Constructed with a Long-Range Dispersion Correction. *... Comput. Chem.* **2006**, *27*, 1787–1799.

(32) Dion, M.; Rydberg, H.; Schröder, E.; Langreth, D. C.; Lundqvist, B. I. Van der Waals density functional for general geometries. *Phys. Rev. Lett.* **2004**, *92* (24), 22–25.

(33) Lee, K.; Murray, É. D.; Kong, L.; Lundqvist, B. I.; Langreth, D. C. Higher-accuracy van der Waals density functional. *Phys. Rev. B - Condens. Matter Mater. Phys.* **2010**, *82* (8), 3–6.

CHAPTER 2. EFFECT OF CONSTANT VOLUME FLEXIBILITY ON ADSORPTION IN METAL-ORGANIC FRAMEWORKS*

2.1 Introduction

Metal-organic frameworks (MOFs) have attained significant attention in the scientific community due to their diverse applications in gas storage, separations, catalysis, sensing, and drug delivery. MOFs have highly tunable chemical and geometrical properties, high surface area and a wide range of pore sizes. One interesting aspect of MOFs is the flexibility of the frameworks can be responsive to external stimuli such as adsorption of guests, temperature, pressure, light irradiation and mechanical forces[1–5]. Structural flexibility in MOFs can be divided into two classes: variations resulting in changes in the unit cell volume and changes that occur without variation in the unit cell volume, V. Flexibility with $\Delta V \neq 0$, which includes breathing, swelling and subnetwork displacement, has been extensively studied[6,7]. It is important to note, however, a material that goes through significant variations in volume may cause significant operational complications in many practical applications. It is therefore not clear from an applied point of view whether the subset of MOFs with these properties are desirable. Flexibility that occurs with $\Delta V = 0$ includes effects such as thermal vibrations and linker rotation[5,6,8–10]. This second kind of flexibility occurs in all MOFs. It is therefore interesting to understand how modes of flexibility with $\Delta V = 0$ affect the properties of MOFs.

* Material in this chapter has been previously published as Agrawal, M; Sholl, D.S. "Effect of Intrinsic Flexibility on Adsorption Properties of Metal-Organic Frameworks at Dilute and Nondilute Loadings" *ACS Appl. Mater. Interfaces* **2019**, 11, 34, 31060-31068

Molecular simulations have become a useful tool for predicting the adsorption properties of molecules in diverse collection of MOFs and similar materials. These simulations have been used to predict the adsorption properties of a diverse range of molecules in large libraries of MOF structures.[11–18] In almost all molecular simulations of adsorption in MOFs to date, the MOF structure is assumed to be rigid. This assumption is made for reasons of both computational efficiency and convenience; performing simulations with flexible MOFs is far more computationally intensive and also requires specification of more complex force fields (FFs). Even in simulations that examine adsorption in MOFs with breathing modes and related phenomena, a typical approach is to perform simulations for a range of distinct rigid crystal structures and then to combine these results using appropriate thermodynamic criteria.[19,20]

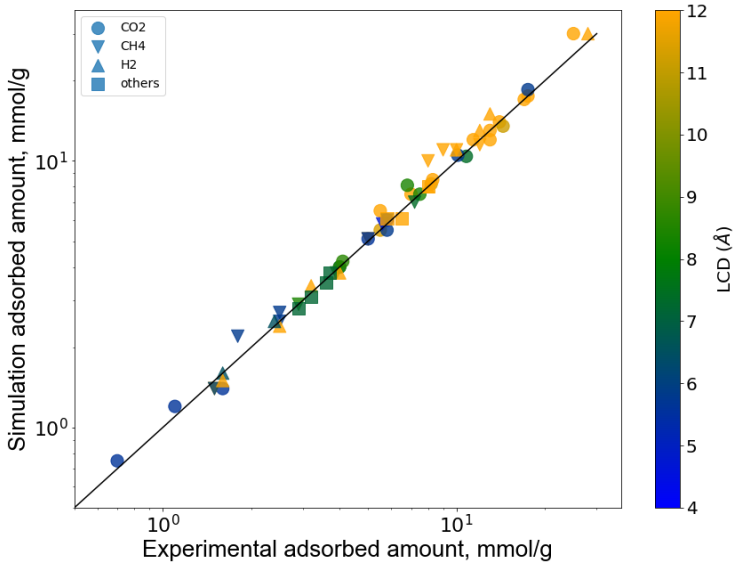

Figure 2.1: Comparison of adsorption uptake of various adsorbates in a range of MOFs between experiments and GCMC simulated values using rigid crystal structures (●=CO_2, ▼=CH_4, ▲=H_2 and ■=other adsorbates) from previous literature. Details of all data points are given in Appendix 2.A.

One common justification for approximating MOFs as rigid during simulations of adsorption is that predictions from this approach are often consistent with experiments. We illustrate this point in **Figure 2.1** with data from rigid structure calculations from 24 studies on 20 different MOFs and 9 different molecules.[21–43] Details of all data points and the force fields (FFs) used in each simulation are given in the **Table 2.A.2**. Most of these simulations used generic FFs such as UFF[44], DREIDING[45], TraPPE[46] and OPLS.[47] Simulation results that were obtained by directly fitting the underlying FF to the experiments used for comparison were excluded from this data set. There are, however, simulation data points in **Figure 2.1** that were scaled by the authors of the simulation studies based on the difference in experimental and theoretical surface area. Park et al.[48] compared experimental results with simulations using 'standard' force fields and rigid crystal structures for CO_2 adsorption for all MOFs for which more than three independent experimental isotherms are available. They found that the simulations results for almost all of the materials overlap with the experimental data when a 15% relative error is allowed.

Despite the apparent success of modeling adsorption in MOFs using rigid structures, there are several studies that suggest that the flexibility with $\Delta V = 0$ in MOFs can significantly affect adsorption. Gee et al.[10] used the so-called 'flexible snapshots' method to show that constant volume flexibility in MIL-47 significantly affects the adsorption selectivity of C_8 aromatic isomers. This work found that the inclusion of framework flexibility in molecular simulations decreased the selectivity of o-xylene to ethylbenzene by an order of magnitude relative to simulations using rigid structures. The lower selectivity predicted by the more detailed calculations was in reasonable agreement with experimental observations. In a recent study, Witman et al.[12] studied the effect of

flexibility on Xe/Kr selectivity in ~3000 MOFs using a model that predicts a material's Henry regime adsorption and selectivity as a function of flexibility. The results obtained from this model were compared with molecular simulations at dilute loadings using the flexible snapshots method at 298 K. Witman et al. concluded that the selectivity of Xe/Kr mixture can increase or decrease by up to 2 orders of magnitude due to inclusion of $\Delta V = 0$ framework flexibility.

These two papers raise the possibility that there in some but not all situations, including framework flexibility in MOFs is necessary to achieve a quantitative description of adsorption in these materials. A limitation of the work by Witman et al.[12] is that it only considered adsorption at dilute loadings and that the analytical model introduced by the authors only applied to spherical molecules. It is conceivable that the impact of MOF flexibility on adsorption is most pronounced at dilute loadings, but it is not possible to test this hypothesis with data already available in the literature. This observation motivated us to use molecular simulations to systematically study the impact of $\Delta V = 0$ flexibility of MOFs on adsorption properties for a range of molecular mixtures at dilute and non-dilute loadings. To do so, we simulated the adsorption properties of five mixtures (CO_2/CH_4, ethane/ethene, propane/propene/butane, and Xe/Kr) at dilute and finite loadings in a set of 100 MOFs randomly chosen from CoRE MOF database.[49] Our simulations demonstrate that the flexibility can either increase or decrease selectivity for all mixtures for a given material at both dilute and finite loadings. Results obtained for Xe/Kr mixtures at dilute loadings are in good agreement with the work of Witman et al.[12] We quantitatively compare the effect of a framework's flexibility on selectivity depending on the material's pore size and adsorbate diameter and find that molecules with kinetic diameters comparable to the

adsorbing material's pore size are affected the most by framework flexibility. This observation is consistent at both dilute and finite loadings. Further, we demonstrate that there is no clear correlation for the dependence of selectivity on framework flexibility between dilute loadings and finite loadings. This suggests that understanding the overall impact of framework flexibility on adsorption in MOFs cannot be achieved in a simple way from simulations at dilute loadings.

2.2 Simulation Methods

For our calculations, 100 MOF structures were randomly chosen from a subset of the CoRE MOF database[49] consisting of >2900 different crystal structures for which high quality atomic point charges have been reported.[50] The REFCODES for these 100 structures are listed in **Table 2.A.3**, along with information on the largest cavity diameter (LCD), pore limiting diameter (PLD) and BET surface area of each structure. All structures in the CoRE MOF database are derived from experimentally reported crystal structures assuming that all free solvent was removed from the crystal. Our simulations used FF-based Monte Carlo (MC) simulations as implemented in RASPA[51] to calculate adsorption properties of nine different compounds that are divided into four different mixtures, CO_2/CH_4, ethane/ethene, propane/propene/butane and Xe/Kr. We studied the adsorption of each adsorbate at non-dilute conditions and each mixture at dilute and non-dilute conditions at room temperature.

Henry constants, K_H, were computed with the Widom insertion method.[52] These calculations also gave the helium void fraction and heat of adsorption (E_{ads}) in the limit of zero loading. We used equilibration and production periods of $1*10^5$ MC cycles;

preliminary tests indicated that this was sufficient to get well converged results. To study adsorption at non-dilute conditions, Grand Canonical Monte Carlo (GCMC) simulations were performed using equilibrium and production periods of $5*10^5$ MC cycles. Each MC cycle consisted of a trial insertion, deletion, reinsertion, translation, or rotation with equal probability. Our multicomponent GCMC simulations also included an additional MC move for exchanging adsorbed molecules to improve convergence. For non-dilute simulations, the composition of all mixtures was taken to be equimolar in the bulk phase and external pressures were chosen to give moderate to high loadings. Multicomponent simulations were performed for CO_2/CH_4 and ethane/ethene mixtures at a total pressure of 20 bar, for Xe/Kr mixtures at 40 bar and for propane/propene/butane mixtures at 10 bar.

The adsorption selectivity of a mixture at dilute loading is defined without approximation as the ratio of the single component Henry constants,[53] while the adsorption selectivity of a mixture at finite loading is defined by,

$$\alpha_i = \frac{q_i}{\sum_{j,j\neq i} q_j} \times \frac{\sum_{j,j\neq i} p_j}{p_i} \qquad (2.1)$$

where α_i is the selectivity of the i^{th} component relative to all other components in the mixture, q_i is the loading of i^{th} component, and p_i is the external partial pressure of the i^{th} component.

Adsorbate-adsorbate interactions were defined using the TraPPE FF.[46] Adsorbate-MOF interactions were defined using Lorentz-Berthelot mixing rules with Lennard-Jones parameters taken from UFF[44] for the framework and the TraPPE[46] for the adsorbates. Coulombic interactions were computed using the Ewald method with a precision of 10^{-6} and a 13 Å cutoff. Point charges of atoms in MOFs were previously assigned using the

DDEC method[50,54] and point charges on atoms in adsorbates were taken from TraPPE.[46] LJ potentials were truncated at a spherical cutoff distance of 13 Å.

All MOF degrees of freedom were described using modified universal force field introduced by Coupry et al. for MOFs known as UFF4MOF[55]. For calculations using rigid structures we first relaxed the MOF structure reported by the CoRE MOF database using classical FFs in the LAMMPS package[56] and then fixed the atoms in the relaxed structure while performing Monte Carlo simulations. To probe the effect of framework flexibility on adsorption, we used the flexible snapshot method developed by Gee et al.[10]. In this approach an ensemble of empty MOF structures is generated by simulating the dynamics of the MOF and GCMC simulations are then performed independently for each structure in the ensemble. This approach is similar to what was used by Witman et al. to study the effect of flexibility on Xe/Kr selectivity at dilute loadings.[12] This method includes effects associated with $\Delta V = 0$ flexibility in the MOFs (e.g. variations in MOF coordinates due to thermal fluctuations), but it cannot give information on possible aspects of MOF flexibility that arise due to coupling with adsorbate degrees of freedom. We performed NVT MD simulations after structure relaxation using LAMMPS at 300 K to account for the flexibility without volume change in the selected MOFs. The temperature in these simulations was controlled using Nosé-Hoover thermostat with decay period of 0.1 ps. MD simulations were performed with a time step of 1.0 fs for an equilibration period of 500 ps and production period of 1 ns. The computational expense of the flexible snapshot method is dominated by the number of distinct snapshots are used, since an independent GCMC simulation must be performed for every snapshot. It is therefore important to select snapshots from structures that are uncorrelated. To this end, snapshots from our MD

simulations were taken every 100 ps from the production period for a total of 10 snapshots. Adsorption properties of flexible materials were described using data averaged over these 10 snapshots. It is also possible to generate MOF snapshots using ab initio MD, which has the advantage of not requiring a FF, but this approach is far more computationally intensive.[57,58]

2.3 Results and Discussions

2.3.1 Effect of flexibility in MOFs on single component adsorption at non-dilute loadings

We first consider single component adsorption in MOFs at high pressures. As shown in **Figure 2.1**, previous literature suggests that simulations using rigid structures are often able to predict single component adsorption in MOFs. To explicitly test the role of the rigid structure approximation, we performed single component adsorption calculations for CO_2, CH_4, ethane, ethene, propane, propene, butane, Xe and Kr at 20 bar, 20 bar, 20 bar, 20 bar, 10 bar, 10 bar, 10 bar, 40 bar and 40 bar respectively. These pressures were chosen to give moderate to high loadings at 298 K. The rigid and flexible single component adsorption uptakes (q_r and q_f) of these 9 adsorbates in 100 MOFs and a histogram of their ratio are shown in **Figure 2.2**. Although including flexibility can influence the adsorption uptake, this effect is not strong. All of the examples we considered show a difference of less than 30% between the rigid and flexible calculations, and the average absolute error between the two sets of calculations is 6.2%. The impact of flexibility is reduced in MOFs with large pores; the average absolute error for MOFs with LCD < 6 Å (LCD > 6 Å) is 9% (5%).

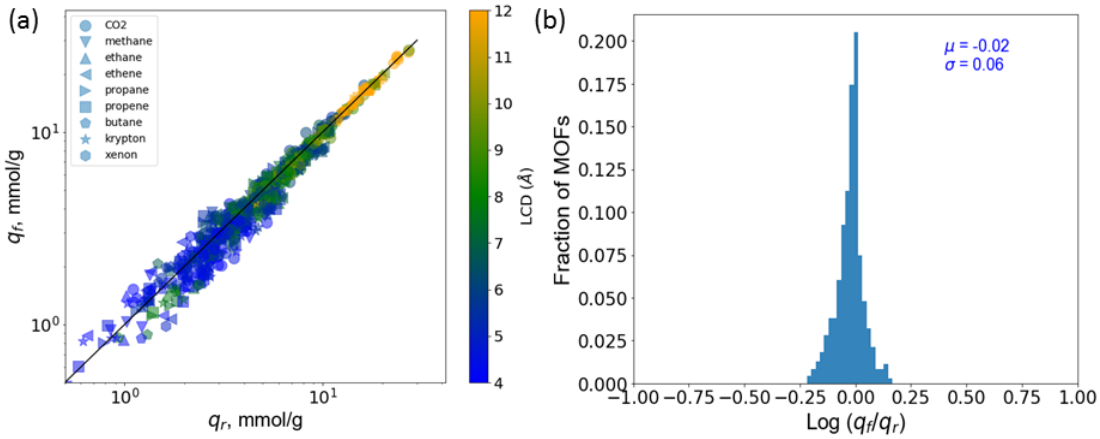

Figure 2.2: (a) Parity plot of single component adsorbed amounts, (b) histogram of the ratio of single component adsorbed amounts, using rigid (q_r) and flexible (q_f) simulations, for 9 adsorbates in 100 MOFs at high pressures (CO_2, CH_4, ethane and ethene: 20 bar each, Xe and Kr: 40 bar each, propane, propene and butane: 10 bar each). The data points in the plot (a) are color coded based on the LCD of each MOF.

It is important to consider whether these results are consistent with the studies discussed above that showed strong effects due to including framework flexibility.[10,12] The work of Gee at al.[10] and Witman et al.[12] examined different adsorption properties than the high pressure single component results shown in **Figure 2.2**. This hints that different kinds of adsorption properties can have different sensitivity to framework flexibility. An example is the work of Gee et al., which showed[36] that calculations using rigid structures approximation gave useful results for single component adsorption isotherms of C_8 aromatics in MIL-47 but that simulations with the same FFs do not accurately predict the selectivity of C_8 aromatic mixtures.[10] To examine this issue further, we studied the effect of flexibility on Henry constants (that is, adsorption at dilute loadings) and mixture selectivity at both dilute and non-dilute loadings.

2.3.2 Effect of flexibility in MOFs on adsorption properties at dilute loadings

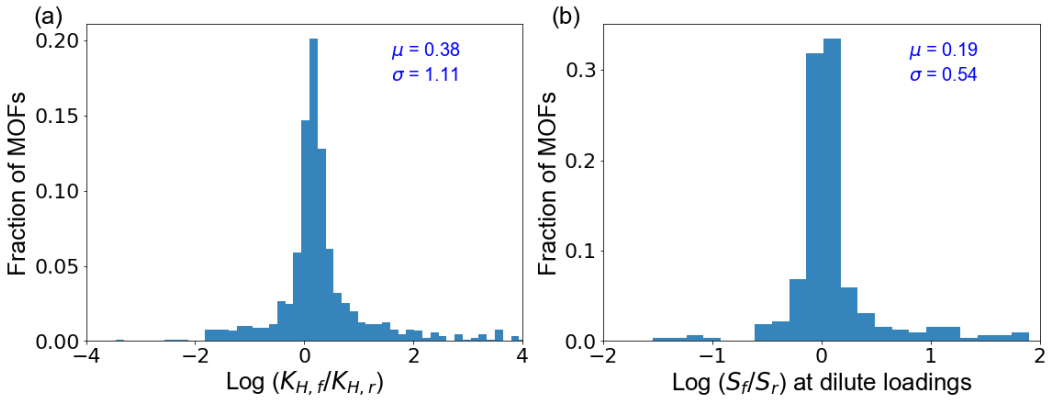

Figure 2.3: Histogram of the ratio of room temperature (a) Henry constants of 9 adsorbates and (b) selectivity of 4 mixtures in 100 MOFs in simulations using flexible and rigid simulations. Mean μ and standard deviation σ are shown for each data set.

In the limit of dilute adsorption, the Henry's constant characterizes adsorption affinity for both pure components and adsorbed mixtures. We calculated the Henry's constants of all 9 adsorbates in the 100 MOFs listed in **Table 2.A.3** using both flexible ($K_{H,f}$) and rigid simulations ($K_{H,r}$). **Figure 2.3a** shows the ratios of the resulting Henry constants. If adsorption in a MOF was completely unaffected by flexibility, the logarithmic ratio shown in **Figure 2.3a** would be zero. **Figure 2.3a** shows, however, that framework flexibility can change the Henry's constants by as much as two orders of magnitude. Out of 900 data points in the histogram, 319 MOF-adsorbate pairs have $|\log(K_{H,f}/K_{H,r})| < 0.1$, which means that change in Henry constants due to flexibility is less than ~25%. 413 pairs have $0.1 < |\log(K_{H,f}/K_{H,r})| < 1$, meaning the change in Henry constants due to flexibility is between a factor of 1.25 and 10, and 72 pairs have $1 < |\log(K_{H,f}/K_{H,r})| < 2$. There are 42 MOF-adsorbate pairs for which $|\log(K_{H,f}/K_{H,r})| > 4$, representing cases where flexibility has an enormous effect on adsorption. In most of these extreme cases, the MOFs have pore

sizes very similar to the adsorbing molecule's diameter. **Figure 2.A.1** shows the histogram of the ratio of $K_{H,f}$ and $K_{H,r}$ for each adsorbate with the standard deviations individually. **Figure 2.A.1** shows that the standard deviations are consistently higher for the larger molecules among the 9 adsorbates, indicating that flexibility typically has more significant effects on larger molecules.

Figure 2.3a makes it clear that in at least a fraction of MOFs, framework flexibility strongly influences adsorption of individual molecules at dilute loadings. However, it might be expected (or perhaps hoped) that these effects might partially cancel when the separation of a mixture is studied if the changes in K_H among different adsorbates are correlated. **Figure 2.3b** shows the impact of framework flexibility at dilute loading for the selectivity for CO_2/CH_4, ethane/ethene, propane/propene/butane and Xe,/Kr mixtures in each MOF. Although the impact of flexibility on selectivity is often less than for the individual adsorbed amounts, there are still plentiful examples where the effect is not negligible. 30% of the MOF-adsorbate pairs show a change in Henry constants less than 25% due to flexibility, but almost 45% of the MOF-mixture pairs show a similar low change in selectivity. The Henry's constants in 46% of the MOF-adsorbate pairs changed by more than a factor of 2 ($|\log(K_{H,f}/K_{H,r})|>0.3$) while the selectivity in 36% of the MOF-mixture pairs changed by more than the same factor. We examine this situation in more detail in **Figure 2.4** by showing the impact of flexibility on mixture selectivity for the four different mixtures. The regions shaded in light-blue in **Figure 2.4** indicate cases where the rigid and flexible simulations make qualitatively different predictions for which molecule in the mixture is favorably adsorbed. This occurs more commonly in examples where the overall selectivities are moderate (e.g. ethane/ethene) than when typical selectivities are

higher (e.g. CO_2/CH_4). For CO_2/CH_4 mixtures, selectivities as high as 10^4 are predicted and the effect of flexibility gets stronger (on average) as the selectivity increases.

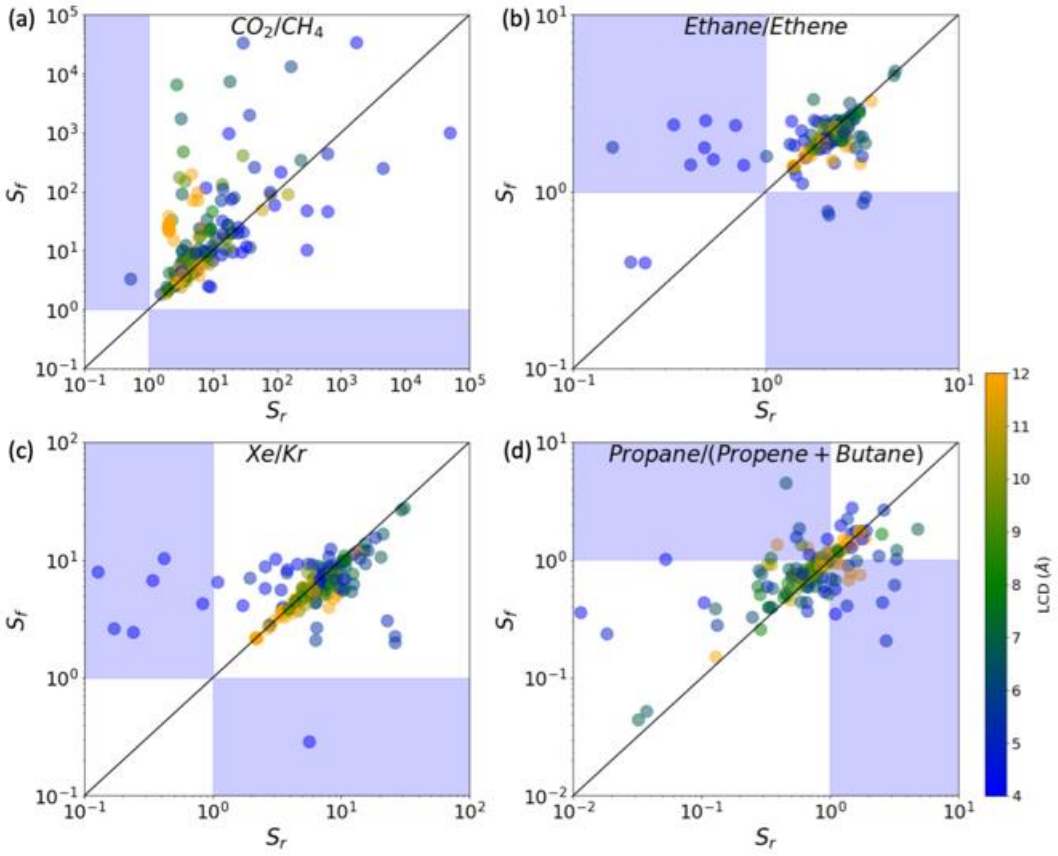

Figure 2.4: Dilute loading mixture selectivities at room temperature in 100 MOFs calculated using flexible simulations (vertical axes) and rigid simulations (horizontal axes) for (a) CO_2/CH_4, (b) ethane/ethene, (c) Xe/Kr, and (d) propane/propene/butane. The data points are color coded based on the LCD of each MOF.

Figure 2.2 and **Figure 2.4** hints that the MOFs whose properties are most strongly affected by their flexibility have diameters below 6 Å. To probe this further, we show the ratios of Henry's constants as a function of Δd, the difference between the adsorbate's kinetic diameter and the MOF's in **Figure 2.5**. The kinetic diameter of a molecule is not a rigorously defined quantity, but it is a useful proxy for molecular size (see **Table 2.A.1**). In MOFs whose cavities are much larger than the adsorbing molecule, the effects of

flexibility on adsorption are typically small except for CO_2, which may be associated with the observation that this is the only charged molecule we simulated. To further explore this issue, we calculated the Henry constants of CO_2 while turning off electrostatic interactions of the molecule with the framework and found that these (unphysical) not-charged CO_2 molecules show behavior consistent with other not-charged molecules (see **Figure 2.A.2**). These observations indicate that flexibility can have significant effects even for some MOFs that have much larger LCDs than the adsorbate's kinetic diameter when electrostatic interactions are important. **Figure 2.5** has some data points for which $\Delta d < 0$, which might superficially suggest that molecules cannot adsorb at all. To avoid being misled by examples in which adsorption is negligible, we excluded from **Figure 2.5** any examples for which the simulated adsorbed loading was less than 0.5 mmol/g at high pressures. Correlations between our simulated Henry constants with the MOF's LCDs and Δd are shown in **Figure 2.A.3** and **Figure 2.A.4**. We performed similar calculations for heats of adsorption of all adsorbates and found that values of Henry constants and heats of adsorption are strongly correlated with each other calculated using both rigid and flexible calculations (see **Figure 2.A.5**). This observation is consistent with one of previous studies on adsorption properties of CWAs in MOFs[11] which indicates that flexibility effects on heat of adsorption would be similar to its effects on Henry constants. Further, the effect of flexibility on the heats of adsorption are described in **Figure 2.A.6** and **Figure 2.A.7** which support our argument.

It is clear from the discussion above that flexibility in a MOF can significantly affect its adsorption properties at dilute loadings. MOFs that have LCDs comparable to the kinetic diameters of the adsorbates of interest have the largest effects of flexibility on their

adsorption properties. These conclusions are entirely consistent with the previous work by Witman et al.[12] for Xe/Kr mixtures at dilute loadings.

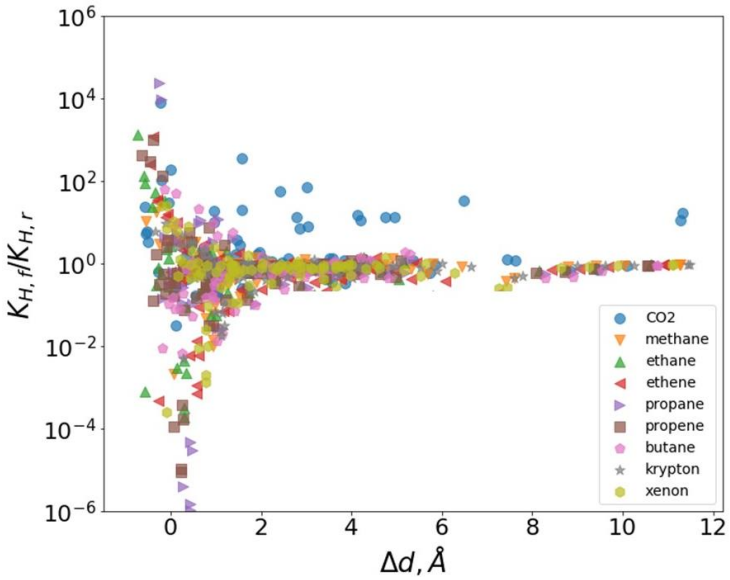

Figure 2.5: Ratio of Henry's constants ($K_{H,f}/K_{H,r}$) in simulations with flexible and rigid MOFs as a function of Δd , the difference between the MOF's LCD and the adsorbate's kinetic diameter.

2.3.3 Effect of flexibility in MOFs on multicomponent adsorption at high loadings

We now consider adsorption selectivity at non-dilute loadings. For non-dilute loadings, we performed multicomponent GCMC simulations to obtain adsorption selectivities for each mixture. In these calculations all bulk mixtures are equimolar and pressures were chosen to give moderate (although not necessarily saturated) pore loadings. **Figure 2.6** shows the impact of flexibility on selectivity at non-dilute loadings. About 50% of the MOF-adsorbate pairs show a change in selectivity less than 25% due to flexibility at non-dilute loadings, similar to the 45% of MOF-mixture pairs at dilute loadings. The selectivity in 27% of cases we considered changed by more than a factor of 2 ($|\log(S_f/S_r)|>0.3$) at non-dilute loadings, compared to 35% at dilute loadings. As with the

results for dilute conditions, there are multiple examples at non-dilute conditions for which the identity of the species that is selectively adsorbed is changed when flexibility is included (shown by the shaded regions in **Figure 2.A.8**). As for dilute loadings, MOFs that have LCDs comparable to the kinetic diameters of the adsorbates in the mixture are affected the most by flexibility (see **Figure 2.A.9**).

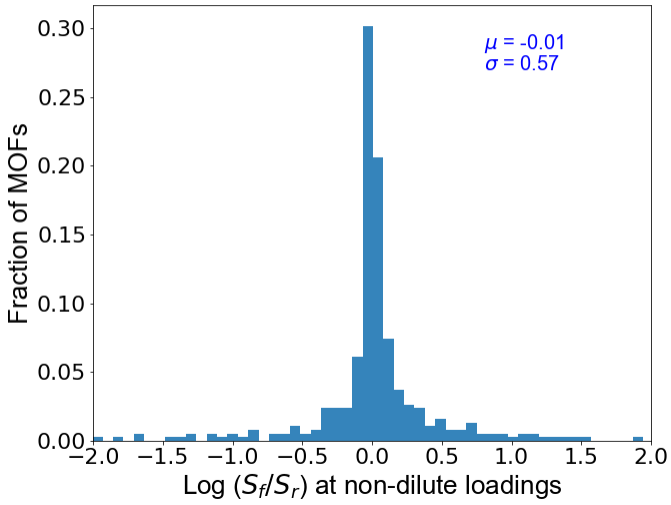

Figure 2.6: Histogram of the ratio of flexible and rigid room temperature selectivity at non-dilute loadings of 4 mixtures of CO_2/CH_4 at P_{total}=20 bar, ethane/ethene at P_{total}=20 bar, Xe/Kr at P_{total}=40 bar, and propane/(propene + butane) at P_{total}=10 bar in 100 MOFs. Mean μ and standard deviation σ are shown for each data set.

2.3.4 Comparison of the effect of flexibility in MOFs on different adsorption properties

The standard deviations for the ratio of various adsorption properties in rigid and flexible MOFs are summarized in **Table 2.1**. Our results show that single component adsorption uptakes in the dilute limit (i.e. Henry's constants) are far more sensitive to the inclusion of framework flexibility than adsorption uptake at moderate and high loadings. Adsorption selectivity is more sensitive to the inclusion of flexibility than single component loadings at non-dilute conditions, but there is not a significant difference

between the sensitivity of adsorption selectivities at dilute and non-dilute conditions. Interestingly, these results imply that on average the effects of framework flexibility tend to partially cancel out between different species at dilute conditions but under non-dilute conditions adsorption selectivity is more strongly impacted by flexibility than the individual loadings.

Table 2.1: Standard deviations of the logarithmic ratio of adsorption properties using flexible and rigid simulations for Henry's constants, K_H, adsorption selectivities, S, and adsorbed amounts, q.

	All MOFs	MOFs with LCD < 6Å
Std(log10($K_{H,f}/K_{H,r}$)) at dilute loading	1.11	1.58
Std(log10(S_f/S_r)) at dilute loading	0.54	0.69
Std(log10(S_f/S_r)) at non-dilute loadings	0.57	0.71
Std(log10(q_f/q_r)) non-dilute loadings	0.06	0.08

With the exception of the single-component loadings at non-dilute loadings, all of the standard deviations listed in **Table 2.1** correspond to effects that are large relative to usual thinking about the precision of computational predictions for adsorption in nanoporous materials. If these standard deviations are used to define an interval estimate, then a mixture selectivity for a flexible structure can be expected to lie within [$0.27S_r$, $3.7S_r$], where S_r is the result from a rigid material. This interval estimate is wider if attention is restricted to molecule/MOF pairs where the adsorbing molecule is similar in size to the MOF's pores. If experimental data was reported with uncertainties that are similar in range it is not clear that such data would be viewed as useful. This observation suggests that the impact of framework flexibility on adsorption selectivity in nanoporous materials may have

been underappreciated and may require more careful consideration in the future. The situation for understanding single component adsorption is perhaps less dramatic. The interval estimate for q_f implied by **Table 2.1** is [0.87q_r, 1.15qr].

From a computational point of view, simulations at dilute loading are much less demanding than simulations at non-dilute loadings. This observation has been used by Tang et al. to develop methods that predict complete isotherms based solely on dilute loading simulations and textural information about the adsorbing material.[59] In our calculations, a similar percentage of MOF-adsorbate pairs show change in selectivity due to flexibility at dilute and non-dilute conditions. An obvious question that emerges is whether it is possible to easily predict the effect of flexibility at non-dilute loadings from simulations at dilute conditions. To answer this question, we compared the ratio of rigid and flexible mixture selectivities for both dilute and non-dilute conditions in **Figure 2.7**. Although the variance in the relative impact of flexibility on selectivity is not significantly different between the two situations, there is not a clear correlation between the effect of flexibility at dilute loadings and non-dilute loadings. More specifically, the Pearson product-moment correlation coefficient[60] is 0.66, 0.83, 0.93 and 0.75 for CO_2/CH_4, ethane/ethene, Kr/Xe and propane/(propene+butane) mixtures, respectively. Further detail is provided for individual mixtures in **Figure 2.A.10**. The effect of flexibility at dilute and non-dilute conditions is the least correlated for CO_2/CH_4 mixtures and it is the most correlated for Kr/Xe mixtures. This hints that the approximate model for spherical species at dilute loadings developed by Witman et al.[12] may be of limited applicability in predicting the sensitivity to flexibility in more complex adsorbed mixtures.

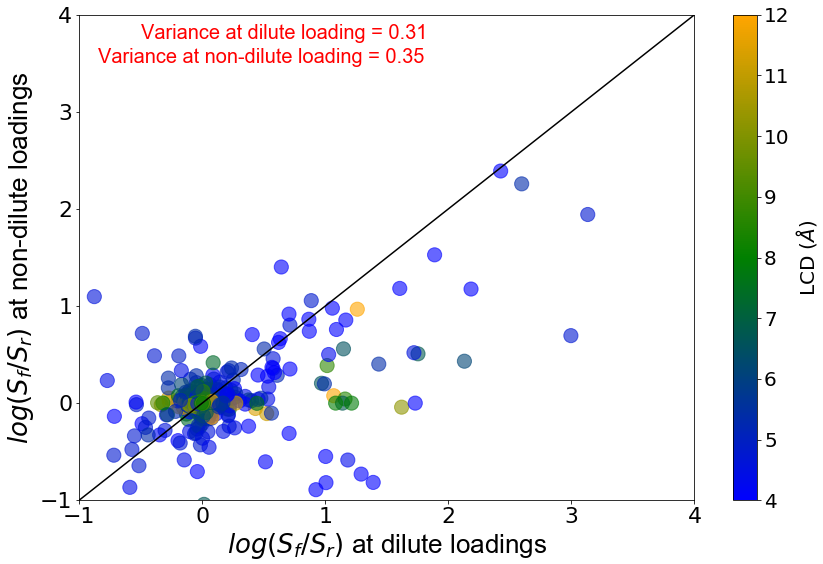

Figure 2.7: Ratio of room temperature flexible and rigid selectivities (S_f/S_r) at non-dilute conditions and dilute conditions for 100 MOFs. Data points are color-coded according to the MOF's LCD.

We have established that effects of flexibility on adsorption selectivity at dilute loadings and non-dilute loadings are similar in magnitude but are not always correlated with each other. To better understand the impact of loading, we studied the effect of flexibility on selectivity of equimolar Xe/Kr and CO_2/CH_4 mixtures at different total pressures/loadings in the range of 1 bar to 40 bar. **Figure 2.A.11** compares S_f/S_r at different pressures and shows that the mean and standard deviations at all pressures are similar for both mixtures. **Figure 2.8** shows the Pearson product-moment correlation coefficients between S_f/S_r at different pressures for CO_2/CH_4 and Xe/Kr mixtures. For CO_2/CH_4 mixture (**Figure 2.8a**), the correlation coefficients between S_f/S_r at different pressures are between 0.65 and 0.83, which indicates that even though the means and variances of S_f/S_r are similar the results at one pressure are of limited value to predict the effect of flexibility at another pressure. As might be expected, the correlation coefficients are higher for the pressures that are closer to each other. For Xe/Kr mixtures (**Figure 2.8b**) the correlation

coefficients at all conditions are above 0.9. This suggests that the mathematical model for spherical species at dilute loadings developed by Witman et al.[12] might be useful for predicting flexibility effects at non-dilute conditions for this simple mixture.

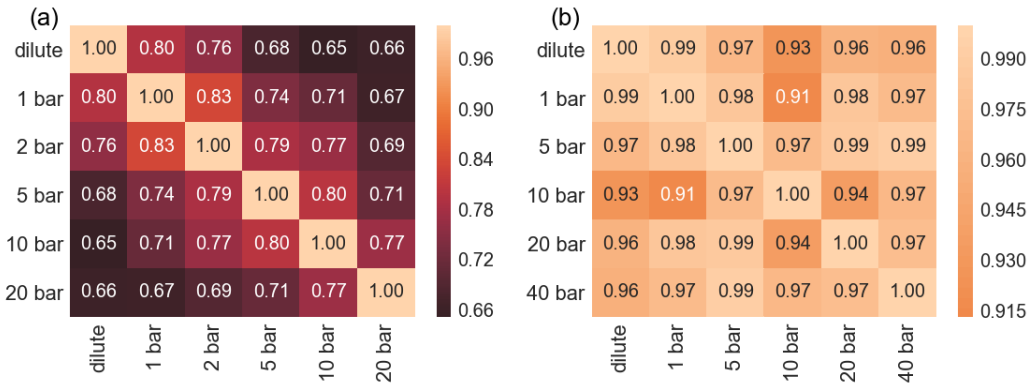

Figure 2.8: Correlation coefficients between S_f/Sr at different loading conditions for (a) CO_2/CH_4, (b) Xe/Kr mixtures. Both mixtures are equimolar, and x and y axis in the plot show the total pressure.

2.4 Summary

In this chapter, we have used molecular simulations to probe the role of framework vibrations on the adsorption properties of MOFs. The effects we examined are relevant to all MOFs, an observation emphasized by our choice to study only flexibility associated with no volume change. The sizeable literature that exists modeling molecular adsorption in MOFs almost uniformly assumes that these flexibility effects can be neglected, an assumption which, if accurate, greatly improves the numerical efficiency of simulating adsorption. We used a "flexible snapshot" approach in which adsorption in multiple realizations of a flexible MOF are separately simulated as rigid structures. This approach is computationally efficient, but it does not account for effects due to deformation or flexibility of the MOF induced by adsorbed species. It seems plausible, however, that if

the effects of flexibility detected by this method are small that the impact of further adsorbate/MOF coupling is also small in many cases. We presented results for multiple adsorbing molecules and adsorbing mixtures in 100 MOFs at both dilute and non-dilute loadings, allowing us to systematically examine several distinct regimes.

A key outcome from our calculations is that the importance of framework flexibility on adsorption in MOFs varies considerably depending on the specific aspect of adsorption of interest. For single component adsorption, the impact of flexibility is much more pronounced in the dilute adsorption limit (that is, for Henry's constants), than it is at non-dilute loadings. In mixture adsorption, the selectivity of adsorption is considering more sensitive to flexibility than the uptake of individual components, an observation that holds at both dilute and non-dilute loadings. These results are fully consistent with previous simulation studies that examined a much smaller range of situations.[10,12]

Our results show that MOFs that have pore sizes comparable to the kinetic diameters of adsorbing molecules are the most affected by framework flexibility. For MOFs that have LCDs less than 6 Å, flexibility affects the Henry constants of the molecules we considered by an average factor of 33. For the same MOFs, flexibility affects the selectivity at dilute and non-dilute by an average factor of 3.5. For about 5% of the examples we considered, including flexibility reversed the predicted selectivity for mixtures. Moreover, we found that the effect of flexibility at dilute loadings does not correlate in a simple way with the effects at non-dilute loadings.

Overall, our results indicate that appropriate consideration of framework flexibility may be important in any effort to make quantitative predictions about molecular adsorption

in MOFs. The snapshot-based approach we have used provides a relatively straightforward means to estimate these effects, albeit one that is 5-10 times more computationally expensive that standard simulation methods based on rigid crystal structures.

APPENDEX 2.A. SUPPORTING INFORMATION FOR CHAPTER 2

Table 2.A.1: Kinetic diameters of molecules

Adsorbate	**Kinetic Diameter, Å**	**Reference**
CO_2	3.76	https://en.wikipedia.org/wiki/Kinetic_diameter
methane	3.8	wikipedia
ethane	4.443	10.1021/ja305663k
ethene	4.163	10.1021/ja305663k
propane	4.3	wikipedia
propene	4.5	wikipedia
butane	4.3	FuelChemistryDivisionPreprints2003-48(1)-436
krypton	3.6	wikipedia
xenon	3.96	wikipedia

Table 2.A.2: Experimental adsorption uptake[a] for MOFs compared with GCMC simulations using rigid structure approximation

Adsorbent	Adsorbate	T (K)	Experimental capacity, mmol/g	Simulation capacity, mmol/g	Force Field (FF) - LJ	FF - Coulombic	Scaling Factor
Bio-MOF-11[21]	CO_2	77	4	4	UFF	CHelpG	1.0
Bio-MOF-11[21]	H_2	77	1.6	1.6		Scheme	1.0
MIL-47[22]	CO_2	298	10.8	10.4	Derived	DFT	1.0
MIL-47[33]	CO2	303	10.3	10.4	Adapted	Adapted	1.0
MIL-47[33]	CH_4	303	7.2	7.0			1.0
ZIF-8[38]	CO_2	298 303	5.5 8.2	5.5 8.2	Scaled to reproduce experiment isotherms	DFT derived	< 1.0
ZIF-8[38]	CH_4	303	5	5.1			< 1.0
ZIF-76[38]	CO_2	303	10	14			< 1.0
ZIF-76[38]	CH_4	303	5	5.1			< 1.0
MgMOF-74[39]	CO_2	300 313	17.5 17	17.5 17	Adapted	Adapted	1.0
IRMOF-1[40]	CO_2	195 208 218	14 13 11.4	14 13 12	Dreiding, TraPPE	TraPPE	1.0
IRMOF-1[41,42]	H_2	298 77	3.2 12	3.4 13	Derived	Derived	1.0
IRMOF-3[40,43]	CO_2	298 313 333 353	8.3 13 7 5.5	8.5 12 7.5 6.5	Dreiding, TraPPE	TraPPE	1.0
MOF-177[40]	CO_2	298	14.4	13.5	Dreiding, TraPPE	TraPPE	1.0

Table 2.A.2 continued…

PCN-26[23]	CO_2	195 273 298	5.8 17.5 10.1	5.5 18.5 10.5	Dreiding, TraPPE	Dreiding, TraPPE	1.0
PCN-26[23]	H_2	77 87	2.5 1.6	2.4 1.5			1.0
PCN-26[23]	CH_4	195 273 298	2.5 2.5 1.8	2.5 2.7 2.2			1.0
UiO-66 (Zr)[24–26]	CO_2	303 273 273	4 6.8 7.5	4 8.1 7.5	UFF, Dreiding, TraPPE	UFF, Dreiding, TraPPE	1.0
UiO-66 (Zr)[24,26]	CH_4	303 273	2.9 3.9	2.9 3.8	Dreiding, TraPPE, OPLS	Dreiding, TraPPE, OPLS	1.0
UiO-66(Ti) [26]	CO_2	273	4.1	4.2			1.0
FeMOF-74[27]	CO_2	298 308 318	7 6 4.9	7.6 6.7 5.2	DFT derived	LoProp method	1.0
Cu-TDPAT[28]	CO_2	298	5.8	6	OPLA-AA, TraPPE	OPLS-AA, TraPPE	1.0
Cu-TDPAT[28]	CH_4	298	5.6	5.8			1.0
HKUST-1[43]	CO_2	313 333 353	1.6 1.1 0.7	1.4 1.2 0.75	Dreiding, TraPPE	Dreiding, TraPPE	1.0
UMCM-1[29]	CO_2 H_2 CH_4	298 77 298 298	25 28 4 8	30 30 3.8 10	TraPPE, UFF	TraPPE, UFF	1.0
soc-MOF[61]	H_2	78	2.4	2.5	OPLS-AA	DFT fitted	1.0
MIL-102[30]	H_2	77	10	11	UFF	UFF	1.0

Table 2.A.2 continued…

Cu-BTC[31]	H_2	78	95	92	TraPPE, OPLS-AA, UFF	TraPPE, OPLS-AA, UFF	1.0
Cu-BTC[31,32,62]	CH_4	295 295 303	10 12 9	11 11.5 11			1.0
IRMOF-8[31]	H_2	77	13	15			1.0
IRMOF-18[31]	H_2	77	8	8			1.0
MIL-100 (Cr)[34]	CH_4	303	1.5	1.4	Dreiding, TraPPE	Dreiding, TraPPE	1.0
PCN-14[35]	CH_4	150 290	5.8 1.5	6 1.4	Adjusted Generic FF	N/A	1.0
Cu-BTC[34]	Ethane Propane Butane	295 323 298	8 6 6	9 7 7.5	Dreiding, TraPPE	Dreiding, TraPPE	1.0
MIL-47[36]	o-xylene m-xylene p-xylene ethylbenzene	423 423 423 423	3.7 3.2 3.6 2.9	3.8 3.1 3.5 2.8	DFT derived	DFT derived	0.8

[a]*Uptake at the highest pressure in each isotherm is taken.*

Table 2.A.3: The REFCODES for 100 MOFs selected from CoRE MOF with their largest cavity diameter (LCD), pore limiting diameter (PLD) and BET surface area

MOF REFCODE	LCD, Å	PLD, Å	Surface Area, m^2/g
ABUWOJ	5.07969	4.03039	2266.21
ACOLIP	4.91034	3.57647	1794.37
AGARUW	6.77693	6.25183	1575.94
AHOKIR01	4.30721	3.46838	1425.49
AMILUE	11.39418	11.07263	1423.33
AMIMEP	11.21563	10.87494	1436.07
AMUCOB	4.03894	3.31743	350.786
ANUGIA	13.85309	6.75838	2379.55
APEBED	4.58202	3.62787	996.143
AROFET	8.28593	5.15676	2410.52
ATOXEN	4.55968	3.64615	879.243
AVAQIX	5.44587	3.64311	1675.2
AVIMOI	5.73292	4.38571	1557.93
BAEDTA01	5.34617	4.27166	484.141
BALMUW01	3.18746	2.61191	256.235
BALMUW	3.22163	2.73038	261.241
BARZAW	7.73839	2.55686	612.145
BENXUP	4.10218	3.42336	1294.9
BERGAI	5.28761	2.67572	521.11
BIBBUL	3.85878	3.31702	531.391
BOJCIN	5.54889	5.25047	894.187
BONWAD	3.83514	2.72512	238.642
BONWIL	3.70731	2.93141	456.344
BOWQAG	3.49003	3.13948	538.431
BUVXOG	6.82532	5.20994	909.883
CATART03	3.52552	2.45245	128.65
CEGFAW	4.76954	3.53933	1187.25
CICYIX	3.23853	2.71886	612.32
CIGYAU	3.87967	2.66619	356.54
COGWEB	6.3699	5.6966	2242.6
CUHPUR	7.61025	5.84126	2363.86
CUNWEO	7.09668	6.48549	1355.76
CUNXIS10	4.73091	2.77205	214.235
CUNXIS	4.73091	2.77205	421.652
CUTKOS	5.45963	4.13818	1251.22
CUYHIO	3.56239	3.1474	514.597
DAGDIZ	6.53637	3.58733	1643.14
DAJHUS	4.35025	3.20599	809.526
DEGJIK	4.49857	3.8442	1007.41
DEYLUQ	7.28064	4.66536	1212.64

Table 2.A.3 continued…

DEYVUA	5.3557	4.43475	2946.03
DIDDOK	9.60031	8.17399	2701.21
DOGZIJ	5.26678	3.36062	1138.59
DOQGUM	3.55189	3.16205	667.701
ECIWUJ	3.25413	2.62453	352.21
ECODEG	5.33632	3.54871	1636.26
EDADIX	4.63332	3.88728	1709.25
EDUSIF	15.05124	7.91583	2198.06
EKOPIE	6.61542	5.14354	2334.84
EKOPOK	7.61675	7.30447	1614.25
EMITUQ	7.79889	5.62107	1972.46
ESEVIH	6.88268	6.30555	1478.22
EZABEN	5.22809	3.75233	1953.26
EZUCIM	5.27092	4.42324	2346.32
FAKLOU	9.12795	8.03305	1832.96
FAPTIB	7.34478	4.33247	2094.15
FAPTOH	7.60793	4.15774	2149.32
FECWOB01	4.17085	3.04516	1007.59
FECZAQ	8.50021	5.35603	2504.58
FERHAN	10.23981	6.40536	1918.96
FEWGUL	4.38967	3.93713	905.699
FEZREJ	6.80795	5.29768	2358.08
FIJCUX01	7.34002	6.13055	1828.22
FIJCUX	7.05898	5.83044	1853.72
FIPWOS	5.20561	3.82141	1264.09
FIPXEJ	4.43579	3.68809	1075.83
FIRVEH	4.11749	3.26577	1264.26
FOHCIP	4.9595	4.13642	1807.52
FUNBAS	6.30412	4.59254	1643.51
FUNBIA	7.93212	6.3165	1683
FUNBOG	12.59077	11.01228	2168.87
FUNCAT	9.48773	8.77545	1672.98
FUNCEX	13.21557	12.47689	2082.66
GACQAE	8.56972	8.26373	2215.21
GALCED	7.33377	5.39043	1499.96
GAXWEJ	4.40485	2.71207	521.22
GAYFUJ	5.68191	5.17685	2350.07
GIDKOU	4.78674	3.41448	1192.28
GIHBII	4.5778	2.7831	265.23
GIMSIG	8.71631	5.7057	1762.11
GINLIA	6.39385	4.60431	2573.96
GITWIQ	5.04878	3.98781	1279.85

Table 2.A.3 continued…

GIZJOP	5.3179	2.78115	368.541
GOMRAC	5.32693	3.3664	1162.6
GOMREG	5.3838	3.6396	1194.28
GULPIN	4.24475	3.50387	1025.04
GUWDUY	6.18049	4.11372	2181.37
GUXLIU	3.7664	2.40014	754.235
GUYLUI01	4.78396	3.88146	711.355
GUYLUI	4.74374	3.84472	688.938
HABRIN	3.86703	2.43469	254.652
HAFQUC	6.71368	5.31482	2175.23
HAKWUM	3.50559	2.63697	452.327
HAMJOW	5.97637	5.66826	2629.78
HEGJUZ	6.22529	4.73915	1650.42
HICVUM	5.70734	4.18424	1907.59
HIFTOG01	15.08334	7.94198	2221.35
HIFTOG02	7.88297	4.15104	2457.59
HIFTOG	7.95891	4.14066	2427.59
HIFVOI	9.00136	6.57223	2472.67

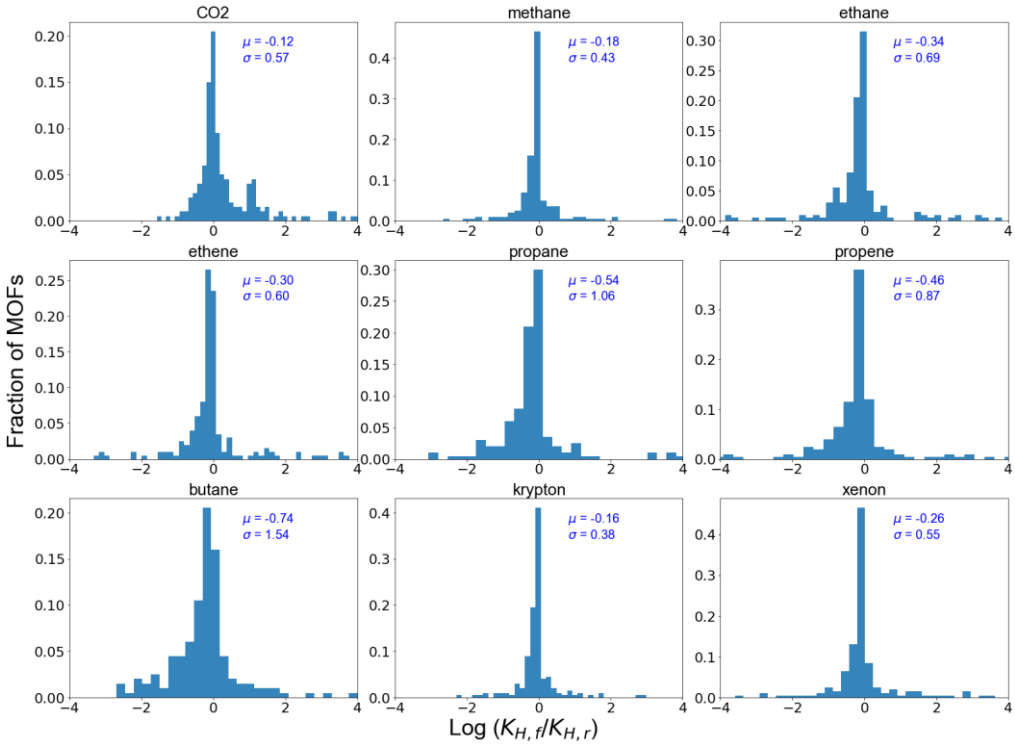

Figure 2.A.1: Histograms of the ratio of Henry Coefficients of individual adsorbate at dilute loading calculated using flexible simulations to the rigid structure simulations. Mean and standard deviation of each distribution is reported in the respective plot.

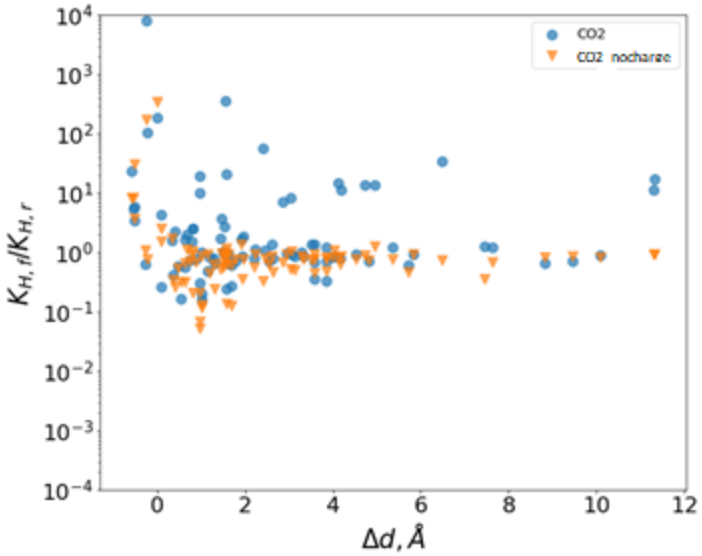

Figure 2.A.2: Ratio of Henry constants ($K_{H,f}/K_{H,r}$) in simulations with flexible and rigid MOFs as a function of Δd , the difference between the MOF's LCD and the adsorbate's kinetic diameter, for CO_2 adsorbate with (blue) and without (orange) electrostatic interactions.

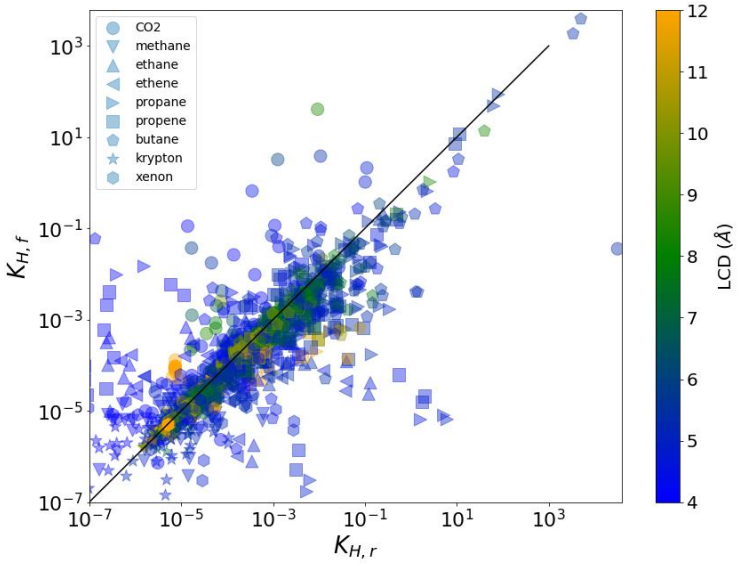

Figure 2.A.3: Parity plot between rigid and flexible Henry constants for 9 adsorbates in 100 MOFs. The data points are color coded based on MOFs LCDs.

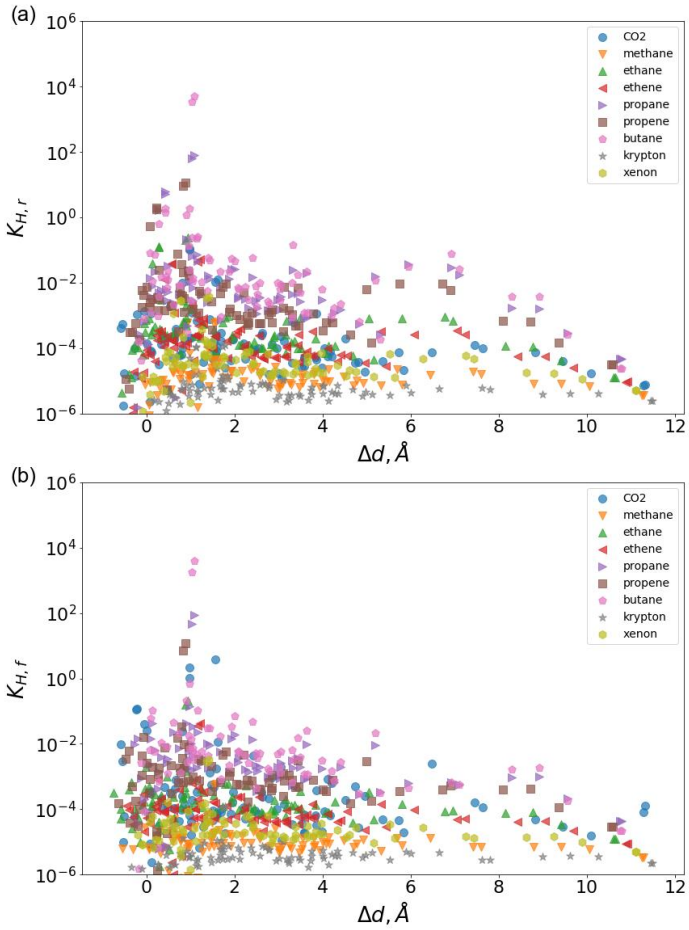

Figure 2.A.4: Correlation between Δd , the difference between the MOF's LCD and the adsorbate's kinetic diameter and (a) rigid Henry constants, (b) flexible Henry constants.

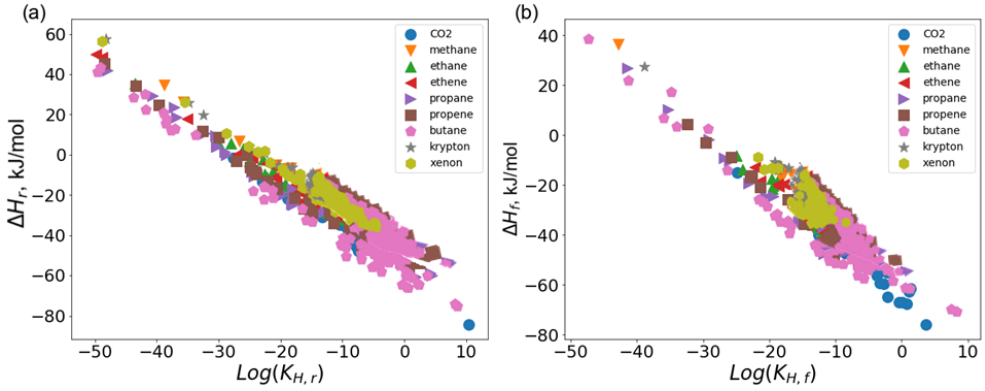

Figure 2.A.5: Correlation between Henry constants (K_H) and heat of adsorption (ΔH) for all adsorbates using (a) rigid simulations, (b) flexible simulations

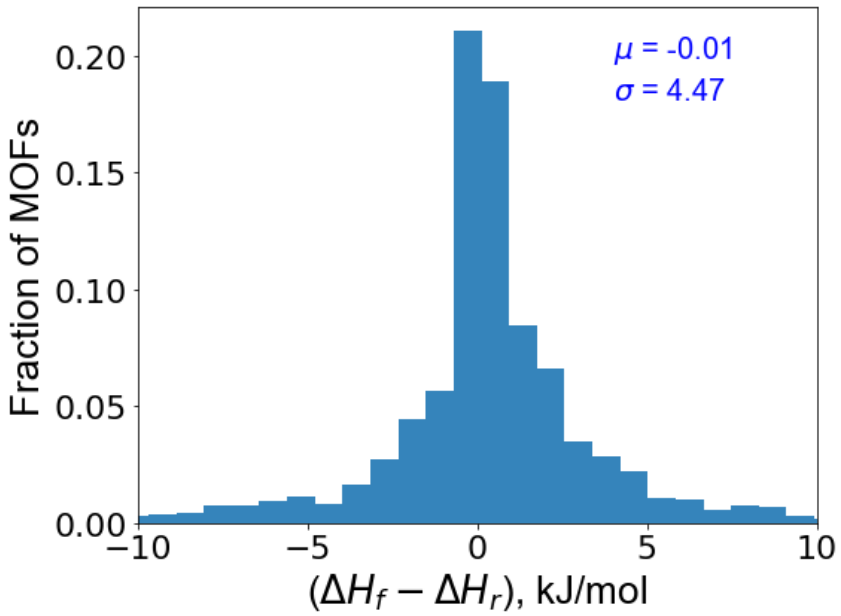

Figure 2.A.6: Histograms of the difference in heat of adsorption (ΔH_f - $\Delta H_{,r}$) at dilute loading calculated using flexible simulations and the rigid structure simulations. Mean and standard deviation of the distribution is reported in the plot.

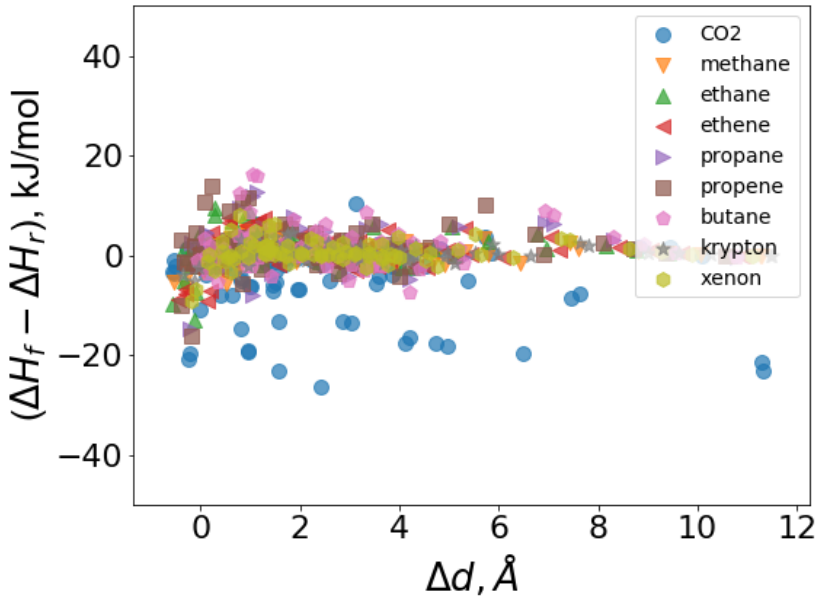

Figure 2.A.7: Difference in heat of adsorption (ΔH_f - $\Delta H_{,r}$) in simulations with flexible and rigid MOFs as a function of Δd , the difference between the MOF's LCD and the adsorbate's kinetic diameter, for CO_2 adsorbate with (blue) and without (orange) electrostatic interactions.

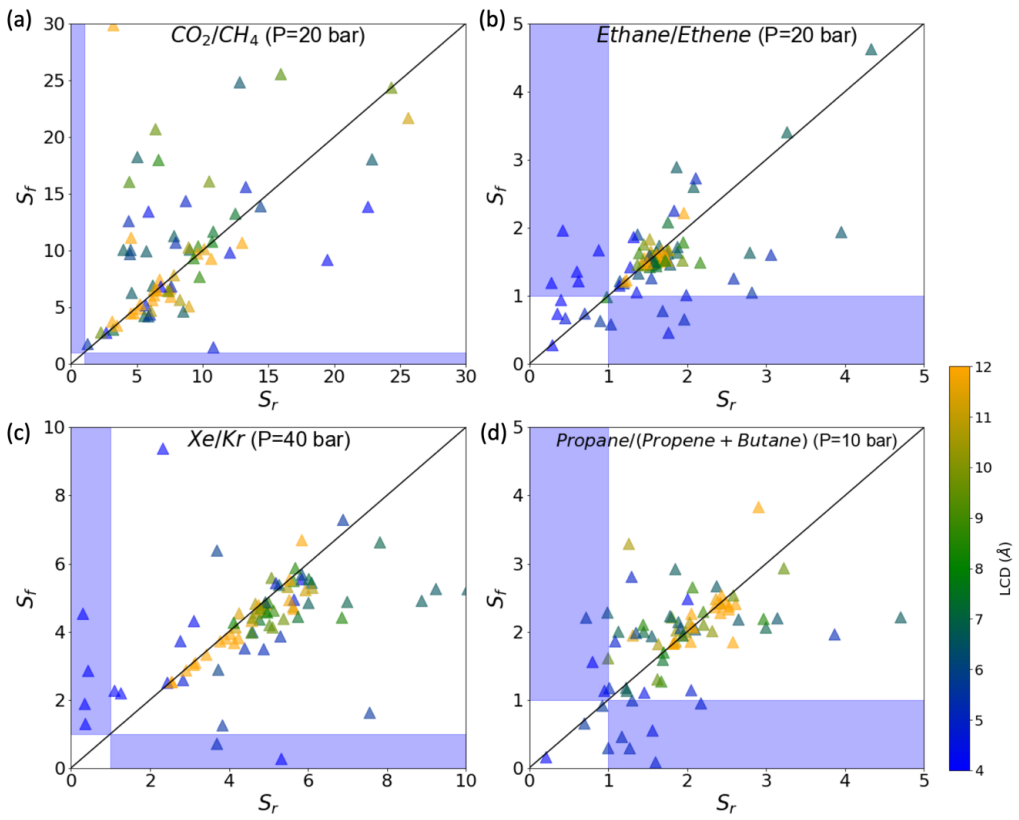

Figure 2.A.8: Comparison of room temperature selectivities calculated using rigid structure and flexible simulations at non-dilute loading for mixtures of (a) CO_2/CH_4 at P_{total}=20 bar, (b) ethane/ethene at P_{total}=20 bar, (c) Xe/Kr at P_{total}=40 bar, and (d) propane/(propene + butane) at P_{total}=10 bar. All bulk mixtures are equimolar. The data points are color coded based on MOF's LCD.

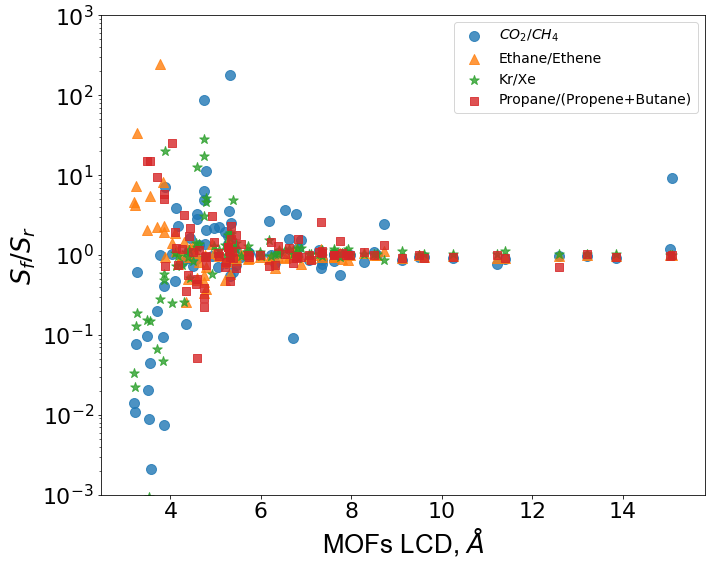

Figure 2.A.9: Ratio of selectivity of mixtures calculated using flexible simulations to rigid simulations at non-dilute loadings with MOFs largest cavity diameters (LCDs) for all four mixtures.

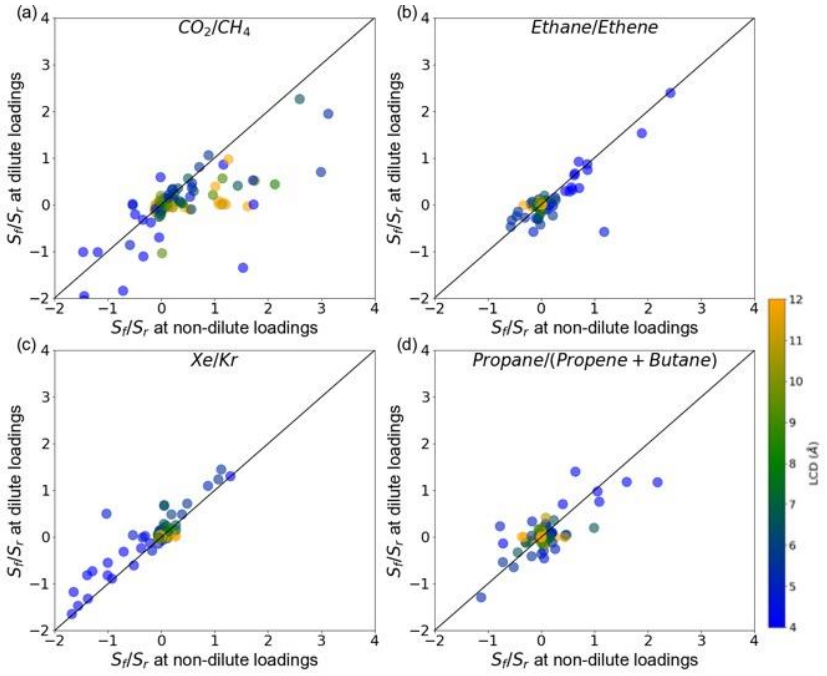

Figure 2.A.10: Ratio of flexible and rigid selectivity at non-dilute conditions vs dilute conditions for (a) CO_2/CH_4, (b) ethane/ethene, (c) Xe/Kr, and (d) propane/(propene+butane). The data points are color coded based on MOF's LCD.

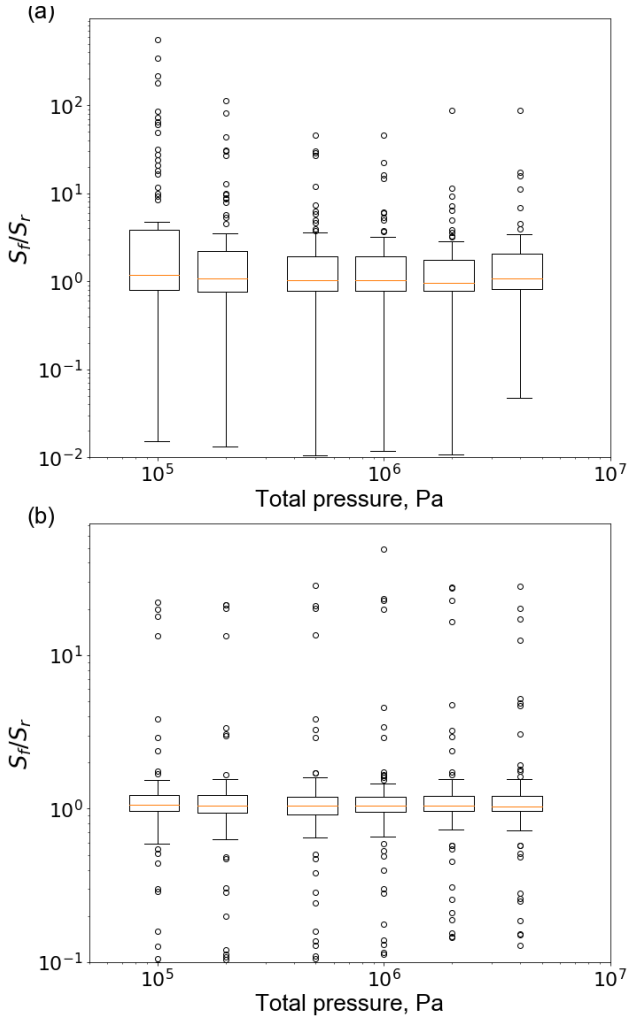

Figure 2.A.11: Ratio of flexible and rigid selectivity at different pressures/loadings for (a) CO_2/CH_4, (b) Kr/Xe mixtures. All the mixtures are equimolar at the specified total pressures in the plot.

2.5 References

(1) Férey, G.; Serre, C. Large breathing effects in three-dimensional porous hybrid matter: Facts, analyses, rules and consequences. *Chem. Soc. Rev.* **2009**, *38* (5), 1380–1399.

(2) Serre, C.; Millange, F.; Thouvenot, C.; Noguès, M.; Marsolier, G.; Louër, D.; Férey, G. Very Large Breathing Effect in the First Nanoporous Chromium(III)-Based Solids: MIL-53 or CrIII (OH)·{$O_2C-C_6H_4-CO_2$}·{$HO_2C-C_6H_4-CO_2H$}x ·H_2O_y. *J. Am. Chem. Soc.* **2002**, *124* (45), 13519–13526.

(3) Agrawal, M.; Bhattacharyya, S.; Huang, Y.; Jayachandrababu, K. C.; Murdock, C. R.; Bentley, J. A.; Rivas-Cardona, A.; Mertens, M. M.; Walton, K. S.; Sholl, D. S.; et al. Liquid-Phase Multicomponent Adsorption and Separation of Xylene Mixtures by Flexible MIL-53 Adsorbents. *J. Phys. Chem. C* **2018**, *122* (1), 386–397.

(4) Kitaura, R.; Fujimoto, K.; Noro, S. I.; Kondo, M.; Kitagawa, S. A pillared-layer coordination polymer network displaying hysteretic sorption: $[Cu_2(pzdc)_2(dpyg)]_n$(pzdc= pyrazine-2,3-dicarboxylate; dpyg = 1,2-Di(4-pyridyl)glycol). *Angew. Chemie - Int. Ed.* **2002**, *41* (1), 133–135.

(5) Schneemann, A.; Bon, V.; Schwedler, I.; Senkovska, I.; Kaskel, S.; Fischer, R. A. Flexible metal-organic frameworks. *Chem. Soc. Rev.* **2014**, *43* (16), 6062–6096.

(6) Zhang, J.-P.; Zhou, H.-L.; Zhou, D.-D.; Liao, P.-Q.; Chen, X.-M. Controlling flexibility of metal–organic frameworks. *Natl. Sci. Rev.* **2017**, 907–919.

(7) Bon, V.; Kavoosi, N.; Senkovska, I.; Kaskel, S. Tolerance of Flexible MOFs toward Repeated Adsorption Stress. *ACS Appl. Mater. Interfaces* **2015**, *7* (40), 22292–22300.

(8) Jiao, Y.; Li, Z.; Ma, Y.; Zhou, G.; Wang, S.; Lu, G. The studies on gas adsorption properties of MIL-53 series MOFs materials. *AIP Adv.* **2017**, *7* (8).

(9) Triguero, C.; Coudert, F. X.; Boutin, A.; Fuchs, A. H.; Neimark, A. V. Mechanism of breathing transitions in metal-organic frameworks. *J. Phys. Chem. Lett.* **2011**, *2* (16), 2033–2037.

(10) Gee, J. A.; Sholl, D. S. Effect of Framework Flexibility on C_8 Aromatic Adsorption at High Loadings in Metal-Organic Frameworks. *J. Phys. Chem. C* **2016**, *120* (1), 370–376.

(11) Agrawal, M.; Sava Gallis, D. F.; Greathouse, J. A.; Sholl, D. S. How Useful Are Common Simulants of Chemical Warfare Agents at Predicting Adsorption Behavior? *J. Phys. Chem. C* **2018**, *122* (45), 26061–26069.

(12) Witman, M.; Ling, S.; Jawahery, S.; Boyd, P. G.; Haranczyk, M.; Slater, B.; Smit,

B. The Influence of Intrinsic Framework Flexibility on Adsorption in Nanoporous Materials. *J. Am. Chem. Soc.* **2017**, *139* (15), 5547–5557.

(13) Li, S.; Chung, Y. G.; Snurr, R. Q. High-throughput screening of metal-organic frameworks for CO_2 capture in the presence of water. *Langmuir* **2016**, *32* (40), 10368–10376.

(14) Zhang, H.; Snurr, R. Q. Computational study of water adsorption in the hydrophobic metal-organic framework ZIF-8: Adsorption mechanism and acceleration of the simulations. *J. Phys. Chem. C* **2017**, *121* (39), 24000–24010.

(15) Altintas, C.; Avci, G.; Daglar, H.; Nemati, A.; Azar, V.; Velioglu, S.; Erucar, I.; Keskin, S. Database for CO_2 Separation Performances of MOFs Based on Computational Materials Screening. *ACS Appl. Mater. Interfaces* **2018**, *10*, 17257–17268.

(16) Brandt, P.; Nuhnen, A.; Lange, M.; Möllmer, J.; Weingart, O.; Janiak, C. Metal-Organic Frameworks with Potential Application for SO_2 Separation and Flue Gas Desulfurization. *ACS Appl. Mater. Interfaces* **2019**, *11* (19), 17350–17358.

(17) Avci, G.; Velioglu, S.; Keskin, S. High-Throughput Screening of MOF Adsorbents and Membranes for H_2 Purification and CO_2 Capture. *ACS Appl. Mater. Interfaces* **2018**, *10* (39), 33693–33706.

(18) Tarzia, A.; Takahashi, M.; Falcaro, P.; Thornton, A. W.; Doonan, C. J.; Huang, D. M. High-Throughput Screening of Metal-Organic Frameworks for Macroscale Heteroepitaxial Alignment. *ACS Appl. Mater. Interfaces* **2018**, *10* (47), 40938–40950.

(19) Coudert, F. X. The osmotic framework adsorbed solution theory: Predicting mixture coadsorption in flexible nanoporous materials. *Phys. Chem. Chem. Phys.* **2010**, *12* (36), 10904–10913.

(20) Zhang, C.; Gee, J. A.; Sholl, D. S.; Lively, R. P. Crystal-size-dependent structural transitions in nanoporous crystals: Adsorption-induced transitions in ZIF-8. *J. Phys. Chem. C* **2014**, *118* (35), 20727–20733.

(21) Chen, Y.; Jiang, J. A bio-metal-organic framework for highly selective CO_2 capture: A molecular simulation study. *ChemSusChem* **2010**, *3* (8), 982–988.

(22) Ramsahye, N. A.; Maurin, G.; Bourrelly, S.; Llewellyn, P. L.; Devic, T.; Serre, C.; Loiseau, T.; Ferey, G. Adsorption of CO_2 in metal organic frameworks of different metal centres: Grand Canonical Monte Carlo simulations compared to experiments. *Adsorption* **2007**, *13* (5–6), 461–467.

(23) Zhuang, W.; Yuan, D.; Liu, D.; Zhong, C.; Li, J. R.; Zhou, H. C. Robust metal-organic framework with an octatopic ligand for gas adsorption and separation: Combined characterization by experiments and molecular simulation. *Chem. Mater.*

2012, *24* (1), 18–25.

(24) Yang, Q.; Wiersum, A. D.; Jobic, H.; Guillerm, V.; Serre, C.; Llewellyn, P. L.; Maurin, G. Understanding the thermodynamic and kinetic behavior of the CO_2/CH_4 gas mixture within the porous zirconium terephthalate UiO-66(Zr): A joint experimental and modeling approach. *J. Phys. Chem. C* **2011**, *115* (28), 13768–13774.

(25) Hon Lau, C.; Babarao, R.; Hill, M. R. A route to drastic increase of CO_2 uptake in Zr metal organic framework UiO-66. *Chem. Commun.* **2013**, *49* (35), 3634–3636.

(26) Granato, M. A.; Martins, V. D.; Ferreira, A. F. P.; Rodrigues, A. E. Adsorption of xylene isomers in MOF UiO-66 by molecular simulation. *Microporous Mesoporous Mater.* **2014**, *190*, 165–170.

(27) Borycz, J.; Lin, L. C.; Bloch, E. D.; Kim, J.; Dzubak, A. L.; Maurice, R.; Semrouni, D.; Lee, K.; Smit, B.; Gagliardi, L. CO_2 adsorption in Fe_2(dobdc): A classical force field parameterized from quantum mechanical calculations. *J. Phys. Chem. C* **2014**, *118* (23), 12230–12240.

(28) Zhang, Z.; Li, Z.; Li, J. Computational study of adsorption and separation of CO_2, CH_4, and N_2 by an rht-type metal-organic framework. *Langmuir* **2012**, *28* (33), 12122–12133.

(29) Peng, X.; Cheng, X.; Cao, D. Computer simulations for the adsorption and separation of $CO_2/CH_4/H_2/N_2$ gases by UMCM-1 and UMCM-2 metal organic frameworks. *J. Mater. Chem.* **2011**, *21* (30), 11259–11270.

(30) Surble, S.; Millange, F.; Serre, C.; Duren, T.; Latroche, M.; Bourrelly, S.; Llewellyn, P. L. .; Ferey, G. Synthesis of MIL-102, a Chromium Carboxylate Metal-Organic Framework, with Gas Sorption Analysis. *J. Am. Chem. Soc.* **2006**, *128*, 14889–14896.

(31) Garberoglio, G.; Skoulidas, A. I.; Johnson, J. K. Adsorption of gases in metal organic materials: Comparison of simulations and experiments. *J. Phys. Chem. B* **2005**, *109* (27), 13094–13103.

(32) Mileo, P. G. M.; Cavalcante, C. L.; Möllmer, J.; Lange, M.; Hofmann, J.; Lucena, S. M. P. Molecular simulation of natural gas storage in Cu-BTC metal-organic framework. *Colloids Surfaces A Physicochem. Eng. Asp.* **2014**, *462*, 194–201.

(33) Llewellyn, P. L.; Bourrelly, S.; Vagner, C.; Heymans, N.; Leclerc, H.; Ghoufi, A.; Bazin, P.; Vimont, A.; Daturi, M.; Devic, T.; et al. Evaluation of MIL-47(V) for CO_2-related applications. *J. Phys. Chem. C* **2013**, *117* (2), 962–970.

(34) Hamon, L.; Heymans, N.; Llewellyn, P. L.; Guillerm, V.; Ghoufi, A.; Vaesen, S.; Maurin, G.; Serre, C.; De Weireld, G.; Pirngruber, G. D. Separation of CO_2-CH_4 mixtures in the mesoporous MIL-100(Cr) MOF: Experimental and modelling

approaches. *Dalt. Trans.* **2012**, *41* (14), 4052–4059.

(35) Lucena, S. M. P.; Mileo, P. G. M.; Silvino, P. F. G.; Cavalcante, C. L. Unusual adsorption site behavior in PCN-14 metal-organic framework predicted from Monte Carlo simulation. *J. Am. Chem. Soc.* **2011**, *133* (48), 19282–19285.

(36) Gee, J. A.; Sholl, D. S. Prediction of Adsorption Properties of Cyclic Hydrocarbons in MOFs Using DFT-Derived Force Fields. *J. Phys. Chem. C* **2015**, *119* (29), 16920–16926.

(37) Cui, Y. W.; Li, J.; Du, Z. F.; Peng, Y. Z. Cr(VI) adsorption on red mud modified by lanthanum: Performance, kinetics and mechanisms. *PLoS One* **2016**, *11* (9), 1–16.

(38) Pérez-Pellitero, J.; Amrouche, H.; Siperstein, F. R.; Pirngruber, G.; Nieto-Draghi, C.; Chaplais, G.; Simon-Masseron, A.; Bazer-Bachi, D.; Peralta, D.; Bats, N. Adsorption of CO_2, CH_4, and N_2 on zeolitic imidazolate frameworks: Experiments and simulations. *Chem. - A Eur. J.* **2010**, *16* (5), 1560–1571.

(39) Krishna, R.; van Baten, J. M. Investigating the potential of MgMOF-74 membranes for CO_2 capture. *J. Memb. Sci.* **2011**, *377* (1–2), 249–260.

(40) Walton, K. S.; Millward, A. R.; Dubbeldam, D.; Frost, H.; Low, J. J.; Yaghi, O. M.; Snurr, R. Q. Understanding inflections and steps in carbon dioxide adsorption isotherms in metal-organic frameworks. *J. Am. Chem. Soc.* **2008**, *130* (2), 406–407.

(41) Yang, Q.; Zhong, C. Molecular simulation of adsorption and diffusion of hydrogen in metal-organic frameworks. *J. Phys. Chem. B* **2005**, *109* (24), 11862–11864.

(42) Greathouse, J. A.; Kinnibrugh, T. L.; Allendorf, M. D. Adsorption and separation of noble gases by IRMOF-1: Grand canonical monte carlo simulations. *Ind. Eng. Chem. Res.* **2009**, *48* (7), 3425–3431.

(43) Farrusseng, D.; Daniel, C.; Gaudillère, C.; Ravon, U.; Schuurman, Y.; Mirodatos, C.; Dubbeldam, D.; Frost, H.; Snurr, R. Q. Heats of Adsorption for Seven Gases in Three Metal - Organic Frameworks: Systematic Comparison of Experiment and Simulation. *Langmuir* **2009**, *25* (13), 7383–7388.

(44) Rappé, A. K.; Casewit, C. J.; Colwell, K. S.; Goddard, W. A.; Skiff, W. M. UFF, a Full Periodic Table Force Field for Molecular Mechanics and Molecular Dynamics Simulations. *J. Am. Chem. Soc.* **1992**, *114* (25), 10024–10035.

(45) Mayo, S. L.; Olafson, B. D.; Goddard, W. A. DREIDING: A generic force field for molecular simulations. *J. Phys. Chem.* **1990**, *94* (26), 8897–8909.

(46) Martin, M. G.; Siepmann, J. I. Transferable Potentials for Phase Equilibria. 1. United-Atom Description of n-Alkanes. *J. Phys. Chem. B* **1998**, *102*, 2569–2577.

(47) Jorgensen, W. L.; Maxwell, D. S.; Tirado-Rives, J. Development and testing of the

OPLS all-atom force field on conformational energetics and properties of organic liquids. *J. Am. Chem. Soc.* **1996**, *118* (45), 11225–11236.

(48) Park, J.; Howe, J. D.; Sholl, D. S. How Reproducible Are Isotherm Measurements in Metal-Organic Frameworks? *Chem. Mater.* **2017**, *29* (24), 10487–10495.

(49) Chung, Y. G.; Camp, J.; Haranczyk, M.; Sikora, B. J.; Bury, W.; Krungleviciute, V.; Farha, O. K.; Sholl, D. S.; Snurr, R. Q. Computation-Ready, Experimental Metal−Organic Frameworks: A Tool To Enable High-Throughput Screening of Nanoporous Crystals. *Chem. Mater.* **2014**, *26*, 6185–6192.

(50) Nazarian, D.; Camp, J. S.; Sholl, D. S. A Comprehensive Set of High-Quality Point Charges for Simulations of Metal−Organic Frameworks. *Chem. Mater.* **2016**, *28*, 785–793.

(51) Dubbeldam, D.; Calero, S.; Ellis, D. E.; Snurr, R. Q. RASPA: Molecular Simulation Software for Adsorption and Diffusion in Flexible Nanoporous Materials. *Mol. Simul.* **2015**, *42* (2).

(52) Widom, B. Some Topics in the Theory of Fluids. *J. Chem. Phys.* **1963**, *39*, 2808–2812.

(53) Walton, K. S.; Sholl, D. S. Predicting Multicomponent Adsorption: 50 Years of the Ideal Adsorbed Solution Theory. *AIChE J. 61* (9), 2757–2762.

(54) Manz, T. A.; Limas, N. G. DDEC6: A Method for Computing Even-Tempered Net Atomic Charges in Periodic and Nonperiodic Materials. *arXiv:1512.08270 [physics.chem-ph]* **2015**.

(55) Coupry, D. E.; Addicoat, M. A.; Heine, T. Extension of the Universal Force Field for Metal-Organic Frameworks. *J. Chem. Theory Comput.* **2016**, *12* (10), 5215–5225.

(56) Plimpton, S. Fast Parallel Algorithms for Short–Range Molecular Dynamics. *J. Comput. Phys.* **1995**, *117*, 1–19.

(57) Watanabe, T.; Sholl, D. S. Accelerating applications of metal-organic frameworks for gas adsorption and separation by computational screening of materials. *Langmuir* **2012**, *28* (40), 14114–14128.

(58) Haldoupis, E.; Watanabe, T.; Nair, S.; Sholl, D. S. Quantifying large effects of framework flexibility on diffusion in MOFs: CH_4 and CO_2 in ZIF-8. *ChemPhysChem* **2012**, *13* (15), 3449–3452.

(59) Tang, D.; Wu, Y.; Verploegh, R. J.; Sholl, D. S. Efficiently Exploring Adsorption Space to Identify Privileged Adsorbents for Chemical Separations of a Diverse Set of Molecules. *ChemSusChem* **2018**, *11* (9), 1567–1575.

(60) Cox, N. J. Speaking Stata: Correlation with confidence. *Stata J.* **2008**, *8* (3), 413–439.

(61) Pham, T.; Forrest, K. A.; Hogan, A.; Tudor, B.; McLaughlin, K.; Belof, J. L.; Eckert, J.; Space, B. Understanding hydrogen sorption in In-soc-MOF: A charged metal-organic framework with open-metal sites, narrow channels, and counterions. *Cryst. Growth Des.* **2015**, *15* (3), 1460–1471.

(62) Karra, J.; Walton, K. S. Effect of Open Metal Sites on Adsorption of Polar and Nonpolar Molecules in Metal-Organic Framework Cu-BTC. *Langmuir* **2008**, *24*, 8620–8626.

CHAPTER 3. EFFECT OF BREATHING IN MIL-53 ON ADSORPTION OF C_8 AROMATICS[†]

3.1 Introduction

In chapter 2, we discussed the effects of constant volume flexibility on adsorption of various adsorbates and mixtures in a large set of MOFs. Flexibility associated with volume changes, e.g. breathing are harder to take into account in computational studies and those studies have not been be performed on a large scale. However, to understand the effect of flexibility with volume changes, we performed a combined experimental and computational study on a breathing MOF MIL-53 for C_8 aromatics adsorption.

C_8 aromatics are important raw materials for a variety of chemical processes[1–3]. Xylene isomer product streams are obtained from processes such as toluene disproportionation, gasoline pyrolysis or catalytic reforming of naphtha, and consist of four isomers: *p*-xylene (pX), *m*-xylene (mX), *o*-xylene (oX), and ethylbenzene (EB). In purified form, all these components have commercial value as feedstocks.[4] pX is widely used to produce polyethylene terephthalate (PET), which is then used in the production of polyester resins, fibers, and packaging containers. mX is used to synthesize isophthalic acid, which is used in PET resin blends.[5,6] EB is dehydrogenated to styrene for polystyrene production and oX is utilized in the synthesis of phthalic anhydride, a plasticizer.[4,6] The similarity in molecular structures, close kinetic diameters (5.8-6.8 Å), and similar boiling points (138-

[†] Material in this chapter has been previously published as Agrawal, M.; Bhattacharya S.; Huang Y.; Jayachandrababu K.; Murdock C.R.; Bentley J.A.; Rivas-Cardona A.; Mertens M.M.; Walton K.S.; Sholl, D.S.; Nair S. "Liquid Phase Multicomponent Separation of Xylene Mixtures by Flexible MIL-53 Adsorbents" *JPCC* **2018**, 122, 1, 386-397

144 °C) make cost-effective separation of these four isomers challenging, with the cost of production largely dependent on the cost of separation.[5,7,8] While crystallization and azeotropic distillation can be used to separate C_8 mixtures, the currently preferred separation technology is the Parex process, which uses simulated moving-bed adsorption.[5,8] The adsorbent used is a faujasite (FAU)-type zeolite exchanged with cations like K^+ or Ba^{2+}, and it shows moderate pX selectivity attributed to xylene-cation interactions and favorable packing under high xylene loadings within the zeolite pores.[6]

Recently, metal-organic frameworks have created interest for C_8 isomer separation. Among the MOFs investigated for xylene mixture separations, the MIL-47 and the MIL-53 series have shown promise for separating xylene mixtures.[4,9,10] MIL-53 materials are especially interesting as they exhibit differing framework flexibility depending on the metal center.[11,12] Previous experimental studies have shown the potential for xylene isomer separations by MIL-53 MOFs.[11–14] Finsy *et al.*[12] carried out single-component adsorption and binary breakthrough experiments of C_8 aromatics in MIL-53(Al) with vapor phase feeds at 110 °C and demonstrated that framework flexibility enables selective xylene adsorption. Binary batch adsorption and binary breakthrough experiments in the liquid phase showed MIL-53(Al) to be oX-selective.[15] The binary oX/mX selectivities for dilute xylene mixtures (0.028 M and 0.06 M) in hexane were reported to be 2.7 and 2.2 respectively from batch adsorption and binary breakthrough measurements respectively.[15] Ternary liquid breakthrough measurements of concentrated (2.8 M) equimolar oX, pX and mX solutions at 9 bar and 30 °C were carried out with pelletized MIL-53(Al), and the oX/mX selectivity was reported to be ~2 using either heptane or hexane as desorbent.[4,14] Another MOF from the MIL-53 series, MIL-53(Fe) has been studied for separation of

multicomponent liquid-phase binary mixtures of C_8 aromatics.[11] The material showed high oX selectivity in pulse chromatography and binary breakthrough experiments with dilute xylene mixtures (0.05 M) and was also able to separate mX from pX, unlike MIL-53(Al). There are, however, no reports of the performance of the other MOFs in the MIL-53 series. It is well known that the metal center has significant effects on the framework flexibility of different MOFs in the MIL-53 series, and hence a systematic investigation into the xylene separation performance of other MOFs of the MIL-53 series would be useful.[16] None of the MIL-53 materials have been studied for their separation properties with industrially relevant quaternary (EB/pX/mX/oX) liquid-phase feeds.

In addition to experimental work, the development of reliable computational methods for prediction of framework flexibility effects on C_8 aromatics separation is a topic of considerable interest. Several groups have used molecular simulations to study the effect of framework flexibility on adsorption in MIL-53 and MIL-47.[17–19] Molecular dynamics (MD) simulations have been used to study the effects of the 'breathing' behavior of MIL-53(Cr) during CO_2 adsorption.[15,17] Recently, we developed a 'flexible snapshots' method to account for the internal flexibility of MOFs (e.g. linker rotation) during C_8 aromatics adsorption.[17] We have also studied flexible MIL-47 materials and computationally demonstrated that functionalization of the BDC linker in MIL-47 considerably changes the selectivity of the adsorbent for C_8 aromatics.[20] However, a general methodology that accounts for all relevant modes of MIL-53 framework flexibility has not been established, and there are no reports of computational studies of C_8 aromatics adsorption in the MIL-53 series.

In this chapter, we address the above issues systematically thorough a combined experimental and computational study of single-component and multi-component C_8 isomers in several MIL-53 materials.‡ We develop computational methods to account for different types of flexibility in MIL-53, and initially validate these methods with detailed experimental single- component isotherm data from MIL-53(Al), MIL-53(Cr), MIL-53(Ga), MIL-53(Fe) and MIL-53(Sc) materials. Based upon these results, we select three materials – MIL-53(Al), MIL-53(Cr) and MIL-53(Ga) – for detailed multicomponent quaternary liquid breakthrough measurements with industrially relevant xylene mixtures and operational conditions. We then compare our experimental multicomponent separate data with predictions from our flexible-structure multicomponent adsorption simulations, the effects of different metal centers and framework flexibility on C_8 mixture separations is discussed in detail. Our experimental work also involved significant scale-up of MIL-53 materials synthesis to produce high-quality materials in sufficient quantities for the adsorption and breakthrough measurements.

3.2 Simulation Methods

Experimental methods are described in detail in our published work.[21] For adsorption simulations, MIL-53 structures, initially taken from RASPA[22] library, were geometrically optimized using density functional theory (DFT) in the Vienna ab initio Simulation Package (VASP)[23] with the projector augmented wave (PAW)[24] approach. The cutoff energy of the plane wave basis set was 520 eV. For all simulations, the Brillouin zone was sampled with a Monkhorst-Pack grid. A *k*-point mesh of 2×3×5 for one unit cell

‡ All experimental data in this chapter was produced by S. Bhattacharya, Y. Huang, K. Jayachandrababu and C.R. Murdock

of MIL-47 or MIL-53 large-pore structure and a mesh of 2×5×5 for one unit cell of MIL-53 narrow-pore structure were used. The cutoff energy and *k*-point mesh was tested to ensure energy convergence within 0.001 eV/atom. A conjugate gradient method was used to optimize atomic positions until the forces on each atom was converged within 0.01 eV/atom. The Perdew-Burke-Ernzerhof (PBE)[25] exchange correlation functional was adopted to perform calculations with the DFT-D2[26] functional to account for dispersion forces.

Adsorption isotherms in MOFs were simulated using GCMC simulations as implemented in RASPA.[22] Non-bonded interactions between adsorbates and the framework atoms were calculated using a Lennard-Jones (L-J) potential truncated at a spherical cutoff distance of 13 Å. Cross-terms are specified using Lorentz-Berthelot mixing rules with L-J parameters taken from the DREIDING force field[27] for the framework atoms and the TraPPE force field[28] for adsorbates. To calculate Coulombic forces, electrostatic charges on atoms in the MOFs were assigned on the entire periodic framework using the DDEC methods.[29] We used equilibration and production periods of 5×10^4 and 1×10^5 Monte Carlo (MC) cycles respectively. In each MC cycle, adsorbate insertion/deletion, rotation, translation and identity change moves were attempted. Coulombic interactions were computed using the Ewald method with 10^{-6} Ewald precision and 12 Å cutoff.

The osmotic framework adsorbed solution theory (OFAST)[30,31] was used to describe structural transitions in the flexible MIL-53 frameworks. This method uses adsorption isotherms to predict the equilibrium-favored structure at given conditions. MIL-53 materials are known to exist in narrow-pore (NP) and large-pore (LP) structures[18,32,33] and OFAST was used to predict transitions from one structure to another. To describe

swelling of the frameworks, molecular dynamics (MD) simulations were performed in the NPT ensemble at 323 K and 10^5 Pa. A time step of 1.0 fs was used and runs were carried out for 1 ns. The van der Waals interaction cutoff was set to 16 Å. The force field parameters for MIL-53 are taken from those previously reported by Ma *et al.*[18] that used CVFF[34] parameters for organic part and UFF[35] parameters for inorganic part of the MOF. Additional simulation details of OFAST and force field parameters for MD calculations are provided in **Appendix 3.A** (see section 3.A.2 and 3.A.3). **Table 3.A.6** shows the DFT-optimized lattice parameters for the MIL-53 materials.

3.3 Results and Discussions

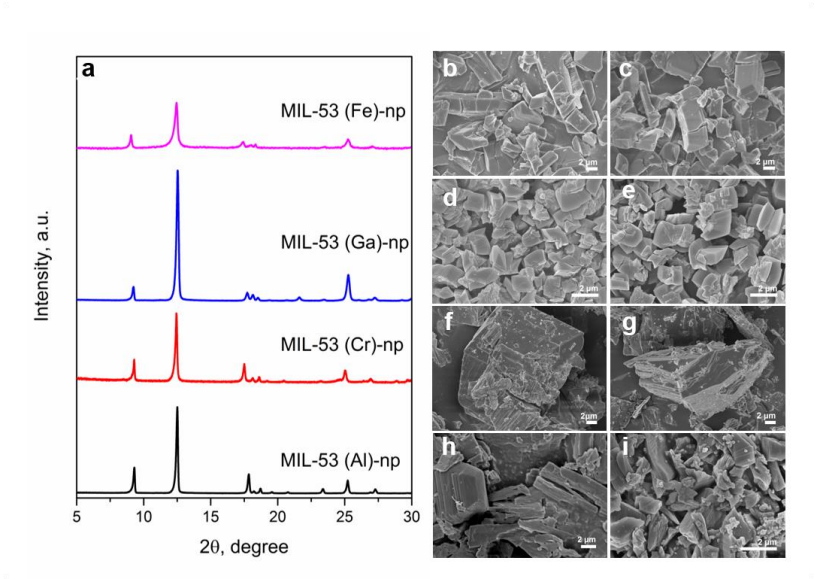

Figure 3.1: (a) PXRD patterns of activated MIL-53 materials obtained by scaled-up synthesis; SEM images after hot DMF extraction and activation respectively: (b-c) MIL-53(Al), (d-e) MIL-53(Cr), (f-g) MIL-53(Ga), and (h-i) MIL-53 (Fe). See Figure S3 for SEM images of MIL-53(Sc).

Figure 3.1a shows the PXRD patterns of the activated MIL-53 (Al/Cr/Ga/Fe) materials synthesized using our scaled-up methods. The crystal structures were all

determined to be of the narrow pore (NP) form. MIL-53 adsorbents exhibit reversible structural transformations from LP form to NP form upon adsorption of some guest molecules (*e.g.* water), which is known as the 'breathing effect'.[32,36] PXRD confirmed that our MIL-53 samples were highly crystalline without any detectable impurity phases. The PXRD patterns showed the complete absence of BDC peaks, which were clearly present in all the as-synthesized materials (**Figure 3.A.2**). Thus, excess linker molecules (BDC) were completely removed during the hot DMF extraction step of the activation process. SEM images of the DMF-extracted and activated materials (**Figure 3.1** and **Figure 3.A.2**) show that there is no apparent change in crystal morphology and size after the extraction step and after complete activation. Moreover, the crystal morphologies and sizes were similar to those seen in small batch syntheses.[37–39] The BET surface areas and micropore volumes are shown in **Table 3.1**, with error bars obtained from three independent samples. These values are comparable to or even higher than the previously reported values,[37–39] indicating that high quality materials were synthesized. The increased surface area could be due to the improvements in the activation protocol of MIL-53s, particularly for MIL-53(Al/Cr/Ga). As observed previously,[38,39] MIL-53(Fe) and MIL-53(Sc) did not physisorb nitrogen at 77 K.

The xylene adsorption characteristics of four different MIL-53 materials were initially probed using single-component/unary vapor adsorption isotherms at 323 K (**Figure 3.2**). The step in the adsorption isotherms occurs at the transition between the NP and LP structures. The transition pressure and the saturation capacity are different for each adsorbate and also differ between materials. MIL-53(Sc) demonstrated an essentially nonporous structure with no significant NP→LP transition, and the two xylene isotherms

(mX and oX) collected for this material showed negligible adsorption (**Figure 3.A.3**). MIL-53(Al) has the highest gravimetric oX saturation capacity (4.5 mmol/g) and the lowest transition pressure for oX uptake. MIL-53(Cr) and MIL-53(Ga) show the lowest transition pressures for pX adsorption, but the highest pX capacity is exhibited by MIL-53(Al). MIL-53(Fe) had the highest mX capacity at saturation, but had the most difficulty in reaching the NP→LP transition. Even after the transition pressure was reached, the isotherm collection took an unusually long amount of time, indicating that the structure may not have fully reached the LP form. The EB capacity is consistently the lowest among all the C_8 isomers in all four materials.

Table 3.1: Specific surface areas and pore volumes of MIL-53 materials.

Material	**S_{BET}, $m^2 \cdot g^{-1}$**	**$V_{p,\ micro}$, $cm^3 \cdot g^{-1}$**	**Activation Conditions**
MIL-53(Al)	1706±102	0.60±0.01	523 K – 623 K for 24 h in vacuum
MIL-53(Cr)	1690±82	0.61±0.02	553 K – 623 K in air for 24 h
MIL-53(Ga)	1120±55	0.40±0.04	553 K – 623 K in air for 24 h
MIL-53(Fe)	NA	NA	398 K in air for 12 h
MIL-53(Sc)	NA	NA	623 K in air for 12 h

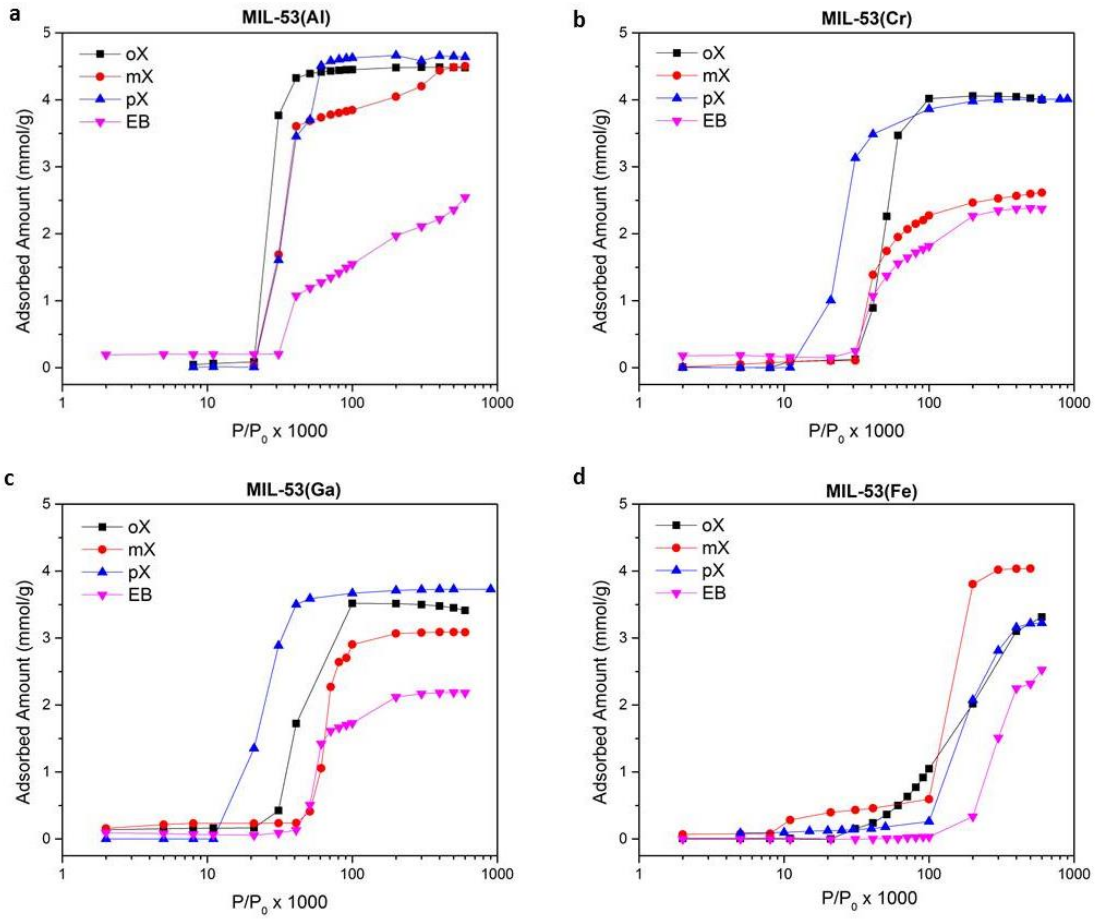

Figure 3.2: Unary adsorption isotherms of pX, mX, oX, EB and hexane on (a) MIL-53(Al), (b) MIL-53(Cr), (c) MIL-53(Ga) and (d) MIL-53(Fe) at 323 K.

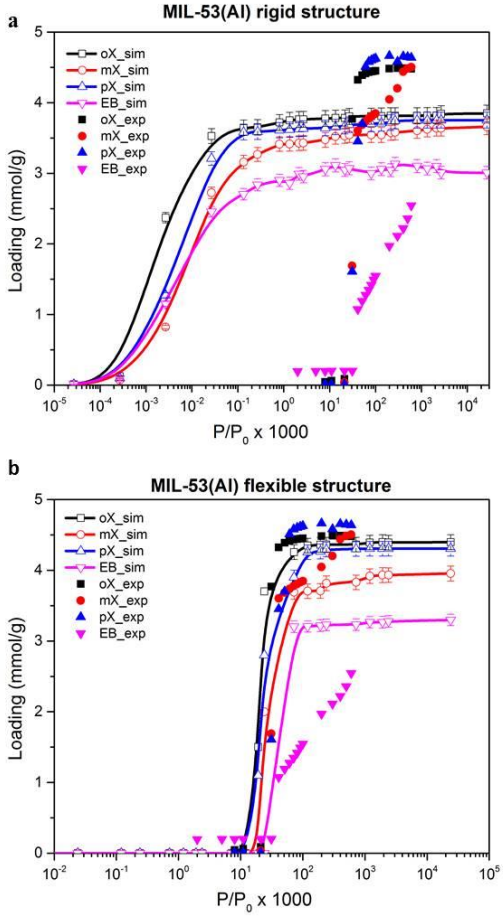

Figure 3.3: Simulated adsorption isotherms (open symbols) for C_8 aromatics in MIL-53(Al) at 323 K with (a) rigid LP structure and (b) flexible structures. The experimental data (closed symbols) are shown in both plots. The curves connecting the simulation data points are only a guide to the eye.

Computational investigations were then conducted on unary C_8 aromatics adsorption in MIL-53 to predict the effects of framework flexibility. First, GCMC calculations were carried out to obtain unary isotherms for all four adsorbates in *rigid* LP structures of MIL-53(Al). **Figure 3.3a** shows the results for MIL-53(Al), whereas the results for the other three materials are shown in (**Figure 3.A.4**). With the rigid structure approximation, the simulations show poor agreement with the experimentally obtained uptake pressures and adsorption capacities. It has been reported that it is critical to account

for the different flexibility modes (NP→LP breathing and lattice expansion effects) of MIL-53 while simulating adsorption properties.[18,40] To account for the NP→LP breathing, OFAST calculations were performed. It was found that C_8 aromatics do not adsorb in the NP structures of MIL-53 at 323 K. Previous studies have reported non-zero adsorption in the NP structure leading to two-step isotherms for xylene adsorption in MIL-53(Al) at 383 K.[12,13] However, it is also reported that the two-step isotherms in MIL-53(Al) are replaced with a one-step isotherm at lower temperatures.[13] XRD patterns indicate that the MIL-53 adsorbents are in the NP structure initially, which have essentially zero adsorption capacity at 323 K. As pressure is increased, the NP→LP transition results in a high uptake as observed in the unary isotherms. Adsorption isotherms in both pore structures were then calculated using GCMC for all the MIL-53 adsorbents, and then combined using the OFAST method. Other than breathing, MIL-53 adsorbents are also known to expand to a certain extent at high loadings of xylene isomers. It has been reported that the unit cell volumes of MIL-53 and MIL-47 increased at high loadings of xylene isomers.[14,15,17] To model this flexibility, the adsorbate-loaded frameworks obtained from GCMC simulations were relaxed with MD using fully-bonded force fields. GCMC simulations were then performed using the MD-relaxed structure, and GCMC+MD simulations were iteratively carried out to obtain converged lattice parameters (**Table 3.A.6**) and adsorption capacity of each C_8 isomer. After accounting for both the breathing and swelling modes of MIL-53 framework flexibility, the predicted unary isotherms are in closer agreement with the experimental data (**Figure 3.3b** and **Figure 3.A.4**). The simulated uptake pressures shift by about 5 orders of magnitude and come into good agreement with the experimental observations. The simulated capacities for all adsorbates also increased. The EB adsorption

capacities show the largest differences with the experiments, possibly because the MIL-53 structural transitions occur more slowly in presence of EB and thus the experimental EB adsorption isotherms may not have reached saturation even at long times. A detailed comparison of the computational and experimental saturation capacities is shown in **Table 3.A.7**. For all the materials, the simulations predict that oX has the highest adsorption capacity followed by pX and then mX, in agreement with experiments and with previous studies performed on MIL-53(Al).[13] Among all the frameworks, both the experimental and simulation results point to MIL-53(Al) having the highest adsorption capacity for each adsorbate.

We then performed quaternary liquid breakthrough measurements on three of the materials: MIL-53(Al), MIL-53(Cr) and MIL-53(Ga). We excluded MIL-53(Fe) from this study since it showed significantly lower unary saturation capacities (**Table 3.A.7**). C_8 aromatic separations are typically conducted in the liquid-phase at higher pressures (~ 100 psi), and the observed unary characteristics of MIL-53(Fe) would likely limit its separation performance. **Figure 3.4** shows the results of liquid breakthrough measurements for each of the three MIL-53 materials. It is evident that all the MIL-53 adsorbents investigated are oX-selective, with MIL-53(Al) being the most selective among the three. The TIPB tracer breakthrough is much faster than that of the C_8 aromatics, since it is weakly adsorbed. A careful observation of **Figure 3.4** also reveals that in MIL-53(Cr) and MIL-53(Ga), some separation of pX and mX can be achieved with breakthrough occurring in the following order: EB < pX < mX < oX. However in MIL-53(Al), there is insignificant relative separation of pX and mX with the relative order of breakthrough times: EB < pX ~ mX <

oX. A ‘roll-up’ effect is also observed in all the three adsorbents studied, with the greatest effect occurring in MIL-53(Al).

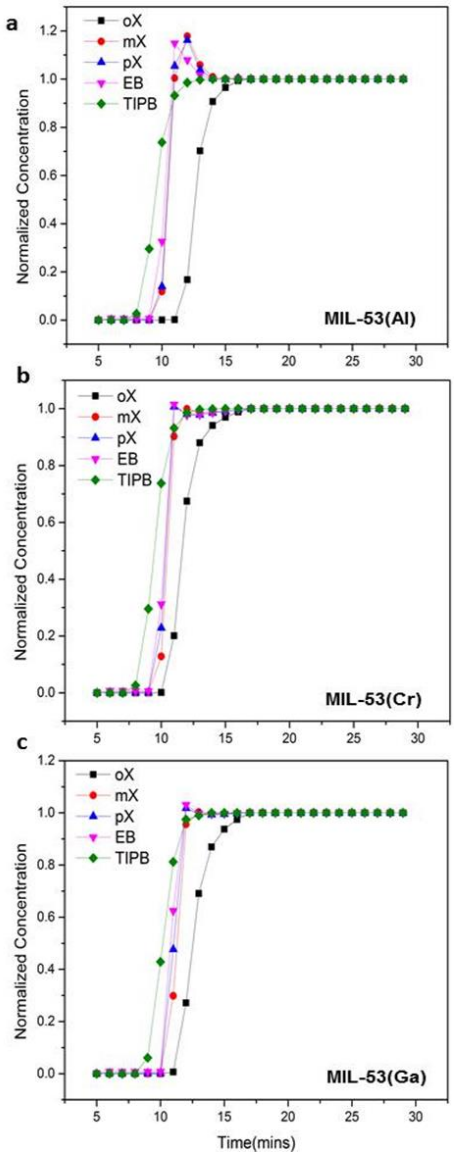

Figure 3.4: Liquid breakthrough traces for (a) MIL-53(Al), (b) MIL-53(Cr), and (c) MIL-53(Ga). The feed mixture was 0.5:1:2:1 EB:pX:mX:oX at 100 psi and 323 K. TIPB was used as a tracer.

In all the materials, the roll-up effect is synchronous with the breakthrough of oX, indicating that the more strongly adsorbing oX displaces the initial adsorbed pX, mX and EB from the MIL-53 pores. In order to obtain quantitative information from the

breakthrough data, the roll-up effects as well as the variations in the outlet flowrate must be taken into account when calculating the adsorbed amounts of each component. The time-dependent outlet liquid flowrate (and also the pressure drop) are recorded for each MIL-53 column. **Figure 3.A.5** shows typical data from a MIL-53(Al) column. The flow rate data in **Figure 3.A.5** are used to obtain the time-dependent flow.

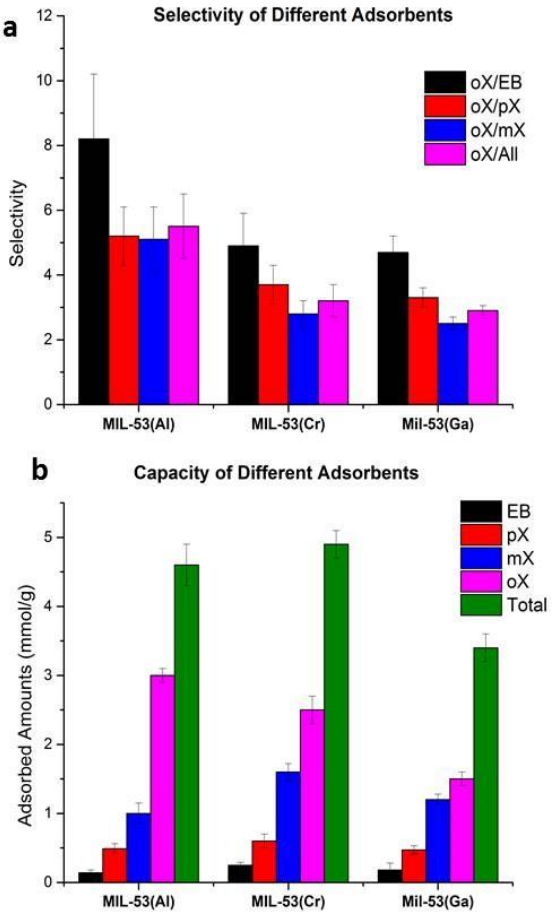

Figure 3.5: (a) oX selectivity (relative to each of the other components and relative to all other components); and (b) adsorption capacity (by each component as well as total), for MIL-53(Al), MIL-53(Cr) and MIL-53(Ga) as obtained from quaternary liquid breakthrough measurements at 323 K and 100 psi.

Quantitative values of selectivity and capacity were obtained from the experimental data and are depicted in **Figure 3.5**. A detailed listing of the obtained values is given in

Table 3.A.8. The oX selectivity relative to all other components combined ('oX/All') of MIL-53(Al) is around 5 while MIL-53(Cr) gives a selectivity of 3 and MIL-53(Ga) leads to a selectivity of 2.5. There is no statistically significant difference between the oX/pX and oX/mX selectivities of MIL-53(Al), the mean values of which were computed to be 5.2 and 5.1 respectively. This is in agreement with previous work on MIL-53(Al) that reports no relative pX and mX selection in this adsorbent from binary liquid-phase breakthrough experiments.[15] However, MIL-53(Cr) and MIL-53(Ga) both show a mX/pX selectivity of around 1.4. The oX/EB selectivity in MIL-53(Cr) is 4.9, which is less than MIL-53(Al) where it is around 8. In terms of overall capacities, MIL-53(Cr) (4.9 mmol/g) is similar to that of MIL-53(Al) (4.6 mmol/g). MIL-53(Ga) had the lowest overall capacity of 3.4 mmol/g. This is consistent with its smaller BET surface area even when accounting for the different framework densities of the MOFs due to their different metal centers (**Table 3.1**). In terms of the oX capacity, MIL-53(Al) had the highest value (3 mmol/g).

The above findings clearly point to the dominance of competitive oX adsorption over the other isomers in all of the MIL-53 series of adsorbents under industrially relevant conditions (liquid phase, higher pressure, quaternary mixture) regardless of the saturation loadings and uptake pressures observed in single-component adsorption. The observation that MIL-53(Al) cannot discriminate between mX and pX has been made in previous literature reports,[14,15] but here it is interesting to observe that both MIL-53(Cr) and MIL-53(Ga) adsorb mX preferentially over pX in multicomponent breakthrough. The breathing behavior of the adsorbents in the MIL-53 series with respect to temperature or humidity are different due to the known effect of the metal center on the adsorbent-adsorbate interactions.

We now comment upon the oX selectivity in MIL-53(Al) obtained in this work relative to those reported in two previous studies. In one of the previous works,[15] separate binary batch adsorption measurements from a liquid phase feed (0.014 M concentration of each of the two isomers in hexane) led to the following selectivities: oX/EB = 10.9, oX/pX = 3.5, and oX/mX = 2.7. However, the authors also reported that whereas in unary adsorption both oX and pX displayed 40-45 wt% uptake in MIL-53(Al), in equimolar binary mixtures oX dominated the adsorption (up to 45 wt% uptake) while pX never exceeded more than 5 wt% uptake. The authors predicted an increasing binary oX/pX selectivity with increasing bulk-phase liquid concentrations, with selectivity up to 12 at 0.6 M bulk concentration of each isomer.[15] In this study, multicomponent breakthrough runs were conducted at an oX isomer concentration of 1.8 M, so it is reasonable that we obtain higher selectivity values than those previously reported from binary batch measurements at 0.014 M and comparable selectivities to the previous measurements at 0.6 M. In another previous work, ternary breakthrough measurements for oX, pX and mX have been reported in MIL-53(Al) at 313 K and 2.7 M equimolar bulk isomers concentrations in heptane.[14] The authors used MIL-53(Al) pellets (also containing binders) that were supplied by BASF. They reported a low oX/pX selectivity of ~2, and justified this value by hypothesizing that the binder may have prevented the full NP→LP breathing and/or caused pore blockage. Compared to the reported BET surface area (550 m^2/g) of MIL-53(Al)/binder pellets used in their work, our samples of pure MIL-53(Al) have a much higher BET surface area (**Table 3.1**).

Multicomponent (quaternary) adsorption simulations were then performed accounting for MIL-53 framework flexibility, in order to predict the experimentally

observed behavior. This is the first attempt in the literature to study multicomponent adsorption of C_8 aromatics in MIL-53 while taking the adsorbate-framework structural coupling into account. Since the multicomponent adsorption occurs at high pressure and high loadings, the MIL-53 frameworks are already in their LP form and consideration of the NP→LP transition is not necessary. However, the LP framework swelling/relaxation at high loadings must be accounted for. In our unary adsorption simulations described earlier in this chapter, we used iterative GCMC+MD calculations to describe this effect. It proved difficult to obtain converged results using the same method for multicomponent adsorption. To simplify the calculations, it was proposed that the relaxation of MIL-53 LP structures due to adsorbates at high loading is not significantly dependent on the type of adsorbate among the C_8 aromatic isomers, even though it is significantly different compared to the empty structure. This is initially supported by the fact that the relaxation of frameworks in single-component studies show that the increase in volume due to adsorbate loading is similar for all C_8 adsorbates. To test this hypothesis further, histograms of the linker dihedral angle were plotted for MIL-53(Al) loaded with each of the four adsorbates (**Figure 3.6**). Similar histograms for MIL-53(Cr) and MIL-53(Ga) are shown in **Figure 3.A.7**. It is seen that the linker dihedral angle distribution is not significantly dependent on the type of C_8 aromatic adsorbate. Note that the dihedral distribution is significantly different in the empty framework than in the adsorbate-loaded frameworks. The above findings allow a simplification in modeling the flexibility of MIL-53 during multicomponent adsorption. Dynamical snapshots of each relaxed MIL-53 framework containing oX at high loading were generated using NPT MD simulations in order to describe the adsorbate-framework structural coupling. The adsorption properties of C_8 aromatics were then calculated using

GCMC simulations for ten distinct snapshot structures and averaged to obtain physically realistic values.

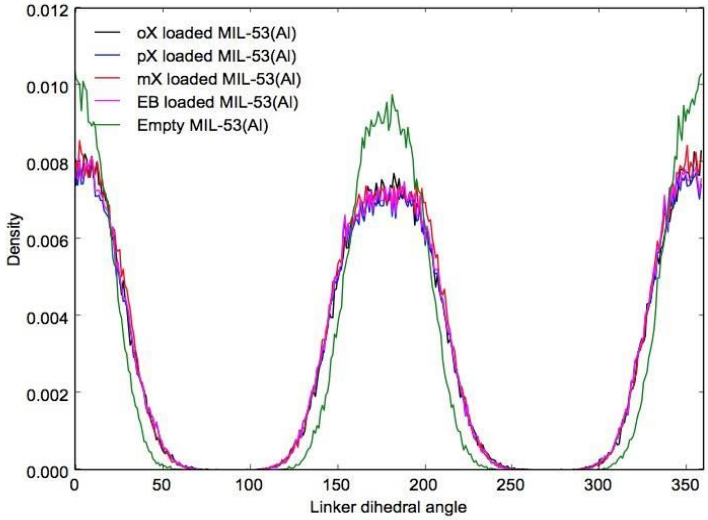

Figure 3.6: Histograms of the linker dihedral angle distribution for C_8 aromatics in MIL-53(Al).

A detailed comparison of experimental and computational multicomponent capacities and selectivities for the three MIL-53 adsorbents is given in **Table 3.A.8**. **Figure 3.7** shows comparisons between four computed selectivites (oX/mX, oX/pX, oX/EB, and oX/All) versus those obtained experimentally. For MIL-53(Al), data from the two previous experimental studies[14,15] are also shown for comparison, even though they were obtained only for binary mixtures as discussed earlier. In general, the simulations are in qualitative agreement with our experimental data. The total capacities (**Table 3.A.8**) are in good agreement (2-20% difference between experiment and simulation). In **Figure 3.7**, the four selectivities show the same trends in experiment and simulation, with oX/EB selectivities being the highest. Both simulations and experiments concur that MIL-53(Al) has the highest oX selectivity among all MIL-53 adsorbents, and that all MIL-53 series of

adsorbents are oX selective. Quantitatively speaking, the simulations under-predict the selectivities. A previous report explained the oX-selective nature of MIL-53(Al) as being due to preferred interactions of C_8 aromatics with the MOF framework.[12] Methyl groups in oX are at adjacent positions, allowing the interaction of both methyl groups with the carboxylate groups of the MIL-53 framework, whereas mX and pX molecules can only interact with carboxylate groups *via* one methyl group. The methyl group in *meta*-position of mX can interact with carbon atoms of the aromatic ring of the framework, but the geometry of pX prevents the interaction of the *para*- methyl group with the framework. This theory supports the selectivity order of xylene isomers observed in MIL-53. However, the adsorption energies of C_8 aromatics calculated by our GCMC simulations are not found to be significantly different (oX: -60.7, mX: -59.53, pX: -59.45, and EB: -59.1 kJ/mol). Another study suggested that the oX-selective nature of MIL-53(Al) is related to the dynamic rotation of the organic linker in the MIL-53 framework and its sensitivity to the type of aromatic isomer adsorbate.[41] However, our MD calculations show (**Figure 3.6**) that the distribution of linker rotation angle is not significantly different for the different isomers. Rather, the high experimental oX selectivity observed in multicomponent liquid breakthrough, the roll up effects showing preferential oX adsorption at high xylene loadings, and a lack of correlation of multicomponent oX selectivity with unary oX capacities (**Table 3.A.7**), lead us to hypothesize that entropic effects such as better packing efficiency of oX under high xylene loadings - along with preferred interactions of oX with the MIL-53 framework - lead to the observed oX selectivity.

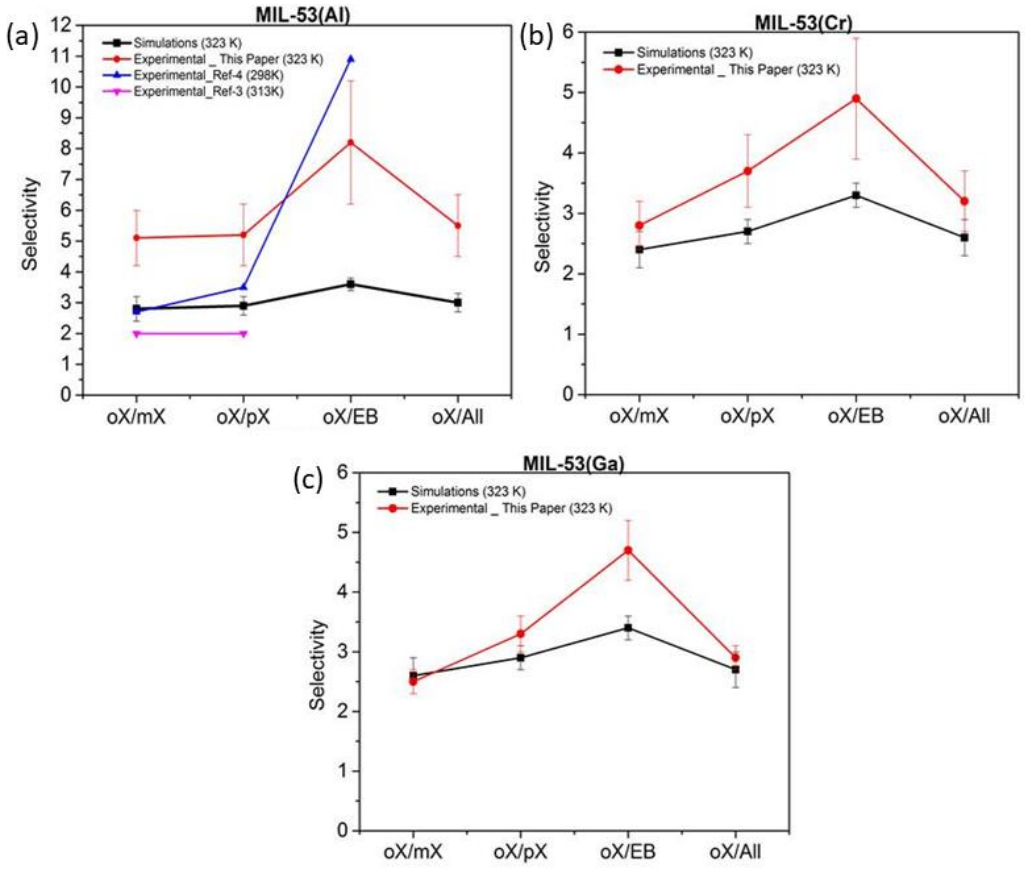

Figure 3.7: Multicomponent adsorption selectivity comparison between simulations and experiments: (a) MIL-53(Al), (b) MIL-53(Cr), and (c) MIL-53(Ga).

3.4 Summary

We have investigated C_8 aromatic isomer separation by different members of the flexible MIL-53 MOF series with a combined experimental and computational methodology. The inclusion of flexibility effects in adsorption simulations through the use of OFAST methods was found to be effective in correctly predicting unary C_8 isomer adsorption in several MIL-53 materials. Quaternary liquid phase breakthrough measurements showed all the MIL-53 adsorbents to be oX-selective. MIL-53(Al) showed the highest oX selectivity, while both MIL-53(Cr) and MIL-53(Ga) showed significant mX/pX separation unlike MIL-53(Al). Though previous reports exist on the oX selectivity

of MIL-53(Al) and MIL-53(Fe), this work is the first to report quaternary liquid phase breakthrough measurements in MIL-53 materials under industrially relevant xylene feeds and operating conditions. Furthermore, we report the first simulations of C_8 aromatic isomer multicomponent adsorption in MIL-53, and the results are shown to be in good qualitative agreement with experiment. Based upon consideration of all our results, it appears that both the packing efficiency of oX in MIL-53 under high xylene loadings as well as its preferential interaction with the linker determine the observed oX selectivity in MIL-53 materials.

APPENDEX 3.A. SUPPORTING INFORMATION FOR CHAPTER 3

3.A.1 OFAST Simulation Details

The osmotic framework adsorption solution theory (OFAST) method[30,31] was used to describe structural transition of MIL-53 due to C_8 aromatics adsorption. In the method, the osmotic potential, **Ω**, is calculated for adsorption of any adsorbates for metastable host rigid frameworks. The system having the lowest osmotic potential at a given set of conditions is favored to be at equilibrium by thermodynamics. Here, we have considered only single component adsorption, for which **Ω** is defined as:

$$\Omega_k(T,f) = F_{host}^k(T) + PV_k - RT\int_0^f \frac{n_k^e(f,T)}{f}df \qquad (3.A.1)$$

Here F_{host} is the Helmholtz free energy of the empty framework, n^e is the excess amount of adsorbate molecules adsorbed in the framework, and f is the fugacity of the bulk fluid phase. At low pressures, the excess adsorbed amount is equal to absolute adsorbed amount and the fugacity is equal to the pressure. For two pore structures in MIL-53, Equation 3.A.1 becomes:

$$\Delta G_{total} = \Delta\Omega_{total} = \Delta F_{host} + P\Delta V - RT\int_0^f \frac{\Delta n^e}{f}df \qquad (3.A.1)$$

At a transition pressure at which one structure makes a transition to another structure, Equation 3.A.2 becomes equal to zero as both structures have same osmotic potential at that pressure. So, if we have free energy difference between both structures, transition pressure can be calculated and vice versa. It is difficult to accurately calculate free energy differences between frameworks, we used the transition pressure of one adsorbate from the

experiments (oX in this chapter) to calculate free energy difference of narrow pore and large pore frameworks, and then used that free energy difference to calculate transition pressures for other C_8 aromatics in single component adsorption. Because the narrow-pore structures show no adsorption in our calculations, this transition pressures is same as the pressure at which adsorbate loading starts in the isotherms.

3.A.2 Force Field Parameters for MD calculations

The flexible force fields for MIL-53 have been derived starting with those previously reported for MIL-53(Cr) by Ma *et al.*[18] In this force field, the intramolecular force constant for organic moiety were extracted from the widely used Consistent Valence Force Field (CVFF) same as for the inorganic part. For metal-oxygen intramolecular and non-bonded interactions parameters were adopted from UFF force field.[35] C3-O2-M(metal) three body interactions were considered to have the same values for all metals. The torsion terms are adjusted to reproduce basic structural features of MIL-53 frameworks. Note that the non-bonded interactions concern atoms separated by exactly three bonds usually described as 1-4 van der Waals interactions with LJ potentials.

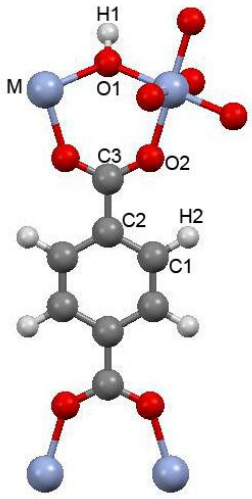

Figure 3.A.1: Atomic configuration of MIL-53 with atom types labeled. Here, M = Cr, Al, Ga, Fe.

Table 3.A.1: Lennard Jones parameters for framework atoms.

Atom Type	**ε_{ii} (kJ/mol)**	**σ_{ii} (Å)**
C	0.2478	3.81
H	0.1602	2.45
O	0.2495	3.12
Cr	0.0627	2.69
Al	1.2955	3.91
Ga	1.7343	3.91
Fe	0.0543	2.59

Note: These parameters are taken from the force field for MIL-53(Cr) derived by Ma et al.[18] Parameters for Al, Ga and Fe are taken from UFF.[35]

Table 3.A.2: DDEC charges for frameworks.

Atom Type	MIL-53(Cr)	MIL-53(Al)	MIL-53(Ga)	MIL-53(Fe)
C1	-0.0789	-0.0732	-0.0763	-0.0779
C2	-0.0946	-0.1042	-0.0937	-0.0868
C3	0.6804	0.7342	0.7133	0.6470
O1	-0.9432	-1.0993	-1.0004	-0.7279
O2	-0.6099	-0.6479	-0.6251	-0.5143
H1	0.4644	0.4788	0.4691	0.4374
H2	0.1113	0.1120	0.1138	0.1093
Cr	1.6172	-	-	-
Al	-	1.7969	-	-
Ga	-	-	1.6425	-
Fe	-	-	-	1.1016

Note: These values are derived using plane wave DFT calculations.

Table 3.A.3: Bond stretch parameters for MIL-53.

i-j	k_{ij} [kJ/(mol.Å^2)]	r_0 (Å)
C1-C1	4015.05	1.34
C1-C2	4015.05	1.34
C2-C3	2943.72	1.47
C3-O2	4516.93	1.25
C1-H2	2850.14	1.09
O1-Cr	2041.72	1.95
O2-Cr	2041.72	1.95
O1-Al	1830.24	1.93
O2-Al	1830.24	1.93
O1-Ga	1755.99	2.02
O2-Ga	1755.99	2.02
O1-Fe	2109.65	1.93
O2-Fe	2109.65	1.93

Table 3.A.4: Bond bending parameters for MIL-53.

i-j-k	k_{ij} [kJ/(mol.rad^2)]	Θ (^{0})
C1-C2-C1	753.30	120
C1-C1-C2	753.30	120
C1-C1-H2	309.72	120
C2-C1-H2	309.72	120
C1-C2-C3	290.32	120
C2-C3-O2	569.25	120
O2-C3-O2	114.16	123
C3-O2-Cr	115.9	136
C3-O2-Al	115.9	136
C3-O2-Ga	115.9	136
C3-O2-Fe	115.9	136

Table 3.A.5: Torsional parameters for MIL-53.

i-j-k-l	k_{ij} [kJ/(mol.rad^2)]	N	Θ (^{0})
C2-C1-C1-C2	2.0	2	180
C3-C2-C1-C1	2.0	2	180
C2-C1-C1-H2	2.0	2	180
H2-C1-C1-H2	2.0	2	180
C3-C2-C1-H2	2.0	2	180
H2-C1-C2-C1	2.0	2	180
C1-C1-C2-C1	2.0	2	180
C1-C2-C3-O2	5.0	2	180
C2-C3-O2-Cr	20.0	2	180
C2-C3-O2-Al	18.0	2	180
C2-C3-O2-Ga	22.0	2	180
C2-C3-O2-Fe	22.0	2	180

Table 3.A.6: DFT-optimized lattice parameters for MIL-53 materials.

	a (Å)	b (Å)	c (Å)	a (Å)	b (Å)	c (Å)
	DFT Simulations	Experiments[32,42]				
MIL-53(Cr)						
Large pore (LP)	16.73	13.29	6.74	16.77	13.03	6.81
Narrow pore (NP)	19.85	6.20	6.51	19.68	7.84	6.78
NP_water loaded	19.62	7.76	6.62			
MIL-53(Al)						
Large pore	16.64	13.42	6.76	16.67	13.33	6.80
Narrow pore	19.75	6.26	6.62	19.79	7.94	6.81
NP_waterloaded	19.68	7.83	6.68			
MIL-53(Ga)						
Large pore	16.93	13.12	6.76	16.85	13.01	6.82
Narrow pore	19.89	6.12	6.82	19.81	7.96	6.80
NP_waterloaded	19.78	7.72	6.86			
MIL-53(Fe)						
Large pore	16.67	13.20	6.60	16.89	12.54	6.58
Narrow pore	19.54	6.24	6.35	19.51	7.61	6.57
NP_waterloaded	19.44	7.65	6.63			

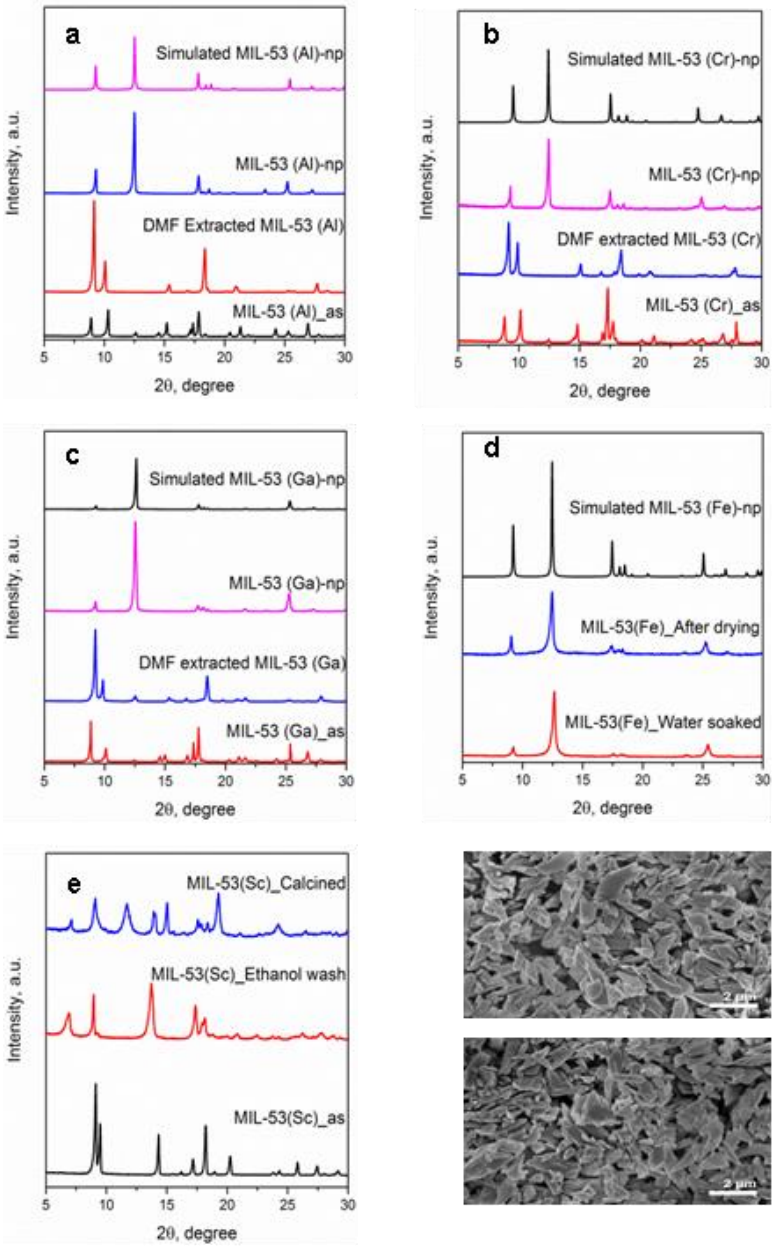

Figure 3.A.2: Powder-XRD patterns (a)-(e) and SEM images (f)-(g) of MIL-53 adsorbents at different stage of synthesis. (a) MIL-53 (Al), (b) MIL-53 (Cr), (c) MIL-53 (Ga), (d) MIL-53 (Fe), (e) MIL-53 (Sc), (f) washed MIL-53 (Sc), and (g) calcined MIL-53 (Sc). Impure peak at 2θ angle of ~ 17.3° in (a)~(e) was ascribed to the excess BDC linkers in the as-synthesized (as) sample.

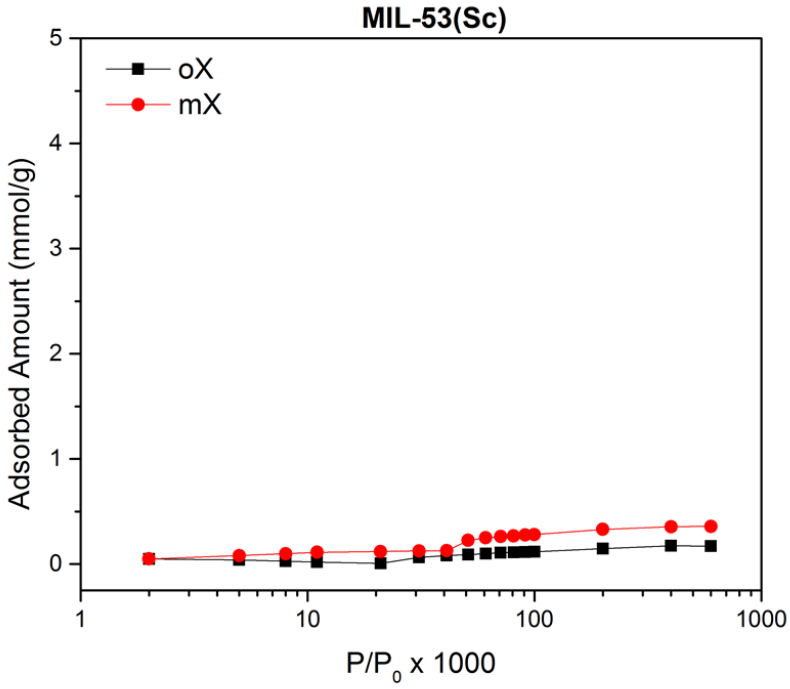

Figure 3.A.3: Adsorption isotherms of mX and oX on MIL-53(Sc) at 323 K.

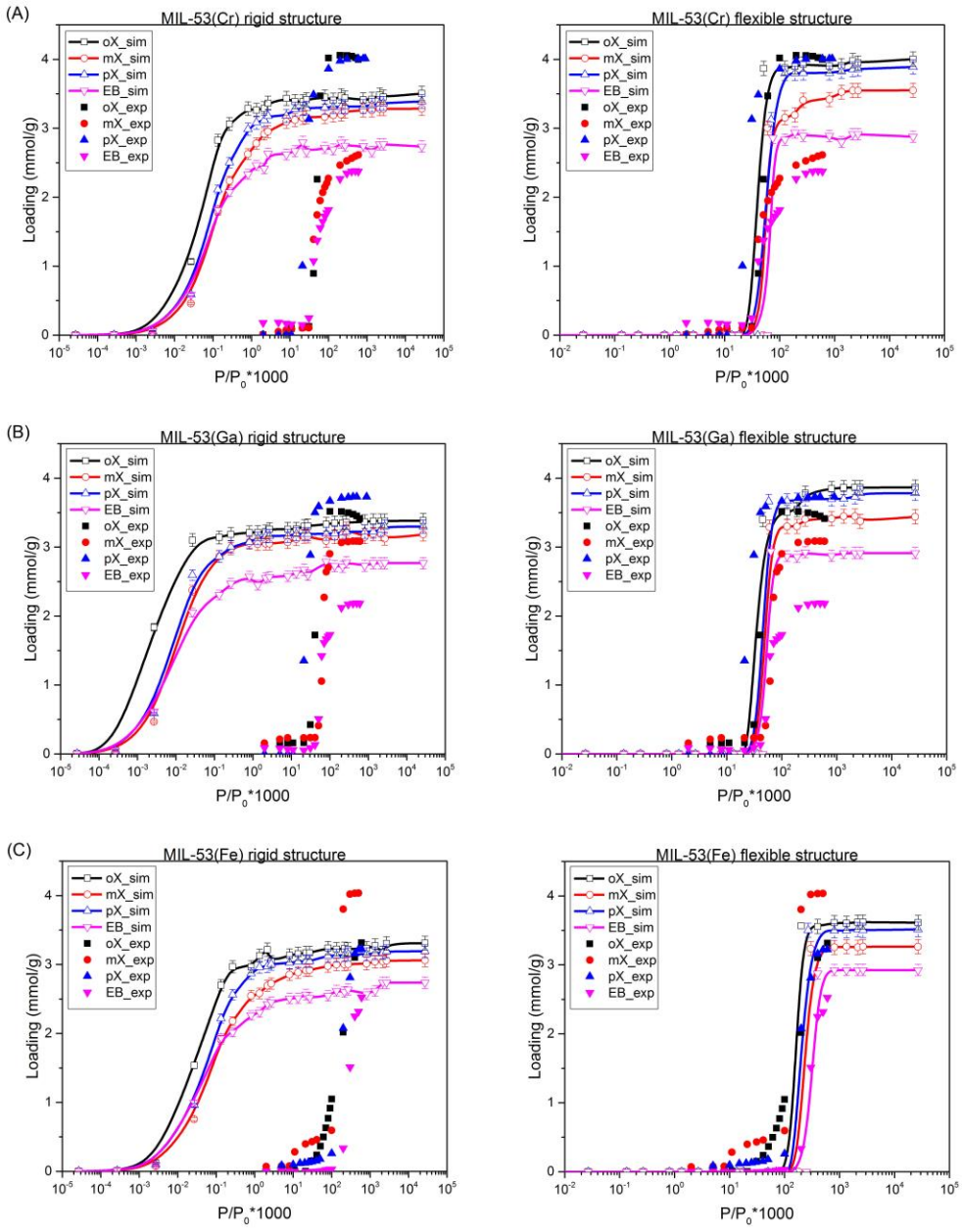

Figure 3.A.4: Rigid-structure and flexible-structure simulations compared with experimental data for single-component adsorption of xylene isomers in (a) MIL-53(Cr), (b) MIL-53(Ga) and (c) MIL-53(Fe).

Table 3.A.7: Summary comparison of experimental and simulated unary adsorption characteristics of C_8 aromatics in MIL-53 materials. The error bars on the data are approximately 0.1 mmol/g.

Material	**Single-component saturation capacity (mmol/g)**			
	oX	**pX**	**mX**	**EB**
MIL-53(Al)				
Experiment	4.5	4.6	4.5	2.5
Simulation	4.4	4.3	4.0	3.3
MIL-53(Cr)				
Experiment	4.0	4.2	2.6	2.4
Simulation	3.9	3.8	3.6	2.9
MIL-53(Ga)				
Experiment	3.4	3.7	3.1	2.2
Simulation	3.8	3.75	3.5	2.9
MIL-53(Fe)				
Experiment	3.3	4.0	3.2	2.5
Simulation	3.7	3.6	3.3	2.8

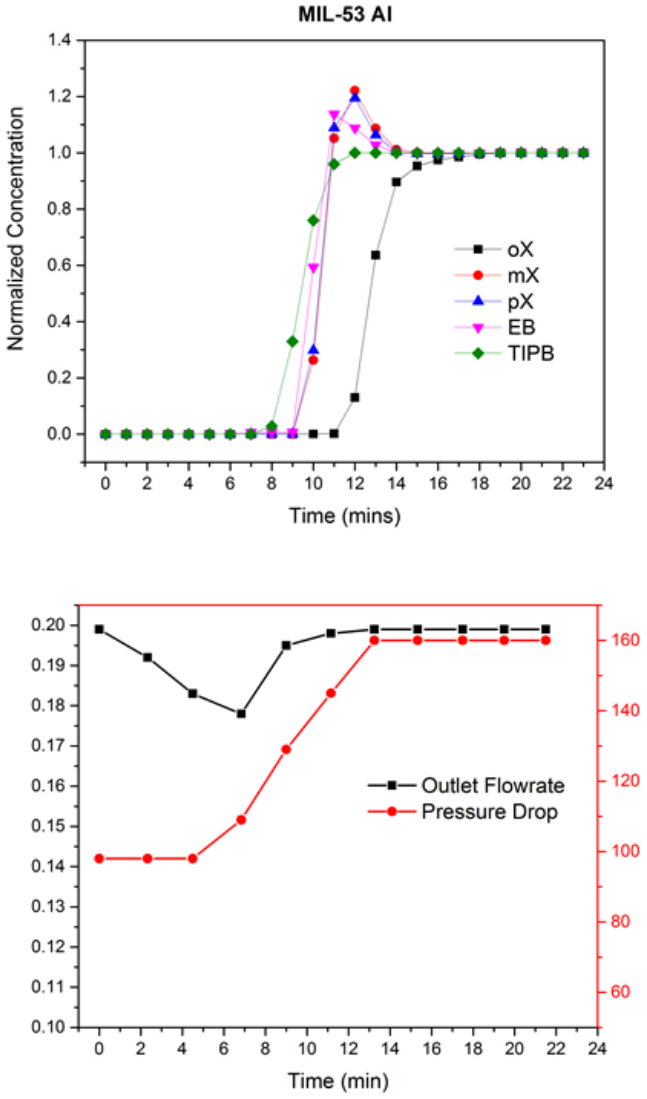

Figure 3.A.5: Variation of outlet flowrate and pressure drop observed across a MIL-53(Al) column during breakthrough of a 0.5:1:2:1 EB:pX:mX:oX feed mixture at 100 psi backpressure and 323 K. The data shown in the top panel is the same as **Figure 4a**.+

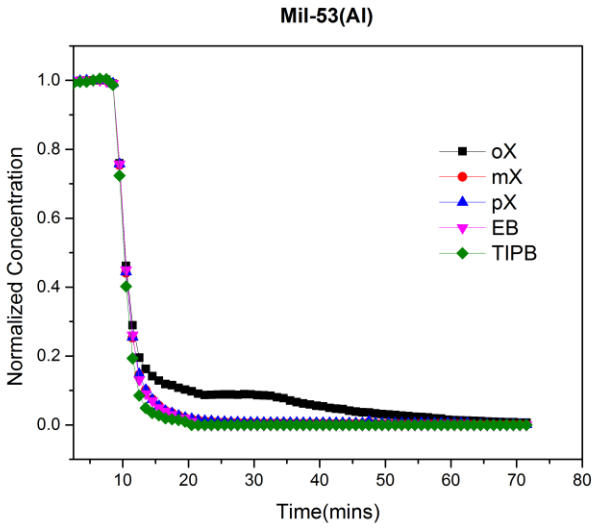

Figure 3.A.6: Desorption trace of adsorbed aromatic isomers in a MIL-53(Al) column using a hexane desorbent, following a breakthrough adsorption run with feed mixture 0.5:1:2:1 EB:pX:mX:oX at 100 psi and 323 K.

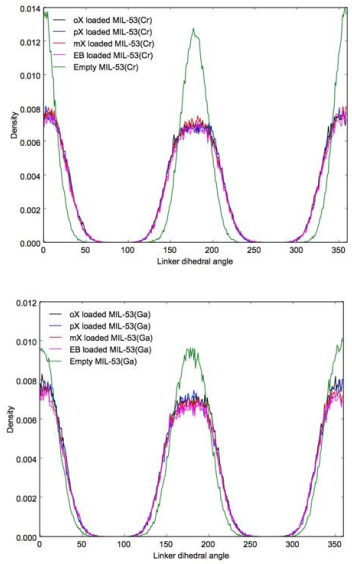

Figure 3.A.7: Calculated distribution of linker dihedral angles in MIL-53(Cr) and MIL-53(Ga).

Table 3.A.8: Comparison of computational and experimental adsorption capacity and selectivity values for different MIL-53 adsorbents under quaternary liquid-phase adsorption with a 0.5:1:2:1 EB:pX:mX:oX mixture at 323 K and 100 psi.

	Capacity (mmol/g)					Selectivity				
Material	**oX**	**mX**	**pX**	**EB**	**Total**	**oX/oX**	**oX/mX**	**oX/pX**	**oX/EB**	**oX/All**
MIL-53(Cr)										
Simulations	1.7±0.2	1.4±0.1	0.6±0.1	0.3±0.02	3.9±0.2	1.0	2.4±0.3	2.7±0.2	3.3±0.2	2.6±0.3
Experiments	2.5±0.2	1.6±0.1	0.6±0.1	0.25±0.04	4.9±0.2	1.0	2.8±0.4	3.7±0.6	4.9 ±1	3.2±0.5
MIL-53(Al)										
Simulations	2.0±0.2	1.5±0.2	0.7±0.1	0.3±0.03	4.5±0.2	1.0	2.8±0.4	2.9 ±0.3	3.6±0.2	3±0.3
Experiments	3±0.1	1±0.2	0.49±0.1	0.14±0.04	4.6±0.3	1.0	5.1±0.9	5.2±1	8.2±2	5.5±1
MIL53(Ga)										
Simulations	1.6±0.2	1.3±0.1	0.6±0.1	0.2±0.03	3.7±0.2	1.0	2.6±0.3	2.9±0.2	3.4±0.2	2.7±0.3
Experiments	1.5±0.1	1.2±0.1	0.47±0.1	0.18±0.06	3.4±0.2	1.0	2.5±0.2	3.3±0.3	4.7±0.5	2.9±0.2
MIL-53(Cr)										
Simulations	1.7±0.2	1.4±0.1	0.6±0.1	0.3±0.02	3.9±0.2	1.0	2.4±0.3	2.7±0.2	3.3±0.2	2.6±0.3
Experiments	2.5±0.2	1.6±0.1	0.6±0.1	0.25±0.04	4.9±0.2	1.0	2.8±0.4	3.7±0.6	4.9 ±1	3.2±0.5

3.5 References

(1) Fabri, J.; Simo, T. A. *Xylenes. Ullmann's Encyclopedia of Industrial Chemistry*; John Wiley & Sons: New York, 2000; Vol. 6.

(2) Franck, H. G.; Stadelhofer, J. W. *Industrial Aromatic Chemistry. Raw Materials, Process, Products*; Springer-Verlag: Berlin, 1988.

(3) Sholl, D. S.; Lively, R. P. Seven Chemical Separations to Change the World. *Nature* **2016**, *532* (7600), 435–437.

(4) Moreira, M. A.; Santos, J. C.; Ferreira, A. F. P.; Loureiro, J. M.; Rodrigues, A. E. Influence of the Eluent in the MIL-53(Al) Selectivity for Xylene Isomers Separation. *Ind. Eng. Chem. Res.* **2011**, *50* (12), 7688–7695.

(5) Broughton, D. B.; Neuzil, R. W.; Pharis, J. M.; Brearley, C. S. Parex Process for Recovering Paraxylene. *Chem. Eng. Prog.* **1970**, *66*, 70–82.

(6) Kurup, A. S.; Hidajat, K.; Ray, A. K. Optimal Operation of an Industrial-Scale Parex Process for the Recovery of p-Xylene from a Mixture of C_8 Aromatics. *Ind. Eng. Chem. Res.* **2005**, *44* (15), 5703–5714.

(7) Methivier, A. Separation of Paraxylene by Adsorption. In *Zeolites for Cleaner Technologies*; Imperial College Press, 2011; pp 209–221.

(8) Xomeritakis, G.; Lai, Z. P.; Tsapatsis, M. Separation of Xylene Isomer Vapors with Oriented MFI Membranes Made by Seeded Growth. *Ind. Eng. Chem. Res.* **2001**, *40* (2), 544–552.

(9) Gee, J. A.; Zhang, K.; Bhattacharyya, S.; Bentley, J.; Rungta, M.; Abichandani, J. S.; Sholl, D. S.; Nair, S. Computational Identification and Experimental Evaluation of Metal-Organic Frameworks for Xylene Enrichment. *J. Phys. Chem. C* **2016**, *120* (22), 12075–12082.

(10) Finsy, V.; Verelst, H.; Alaerts, L.; De Vos, D.; Jacobs, P. A.; Baron, G. V; Denayer, J. F. M. Pore-Filling-Dependent Selectivity Effects in the Vapor-Phase Separation of Xylene Isomers on the Metal-Organic Framework MIL-47. *J. Am. Chem. Soc.* **2008**, *130* (22), 7110–7118.

(11) El Osta, R.; Carlin-Sinclair, A.; Guillou, N.; Walton, R. I.; Vermoortele, F.; Maes, M.; de Vos, D.; Millange, F. Liquid-Phase Adsorption and Separation of Xylene Isomers by the Flexible Porous Metal–Organic Framework MIL-53(Fe). *Chem. Mater.* **2012**, *24* (14), 2781–2791.

(12) Finsy, V.; Kirschhock, C. E. A.; Vedts, G.; Maes, M.; Alaerts, L.; Vos, D. E. De; Baron, G. V; Denayer, J. F. M. Framework Breathing in the Vapour-Phase Adsorption and Separation of Xylene Isomers with the Metal–Organic Framework

MIL-53. *Chem. - A Eur. J.* **2009**, *15*, 7724–7731.

(13) Duan, L.; Dong, X.; Wu, Y.; Li, H.; Wang, L.; Song, L. Adsorption and Diffusion Properties of Xylene Isomers and Ethylbenzene in Metal–Organic Framework MIL-53(Al). *J. Porous Mater.* **2012**, *20* (2), 431–440.

(14) Moreira, M. A.; Santos, J. C.; Ferreira, A. F. P.; Müller, U.; Trukhan, N.; Loureiro, J. M.; Rodrigues, A. E. Selective Liquid Phase Adsorption and Separation of Ortho-Xylene with the Microporous MIL-53(Al). *Sep. Sci. Technol.* **2011**, *46* (13), 1995–2003.

(15) Alaerts, L.; Maes, M.; Giebeler, L.; Jacobs, P. A.; Martens, J. A.; Denayer, J. F. M.; Kirschhock, C. E. A.; De Vos, D. E. Selective Adsorption and Separation of Ortho-Substituted Alkylaromatics with the Microporous Aluminum Terephthalate MIL-53. *J. Am. Chem. Soc.* **2008**, *130* (43), 14170–14178.

(16) Millange, F.; Guillou, N.; Walton, R. I.; Greneche, J. M.; Margiolaki, I.; Fereya, G. Effect of the Nature of the Metal on the Breathing Steps in MOFs with Dynamic Frameworks. *Chem. Commun.* **2008**, No. 39, 4732–4734.

(17) Gee, J. A.; Sholl, D. S. Effect of Framework Flexibility on C_8 Aromatic Adsorption at High Loadings in Metal-Organic Frameworks. *J. Phys. Chem. C* **2016**, *120* (1), 370–376.

(18) Ma, Q.; Yang, Q.; Ghoufi, A.; Ferey, G.; Zhong, C.; Maurin, G. Guest Dependent Pressure Behavior of the Flexible MIL-53(Cr): A Computational Exploration. *Dalt. Trans.* **2012**, *41* (14), 3915–3919.

(19) Yot, P. G.; Ma, Q.; Haines, J.; Yang, Q.; Ghoufi, A.; Devic, T.; Serre, C.; Dmitriev, V.; Férey, G.; Zhong, C.; et al. Large Breathing of the MOF MIL-47(V^{IV}) under Mechanical Pressure: A Joint Experimental-Modelling Exploration. *Chem. Sci.* **2012**, *3* (4), 1100–1104.

(20) Gee, J. A.; Sholl, D. S. Prediction of Adsorption Properties of Cyclic Hydrocarbons in MOFs Using DFT-Derived Force Fields. *J. Phys. Chem. C* **2015**, *119* (29), 16920–16926.

(21) Agrawal, M.; Bhattacharyya, S.; Huang, Y.; Jayachandrababu, K. C.; Murdock, C. R.; Bentley, J. A.; Rivas-Cardona, A.; Mertens, M. M.; Walton, K. S.; Sholl, D. S.; et al. Liquid-Phase Multicomponent Adsorption and Separation of Xylene Mixtures by Flexible MIL-53 Adsorbents. *J. Phys. Chem. C* **2018**, *122* (1), 386–397.

(22) Dubbeldam, D.; Calero, S.; Ellis, D. E.; Snurr, R. Q. RASPA: Molecular Simulation Software for Adsorption and Diffusion in Flexible Nanoporous Materials. *Mol. Simul.* **2015**, *42* (2).

(23) Kresse, G.; Furthmüller, J. Efficient Iterative Schemes for Ab Initio Total-Energy Calculations Using a Plane-Wave Basis Set. *Phys. Rev. B - Condens. Matter Mater.*

Phys. **1996**, *54* (16), 11169–11186.

(24) Joubert, D. From Ultrasoft Pseudopotentials to the Projector Augmented-Wave Method. *Phys. Rev. B - Condens. Matter Mater. Phys.* **1999**, *59* (3), 1758–1775.

(25) Perdew, J. P.; Burke, K.; Ernzerhof, M. Generalized Gradient Approximation Made Simple. *Phys. Rev. Lett.* **1996**, *77* (18), 3865–3868.

(26) Grimme, S.; Antony, J.; Ehrlich, S.; Krieg, H. A Consistent and Accurate Ab Initio Parametrization of Density Functional Dispersion Correction (DFT-D) for the 94 Elements H-Pu. *J. Chem. Phys.* **2010**, *132* (15), 154104–154122.

(27) Mayo, S. L.; Olafson, B. D.; Goddard, W. A. DREIDING: A Generic Force Field for Molecular Simulations. *J. Phys. Chem.* **1990**, *94* (26), 8897–8909.

(28) Martin, M. G.; Siepmann, J. I. Transferable Potentials for Phase Equilibria. 1. United-Atom Description of n-Alkanes. *J. Phys. Chem. B* **1998**, *102*, 2569–2577.

(29) Manz, T. A.; Sholl, D. S. Chemically Meaningful Atomic Charges That Reproduces the Electrostatic Potential in Periodic and Nonperiodic Materials. *J. Chem. Theory Comput.* **2010**, *6*, 2455–2468.

(30) Coudert, F. X. The Osmotic Framework Adsorbed Solution Theory: Predicting Mixture Coadsorption in Flexible Nanoporous Materials. *Phys. Chem. Chem. Phys.* **2010**, *12* (36), 10904–10913.

(31) Zhang, C.; Gee, J. A.; Sholl, D. S.; Lively, R. P. Crystal-Size-Dependent Structural Transitions in Nanoporous Crystals: Adsorption-Induced Transitions in ZIF-8. *J. Phys. Chem. C* **2014**, *118* (35), 20727–20733.

(32) Serre, C.; Millange, F.; Thouvenot, C.; Noguès, M.; Marsolier, G.; Louër, D.; Férey, G. Very Large Breathing Effect in the First Nanoporous Chromium(III)-Based Solids: MIL-53 or CrIII (OH)·{$O_2C{-}C_6H_4{-}CO_2$}·{$HO_2C{-}C_6H_4{-}CO_2H$}$_X$ ·H_2O_Y. *J. Am. Chem. Soc.* **2002**, *124* (45), 13519–13526.

(33) Triguero, C.; Coudert, F. X.; Boutin, A.; Fuchs, A. H.; Neimark, A. V. Mechanism of Breathing Transitions in Metal-Organic Frameworks. *J. Phys. Chem. Lett.* **2011**, *2* (16), 2033–2037.

(34) Dauber-Osguthorpe, P.; Roberts, V. A.; Osguthorpe, D. J.; Wolff, J.; Genest, M.; Hagler, A. T. Structure and Energetics of Ligand Binding to Proteins: Escherichia Coli Dihydrofolate Reductase-Trimethoprim, A Drug Receptor System. *Proteins* **1988**, *47*, 31–47.

(35) Rappé, A. K.; Casewit, C. J.; Colwell, K. S.; Goddard, W. A.; Skiff, W. M. UFF, a Full Periodic Table Force Field for Molecular Mechanics and Molecular Dynamics Simulations. *J. Am. Chem. Soc.* **1992**, *114* (25), 10024–10035.

(36) Ferey, G.; Latroche, M.; Serre, C.; Millange, F.; Loiseau, T.; Percheron-Guegan, A. Hydrogen Adsorption in the Nanoporous Metal-Benzenedicarboxylate $M(OH)(O_2C\text{-}C_6H_4\text{-}CO_2)$ ($M = Al^{3+}$, Cr^{3+}), MIL-53. *Chem. Commun.* **2003**, No. 24, 2976–2977.

(37) Khan, N. A.; Jun, J. W.; Jhung, S. H. Effect of Water Concentration and Acidity on the Synthesis of Porous Chromium Benzenedicarboxylates. *Eur. J. Inorg. Chem.* **2010**, No. 7, 1043–1048.

(38) Millange, F.; Guillou, N.; Medina, M. E.; Ferey, G.; Carlin-Sinclair, A.; Golden, K. M.; Walton, R. I. Selective Sorption of Organic Molecules by the Flexible Porous Hybrid Metal-Organic Framework MIL-53(Fe) Controlled by Various Host-Guest Interactions. *Chem. Mater.* **2010**, *22* (14), 4237–4245.

(39) Mowat, J. P. S.; Miller, S. R.; Slawin, A. M. Z.; Seymour, V. R.; Ashbrook, S. E.; Wright, P. A. Synthesis, Characterisation and Adsorption Properties of Microporous Scandium Carboxylates with Rigid and Flexible Frameworks. *Microporous Mesoporous Mater.* **2011**, *142*, 7724–7731.

(40) Salles, F.; Ghoufi, A.; Maurin, G.; Bell, R. G.; Mellot-Draznieks, C.; Ferey, G. Molecular Dynamics Simulations of Breathing MOFs: Structural Transformations of MIL-53(Cr) upon Thermal Activation and CO2 Adsorption. *Angew. Chemie - Int. Ed.* **2008**, *47*, 8487–8491.

(41) Khudozhitkov, A. E.; Jobic, H.; Freude, D.; Haase, J.; Kolokolov, D. I.; Stepanov, A. G. Ultraslow Dynamics of a Framework Linker in MIL-53(Al) as a Sensor for Different Isomers of Xylene. *J. Phys. Chem. C* **2016**, *120* (38), 21704–21709.

(42) Biswa, S.; Vanpouck, D. E. P.; Verstraelen, T.; Vandichel, M.; Couck, S.; Leus, K.; Liu, Y.-Y.; Waroquier, M.; Speybroeck, V. Van; Denayer, J. F. M.; et al. New Functionalized Metal–Organic Frameworks MIL-47-X (X = −Cl, −Br, $-CH_3$, $-CF_3$, −OH, $-OCH_3$): Synthesis, Characterization, and CO_2 Adsorption Properties. *J. Phys. Chem. C* **2013**, *117* (44), 22784–22796.

CHAPTER 4. ADSORPTION OF CHEMICAL WARFARE AGENTS AND THEIR SIMULANTS IN MOFS[d]

4.1 Introduction

Chemical Warfare Agents (CWAs) are extremely toxic synthetic chemicals that are organized into several categories according to the physiological manner in which they affect the human body.[1–3] Our focus in this chapter is on the nerve agents Sarin and Soman, which contain free phosphonic acid terminal groups that can form strong complexes with divalent metal ions. Most laboratory studies of CWAs of this kind use simulant molecules rather than the CWAs themselves. It is therefore important to understand what constitutes a useful simulant for various processes that involves CWAs; it is this issue that is addressed in this chapter.

Metal-organic frameworks (MOFs) or porous-coordination polymers (PCPs) are crystalline nanoporous material consisting of inorganic and organic linkers. Because of the extraordinary degree of diversity in both organic and inorganic parts, high surface area and high porosity, MOFs have been studied for a large number of potential applications including gas storage,[4] chemical separations,[5] catalysis,[6,7] sensing,[8] drug delivery,[9] and more recently the capture and detoxification of CWAs.[10–17] Among MOFs that have been explored as catalysts for CWA detoxification, MOFs containing Zr-based clusters, including UiO-type MOFs, NU-1000, MOF-808, and PCN-222/MOF-545, have shown

[d] Material in this chapter has been previously published as Agrawal, M; Sava-Gallis D.F.; Greathouse J.A.; Sholl D.S. "How Useful Are Common Simulants of Chemical Warfare Agents at Predicting Adsorption Behavior?" *J. Phys. Chem. C* **2018**, 122, 45, 26061-26069

promising performance in adsorbing and degrading CWAs and CWA simulants.[12–14,16–22] Katz et al. studied CWA simulants in UiO-66, UiO-67 and their derivatives to conclude that the amino derivatives of these MOFs are more active catalysts than non-functionalized materials.[20] Liu et al. used a Zr-based MOF, PCN-222, as a dual function catalyst for the simultaneous detoxification of simulants of two CWAs at room temperature.[16] Other than Zr-based clusters, Zn-based MOFs have also shown potential in degrading CWAs and CWA simulants. Zou et al. developed a metal-organic replica of α-PbO_2 that exhibited high capacity for capture of nerve agent simulants.[23] Montoro et al. conducted a series of experiments on diisopropylfluorophosphonate (DFP), a simulant for Sarin, to confirm the suitability of the MOF [Zn_4(μ_4-O)-(μ_4-4-carboxy-3.5-dimethyl-4-carboxy-pyrazolato)$_3$] to capture this molecule.[15]

CWA simulants generally feature similar chemical structures to those of real agents but with reduced toxicity. Although there are several molecules that have been studied as CWA simulants, it is not obvious how the similarity between putative simulants and real agents can be established in novel processes or environments. Bartelt-Hunt et al. reviewed the properties of CWAs and surrogates to identify the appropriate surrogate for hydrolysis and volatilization.[24] An alternative to studying these materials with experiments is to use molecular simulations to search for high performing materials. A striking example of this approach was reported recently by Matito-Martos et al.,[10] who used computational models to consider a large library of MOFs (specifically, the CoRE MOF database[25]) for CWA removal under humid conditions. The results of these simulations led the authors to synthesize and test a promising sorbent.[10] There have been no studies, however, systematically comparing the adsorption properties of CWAs and simulants in nanoporous

adsorbents such as MOFs. Also, to the best of our knowledge, no literature exists on validating the accuracy of generic force fields (FFs) in predicting adsorption properties of molecules such as CWAs and simulants.

Molecular simulations have become a useful tool for predicting the adsorption properties of molecules in diverse collections of MOFs and similar materials. Multiple studies are available in which the adsorption of small molecules such as CO_2, CH_4 or noble gases in thousands of MOF structures has been simulated.[26–28] Recent work has shown how these approaches can be extended to large collections of adsorbing molecules.[29] In this chapter, we use molecular simulations to predict the adsorption properties of several CWAs and CWA simulants in a library of thousands of MOF structures. Specifically, we simulate adsorption of Sarin, Soman, dimethylmethylphosphonate (DMMP), diethylchlorophosphate (DCP), DFP and dimethyl p-nitrophenyl phosphate (DMNP) in a set of ~3000 experimentally-derived MOF crystal structures from the CoRE MOF database.[25,30] The molecular structures of the six molecules we considered are shown in **Figure 4.A.1** (Appendix 4.A). Our results extend the recent work of Matito-Martos et al. in two important ways. First, we use our data to address the question of whether molecules commonly considered to be simulants for CWAs are truly similar to CWAs in terms of their adsorption properties. This important question, somewhat surprisingly, does not seem to have been considered before in work on adsorption of CWAs. This analysis can have important implications for experimental studies of these challenging species.

The second extension beyond the work of Matito-Martos et al. in our work is to consider the FF used in our simulations. All molecular simulations of adsorption require a FF that defines the energy of interactions between adsorbing molecules and the adsorbent

material. The most common approach in high throughput computational studies is to use "generic" FFs.[26,27,31] A recent analysis of experimental uncertainty in reported gas adsorption isotherms in MOFs suggested that simulations with generic FFs make predictions with similar precision to adsorption experiments, at least for small physisorbing molecules.[32] Nevertheless, to draw robust conclusions about the question posed above, it is useful to probe the sensitivity of our results to the FFs that are used. To this end, we supplement molecular simulations performed with generic FFs with additional simulations using a FF for CWAs and CWA simulants in MOFs we derive from quantum chemistry calculations. This FF is obtained by adapting methods from the growing literature on developing high quality FFs for adsorption of molecules such as H_2,[33] CO_2,[34–36] H_2O,[37] alkanes,[38] and cyclic hydrocarbons[39] in MOFs and similar materials using quantum chemistry data.[40–42]

4.2 Simulation Methods

For our calculations, MOF structures were taken from a subset of the CoRE MOF database[25] consisting of 2932 different crystal structures for which high quality atomic point charges have been reported.[30] All structures in the CoRE MOF database are derived from experimentally reported crystal structures assuming that all free solvent was removed from the crystals. The structures of MIL-101,[43] NU-1000,[43] UiO-67,[44] UiO-66 and its derivatives[45] were also included because of prior reports on using these materials for capture of CWAs. Details of the MOF database used in our simulations is provided in the Appendix 4.A.

Force-field based adsorption calculations in MOFs were performed using Monte Carlo simulations as implemented in RASPA.[43] All calculations of this kind assumed that the MOF structures were rigid, a common assumption in calculations using large numbers of adsorbent structures. We used equilibration and production periods of 5×10^4 Monte Carlo (MC) cycles; preliminary tests indicated this was sufficient to get well converged results. Calculations were carried out with the Widom insertion method, giving the Helium void fraction, Henry coefficients (K_H) and heats of adsorption (E_{ads}) in the limit of zero loading.

Calculations using what we will refer to as a "generic" FF for adsorbate-MOF interactions were performed as follows. Non-bonded interactions between adsorbates and the framework atoms were calculated using a Lennard-Jones (L-J) potential truncated at a spherical cutoff distance of 13 Å. Cross-terms for this potential were specified using Lorentz-Berthelot mixing rules with L-J parameters taken from UFF[46] force field for the framework and the TraPPE[47,48] force field for adsorbates. To define Coulombic forces, electrostatic charges on atoms in the MOFs were assigned on the entire periodic framework using DDEC[49] methods.[30] Point charges on atoms in DFP, DMNP and DCP that are not defined in TraPPE force field, were calculated using the charge equilibration (EQ_{eq}) method.[50] Coulombic interactions were computed using the Ewald method with a precision of 10^{-6} and a 13 Å cutoff. This approach is very similar to the FFs used in the recent work by Matito-Mantos et al.[10]

It is challenging to directly assess the accuracy of the generic FF described above for a diverse library of MOFs because of the extreme sparsity of experimental data that exists. It is important, however, to understand how sensitive molecular simulation results are to

details of the FFs used. We therefore performed extensive plane wave Density Functional Theory (DFT) calculations of adsorption of CWAs and simulants in a prototypical MOF, UiO-66, and used those results to develop a FF that is transferable to other MOFs. We refer below to this FF as a DFT-derived FF. For each molecule, 500 independent configurations were initially generated using the generic FF described above. The adsorption energy for each of these configurations was calculated using DFT with the PBE-D3 functional.[51] Prior work by Fang et al.[36,42] has shown that dispersion corrected PBE functionals performs well among DFT functionals to calculate interaction energies of this kind. The adsorption energies were defined by,

$$E_{ads} = E_{adsorbate\text{-}MOF} - (E_{adsorbate} + E_{MOF}) \qquad (4.1)$$

where E_{ads}, $E_{adsorbate\text{-}MOF}$, $E_{adsorbate}$ and E_{MOF} are the adsorption energy, the energy of the adsorption complex, the energy of the isolated adsorbate and the energy of the isolated MOF, respectively. Classical FFs for the adsorbates were then scaled to fit the DFT data. Specifically, we defined adsorbate-MOF dispersion interactions using L-J potentials defined via unconventional mixing rules from the adsorbate-adsorbate potentials and UFF parameters for MOF atoms. These adsorbate-MOF potentials had the form,

$$E_{LJ}(r_{ij}) = \sum 4\varepsilon_{ij}^{*}\left[\left(\frac{\sigma_{ij}^{*}}{r_{ij}}\right)^{12} - \left(\frac{\sigma_{ij}^{*}}{r_{ij}}\right)^{6}\right] \qquad (4.2)$$

where $\varepsilon_{ij}^{*} = \sqrt{\varepsilon_i(C_1\varepsilon_j)}$, $\sigma_{ij}^{*} = \frac{\sigma_i + C_2\sigma_j}{2}$, C_1 and C_2 are scaling coefficients for the unconventional mixing rules that are defined for each adsorbate atom-type individually, r_{ij} is the distance between atoms *i* and *j*, ε is the well depth, and σ is the interatomic potential's distance parameter. Here, *i* and *j* are subscripts for MOF and adsorbate atoms respectively.

If C_1 and C_2 are both equal to 1.0 for all adsorbate atoms, then this approach reduces to the standard generic FF described above. For electrostatic interactions, a standard point charge model is used,

$$E_{Coul}(r_{ij}) = \frac{e^2}{4\pi\varepsilon_0}\frac{q_i q_j}{R_{ij}} \qquad (4.3)$$

where e is the electron charge, ε_0 is the vacuum dielectric permittivity, and q_i and q_j are partial charge for atoms *i* and *j*. The same atomic point charges defined above for the generic FF were used.

Fitting the parameters for the DFT-derived FF involves determining C_1 and C_2 for each pair of interacting atoms. To reduce the complexity of the non-linear fitting problem, values of C_1 and C_2 for all adsorbate atom-types except six atom-types in the phosphonate group that is common in all CWAs and simulants were assumed to be equal to 1. For each atom-type in the phosphonate group, values of C_1 and C_2 were kept same across all adsorbates. Values of these scaling coefficients were then fitted for the six atom-types in phosphonate group using DFT data from the 3000 adsorbate configurations described above (500 configurations each for Sarin, Soman, DMMP, DMNP, DFP and DCP). Using this form for the mixing rules requires non-linear fitting when deriving the FF, but is useful because it allows the FFs to be used readily for any MOF. Details of the generic FF parameters and calculated scaling coefficients are given in the Appendix 4.A (see **Table 4.A.1** and **Table 4.A.2**).

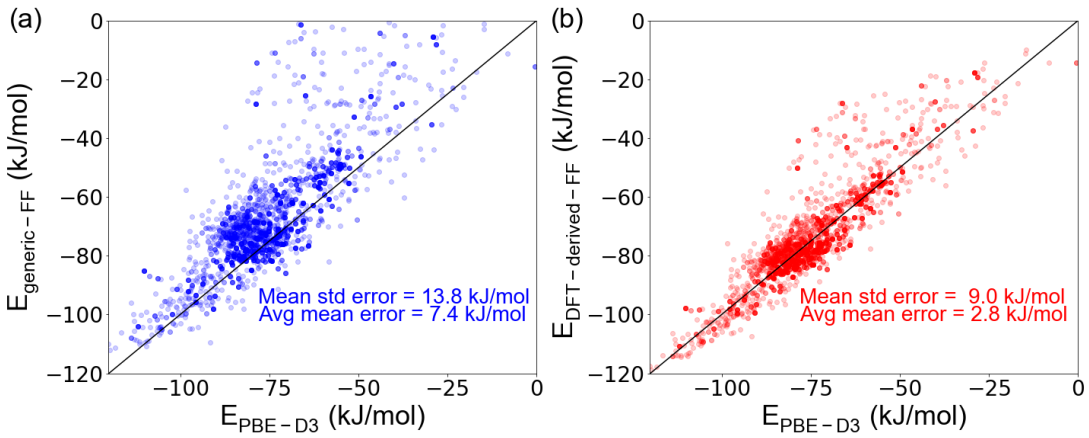

Figure 4.1: A parity plot between interaction energies calculated using classical force fields and quantum chemistry calculations using (a) a generic FF and (b) a DFT-derived FF for 3000 configurations of CWAs and simulants in UiO-66.

Figure 4.1 shows the performance of the generic FF and our DFT-derived FF compared to DFT results for molecular adsorption in UiO-66. The generic FF captures the overall trends seen in the DFT data, but as expected there is some variation between the two sets of results. The mean standard error of the adsorption energies from the generic FF with respect to the DFT data is 13.8 kJ/mol. Notably, the FF-based binding energies have poor agreement with the DFT results for configurations associated with weaker binding energies. Although it is not the topic of this chapter, this observation hints that the generic FF may be considerably less accurate for describing molecular diffusion in materials of this kind than it is for describing adsorption, since the latter is dominated by low energy configurations. This topic has been explored in more detail recently by Fang et al. for molecular diffusion in zeolites.[52] Our DFT-derived FF is fitted to match the underlying DFT data, so it is not surprising that the agreement shown in **Figure 4.1b** is better than for the generic FF. The mean standard error of our DFT-derived FF is 9.0 kJ/mol. In general,

the DFT-derived FF predicts stronger binding energies than the generic FF (see **Figure 4.A.2**).

Our DFT-derived FF was obtained from calculations in a single MOF, UiO-66. In order to test the transferability of this FF to other MOFs, we randomly chose five MOFs from the full set of materials we considered and compared the performance of both FFs with adsorption energies calculated using DFT. Details of these comparisons are given in the Appendix 4.A (see **Figure 4.A.3**). While both FFs perform reasonably well, the DFT-derived FF has a better overall result than the generic FF. In the rest of the chapter, therefore, we primarily present results calculated using the DFT-derived FF and use comparisons with results from the generic FFs to consider the sensitivity of our conclusions to details of the adsorbate-MOF FF.

4.3 Results and Discussion

We aim to understand whether the adsorption of a simulant molecule in a MOF is a good predictor of the adsorption properties of CWAs in the same MOF. We focus on the limit of dilute adsorption, since adsorbents are most likely to be challenged by low concentrations of CWAs if used in practice. In this limit, both the heat of adsorption and the Henry's constant are useful indicators of adsorption affinity. The two quantities are strongly correlated, as can be seen in **Figure 4.A.10**. For this reason, we focused below on the heat of adsorption.

Figure 4.2 represents an example of how we compared a CWA (Sarin) and a simulant (DMMP) to consider how well a simulant mimics a CWA's adsorption properties. **Figure 4.2a** compares the heats of adsorption of Sarin with DMMP. We excluded MOFs

that have positive heat of adsorption for at least one adsorbate among CWAs and simulants, so this figure only includes 1544 of the MOFs we simulated. We used the same number of MOFs for all the calculations done for each adsorbate in this study. Unsurprisingly, the heats of adsorption for the two molecules are quite closely correlated. Fitting a linear model to this correlation (excluding materials with positive heats of adsorption) yields the red line shown in the **Figure 4.2**. Data points in this figure are color coded based on the largest cavity diameter (LCD) of the MOFs. Consistent with previous results for other adsorbates[10], large pore MOFs are in general associated with less favorable heats of adsorption. The MOFs having the most favorable E_{ads} for Sarin have pore limiting diameters in the range of 6-8 Å; pores smaller than 6 Å are too small to accommodate large molecules such as CWAs and simulants and pores larger than 8 Å are too large for molecules to have strong interaction with the frameworks. The information in **Figure 4.2a** compares the numerical values of the heat of adsorption for a simulant and a CWA. An alternative for selecting high performing materials is to rank the MOFs in order of their heat of adsorption for a given molecule. A simulant that generates a ranking of materials very similar to that for a CWA, even if the numerical values of the heats of adsorption were systematically different, would be very useful. **Figure 4.2b** shows the correlation between the ranking based on heat of adsorption for DMMP and Sarin in the 1544 MOFs we simulated, with 0 in the percentage ranking indicating the MOF with the most favorable heat of adsorption. For an ideal simulant all MOFs would lie in the diagonal boxes of **Figure 4.2b**.

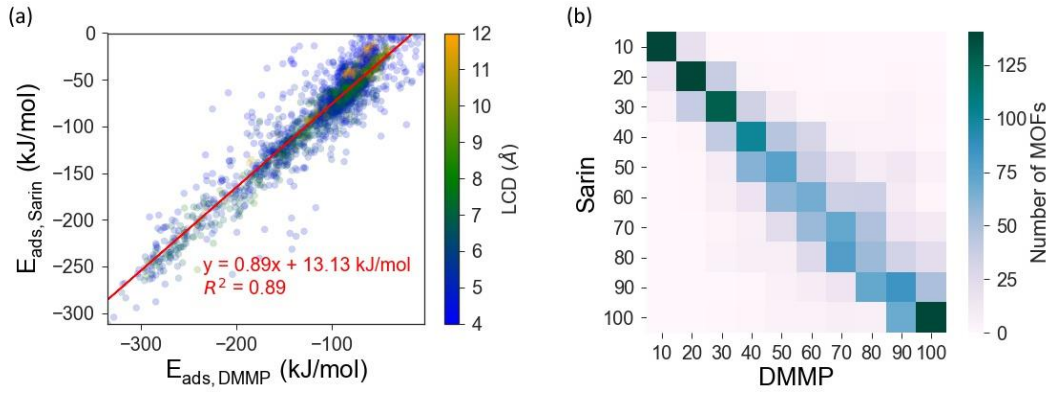

Figure 4.2: (a) Comparison of heats of adsorption of DMMP and Sarin in 1544 MOFs using results from our DFT-derived FF. The red line shows a linear fit to the results. Individual data points are color coded by the MOF's LCDs as shown in the color bar. (b) Correlation of MOFs percentage rankings of the 1544 MOFs when ordered by the calculated heats of adsorption of Sarin and DMMP, with the number of MOFs in each grid space indicated by the color bar on the right.

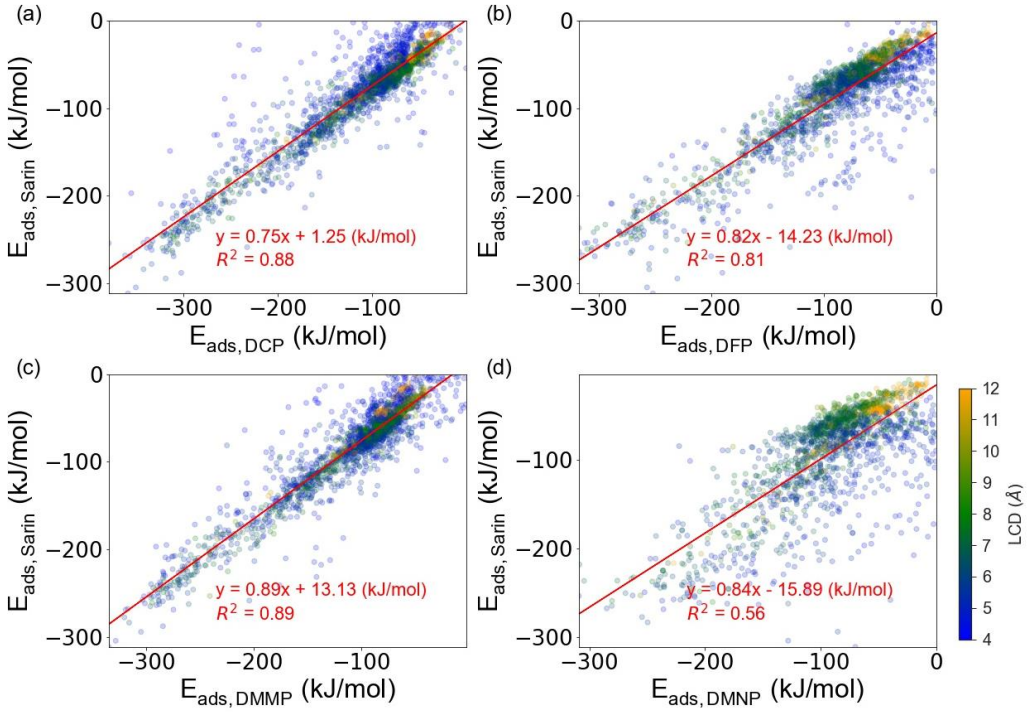

Figure 4.3: Comparison of heats of adsorption of Sarin and (a) DCP, (b) DFP, (c) DMMP, and (d) DMNP, in 1544 MOFs using results from our DFT-derived FF. The red lines show linear fits to the results. Individual data points are color coded by the MOF's LCDs as shown in the color bar.

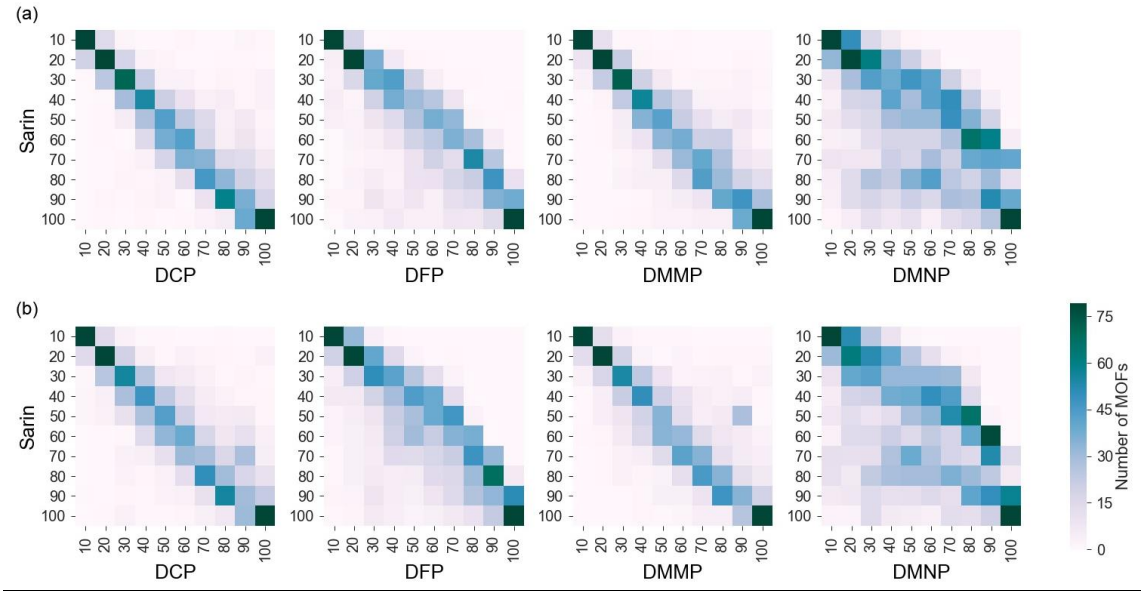

Figure 4.4: Correlation of MOFs percentage rankings of the 1544 MOFs when ordered by the calculated heats of adsorption of Sarin and simulants using (a) DFT-derived FF, (b) generic-FF, with the number of MOFs in each grid space indicated by the color bar on the right.

We have used these two approaches illustrated in **Figure 4.2** to compare all four simulants (DCP, DFP, DMMP and DMNP) with Sarin and Soman. The results for Sarin are shown in **Figure 4.3** and **Figure 4.4**. **Figure 4.3** shows that DMMP and DCP are the best simulants for the adsorption properties of Sarin, with R^2 value of 0.89 and 0.88 respectively. The correlation between DFP and Sarin is also strong (R^2 = 0.81), but the behavior of DMNP is poorly correlated with Sarin. Similar comparisons using the generic FF are shown in **Figure 4.A.4**. **Figure 4.4** shows the correlations of MOF rankings correlations for Sarin with each simulants, including results from our DFT-derived FF (**Figure 4.4a**) and the generic FF (**Figure 4.4b**). The overall observations from the two FFs are quite similar, supporting the idea that the conclusions from these results are not highly sensitive to the FF. DCP and DMMP have the highest number of MOFs that have rankings

similar to Sarin. Again, DMNP is clearly the worst performing simulant for Sarin adsorption.

It is arguably more important to know whether simulants are able to mimic Sarin's adsorption properties for top performing materials than for the overall collection of MOFs in our simulations. **Figure 4.A.6** replots the ranking data from **Figure 4.4** by focusing on the top 20% of MOFs in the Sarin ranking, an approach that implicitly assume that top performing materials are those with the most favorable heat of adsorption. This group of materials leads to the same conclusions as already discussed for the complete set of MOFs; DMMP and DCP are the simulants better able to mimic Sarin's adsorption properties followed by DFP and DMNP. All of these results indicate that in future work on adsorption of Sarin in MOFs and related materials, DCP and DMMP are useful simulants, DFP is somewhat less useful, and DMNP has little predictive power as a simulant. It should be noted that predictive power of a simulant over the real agent for adsorption might not extend to other processes such as diffusion and degradation. In a recent study, Sava Gallis et al. showed that DMNP is a highly suitable simulant to predict Sarin's degradation in methanol.[11] This example illustrates the necessity of considering the suitability of a simulant within the context of the specific chemical or physical process of interest.

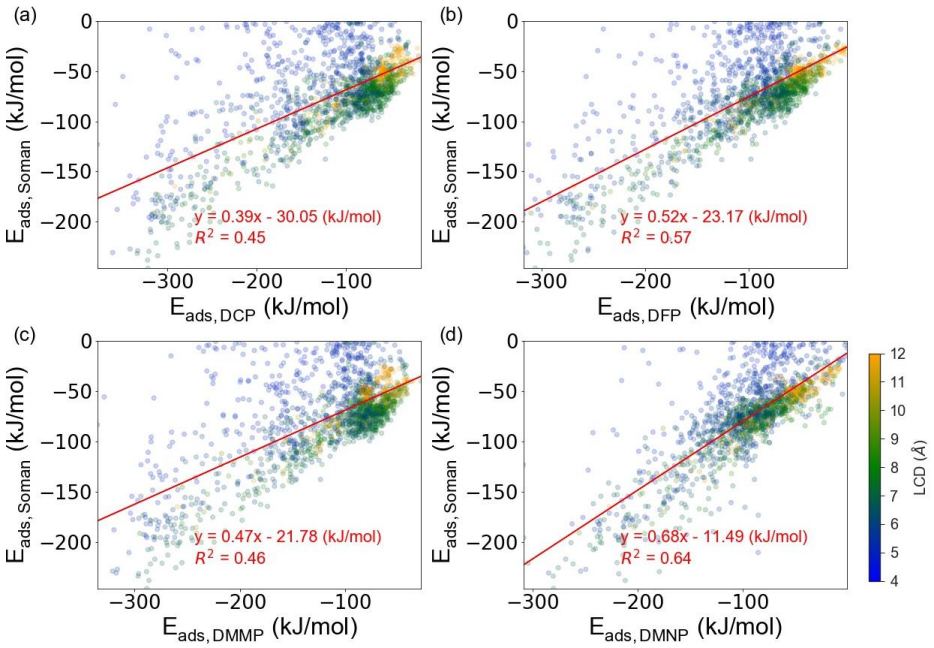

Figure 4.5: Comparison of heats of adsorption of Soman and (a) DCP, (b) DFP, (c) DMMP, and (d) DMNP in 1544 MOFs using results from our DFT-derived FF. The red lines show linear fits to the results. Individual data points are color coded by the MOF's LCDs as shown in the color bar.

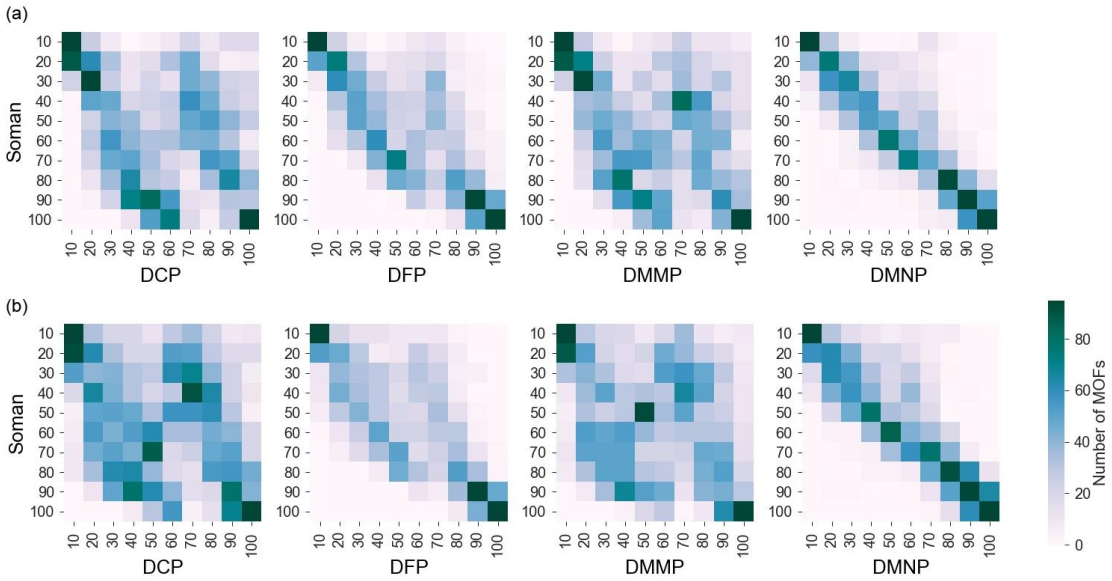

Figure 4.6: Correlation of MOFs percentage rankings of the 1544 MOFs when ordered by the calculated heats of adsorption of Soman and simulants using (a) DFT-derived FF, (b) generic-FF, with the number of MOFs in each grid space indicated by the color bar on the right.

Figure 4.5 and **Figure 4.6** show comparisons for Soman with each simulant. A superficial comparison of the size and shape to Soman to each simulant suggests that DMNP might be a better simulant than DMMP, DCP or DFP. Soman is a larger molecule than DMMP, DCP and DFP but smaller than DMNP (see **Figure 4.A.1**). The results in **Figure 4.5** and **Figure 4.6** bear out this idea. The adsorption properties of DMMP, DCP and DFP are all poorly correlated with Soman, and none of these three species can reliably be used as simulants for Soman. Among the four simulants, DMNP most reliably predicts the adsorption properties of Soman, although the predictive quality of DMNP in not as strong as the best simulants for Sarin. These observations are consistent for both FFs that we used (see **Figure 4.5**, **Figure 4.6** and **Figure 4.A.5**) and when attention is restricted to the top 20% of materials as ranked by the heat of adsorption (**Figure 4.A.7**). These results suggest that it may be worthwhile seeking other molecules that can better mimic the adsorption properties of Soman, although considerable challenges may exist with establishing the safety of putative molecules of this kind.

The discussion above has identified the "best" simulants for adsorption of Sarin and Soman from among the set of simulants we considered. To further illustrate the predictive quality of these simulants, **Figure 4.7** shows the connection between rankings of MOFs using their heat of adsorption and the numerical value of the heat of adsorption. Similar comparisons for all simulants with both CWAs are provided in the Appendix 4.A (see **Figure 4.A.8** and **Figure 4.A.9**). **Figure 4.7a** shows that DMMP systematically overestimates the absolute value of the heat of adsorption of Sarin, but the precision with which DMMP can predict the relative ranking of a pair of MOFs is considerable. **Figure 4.7b** reinforces the comments above that the predictive power of DMNP as a simulant for

adsorption of Soman is less than ideal (although it is far more reliable than the other three simulants).

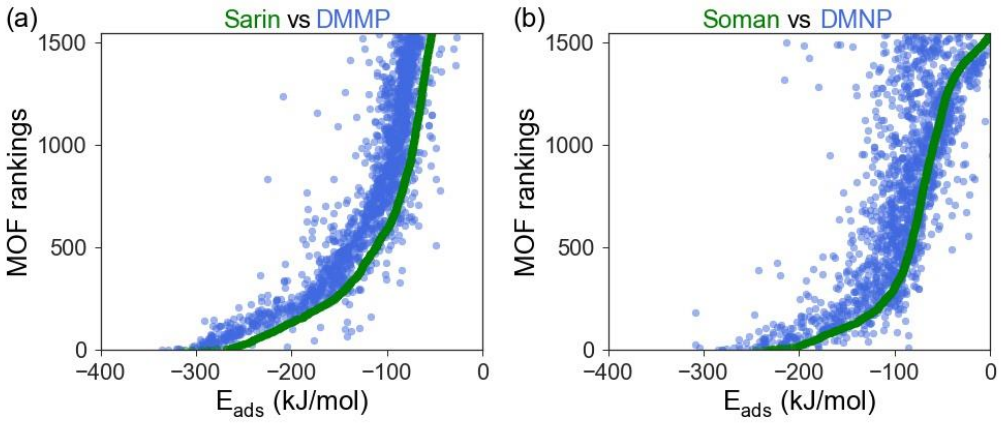

Figure 4.7: MOF rankings of 1544 MOFs for (a) DMMP (blue) and Sarin (green) and (b) DMNP (blue) and Soman (green) when ordered by the heat of adsorption of Sarin and Soman, respectively.

4.4 Summary

There are obvious and compelling reasons why research on capture of CWAs by adsorption (or other processes) must rely on simulant molecules. In this chapter, we have performed the first systematic examination of the ability of simulant molecules (specifically, DMMP, DCP, DFP and DMNP) to predict the adsorption properties of Sarin or Soman. To this end, we simulated the adsorption of each molecule in a collection of 2969 MOFs using molecular simulations in the limit of dilute adsorption. An important feature of these calculations is that we performed them independently with two separate force fields, a generic FF similar to that used in other screening studies of adsorption in MOFs and a DFT-derived FF that we developed based on extensive dispersion-corrected DFT calculations of CWA and simulant adsorption in UiO-66. We provided numerical

evidence that this DFT-derived FF is suitable for simulation of a wide range of other MOFs. More importantly, comparisons of results with these two FFs indicate that our main conclusions are insensitive to the specific details of the FF used to define adsorbate-MOF interactions.

Our primary conclusion can be stated simply: DCP and DMMP are good simulants for adsorption of Sarin in MOFs and DMNP is the best available simulant for adsorption of Soman, although its predictive power is not high as for the best simulants of Sarin. The other simulants we examined have poor predictive power for Soman. These conclusions were based on how well simulants predict the heat of adsorption of each molecule in MOFs and the ranking of a MOF within the overall set of materials as determined by heat of adsorption. We demonstrated explicitly that the heat of adsorption is strongly correlated with the Henry's constant. These conclusions, therefore, are most meaningful for situations in which the ability of an adsorbent to capture a CWA selectively when it is present at very low concentrations.

There are of course a range of other physical properties that may be relevant to the performance of a MOF (or other adsorbent material) in applications involving CWAs. The overall capacity of a material for capturing a CWA may be important, in which case information about the overall adsorption isotherm of the molecule of interest is needed. Methods have been proposed recently that make predictions of complete isotherms using only information from physical properties of the adsorbent and the Henry's constant of the adsorbing molecule[29]; this approach may be useful in considering large collections of materials for CWA capture. If materials are ranked solely on the basis of heat of adsorption (or Henry's constant), the resulting materials tend to have pores similar in size to the

adsorbing molecules. This raises the possibility that the diffusion of molecules into the adsorbent may be too slow for the material to be used in a practical setting. It is very likely that the flexibility of the adsorbents pores in the presence of adsorbed species will be critical in predicting diffusion in these materials in a meaningful way. Predictive molecular simulation methods for this diffusion regime have been applied to the diffusion of a wide range of molecules in small pore MOFs,[53,54] but no information is available at present applying these methods to CWAs or CWA simulants. While the properties just discussed can in principle be obtained from molecular simulations, there are also aspects of material durability, cost and so on that will also be critical in realistic settings.[55]

APPENDIX 4.A. SUPPORTING INFORMATION FOR CHAPTER 4

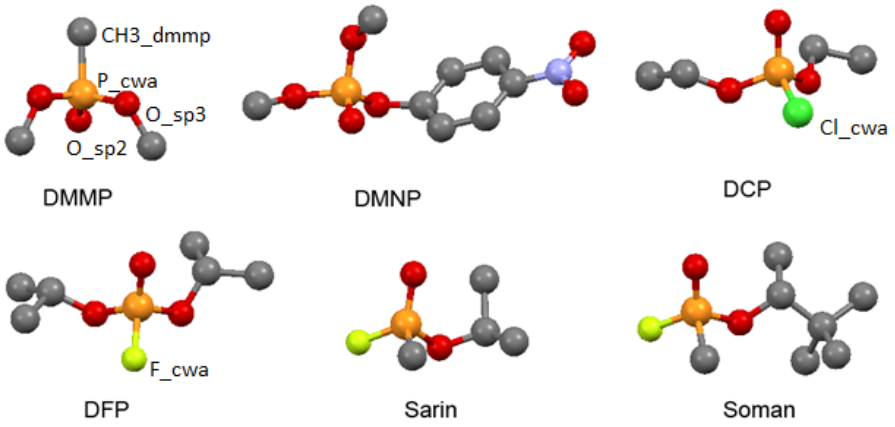

Figure 4.A.1: Atomic representations of two CWAs and four simulants. Grey, red, orange, light blue, green, lemon colors corresponds to carbon, oxygen, phosphorus, nitrogen, chlorine and fluorine respectively. For clarity, hydrogen atoms are not shown.

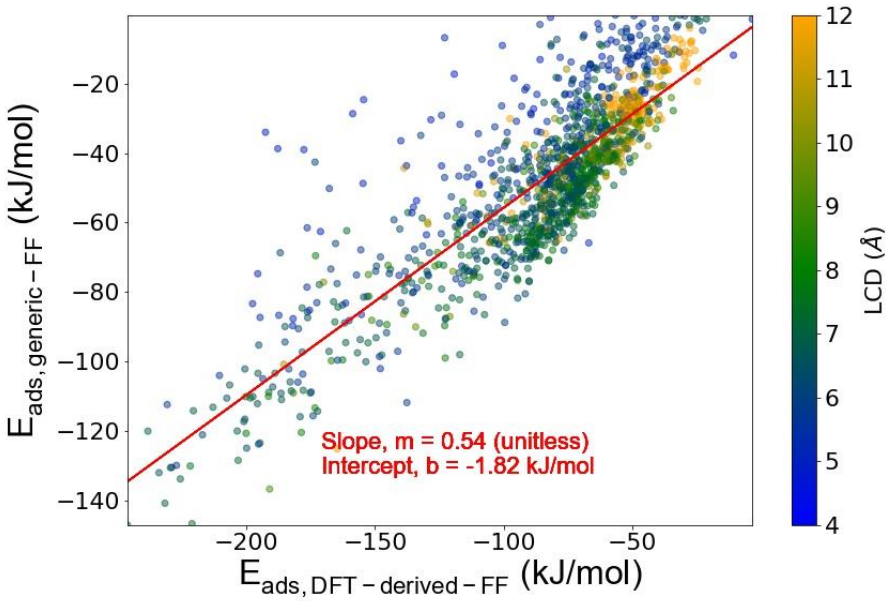

Figure 4.A.2: Comparison of heats of adsorption of CWAs and simulants calculated using DFT-derived FF and generic FF in 1544 MOFs. The red line shows a linear fit to the results. Individual data points are color coded by the MOF's LCDs as shown in the color bar.

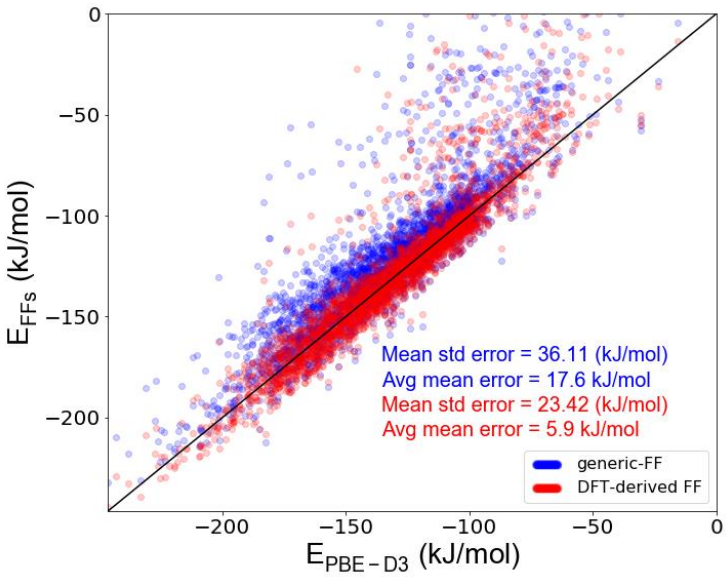

Figure 4.A.3: A parity plot between interaction energies calculated using classical force fields and ab-initio calculations using generic-FF (blue) and DFT-derived FF (red) for 3000 configurations in five randomly selected MOFs (CADQOP, EKOPOK, NALYEG, NIGFUF and MEXJAC).

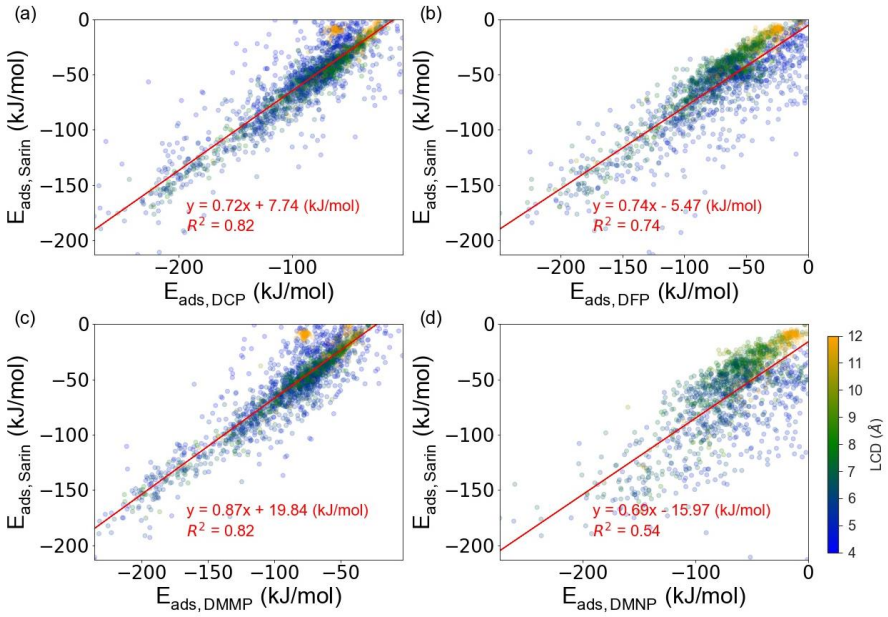

Figure 4.A.4: Comparison of heats of adsorption of Sarin and simulants, (a) DCP, (b) DFP, (c) DMMP, and (d) DMNP, in 1544 MOFs using results from our generic FF. The red lines show linear fits to the results. Individual data points are color coded by the MOF's LCDs as shown in the color bar.

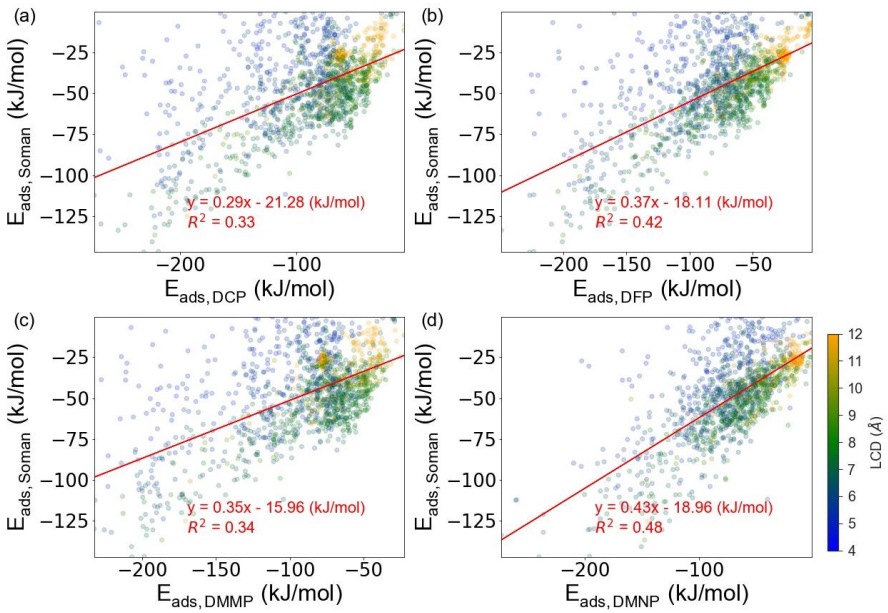

Figure 4.A.5: Comparison of heats of adsorption of Soman and simulants, (a) DCP, (b) DFP, (c) DMMP, and (d) DMNP, in 1544 MOFs using results from our generic FF. The red lines show linear fits to the results. Individual data points are color coded by the MOF's LCDs as shown in the color bar.

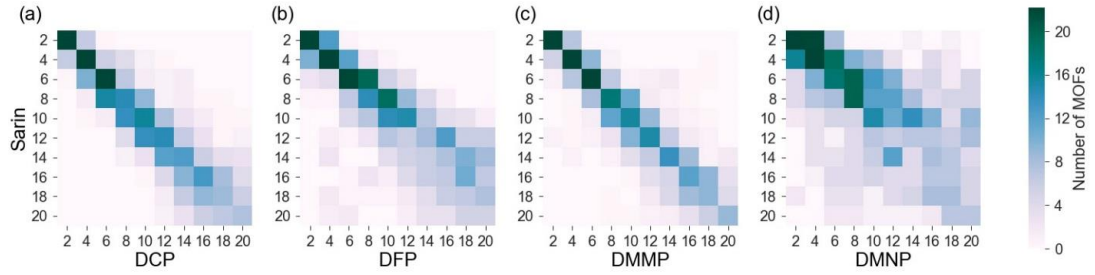

Figure 4.A.6: Correlation of MOFs percentage rankings of the top 20% MOFs when ordered by the calculated heats of adsorption of Sarin and (a) DCP, (b) DFP, (c) DMMP, and (d) DMNP, using the DFT-derived FF with the number of MOFs in each grid space indicated by the color bar on the right.

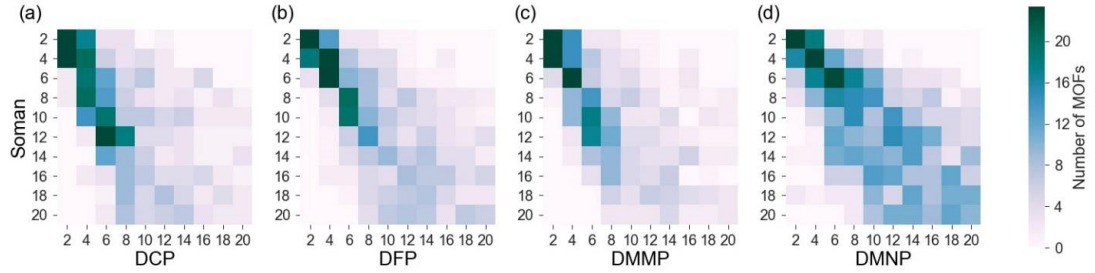

Figure 4.A.7: Correlation of MOFs percentage rankings of the top 20% MOFs when ordered by the calculated heats of adsorption of Soman and (a) DCP, (b) DFP, (c) DMMP, and (d) DMNP, using our DFT-derived FF with the number of MOFs in each grid space indicated by the color bar on the right.

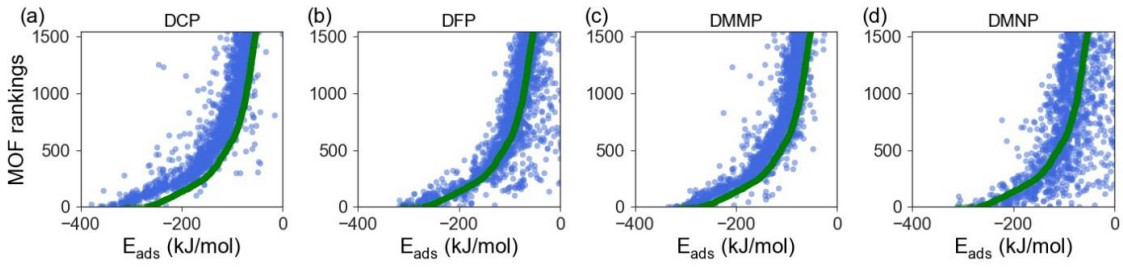

Figure 4.A.8: MOF rankings of 1544 MOFs for Sarin (green) and (a) DCP (blue), (b) DFP (blue), (c) DMMP (blue), and (d) DMNP (blue), when ordered by the heat of adsorption of Sarin.

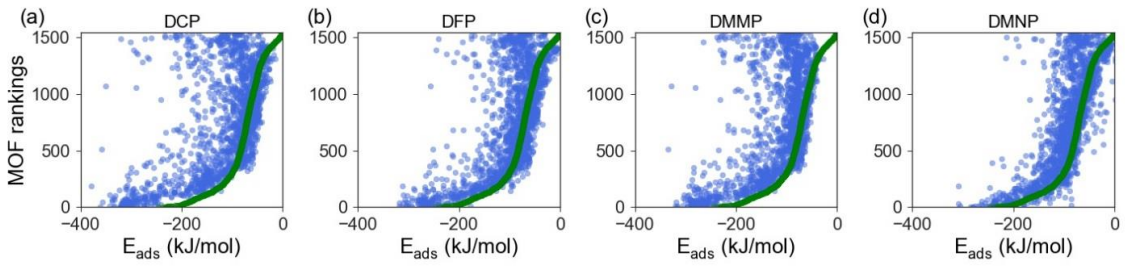

Figure 4.A.9: MOF rankings of 1544 MOFs for Soman (green) and (a) DCP (blue), (b) DFP (blue), (c) DMMP (blue), and (d) DMNP (blue), when ordered by the heat of adsorption of Soman.

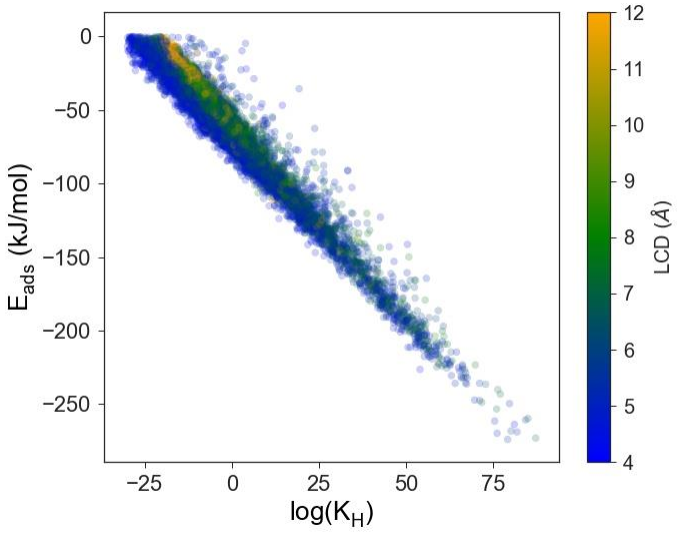

Figure 4.A.10: Correlation between Henry coefficients and the heat of adsorptions for all adsorbates. Individual data points are color coded by the MOF's LCDs as shown in the color bar.

The plot shows that Henry coefficients and the heats of adsorptions are highly correlated adsorption properties for an adsorbate-adsorbent pair, so all the analysis performed using the heats of adsorption would extend to the Henry coefficients as well.

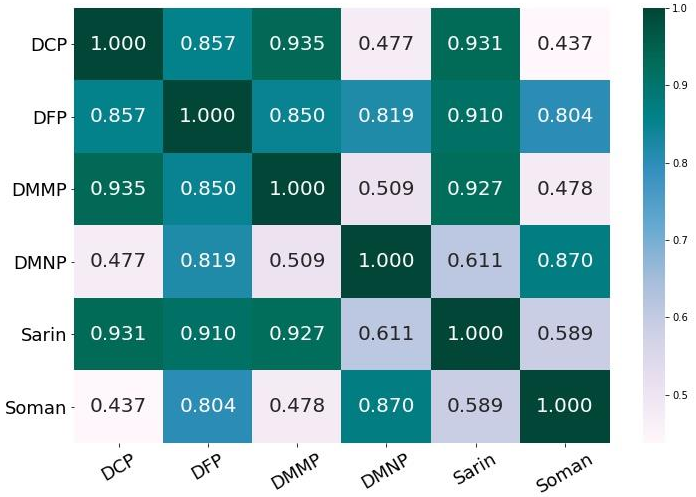

Figure 4.A.11: Correlation matrix of heats of adsorption among all CWAs and simulants using DFT-derived FF. Correlation coefficients were calculated using 'pearson' method.

For Sarin, the highest correlated molecules are DCP, DMMP, DFP and then DMNP in that order. For Soman, the closest molecules are DMNP, DFP, DMMP and then DCP in that order. All these results are consistent with our results described in the main manuscript.

4.A.1 Details of the MOF database used in simulations

We used the CoRE MOF database consisting of 2932 structures in our calculations.[25] This database has charges assigned to all structures that were calculated using DDEC methods.[30] The structures of MIL-101,[43] NU-1000,[43] UiO-67,[44] UiO-66 and its derivatives[45] were also included because of prior reports on using these materials for capture of CWAs. MIL-101, NU-1000 and UiO-67 were geometrically optimized using DFT with the projector augmented wave (PAW)[56] approach in the Vienna ab initio Simulation Package (VASP).[57,58] using the PBE-D3 exchange correlation.[51,59] Prior work by Nazarian et al.[60] has shown that the geometric properties of MOF crystal structures are

insensitive to the choice of exchange correlation functional in DFT calculations.[60] These calculations used a plane wave cutoff energy of 520 eV and the Brillouin zone was sampled using Monkhorst-Pack grid. A conjugate gradient method was used to optimize atomic positions until the forces on each atom were converged within 0.01 eV/atom.

4.A.2 Force-field Details

Table 4.A.1: Scaling coefficients derived from PBE-D3 calculations for our DFT-derived FF. Both scaling coefficients are dimensionless.

Atom Type	C_1 (unitless)	C_2 (unitless)
P_cwa	2.117	1.014
O_sp2	1.668	0.849
O_sp3	1.457	0.714
F_cwa	1.147	0.934
Cl_cwa	1.052	0.887
CH_3_dmmp	1.067	0.956

Table 4.A.2: Non-bonded parameters of generic-FF (TraPPE) for CWAs and simulants

Atom Type	ε/kB (K)	σ (Å)	Charge (e)
Sarin[47,48]			
P_cwa	86.0	4.0	1.4
O_sp2	79.0	3.05	-0.77
O_sp3	55.0	2.8	-0.63
F_cwa	26.7	2.95	-0.34
CH_3_sp3	98.0	3.75	-0.1[a]/-0.08[b]
CH_sp3	10.0	4.33	0.62
Soman[47,48]			
P_cwa	86.0	4.0	1.4
O_sp2	79.0	3.05	-0.77
O_sp3	55.0	2.8	-0.63
F_cwa	26.7	2.95	-0.34
CH_3_sp3	98.0	3.75	-0.1[a]/-0.08[b]/-0.15[c]
CH_sp3	10.0	4.33	0.43
C_sp3	0.6	6.4	0.54
DMMP[47,48]			

Table 4.A.2 continued…

P_cwa	86.0	4.0	1.44
O_sp2	79.0	3.05	-0.8
O_sp3	55.0	2.8	-0.53
CH_3_sp3	98.0	3.75	-0.14[d]/0.28[e]
DCP[47,48]*			
P_cwa	86.0	4.0	1.93
O_sp2	79.0	3.05	-0.93
O_sp3	55.0	2.8	-0.875
Cl_cwa	114.3	3.52	-0.13
CH_3_sp3	98.0	3.75	0.14
CH_2_sp3	46.0	3.95	0.30
DFP[47,48]*			
P_cwa	86.0	4.0	2.1
O_sp2	79.0	3.05	-0.93
O_sp3	55.0	2.8	-0.88
F_cwa	26.7	2.95	-0.55
CH_3_sp3	98.0	3.75	0.11
CH_sp3	10.0	4.33	0.35
DMNP[47,48]*			
P_cwa	86.0	4.0	2.25
O_sp2	79.0	3.05	-0.945
O_sp3	55.0	2.8	-0.86/-0.81[f]
CH_3_sp3	98.0	3.75	0.43
C_aro	15.0	4.5	0.37[g]/0.1[h]
CH_aro	48.0	3.74	0.18[i]/0.07[j]
N	40.0	3.31	0.3
O_NO_2 / -N-(O)[O]	80.0	2.9	-0.41

[a][CH3]-P, [b][CH3]-CH-O-P, [c][CH3]-C-CH-O-P, [d][CH3]-P(=O)-$(OCH3)_2$, [e][CH3]-O-P, [f]P-[O]-aro, [g]P-O-[C_aro]-(CH_aro)-CH_aro, [h][C_aro]-NO_2, [i]P-O-C_aro-[CH_aro], [j][CH_aro]-C_aro-NO_2

*charges calculated using charge equilibrium method[50]

4.5 References

(1) Nishiwaki, Y.; Maekawa, K.; Ogawa, Y.; Asukai, N.; Minami, M.; Omae, K. Effects of Sarin on the Nervous System in Rescue Team Staff Members and Police Officers 3 Years after the Tokyo Subway Sarin Attack. *Environ. Health Perspect.* **2001**, *109* (11), 1169–1173.

(2) Sidell, F. R. Soman and Sarin: Clinical Manifestations and Treatment of Accident of Accidental Poisoning by Organophosphates. *Clin. Toxicol.* **1974**, *7* (1), 1–17.

(3) Delfino, R. T.; Ribeiro, T. S.; Figueroa-Villar, J. D. Organophosphorus Compounds as Chemical Warfare Agents: a Review. *J. Braz. Chem. Soc* **2009**, *20* (3), 407–428.

(4) Li, B.; Wen, H.-M.; Zhou, W.; Chen, B. Porous Metal−Organic Frameworks for Gas Storage and Separation: What, How, and Why? *J. Phys. Chem. Lett.* **2014**, *5*, 3468–3479.

(5) Li, H.; Wang, K.; Sun, Y.; Lollar, C. T.; Li, J.; Zhou, H.-C. Recent advances in Gas Storage and Separation using Metal–Organic Frameworks. *Mater. Today* **2018**, *21* (2), 108–121.

(6) Zhu, L.; Liu, X.-Q.; Jiang, H.-L.; Sun, L.-B. Metal−Organic Frameworks for Heterogeneous Basic Catalysis. *Chem. Rev.* **2017**, *117*, 8129–8176.

(7) Isaeva, V. I.; Kustov, L. M. The Application of Metal-Organic Frameworks in Catalysis (Review). *Pet. Chem.* **2010**, *50* (3), 167–180.

(8) Kreno, L. E.; Leong, K.; Farha, O. K.; Allendorf, M.; Van Duyne, R. P.; Hupp, J. T. Metal-Organic Framework Materials as Chemical Sensors. *Chem. Rev.* **2012**, *112*, 1105–1125.

(9) Huxford, R. C.; Rocca, J. Della; Lin, W. Metal-Organic Frameworks as Potential Drug Carriers. *Curr. Opin. Chem. Biol.* **2010**, *14*, 262–268.

(10) Matito-Martos, I.; Moghadam, P. Z.; Li, A.; Colombo, V.; R Navarro, J. A.; Calero, S.; Fairen-Jimenez, D. Discovery of an Optimal Porous Crystalline Material for the Capture of Chemical Warfare Agents. *Chem. Mater.* **2018**, *30*, 4571–4579.

(11) Sava Gallis, D. F.; Harvey, J. A.; Pearce, C. J.; Hall, M. G.; Decoste, J. B.; Kinnan, M. K.; Greathouse, J. A. Efficient MOF-based degradation of organophosphorus compounds in non-aqueous environments. *J. Mater. Chem. A* **2018**, *6*, 3038–3045.

(12) Liu, Y.; Howarth, A. J.; Vermeulen, N. A.; Moon, S.-Y.; Hupp, J. T.; Farha, O. K. Catalytic degradation of chemical warfare agents and their simulants by metal-organic frameworks. *Coord. Chem. Rev.* **2017**, *346*, 101–111.

(13) Mondloch, J. E.; Katz, M. J.; Isley III, W. C.; Ghosh, P.; Liao, P.; Bury, W.; Wagner,

G. W.; Hall, M. G.; DeCoste, J. B.; Peterson, G. W.; et al. Destruction of chemical warfare agents using metal–organic frameworks. *Nat. Mater.* **2015**, *14* (5), 512–516.

(14) Ji, P.; Feng, X.; Veroneau, S. S.; Song, Y.; Lin, W. Trivalent Zirconium and Hafnium Metal − Organic Frameworks for Catalytic 1,4-Dearomative Additions of Pyridines and Quinolines. *J. Am. Chem. Soc.* **2017**, *139* (44), 15600–15603.

(15) Montoro, C.; Linares, F.; Quartapelle Procopio, E.; Senkovska, I.; Kaskel, S.; Galli, S.; Masciocchi, N.; Barea, E.; Navarro, J. A. R. Capture of nerve agents and mustard gas analogues by hydrophobic robust MOF-5 type metal-organic frameworks. *J. Am. Chem. Soc.* **2011**, *133* (31), 11888–11891.

(16) Liu, Y.; Moon, S. Y.; Hupp, J. T.; Farha, O. K. Dual-Function Metal-Organic Framework as a Versatile Catalyst for Detoxifying Chemical Warfare Agent Simulants. *ACS Nano* **2015**, *9* (12), 12358–12364.

(17) Moon, S. Y.; Liu, Y.; Hupp, J. T.; Farha, O. K. Instantaneous hydrolysis of nerve-agent simulants with a six-connected zirconium-based metal-organic framework. *Angew. Chemie - Int. Ed.* **2015**, *54* (23), 6795–6799.

(18) Katz, M. J.; Mondloch, J. E.; Totten, R. K.; Park, J. K.; Nguyen, S. T.; Farha, O. K.; Hupp, J. T. Simple and compelling biomimetic metal-organic framework catalyst for the degradation of nerve agent simulants. *Angew. Chemie - Int. Ed.* **2014**, *53* (2), 497–501.

(19) Moon, S. Y.; Wagner, G. W.; Mondloch, J. E.; Peterson, G. W.; DeCoste, J. B.; Hupp, J. T.; Farha, O. K. Effective, Facile, and Selective Hydrolysis of the Chemical Warfare Agent VX Using Zr_6-Based Metal-Organic Frameworks. *Inorg. Chem.* **2015**, *54* (22), 10829–10833.

(20) Katz, M. J.; Moon, S.-Y.; Mondloch, J. E.; Beyzavi, M. H.; Stephenson, C. J.; Hupp, J. T.; Farha, O. K. Exploiting parameter space in MOFs: a 20-fold enhancement of phosphate-ester hydrolysis with UiO-66-NH_2. *Chem. Sci.* **2015**, *6* (4), 2286–2291.

(21) Zhao, J.; Lee, D. T.; Yaga, R. W.; Hall, M. G.; Barton, H. F.; Woodward, I. R.; Oldham, C. J.; Walls, H. J.; Peterson, G. W.; Parsons, G. N. Ultra-Fast Degradation of Chemical Warfare Agents Using MOF–Nanofiber Kebabs. *Angew. Chemie - Int. Ed.* **2016**, *55* (42), 13224–13228.

(22) Bobbitt, N. S.; Mendonca, M. L.; Howarth, A. J.; Islamoglu, T.; Hupp, J. T.; Farha, O. K.; Snurr, R. Q. Metal–organic frameworks for the removal of toxic industrial chemicals and chemical warfare agents. *Chem. Soc. Rev.* **2017**, *46* (11), 3357–3385.

(23) Zou, R.; Zhong, R.; Han, S.; Xu, H.; Burrell, A. K.; Henson, N.; Cape, J. L.; Hickmott, D. D.; Timofeeva, T. V.; Larson, T. E.; et al. A porous metal-organic replica of α-PbO_2 for capture of nerve agent surrogate. *J. Am. Chem. Soc.* **2010**, *132* (51), 17996–17999.

(24) Bartelt-Hunt, S. L.; Knappe, D. R. U.; Barlaz, M. A. A Review of Chemical Warfare Agent Simulants for the Study of Environmental Behavior. *Crit. Rev. Environ. Sci. Technol.* **2008**, *38* (2), 112–136.

(25) Chung, Y. G.; Camp, J.; Haranczyk, M.; Sikora, B. J.; Bury, W.; Krungleviciute, V.; Farha, O. K.; Sholl, D. S.; Snurr, R. Q. Computation-Ready, Experimental Metal−Organic Frameworks: A Tool To Enable High-Throughput Screening of Nanoporous Crystals. *Chem. Mater.* **2014**, *26*, 6185–6192.

(26) Keskin, S.; Sholl, D. S. Screening Metal-Organic Framework Materials for Membrane-based Methane/Carbon Dioxide Separations. *J. Phys. Chem. C Lett.* **2007**, *111*, 14055–14059.

(27) Qiao, Z.; Xu, Q.; Jiang, J. High-throughput computational screening of metal-organic framework membranes for upgrading of natural gas. *J. Memb. Sci.* **2018**, *551*, 47–54.

(28) Altintas, C.; Avci, G.; Daglar, H.; Nemati, A.; Azar, V.; Velioglu, S.; Erucar, I.; Keskin, S. Database for CO_2 Separation Performances of MOFs Based on Computational Materials Screening. *ACS Appl. Mater. Interfaces* **2018**, *10*, 17257–17268.

(29) Tang, D.; Wu, Y.; Verploegh, R. J.; Sholl, D. S. Efficiently Exploring Adsorption Space to Identify Privileged Adsorbents for Chemical Separations of a Diverse Set of Molecules. *ChemSusChem* **2018**, *11* (9), 1567–1575.

(30) Nazarian, D.; Camp, J. S.; Sholl, D. S. A Comprehensive Set of High-Quality Point Charges for Simulations of Metal−Organic Frameworks. *Chem. Mater.* **2016**, *28*, 785–793.

(31) Gee, J. A.; Zhang, K.; Bhattacharyya, S.; Bentley, J.; Rungta, M.; Abichandani, J. S.; Sholl, D. S.; Nair, S. Computational Identification and Experimental Evaluation of Metal-Organic Frameworks for Xylene Enrichment. *J. Phys. Chem. C* **2016**, *120* (22), 12075–12082.

(32) Park, J.; Howe, J. D.; Sholl, D. S. How Reproducible Are Isotherm Measurements in Metal-Organic Frameworks? *Chem. Mater.* **2017**, *29* (24), 10487–10495.

(33) Fischer, M.; Kuchta, B.; Firlej, L.; Hoffmann, F.; Fröba, M. Accurate prediction of hydrogen adsorption in metal-organic frameworks with unsaturated metal sites via a combined density-functional theory and molecular mechanics approach. *J. Phys. Chem. C* **2010**, *114* (44), 19116–19126.

(34) Han, S. S.; Kim, D.; Jung, D. H.; Cho, S.; Choi, S. H.; Jung, Y. Accurate Ab initio-based force field for predictive CO_2 uptake simulations in MOFs and ZIFs: Development and applications for MTV-MOFs. *J. Phys. Chem. C* **2012**, *116* (38), 20254–20261.

(35) Chen, L.; Morrison, C. A.; Düren, T. Improving predictions of gas adsorption in metal-organic frameworks with coordinatively unsaturated metal sites: Model potentials, ab initio parameterization, and GCMC simulations. *J. Phys. Chem. C* **2012**, *116* (35), 18899–18909.

(36) Fang, H.; Kamakoti, P.; Zang, J.; Cundy, S.; Paur, C.; Ravikovitch, P. I.; Sholl, D. S. Prediction of CO_2 Adsorption Properties in Zeolites Using Force Fields Derived from Periodic Dispersion-Corrected DFT Calculations. *J. Phys. Chem. C* **2012**, *116*, 10692–10701.

(37) Zang, J.; Nair, S.; Sholl, D. S. Prediction of water adsorption in copper-based metal-organic frameworks using force fields derived from dispersion-corrected DFT calculations. *J. Phys. Chem. C* **2013**, *117* (15), 7519–7525.

(38) Kulkarni, A. R.; Sholl, D. S. DFT-Derived Force Fields for Modeling Hydrocarbon Adsorption in MIL-47(V). *Langmuir* **2015**, *31* (30), 8453–8468.

(39) Gee, J. A.; Sholl, D. S. Prediction of Adsorption Properties of Cyclic Hydrocarbons in MOFs Using DFT-Derived Force Fields. *J. Phys. Chem. C* **2015**, *119* (29), 16920–16926.

(40) Lin, L.-C.; Lee, K.; Gagliardi, L.; Neaton, J. B.; Smit, B. Force-Field Development from Electronic Structure Calculations with Periodic Boundary Conditions: Applications to Gaseous Adsorption and Transport in Metal−Organic Frameworks. *J. Chem. Theory Comput.* **2014**, *10*, 1477–1488.

(41) Mcdaniel, J. G.; Schmidt, J. R. First-Principles Many-Body Force Fields from the Gas Phase to Liquid: A "Universal" Approach. *J. Phys. Chem. B.* **2014**, *118*, 8042–8053.

(42) Fang, H.; Demir, H.; Kamakoti, P.; Sholl, D. S. Recent developments in first-principles force fields for molecules in nanoporous materials. *J. Phys. Chem. A* **2014**, *2*, 274–291.

(43) Dubbeldam, D.; Calero, S.; Ellis, D. E.; Snurr, R. Q. RASPA: Molecular Simulation Software for Adsorption and Diffusion in Flexible Nanoporous Materials. *Mol. Simul.* **2015**, *42* (2).

(44) Øien, S.; Wragg, D.; Reinsch, H.; Svelle, S.; Bordiga, S.; Lamberti, C.; Lillerud, K. P. Detailed structure analysis of atomic positions and defects in zirconium metal-organic frameworks. *Cryst. Growth Des.* **2014**, *14* (11), 5370–5372.

(45) Demir, H.; Walton, K. S.; Sholl, D. S. Computational Screening of Functionalized UiO-66 Materials for Selective Contaminant Removal from Air. *J. Phys. Chem. C* **2017**, *121* (37), 20396–20406.

(46) Rappé, A. K.; Casewit, C. J.; Colwell, K. S.; Goddard, W. A.; Skiff, W. M. UFF, a Full Periodic Table Force Field for Molecular Mechanics and Molecular Dynamics

Simulations. *J. Am. Chem. Soc.* **1992**, *114* (25), 10024–10035.

(47) Martin, M. G.; Siepmann, J. I. Transferable Potentials for Phase Equilibria. 1. United-Atom Description of n-Alkanes. *J. Phys. Chem. B* **1998**, *102*, 2569–2577.

(48) Sokkalingam, N.; Kamath, G.; Coscione, M.; Potoff, J. J. Extension of the transferable potentials for phase equilibria force field to dimethylmethyl phosphonate, sarin, and soman. *J. Phys. Chem. B* **2009**, *113* (30), 10292–10297.

(49) Manz, T. A.; Sholl, D. S. Chemically Meaningful Atomic Charges That Reproduces the Electrostatic Potential in Periodic and Nonperiodic Materials. *J. Chem. Theory Comput.* **2010**, *6*, 2455–2468.

(50) Rappe, A. K.; Goddard, W. A. Charge Equilibration for Molecular Dynamics Simulations. *J. Phys. Chem* **1991**, *95*, 3358–3363.

(51) Grimme, S.; Antony, J.; Ehrlich, S.; Krieg, H. A consistent and accurate ab initio parametrization of density functional dispersion correction (DFT-D) for the 94 elements H-Pu. *J. Chem. Phys.* **2010**, *132* (15), 154104–154122.

(52) Fang, H.; Awati, R.; Boulfelfel, S. E.; Ravikovitch, P. I.; Sholl, D. S. First-Principles-Derived Force Fields for CH_4 Adsorption and Diffusion in Siliceous Zeolites. *J. Phys. Chem. C* **2018**, *122*, 12880–12891.

(53) Verploegh, R. J.; Nair, S.; Sholl, D. S. Temperature and Loading-Dependent Diffusion of Light Hydrocarbons in ZIF-8 as Predicted Through Fully Flexible Molecular Simulations. *J. Am. Chem. Soc.* **2015**, *137* (50), 15760–15771.

(54) Han, C.; Verploegh, R. J.; Sholl, D. S. Assessing the Impact of Point Defects on Molecular Diffusion in ZIF-8 Using Molecular Simulations. *J. Phys. Chem. Lett* **2018**, *9*, 4037–4044.

(55) Walton, K. S.; Sholl, D. S. Research Challenges in Avoiding "Showstoppers" in Developing Materials for Large-Scale Energy Applications. *Joule* **2017**, *1* (2), 208–211.

(56) Joubert, D. From ultrasoft pseudopotentials to the projector augmented-wave method. *Phys. Rev. B - Condens. Matter Mater. Phys.* **1999**, *59* (3), 1758–1775.

(57) Kresse, G.; Furthmüller, J. Efficient iterative schemes for ab initio total-energy calculations using a plane-wave basis set. *Phys. Rev. B - Condens. Matter Mater. Phys.* **1996**, *54* (16), 11169–11186.

(58) Kresse, G.; Furthmüller, J. Efficiency of ab-initio total energy calculations for metals and semiconductors using a plane-wave basis set. *Comput. Mater. Sci.* **1996**, *6* (1), 15–50.

(59) Perdew, J. P.; Burke, K.; Ernzerhof, M. Generalized gradient approximation made

simple. *Phys. Rev. Lett.* **1996**, *77* (18), 3865–3868.

(60) Nazarian, D.; Ganesh, P.; Sholl, D. S. Benchmarking density functional theory predictions of framework structures and properties in a chemically diverse test set of metal–organic frameworks. *J. Mater. Chem. A* **2015**, *3* (44), 22432–22440.

CHAPTER 5. DETERMINING DIFFUSION COEFFICIENTS OF CHEMICAL WARFARE AGENTS IN MOFS

5.1 Introduction

In the last two decades, metal-organic frameworks (MOFs) have shown potential in gas storage, separations, catalysis, chemical sensing, drug delivery and other applications. MOFs are crystalline nanoporous materials that have high surface areas and structural tunability. One application that has received a great interest recently is using MOFs to capture and treat chemical warfare agents (CWAs).[1,2] CWAs are man-made chemical substances that are extremely toxic. Many of these compounds affect the nervous system and are therefore are called nerve agents. Sarin is the most common example of a nerve agent. There have been multiple efforts to use MOFs for detoxification of CWAs.[3–12] Katz et al. studied Zr-based MOFs UiO-66, UiO-67 and their derivatives for CWA simulant degradation and concluded that amino-functionalized MOFs are more active catalysts than nonfunctionalized materials.[11] Montoro et al. conducted a series of experiments on diisopropylfluorophosphonate (DFP), a simulant for sarin, to confirm the suitability of a Zn-based MOF [Zn_4(μ_4-O)-(μ_4-4-carboxy-3.5-dimethyl-4-carboxy-pyrazolato)$_3$] to capture this molecule.[12] Wang et al.[10] studied the Zr-based MOFs UiO-66, UiO-66-NH_2 and NU-1000 to understand solid-phase decontamination of CWAs and concluded that solid-phase decontamination occurs very differently than solution-based approaches. Computational studies have contributed to understanding the degradation and adsorption of CWAs and their simulants in MOFs. Sava-Gallis et al.[7] and Liu et al.[13] used periodic density functional theory (DFT) to provide theoretical insights into catalytic

degradation of CWAs and simulants in MOFs. Matito-Martos[4] used molecular simulations to screen a large library of MOFs (specifically, the CoRE MOF database[14]) for capture of CWAs under humid conditions and synthesized a promising sorbent. For obvious reasons most experimental studies use a simulant rather than active CWAs. In a previous study, we used molecular simulations to compare CWAs with their simulants to understand which simulants are most reliable for predicting adsorption properties of active CWAs in MOFs.[15]

In many applications that can be envisioned for porous adsorbents in capture and treatment of CWAs it is not only the equilibrium capacity of adsorbents that is important but also the kinetics of the processes of interest. To make even approximate estimates of the kinetics of capture of a chemical species in an adsorbent, the diffusion coefficients of the species in the adsorbent must be known. Unfortunately, almost nothing is currently known about the diffusion behavior of CWAs or CWA simulants in porous adsorbents. Dubey et al.16 studied the diffusion of sulfur mustard through butyl and nitrile rubber membranes with a spot disk breakthrough experiment and interpreted the observed diffusion mechanism using an Arrhenius equation. There have been no studies, however, determining diffusivities of CWAs in MOFs. Also, no information exists comparing the diffusion properties of CWAs with their simulants to assess which simulants could better represent the kinetics of CWA diffusion in adsorbents. In this Letter, we use molecular simulations to predict the diffusion coefficients of CWAs and simulants in MOFs. Specifically, we focus on the diffusion of the nerve agent sarin and its simulants dimethylmethylphosphonate (DMMP), diethylchlorophosphate (DCP) and DFP in four MOFs: UiO-66, ZIF-8, Cu-BTC and MIL-47. These MOFs were selected to give a diverse range of pore sizes. The molecular structures of the four molecules we studied are shown

in **Figure 5.A.1**. This is first study to quantify the rate of diffusion of CWAs and simulants in MOFs. As such, our work has significant implications in designing chemical sensors to detect CWAs and devices to provide protection against exposure to CWAs.

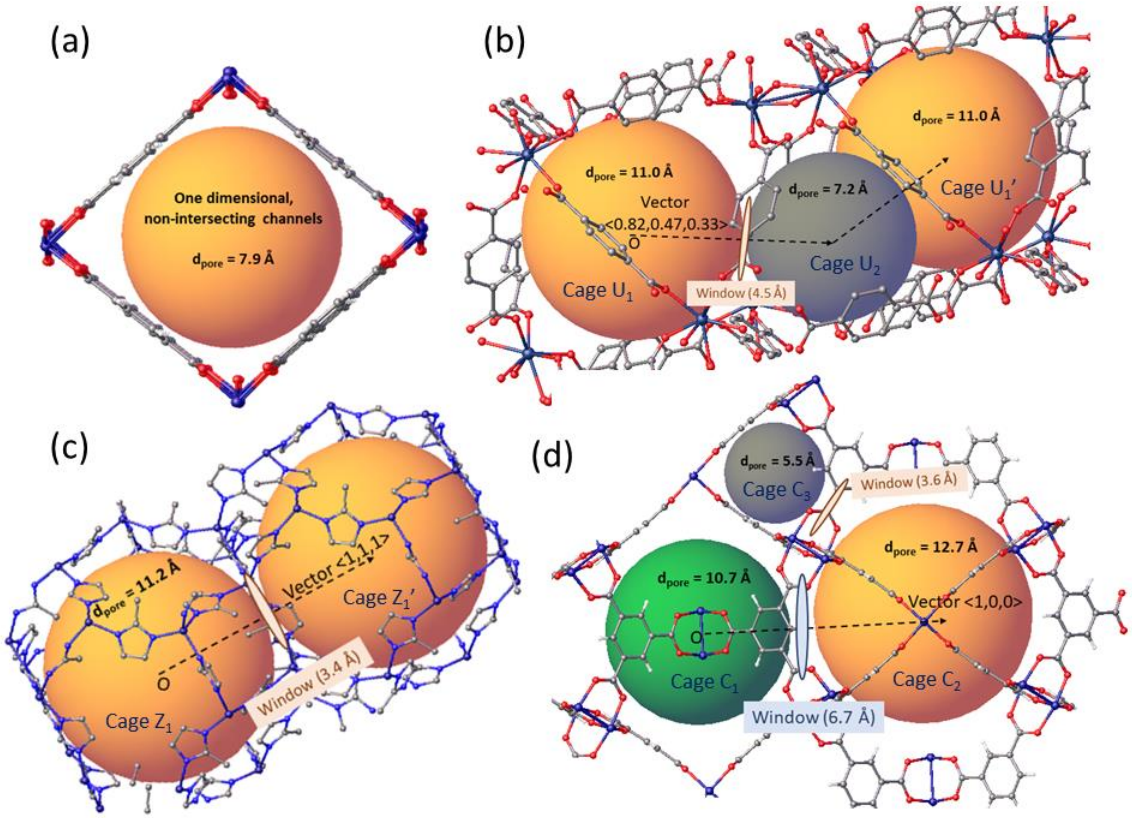

Figure 5.1: Structures of (a) MIL-47, (b) UiO-66, (c) ZIF-8, and (d) Cu-BTC with their pore sizes (shown as spheres) and windows connecting the pores. Reaction coordinate vectors for TST calculations are shown as dotted lines for UiO-66, ZIF-8 and Cu-BTC.

5.2 Theory

Several mathematically distinct diffusion coefficients exist to describe different aspects of molecular diffusion.[16] In this work we consider only self-diffusion, which characterizes Brownian motion of individual molecules under equilibrium conditions. In the limit of low loading, which is relevant in many situations involving CWAs, the self-

diffusivity is equal to the transport diffusivity, which characterizes the net flux of molecules in response to a concentration gradient.[16] We used two different approaches to obtain molecular self-diffusion coefficients, depending on the magnitude of these diffusivities. When diffusion is sufficiently fast, self-diffusion can be measured directly from Molecular Dynamics (MD) trajectories using the mean square displacement (MSD):[17]

$$D = \frac{1}{2n} \lim_{t \to \infty} \frac{\langle (r_{t+t_0} - r_t)^2 \rangle}{t} \quad (1)$$

where *D* is self-diffusivity, *n* is the dimensionality of diffusion in the system, *r* is the position of a molecule and *t* is time. We used this approach to calculate the diffusivity of sarin and simulants in MIL-47.

If diffusion is slow enough that the typical molecular displacements on nanosecond time scales are small, then the approach above is not suitable for giving meaningful results. In these cases we used dynamically corrected Transition State Theory (dcTST).[18–20] The diffusivity from site A to site B when TST is appropriate can be written as

$$D = \frac{1}{2n} k_{A \to B} \lambda^2 \quad (2)$$

where λ is the distance between the sites and $k_{A \to B}$ is the hopping rate. To apply TST, umbrella sampling[21] can be used to explore the energy landscape of an adsorbate moving along a specific reaction coordinate (RC) between site A and site B. The hopping rate, $k_{A \to B}$, is given by

$$k_{A \to B} = \kappa \frac{1}{\sqrt{2\beta\pi m}} \frac{e^{-\beta F^*}}{\int_{stateA} e^{-\beta F(r)} dr} \quad (3)$$

where $\beta = 1/k_BT$, m is the mass of an adsorbate, $F(r)$ is the Helmholtz free energy profile along the RC and F^* is the activation energy, taken as the maximum value of $F(r)$. κ is a dynamical correction factor, which accounts for short-time recrossings of the transition state (TS).[22,23] It is typically expected that κ is smaller than one, since short-time recrossings of the approximate transition state along the RC reduce the overall hopping rate. There are examples, however, where κ is greater than 1 to because of the existence of "correlated flights", trajectories that pass through multiple sites before thermalization.[24,25] This observation is important below in our comparison between dcTST and MD results for high temperature sarin diffusion in Cu-BTC.

In many applications of TST in MOFs, sites A and B are symmetric and represent equivalent minimum energy positions, so $k_{A\to B}$ and $k_{B\to A}$ are the same. In this case, the self-diffusivity can easily be calculated using equation (2). In our results below ZIF-8 is an example of this kind. In some cases, including Cu-BTC and UiO-66, the two sides of the TS are not symmetric. In this case, $k_{A\to B}$ and $k_{B\to A}$ are unequal and have to be calculated separately. A general approach for exactly defining self-diffusivities when hopping rates among a periodically repeated set of sites are known was given by Braun et al.[26] For Cu-BTC and UiO-66, which each have two inequivalent sites, this approach shows that

$$\mathrm{D_{eff}} = 2/\left(\frac{1}{\mathrm{D_{A\to B}}} + \frac{1}{\mathrm{D_{B\to A}}}\right) \qquad (4)$$

where $D_{A\to B}$ is diffusion rate from site A to site B and $D_{B\to A}$ is diffusion rate from site B to site A, both defined by equation (2). From equation (4), if $D_{A\to B} << D_{B\to A}$ then $D_{eff} \sim 2D_{A\to B}$.

5.3 Simulation Methods

For our calculations, initial crystal structures for each MOF were obtained from the Cambridge Structural Database.[27,28] Structures for sarin and CWA simulants were taken from our previous work.[15] **Figure 5.1** shows a structural representation for each MOF. The size of molecules and pore sizes of these MOFs are given in **Table 5.A.1**, **Table 5.A.2** and **Figure 5.A.2**. Although numerous modeling studies of molecular diffusion in MOFs have been performed with rigid MOF structures for computational convenience, there is strong evidence that this approach does not give even qualitatively correct information when the diffusing molecule is similar in size to the pores of the material.[18,29,30] We therefore used fully flexible models for each MOF we simulated. For our calculations, ZIF-8 force-fields (FFs) were adopted from Zhang et al.[31], who parametrized their FF to reproduce pressure-induced structural transitions in ZIF-8. FF parameters for MIL-47 were adopted from Yot et al.[32], who showed this FF described the structural properties of MIL-47 under a variety of different pressures with reasonable accuracy. Cu-BTC was modeled using the FF of Zhao et al.[33], which describes the crystal structure, negative thermal expansion and vibration properties of the framework. FF parameters for UiO-66 force-field parameters were taken Wu et al.,[34] who refined parameters obtained from CVFF[35] and UFF[36] to study CO_2 diffusion in UiO-66. To define the non-bonded and bonded parameters of adsorbates the TraPPE force-field[37] was used. To define Coulombic interactions, point charges on atoms that are not defined in TraPPE were calculated using the charge equilibration (EQ_{eq}) method.[38] Although defects can exist in MOFs either because of intrinsic imperfections or by deliberate design, our models only considered defect-free MOFs.[39]

All molecular dynamics (MD) simulations were carried out with the LAMMPS[40] software package. The calculations were carried out in periodic supercells of MOFs ensuring that size of the simulated cells was at least 26 Å in each direction. Non-bonded interactions between adsorbates and framework atoms were calculated using Lennard-Jones (L-J) potential truncated at a spherical cutoff distance of 13 Å. Cross-terms for this potential were specified using Lorentz-Berthelot mixing rules with L-J parameters taken from the FFs described above. Ewald summation was used to compute long-range Coulombic interactions with a relative error in forces of $< 10^{-6}$. In all cases, the overall systems were charge neutral. To calculate MSDs, MD calculations were carried out in LAMMPS in NVT ensemble for equilibration period of 0.5 ns and production period of 1 - 5 ns with a time step of 1 fs. For each molecule, 10 different MD simulations are run and an order-n algorithm[17] was used to calculate diffusion coefficients using equation (1). Each MD simulation was performed at low loadings where only one molecule was present in the simulation volume (8 unit cells for each MOF).

For TST calculations, umbrella sampling calculations were performed using collective variable package[41] in LAMMPS with umbrella spacing of 0.1 Å along the reaction coordinate (RC). During an umbrella sampling simulation, an adsorbate was constrained in a region orthogonal to the RC by a spring centered at a specified value of the RC. Spring constants ranging from 150-200 kcal mol^{-1} $Å^{-1}$ were applied on the adsorbate where a stiffer spring was applied to molecules with higher molecular weight. For each umbrella, a 1000 ps equilibration was performed followed by 1000 ps production period. The weighted histogram analysis method was used to integrate sampling of all umbrellas into a free energy curve.[42] Dynamical correction factors (κ) were calculated as

described in previous work.[18,19] After determining the position of transition state (TS) using umbrella sampling, a set of configurations were generated by constraining the molecule in the plane of TS orthogonal to RC with a tight spring constant of 1000 kcal mol^{-1} $Å^{-1}$. A set of trajectories starting from these configurations were then simulated for the molecule with no constraints on the molecule, with all atoms initially assigned randomized velocities following the Maxwell-Boltzmann distribution. Each trajectory was run for 10 ps forward and 10 ps backward in time. 2000 trajectories for each molecule were recorded to allow calculations of dynamical correction factor. A modified approach was used to account for the potential contribution of correlated flights[24,25] in the calculation of dynamical correction factor. The end point of each trajectory was used to decide not only which side of the TS molecule ended, but also whether the molecule jumped through more than one cage. When correlated flights were detected, this information was included in the definition of the dynamical correction factor. For MOFs that have different cage structures on both side of TS (UiO-66 and Cu-BTC), dynamical correction factor was separately calculated in both directions and the overall self-diffusion coefficient was calculated using equation (4).

5.4 Results and Discussion

We first describe the diffusion of sarin and simulants in MIL-47, a MOF with one dimensional non-intersecting channels (pore size = 7.9 Å) as shown in **Figure 5.1a**. The pores of MIL-47 are considerably larger than the molecules we considered (see **Table 5.A.1**), so the diffusion coefficients were calculated using standard MD simulations. **Figure 5.2** shows the resulting MSDs of each molecule at 300 K using 100 ps time intervals for block averages in the order-n algorithm. Average displacements of 10-50 Å are observed, indicating that diffusion is fast enough to be readily treated with MD. MSDs of

individual MD runs for sarin are shown in **Figure 5.A.3**. Diffusion coefficients were found to be approximately independent of the time-intervals used for block averaging (see **Figure 5.A.4**), which validates the convergence of these results. Similar calculations were performed at 400 and 500 K. The computed diffusion coefficients at three different temperatures allowed us to estimate the activation energy for diffusion by assuming a simple Arrhenius form, $D = D_0 * exp(-E_A/RT)$ (see **Figure 5.A.5**). The calculated diffusion coefficients and activation energies in MIL-47 are summarized in **Table 5.1**. The room temperature diffusivity of sarin in MIL-47 was calculated to be 8.3×10^{-5} cm^2/s.

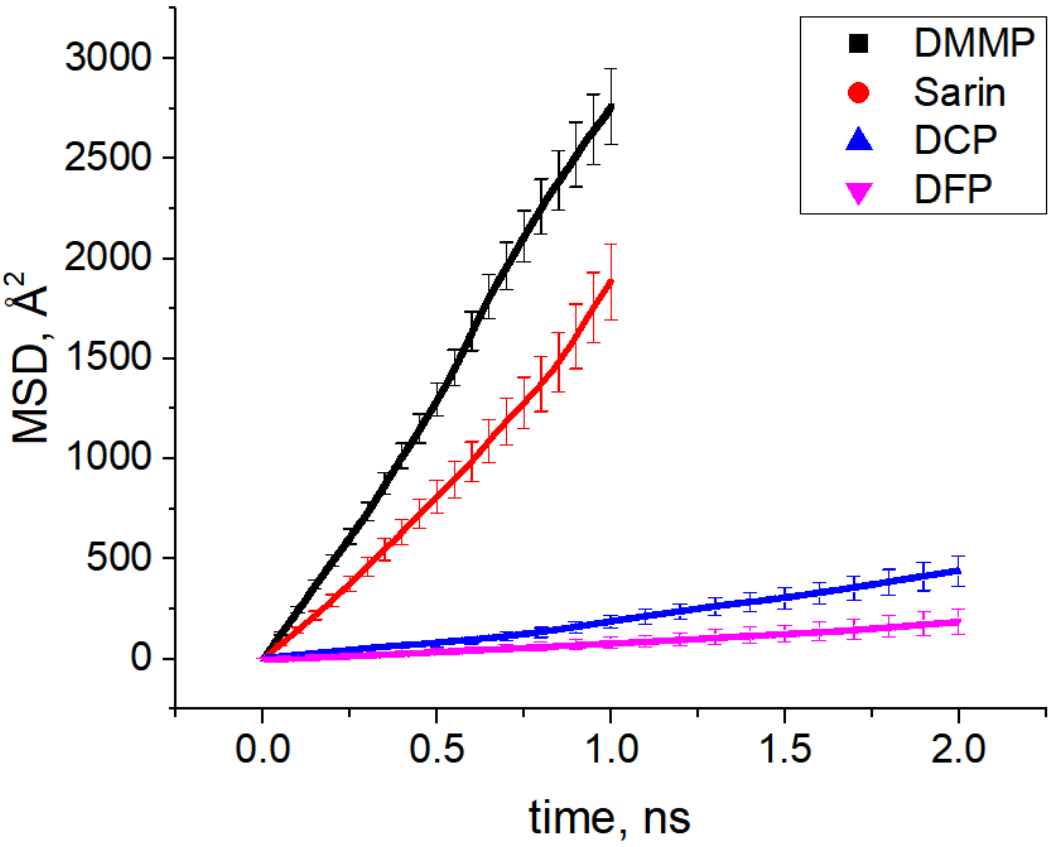

Figure 5.2: MSDs with error bars calculated as described in the text for sarin, DMMP, DCP and DFP in MIL-47 at 300 K. Error bars are only shown for selected time points but were similar for all points. Simulations for DMMP and sarin were run for 1 ns, while DCP and DFP for 2 ns.

Table 5.1: Diffusion coefficients of sarin and simulants in MIL-47 at different temperatures.

	Sarin	**DMMP**	**DCP**	**DFP**
$D_{300\ K}$ (cm^2/s)	2.2×10^{-5}	4.1×10^{-5}	1.7×10^{-6}	5.6×10^{-7}
$D_{400\ K}$ (cm^2/s)	4.7×10^{-5}	8.4×10^{-5}	6.3×10^{-6}	2.2×10^{-6}
$D_{500\ K}$ (cm^2/s)	8.3×10^{-5}	1.2×10^{-4}	1.2×10^{-5}	8.1×10^{-6}
E_A (kJ/mol)	8.2	6.4	12.3	16.3

ZIF-8 is a zeolitic imidazole-based MOF with large cavities (11.2 Å) interconnected by narrow windows (3.4 Å) as shown in **Figure 5.1c**. Several studies have shown that molecules considerably larger than 3.4 Å are able to diffuse through the ZIF-8 due to its flexibility.[18,19] For example, Han et al.[19] used dcTST to simulate diffusion of molecules such as *i*-butane (kinetic diameter 4.8 Å) in ZIF-8 and calculated its diffusion coefficient to be 2.7×10^{-16} cm^2/s. Sarin and simulants are comparable in size to *i*-butane. This suggested that MD would not be sufficient to calculate diffusivities of these molecules in ZIF-8. For this reason we applied dcTST method as described above. As shown in **Figure 5.1c**, the reaction coordinate for diffusion in ZIF-8 connects equivalent cage sites through a 3.4 Å window. The distance between the centers of these cages is 14.7 Å. The computed activation energies, dynamical correction factors and diffusivities of sarin, DMMP, DCP and DFP in ZIF-8 at room temperature are shown in **Table 5.2**. Sarin and DMMP have similar diffusivities of $\sim10^{-14}$ cm^2/s while DCP has a much lower diffusivity of 8.73×10^{-16}. The diffusivity of DCP is comparable to that of *i*-butane reported by Han et al.[19] A surprising observation from **Table 5.2** is that DFP has a diffusivity higher than sarin despite its larger size than sarin. We observed that DFP caused larger distortion in the

window of ZIF-8 connecting the cages compared to other molecules (see **Figure 5.A.7**). Because these window distortions are crucial to hopping of all of the molecules we considered, the larger window distortions for DFP appear to allow more rapid hopping than for sarin.

Table 5.2: Activation energies, dynamical correction factor (DCF) and diffusivities of sarin and simulants in ZIF-8 at 300 K.

Molecule	**Activation energy, kJ/mol**	**DCF**	**Diffusivity, cm^2/s**
Sarin	66.0	0.85	5.44×10^{-14}
DMMP	64.7	0.89	4.81×10^{-14}
DCP	72.5	0.45	8.73×10^{-16}
DFP	54.7	0.31	1.15×10^{-12}

Table 5.3: Activation energies, dynamical correction factors (DCF) and diffusivities of sarin and simulants in UiO-66 at 300 K

Molecule	**$E_{A,U1-U2}$ kJ/mol**	**DCF_{U1-U2}**	**$E_{A,U2-U1}$ kJ/mol**	**DCF_{U2-U1}**	**D, cm^2/s**
Sarin	53.2	0.024	37.4	0.027	4.3×10^{-13}
DMMP	45.8	0.038	56.1	0.032	1.6×10^{-13}
DCP	74.7	0.013	28.9	0.03	3.2×10^{-17}
DFP	76.3	0.008	35.2	0.017	1.2×10^{-17}

UiO-66 is a MOF made up of BDC linkers with Zr metal-centers. It has two different kind of pores denoted as cage U_1 (the primary pore) and U_2 (the secondary pore) in **Figure 5.1b**. Each primary pore is connected to secondary pore through a window of diameter 4.5 Å. The window size is comparable to sarin, so we used dcTST to study

diffusion in UiO-66. As shown in **Figure 5.1b**, the distance between cage U_1 and cage U_2 is approximately 9.1 Å. **Figure 5.1b** shows that cage U_2 is tetrahedral, so different vectors define the reaction coordinates from cage U_1 to cage U_2 and from cage U_2 to cage U_1'. We applied dcTST to obtain free energy profiles from cage U_1 to cage U_2 and applied symmetry operations to define the remainder of the free energy profile for net diffusion. The free energy profiles calculated for sarin and simulants are shown in **Figure 5.A.8**. The free energy of DMMP has its minimum energy position in the secondary cage (U_2) while the other molecules have their energy minimum in the primary cage (U_1). DMMP is the smallest molecule we simulated, which appears to explain why it fits favorably into the smaller secondary cage. DCP and DFP, which are both larger than sarin, have strongly unfavorable free energies in the secondary cage relative to the primary cage. The activation energy and DCF for each type of cage to cage hop in UiO-66 were calculated separately and diffusion coefficients are calculated using equation (4). These results and the overall diffusivities for sarin, DMMP, DCP and DFP in UiO-66 are shown in **Table 5.3**. DMMP and sarin have similar diffusivities that are approximately four orders of magnitude higher than both DCP and DFP. The diffusivities of DMMP and sarin in UiO-66 are higher than in ZIF-8 but the diffusivities of DCP and DFP in UiO-66 are lower than in ZIF-8. This suggests that ZIF-8 is more flexible than UiO-66 because the diffusivity in UiO-66 drops more significantly for molecules that have kinetic diameters larger than window size.

Cu-BTC (also known as HKUST-1) is a MOF consisting of BDC linkers with Cu metal centers. It has three different kinds of cages (C_1, C_2 and C_3) as shown in **Figure 5.1**. Cage C_2 is connected to both C_1 and C_3 through windows of size 6.7 Å and 3.6 Å respectively while cage C_1 and C_3 are not connected with each other. We use dcTST

simulations with umbrella sampling to study diffusion in Cu-BTC. The length of the vector between the centers of cages C_1 and C_2 is approximately 13.1 Å. Free energy profiles generated from simulations for sarin and simulants in Cu-BTC at 300 K are shown in **Figure 5.A.9**. Cage C_1, which is smaller than cage C_2 but larger than cage C_3, defines the minimum energy position for all four molecules. We did not perform dcTST calculations for hopping from cage C_2 to cage C_3, assuming that this rate is very low because of the small window connecting these two cages. To validate this approach, we calculated the average energy of sarin at the center of cages C_1, C_2 and C_3, obtaining values of -34.3, -18.9 and -3.1 kJ/mol. The energy difference between C_1 and C_2 are similar to what dcTST calculations predicted (see **Table 5.4** and **Figure 5.A.9**). This unfavorable energy of cage C_3 strongly suggests that because net diffusion can occur via only cages C_1 and C_2, overall diffusion in Cu-BTC is dominated by this process. This assumption if further supported by **Figure 5.A.11**, which shows the coordinates of sarin in Cu-BTC during a 10 ns MD trajectory at 500 K. Sarin is seen to not enter cage C_3 during this MD simulation. If the hopping rate into cage C_3 is non-zero but far smaller than the hopping rates between cages C_1 and C_2 then the net diffusivity can be accurately calculated assuming that the former rate is zero.

Table 5.4: Activation energies, DCFs and diffusivities of sarin and simulants in Cu-BTC at 300 K

Molecule	**$E_{A,C1-C2}$ kJ/mol**	**DCF_{C1-C2}**	**$E_{A,C2-C1}$ kJ/mol**	**DCF_{C2-C1}**	**D, cm^2/s**
Sarin	30.3	1.21	17.3	1.15	5.4×10^{-8}
DMMP	33.8	1.32	23.1	1.31	1.3×10^{-8}
DCP	45.9	0.87	20.3	0.82	1.7×10^{-10}
DFP	50.6	0.81	16.4	0.86	1.4×10^{-11}

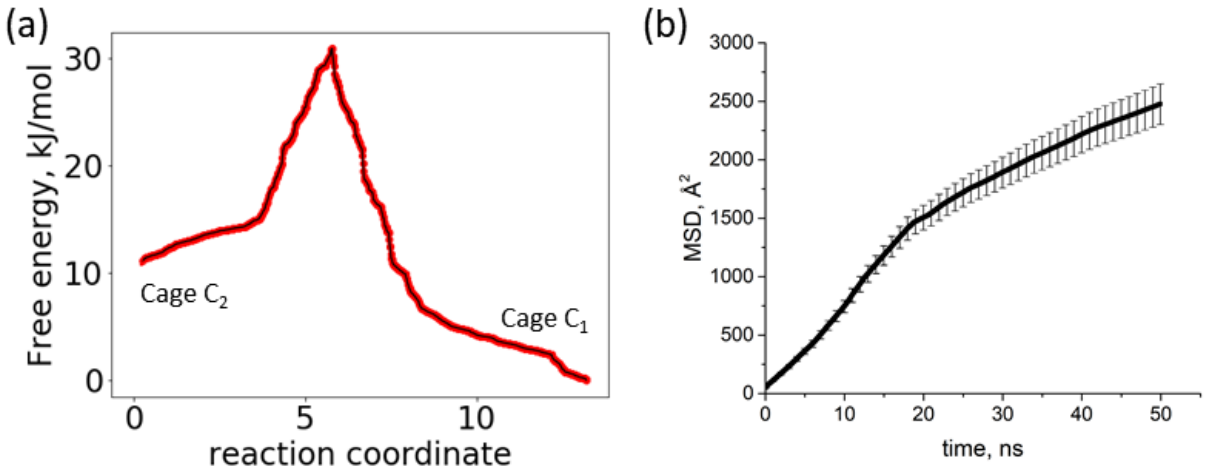

Figure 5.3: (a) Free energy profile, (b) averaged MSD using the order-n method with error bars for sarin in Cu-BTC at 500 K

Table 5.4 shows the cage to cage activation energies, DCFs and overall diffusivities of sarin and simulants in Cu-BTC at 300 K. Like the other MOFs we considered, sarin and DMMP have diffusivities of the same order of magnitude in Cu-BTC which are larger than DCP and DFP. The dynamical correction factors for sarin and DMMP are larger than 1

because of the existence of "correlated flights", trajectories that pass through multiple sites before thermalization.[24,25] The correlated flights in Cu-BTC are more easily observed in the trajectories of sarin obtained from MD calculations at elevated temperatures. Sample data of this kind at 500 K is shown in **Figure 5.A.10**. We observed that the diffusivity of sarin in CuBTC was fast enough to be directly computed from MD at elevated temperatures, which gave us a convenient way to examine the consistency between our MD and dcTST calculations. The free energy profile of sarin in Cu-BTC calculated using umbrella sampling at 500 K is shown in **Figure 5.3a**. The activation energy at 500 K is 30.7 kJ/mol, very similar to the value calculated at 300 K of 30.3 kJ/mol. This supports the use of the activation energies in Tables 2-4 over a wide range of temperatures. The DCF calculated for sarin at 500 K was calculated to be 3.2, higher than the DCF calculated at 300 K because correlated flights are longer in displacement and more frequent at the higher temperature. The diffusion coefficient calculated using dcTST at 500 K was 2.3×10^{-7} cm^2/s while from direct MD simulations we obtained a diffusivity of 6.7×10^{-7} cm^2/s. The averaged MSD of sarin obtained from MD using the order-n method is shown in **Figure 5.3b**. We attribute the 'elbow' in the MSD plot to be a statistical fluctuation associated with the limited number of trajectories available for averaging, not a physical effect. Although there is a difference between two diffusivities calculated using dcTST and MSD, it is very small relative to the variation seen between MOFs in the results above, where the computed diffusivities vary by multiple orders of magnitude. It is clear, therefore, that the two simulation methods give results that are consistent for the purposes of comparing diverse MOFs in terms of molecular diffusivities.

Because there is no prior experimental or modeling work on diffusion of CWAs in MOFs we cannot directly compare our results with experiments or other simulations. We can, however, compare our results to the diffusivities of other molecules in MIL-47. A previous experimental study[43] reported the diffusivity of methane in MIL-47 at 300 K to be 2×10^{-4} cm^2/s, 9 times higher than our result for sarin. Another experimental report[44] gave the diffusivity of neo-pentane in MIL-47 at 300 K to be 6.7×10^{-6} cm^2/s, 3.3 times smaller than our result for sarin. These results are in qualitative agreement with predictions from Knudsen diffusion calculated for each molecule in MIL-47 (see **Table 5.A.3**). Skoulidas *et al.*[45] showed that diffusivities in large pore MOFs can be predicted with reasonable accuracy with Knudsen diffusion. MIL-47 as has large non-intersecting one dimensional pores that are considerably larger than the diffusing molecules, so Knudsen diffusion is a plausible, albeit simplistic, description. In ZIF-8, UiO-66 and Cu-BTC, however, a description based on Knudsen diffusion is inappropriate because molecular diffusion is dominated by hopping over substantial free energy barriers. Predictions based on Knudsen diffusion in these materials are larger than our results from MD by four orders of magnitude or more (see **Table 5.A.3**).

Table 5.5: Characteristic time for diffusion of sarin and simulants across 1 micron in different MOFs at room temperature, with all times seconds.

Adsorbate	MIL-47	Cu-BTC	ZIF-8	UiO-66
Sarin	2.4×10^{-4}	2.2×10^{-2}	9.2×10^{4}	1.2×10^{4}
DMMP	1.2×10^{-4}	5.0×10^{-2}	1.0×10^{5}	3.1×10^{4}
DCP	2.9×10^{-3}	29	5.7×10^{6}	1.6×10^{8}
DFP	1.4×10^{-2}	1.8×10^{2}	4.3×10^{3}	4.2×10^{8}

It can sometimes be difficult to intuitively understand diffusion coefficients that vary as widely as the results we have shown above. To give another view of these results, we compared the amount of time each molecule requires to diffuse a distance of one micron in each MOF. This is a useful characteristic distance in thinking about capture or detoxification of CWAs in MOF particles or films. These diffusion times are listed (in seconds) in **Table 5.5**. Sarin can diffuse one micron in MIL-47 or Cu-BTC in far less than one second, but the same time scale for sarin diffusion in UiO-66 and ZIF-8 is 3.3 hours and more than 25 hours, respectively. This indicates that only particles much smaller than micron dimensions would be suitable for uptake of sarin in small pore materials like UiO-66 and ZIF-8 if rapid uptake kinetics are required. The situation is even more challenging for the CWA simulants we considered. The characteristic diffusion times for DMMP in UiO-66 and ZIF-8 are 9 and 28 hours, respectively, values that are quite similar to sarin. For DCP and DFP, however, the characteristic times are far longer. DCP, for example, has a characteristic diffusion time of more than 40,000 hours in UiO-66 and 1500 hours in ZIF-8. This implies that DCP and DFP cannot be used as meaningful simulants for sarin in small pore MOFs, even though the adsorption properties of these species might be relatively similar.[15] **Table 5.5** shows that DMMP is consistently the most similar in diffusivity to sarin for every MOF we considered. In our previous study[15] comparing adsorption properties of sarin with several simulants we concluded that DMMP was the best simulant to predict sarin's adsorption properties in MOFs. Taken together, our results suggest that DMMP is a much better simulant than DCP or DFP for understanding the adsorption and diffusion in nanoporous materials. We caution that this conclusion does not imply that DMMP is also the best simulant for other CWAs; the strong sensitivity of

molecular diffusivities in materials with pore sizes similar to those of the adsorbed molecules mean that appropriate care must be taken in selecting a simulant for each CWA of interest in any application where uptake kinetics could influence observed outcomes.

APPENDIX 5.A. SUPPORTING INFORMATION FOR CHAPTER 5

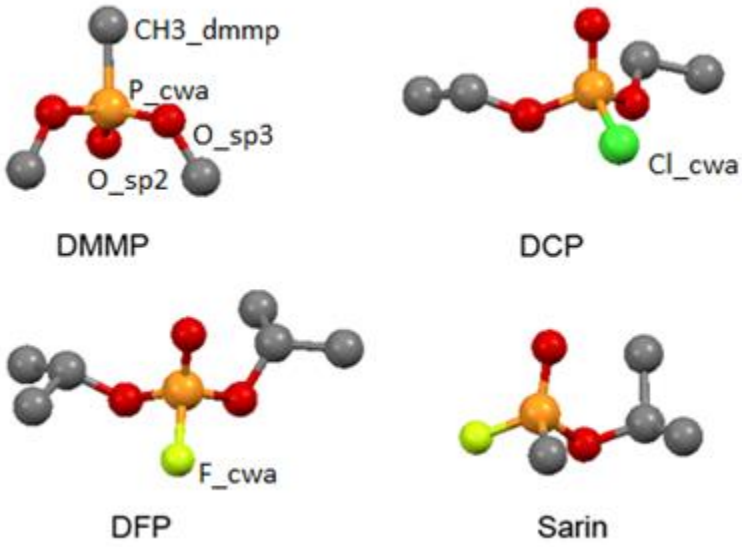

Figure 5.A.1: Atomic representations of sarin and three simulants. Grey, red, orange, dark green, and light green colors corresponds to carbon, oxygen, phosphorus, chlorine and fluorine respectively. For clarity, hydrogen atoms are not shown.

Table 5.A.1: Size of Sarin and simulants

Molecule	Length, Å	Width, Å
Sarin	5.5	4.4
DMMP	5.0	4.2
DCP	7.5	4.6
DFP	8.0	4.8
Methane[46]	3.8	3.8
Neopentane[46]	6.2	6.2

Table 5.A.2: Pore apertures of selected MOFs

MOF	Primary pore, Å	Secondary pore, Å	Tertiary pore, Å	Window size, Å
MIL-47[47]	-	-	-	7.9
UiO-66[48]	11.0	7.2	-	4.5
Cu-BTC[49]	12.7	10.7	5.5	6.7, 3.6
ZIF-8[50]	11.2	-	-	3.4

Table 5.A.3: Molecular weight of sarin, DMMP, DCP, DFP, methane and neopentane and their Knudsen diffusivities in MOFs at 300 K

Molecule	Molecular weight	MOF	D_{KA}, cm^2/s [a]	D_{MD}, cm^2/s	D_{KA} / D_{MD}
Sarin	140.09	MIL-47	5.61×10^{-4}	2.2×10^{-5}	25.5
DMMP	124.07	MIL-47	5.96×10^{-4}	4.1×10^{-5}	14.5
DCP	172.55	MIL-47	5.05×10^{-4}	1.7×10^{-6}	297
DFP	184.15	MIL-47	4.89×10^{-4}	5.6×10^{-7}	873
Methane[46]	16.04	MIL-47	1.66×10^{-3}	2×10^{-4}	8.3
Neopentane[46]	72.15	MIL-47	7.82×10^{-4}	6.7×10^{-6}	117
Sarin	140.09	UiO-66	5.11×10^{-4}	5.44×10^{-14}	$\sim10^{10}$
Sarin	140.09	ZIF-8	7.95×10^{-4}	4.3×10^{-11}	$\sim10^{7}$
Sarin	140.09	Cu-BTC	7.6×10^{-4}	5.4×10^{-8}	$\sim10^{4}$

[a] D_{KA} = Knudsen diffusion of A = $\frac{d_{pore}}{3}\sqrt{\frac{8RT}{\pi M_A}}$, M_A = molecular weight of A

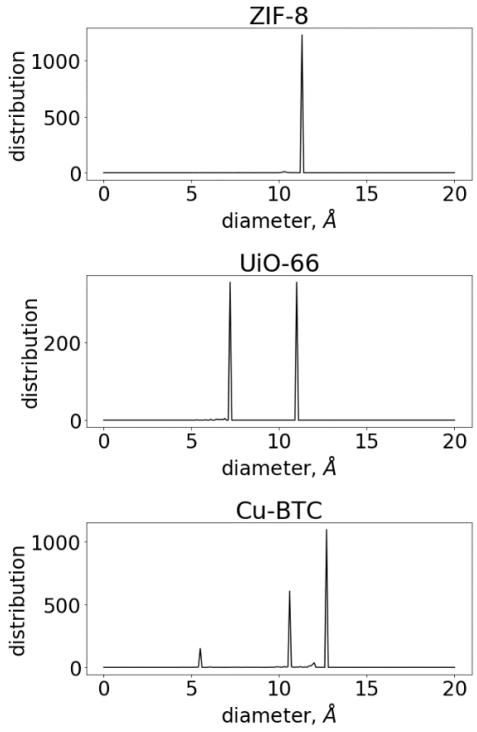

Figure 5.A.2: Pore size distribution of MOFs calculated using probe radius of 1.4 Å in zeo++ software package[51]

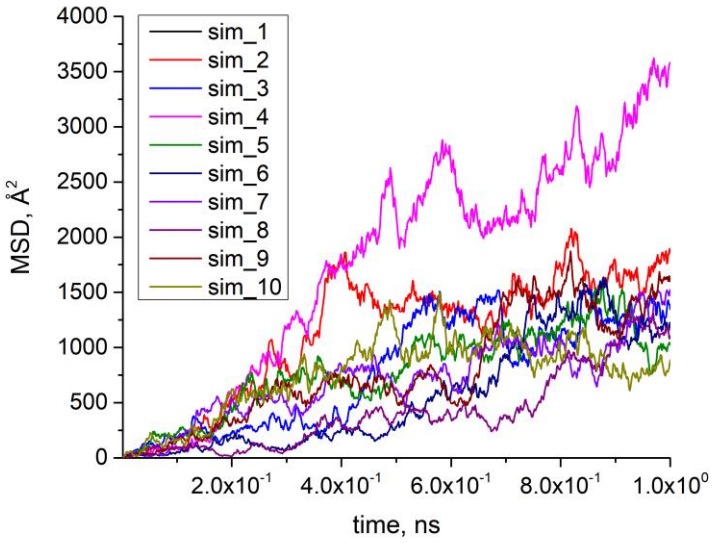

Figure 5.A.3: MSDs with time for sarin in MIL-47 obtained from 10 different simulations at 300 K

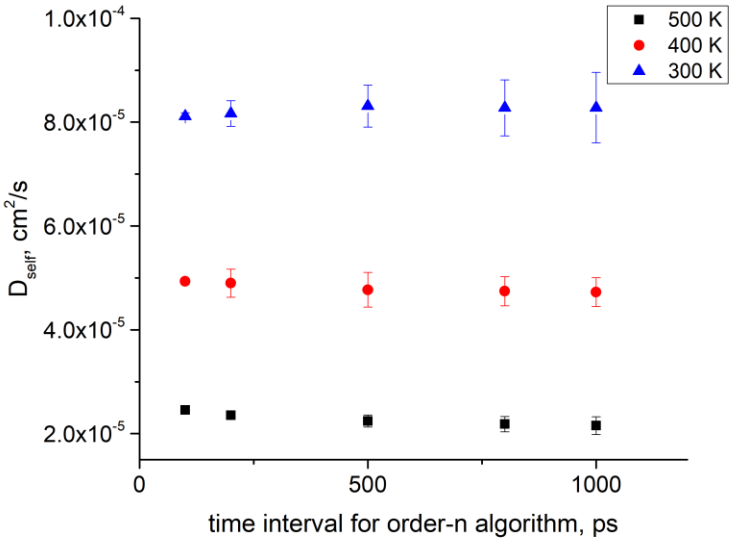

Figure 5.A.4: Diffusion coefficients of sarin in MIL-47 at different temperatures using different time-intervals in the order-n algorithm

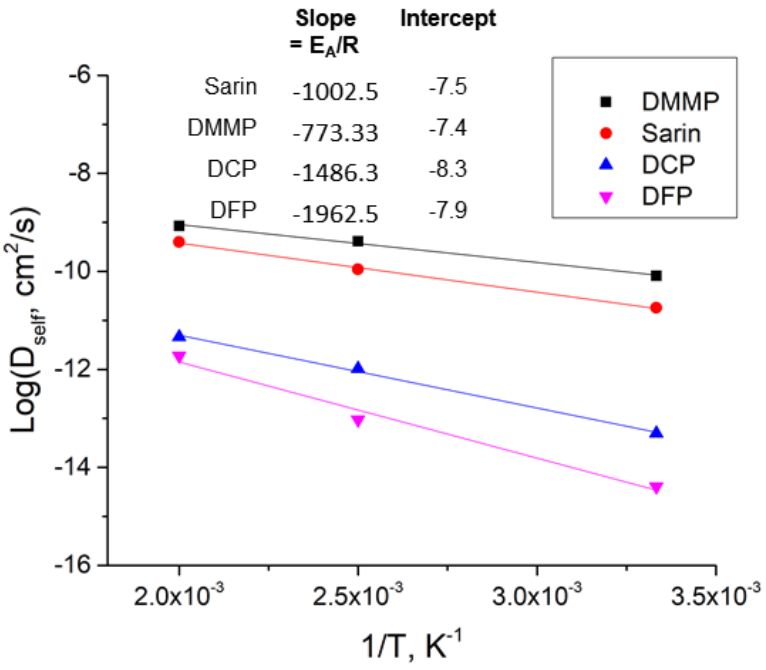

Figure 5.A.5: Diffusion coefficients as a function of temperature for sarin and simulants in MIL-47.

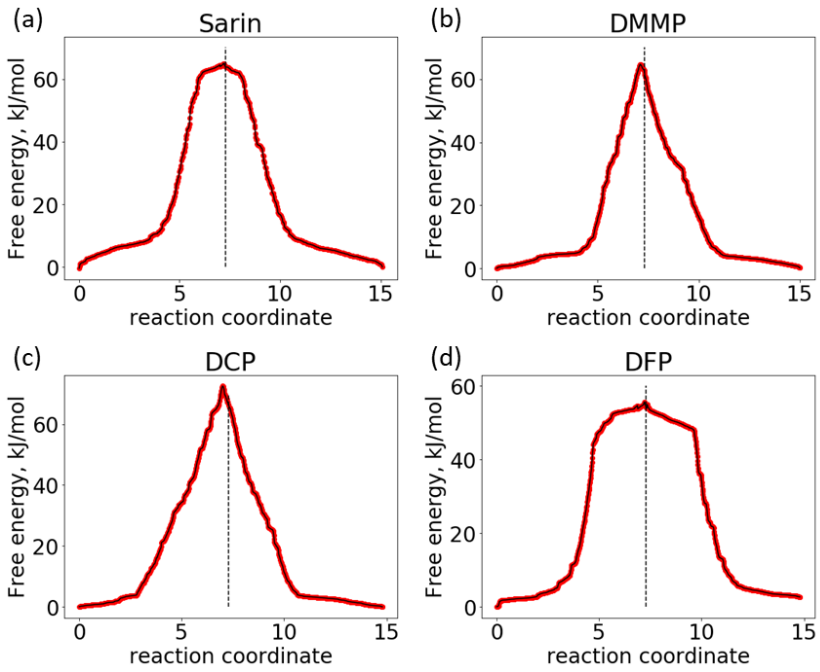

Figure 5.A.6: Free energy profiles of (a) sarin, (b) DMMP, (c) DCP, and (d) DFP in ZIF-8 calculated using TST at 300 K.

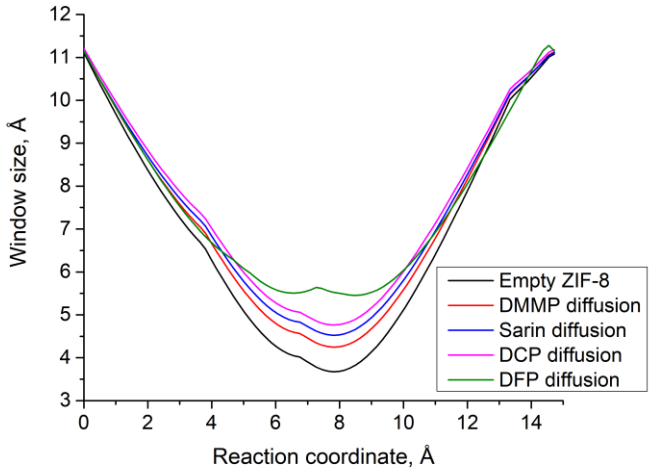

Figure 5.A.7: Cross-sectional window size perpendicular to the reaction coordinate at each point in the umbrella sampling for empty structure and during diffusion of sarin and simulants. At each point along the reaction coordinate, the perpendicular distance from the nearest atom was calculated and window size at that point was calculated after subtracting the vdw radius of atoms involved. The value at zero represents the window size at the center of the cage. The minimum value represents the window connecting two cages in ZIF-8.

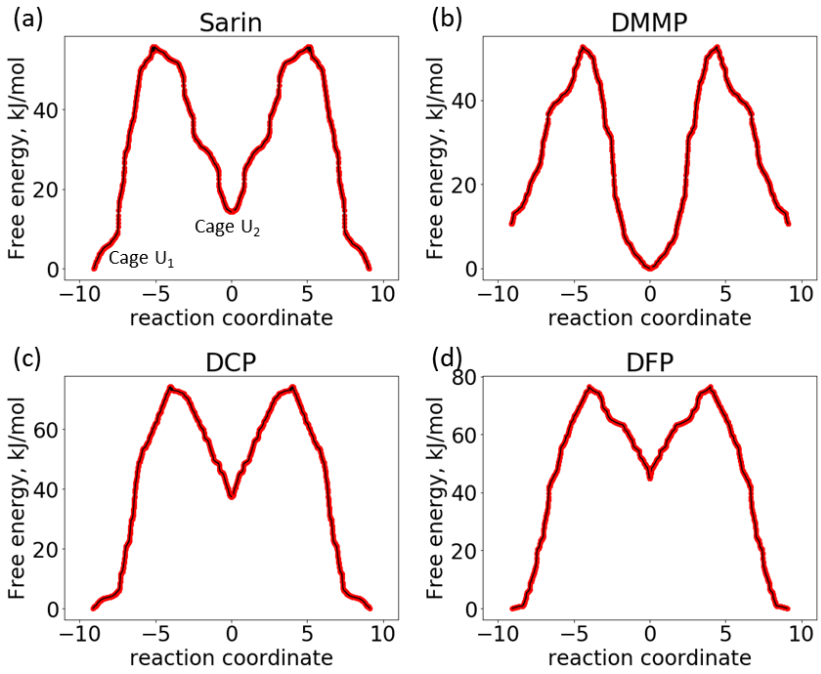

Figure 5.A.8: Free energy profiles of (a) sarin, (b) DMMP, (c) DCP, and (d) DFP in UiO-66 calculated using TST at 300 K.

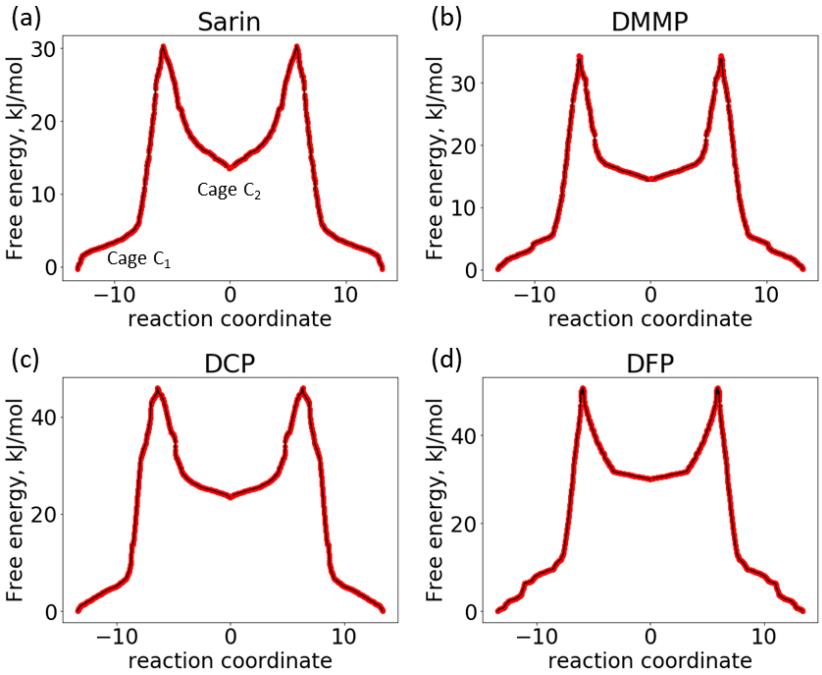

Figure 5.A.9: Free energy profiles of (a) sarin, (b) DMMP, (c) DCP, and (d) DFP in Cu-BTC calculated using TST at 300 K.

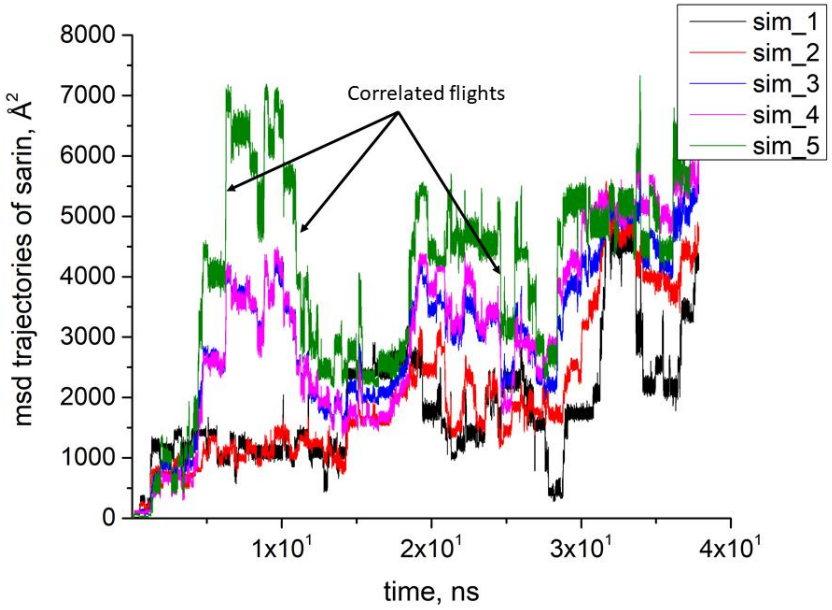

Figure 5.A.10: MSD traces of individual sarin molecules in Cu-BTC at 500 K.

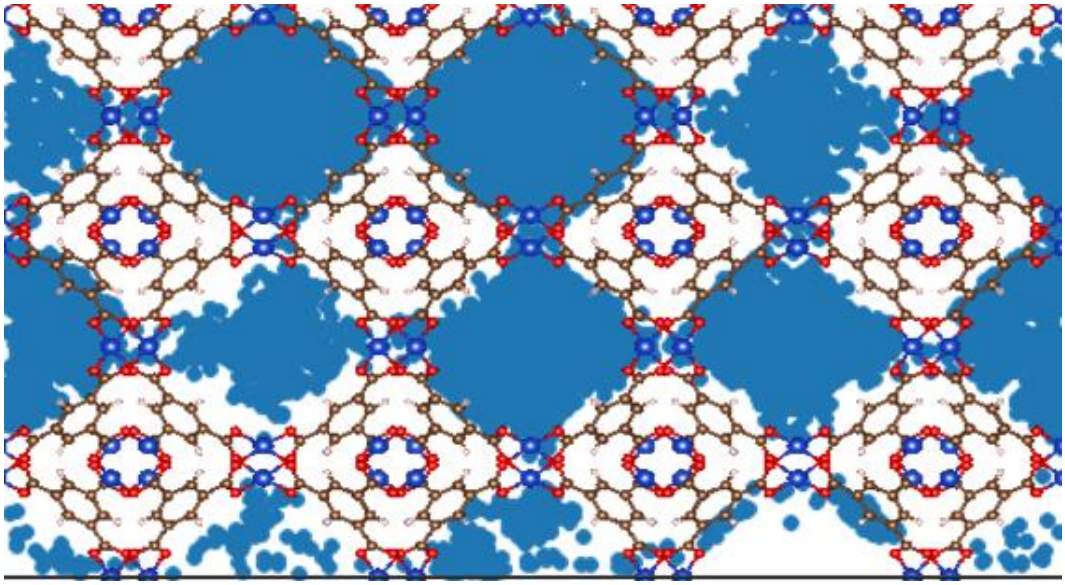

Figure 5.A.11: Distribution of a single sarin molecule during MD simulation in Cu-BTC for 10 ns at 500 K. Each blue point represents the coordinate of the phosphorous atom of sarin during the trajectory.

5.5 References

(1) Liu, Y.; Howarth, A. J.; Vermeulen, N. A.; Moon, S.-Y.; Hupp, J. T.; Farha, O. K. Catalytic Degradation of Chemical Warfare Agents and Their Simulants by Metal-Organic Frameworks. *Coord. Chem. Rev.* **2017**, *346*, 101–111.

(2) Bobbitt, N. S.; Mendonca, M. L.; Howarth, A. J.; Islamoglu, T.; Hupp, J. T.; Farha, O. K.; Snurr, R. Q. Metal–Organic Frameworks for the Removal of Toxic Industrial Chemicals and Chemical Warfare Agents. *Chem. Soc. Rev.* **2017**, *46* (11), 3357–3385.

(3) Ji, P.; Feng, X.; Veroneau, S. S.; Song, Y.; Lin, W. Trivalent Zirconium and Hafnium Metal − Organic Frameworks for Catalytic 1,4-Dearomative Additions of Pyridines and Quinolines. *J. Am. Chem. Soc.* **2017**, *139* (44), 15600–15603.

(4) Matito-Martos, I.; Moghadam, P. Z.; Li, A.; Colombo, V.; R Navarro, J. A.; Calero, S.; Fairen-Jimenez, D. Discovery of an Optimal Porous Crystalline Material for the Capture of Chemical Warfare Agents. *Chem. Mater.* **2018**, *30*, 4571–4579.

(5) Zhao, J.; Lee, D. T.; Yaga, R. W.; Hall, M. G.; Barton, H. F.; Woodward, I. R.; Oldham, C. J.; Walls, H. J.; Peterson, G. W.; Parsons, G. N. Ultra-Fast Degradation of Chemical Warfare Agents Using MOF–Nanofiber Kebabs. *Angew. Chemie - Int. Ed.* **2016**, *55* (42), 13224–13228.

(6) Mondloch, J. E.; Katz, M. J.; Isley III, W. C.; Ghosh, P.; Liao, P.; Bury, W.; Wagner, G. W.; Hall, M. G.; DeCoste, J. B.; Peterson, G. W.; et al. Destruction of Chemical Warfare Agents Using Metal–Organic Frameworks. *Nat. Mater.* **2015**, *14* (5), 512–516.

(7) Sava Gallis, D. F.; Harvey, J. A.; Pearce, C. J.; Hall, M. G.; Decoste, J. B.; Kinnan, M. K.; Greathouse, J. A. Efficient MOF-Based Degradation of Organophosphorus Compounds in Non-Aqueous Environments. *J. Mater. Chem. A* **2018**, *6*, 3038–3045.

(8) Melnychuk, S. A.; Neverov, A. A.; Brown, R. S. Catalytic Decomposition of Simulants for Chemical Warfare V Agents: Highly Efficient Catalysis of the Methanolysis of Phosphonothioate Esters. *Angew. Chemie - Int. Ed.* **2006**, *45* (11), 1767–1770.

(9) Moon, S. Y.; Liu, Y.; Hupp, J. T.; Farha, O. K. Instantaneous Hydrolysis of Nerve-Agent Simulants with a Six-Connected Zirconium-Based Metal-Organic Framework. *Angew. Chemie - Int. Ed.* **2015**, *54* (23), 6795–6799.

(10) Wang, H.; Mahle, J. J.; Tovar, T. M.; Peterson, G. W.; Hall, M. G.; Decoste, J. B.; Buchanan, J. H.; Karwacki, C. J. Solid-Phase Detoxification of Chemical Warfare Agents Using Zirconium-Based Metal Organic Frameworks and the Moisture Effects: Analyze via Digestion. *ACS Appl. Mater. Interfaces* **2019**, *11* (23), 21109–21116.

(11) Katz, M. J.; Moon, S.-Y.; Mondloch, J. E.; Beyzavi, M. H.; Stephenson, C. J.; Hupp, J. T.; Farha, O. K. Exploiting Parameter Space in MOFs: A 20-Fold Enhancement of Phosphate-Ester Hydrolysis with UiO-66-NH_2. *Chem. Sci.* **2015**, *6* (4), 2286–2291.

(12) Montoro, C.; Linares, F.; Quartapelle Procopio, E.; Senkovska, I.; Kaskel, S.; Galli, S.; Masciocchi, N.; Barea, E.; Navarro, J. A. R. Capture of Nerve Agents and Mustard Gas Analogues by Hydrophobic Robust MOF-5 Type Metal-Organic Frameworks. *J. Am. Chem. Soc.* **2011**, *133* (31), 11888–11891.

(13) Liu, Y.; Moon, S. Y.; Hupp, J. T.; Farha, O. K. Dual-Function Metal-Organic Framework as a Versatile Catalyst for Detoxifying Chemical Warfare Agent Simulants. *ACS Nano* **2015**, *9* (12), 12358–12364.

(14) Chung, Y. G.; Camp, J.; Haranczyk, M.; Sikora, B. J.; Bury, W.; Krungleviciute, V.; Farha, O. K.; Sholl, D. S.; Snurr, R. Q. Computation-Ready, Experimental Metal−Organic Frameworks: A Tool to Enable High-Throughput Screening of Nanoporous Crystals. *Chem. Mater.* **2014**, *26*, 6185–6192.

(15) Agrawal, M.; Sava Gallis, D. F.; Greathouse, J. A.; Sholl, D. S. How Useful Are Common Simulants of Chemical Warfare Agents at Predicting Adsorption Behavior? *J. Phys. Chem. C* **2018**, *122* (45), 26061–26069.

(16) Sholl, D. S. Understanding Macroscopic Diffusion of Adsorbed Molecules in Crystalline Nanoporous Materials via Atomistic Simulations. *Acc. Chem. Res.* **2006**, *39* (6), 403–411.

(17) Frenkel, D.; Smit, B. *Understanding Molecular Simulations: From Algorithms to Applications*, 2nd ed.; Academic Press, Inc., 2001.

(18) Verploegh, R. J.; Nair, S.; Sholl, D. S. Temperature and Loading-Dependent Diffusion of Light Hydrocarbons in ZIF-8 as Predicted Through Fully Flexible Molecular Simulations. *J. Am. Chem. Soc.* **2015**, *137* (50), 15760–15771.

(19) Han, C.; Verploegh, R. J.; Sholl, D. S. Assessing the Impact of Point Defects on Molecular Diffusion in ZIF-8 Using Molecular Simulations. *J. Phys. Chem. Lett* **2018**, *9*, 4037–4044.

(20) Verploegh, R. J.; Kulkarni, A.; Boulfelfel, S. E.; Haydak, J. C.; Tang, D.; Sholl, D. S. Screening Diffusion of Small Molecules in Flexible Zeolitic Imidazolate Frameworks Using a DFT-Parameterized Force Field. *J. Phys. Chem. C* **2019**, *123* (14), 9153–9167.

(21) Kästner, J. Umbrella Sampling. *Wiley Interdiscip. Rev. Comput. Mol. Sci.* **2011**, *1* (6), 932–942.

(22) White, G. W. N.; Goldman, S.; Gray, C. G.; White, G. W. N.; Gray, C. G. Test of Rate Theory Transmission Coefficient Algorithms. An Application to Ion Channels

Test of Rate Theory Transmission Coefficient Algorithms. An Application to Ion Channels. *Mol. Phys.* **2000**, *98* (22), 1871–1885.

(23) Dubbeldam, D.; Beerdsen, E.; Calero, S.; Smit, B. Dynamically Corrected Transition State Theory Calculations of Self-Diffusion in Anisotropic Nanoporous Materials. *J. Phys. Chem. B* **2006**, *110* (7), 3164–3172.

(24) Sholl, D. S.; Skodje, R. T. Diffusion of Xenon on a Platinum Surface: The Influence of Correlated Flights. *Phys. D Nonlinear Phenom.* **1994**, *71* (1–2), 168–184.

(25) Sholl, D. S.; Fichthorn, K. A. Effect of Correlated Flights on Particle Mobilities during Single-File Diffusion. *Phys. Rev. E - Stat. Physics, Plasmas, Fluids, Relat. Interdiscip. Top.* **1997**, *55* (6), 7753–7756.

(26) Braun, O.; Sholl, C. Diffusion in Generalized Lattice-Gas Models. *Phys. Rev. B - Condens. Matter Mater. Phys.* **1998**, *58* (22), 14870–14879.

(27) Groom, C. R.; Bruno, I. J.; Lightfoot, M. P.; Ward, S. C. The Cambridge Structural Database. *Acta Cryst.* **2016**, *B72*, 171–179.

(28) Moghadam, P. Z.; Li, A.; Wiggin, S. B.; Tao, A.; Maloney, A. G. P.; Wood, P. A.; Ward, S. C.; Fairen-Jimenez, D. Development of a Cambridge Structural Database Subset: A Collection of Metal-Organic Frameworks for Past, Present, and Future. *Chem. Mater.* **2017**, *29* (7), 2618–2625.

(29) Haldoupis, E.; Watanabe, T.; Nair, S.; Sholl, D. S. Quantifying Large Effects of Framework Flexibility on Diffusion in MOFs: CH_4 and CO_2 in ZIF-8. *ChemPhysChem* **2012**, *13* (15), 3449–3452.

(30) Camp, J. S.; Sholl, D. S. Transition State Theory Methods to Measure Diffusion in Flexible Nanoporous Materials: Application to a Porous Organic Cage Crystal. *J. Phys. Chem. C* **2016**, *120* (2), 1110–1120.

(31) Zhang, L.; Hu, Z.; Jiang, J. Sorption-Induced Structural Transition of Zeolitic Imidazolate Framework-8: A Hybrid Molecular Simulation Study. *J. Am. Chem. Soc.* **2013**, *135* (9), 3722–3728.

(32) Yot, P. G.; Ma, Q.; Haines, J.; Yang, Q.; Ghoufi, A.; Devic, T.; Serre, C.; Dmitriev, V.; Férey, G.; Zhong, C.; et al. Large Breathing of the MOF MIL-47(V^{IV}) under Mechanical Pressure: A Joint Experimental-Modelling Exploration. *Chem. Sci.* **2012**, *3* (4), 1100–1104.

(33) Zhao, L.; Yang, Q.; Ma, Q.; Zhong, C.; Mi, J.; Liu, D. A Force Field for Dynamic Cu-BTC Metal-Organic Framework. *J. Mol. Model.* **2011**, *17* (2), 227–234.

(34) Wu, D.; Maurin, G.; Yang, Q.; Serre, C.; Jobic, H.; Zhong, C. Computational Exploration of a Zr-Carboxylate Based Metal-Organic Framework as a Membrane Material for CO2 Capture. *J. Mater. Chem. A* **2014**, *2* (6), 1657–1661.

(35) Dauber-Osguthorpe, P.; Roberts, V. A.; Osguthorpe, D. J.; Wolff, J.; Genest, M.; Hagler, A. T. Structure and Energetics of Ligand Binding to Proteins: Escherichia Coli Dihydrofolate Reductase-Trimethoprim, A Drug Receptor System. *Proteins* **1988**, *47*, 31–47.

(36) Rappé, A. K.; Casewit, C. J.; Colwell, K. S.; Goddard, W. A.; Skiff, W. M. UFF, a Full Periodic Table Force Field for Molecular Mechanics and Molecular Dynamics Simulations. *J. Am. Chem. Soc.* **1992**, *114* (25), 10024–10035.

(37) Martin, M. G.; Siepmann, J. I. Transferable Potentials for Phase Equilibria. 1. United-Atom Description of n-Alkanes. *J. Phys. Chem. B* **1998**, *102*, 2569–2577.

(38) Rappe, A. K.; Goddard, W. A. Charge Equilibration for Molecular Dynamics Simulations. *J. Phys. Chem* **1991**, *95*, 3358–3363.

(39) Sholl, D. S.; Lively, R. P. Defects in Metal-Organic Frameworks: Challenge or Opportunity? *J. Phys. Chem. Lett.* **2015**, *6* (17), 3437–3444.

(40) Plimpton, S. Fast Parallel Algorithms for Short–Range Molecular Dynamics. *J. Comput. Phys.* **1995**, *117*, 1–19.

(41) Fiorin, G.; Klein, M. L.; Hénin, J. Using Collective Variables to Drive Molecular Dynamics Simulations. *Mol. Phys.* **2013**, *111* (22–23), 3345–3362.

(42) Grossfield, A. WHAM: the Weighted Histogram Analysis Method, version 2.0.9.

(43) Salles, F.; Jobic, H.; Devic, T.; Guillerm, V.; Serre, C.; Koza, M. M.; Ferey, G.; Maurin, G. Diffusion of Binary CO_2/CH_4 Mixtures in the MIL-47(V) and MIL-53(Cr) Metal-Organic Framework Type Solids: A Combination of Neutron Scattering Measurements and Molecular Dynamics Simulations. *J. Phys. Chem. C* **2013**, *117* (21), 11275–11284.

(44) Ghoufi, A.; Maurin, G. Single-File Diffusion of Neo-Pentane Confined in the MIL-47(V) Metal–Organic Framework. *J. Phys. Chem. C* **2019**, *123* (28), 17360–17367.

(45) Skoulidas, A. I.; Sholl, D. S. Transport Diffusivities of CH_4, CF_4, He, Ne, Ar, Xe, and SF_6 in Silicalite from Atomistic Simulations. *J. Phys. Chem. B* **2002**, *106* (19), 5058–5067.

(46) Sing, K. S. W.; Williams, R. T. The Use of Molecular Probes for the Characterization of Nanoporous Adsorbents. *Part. Part. Syst. Charact.* **2004**, *21* (2), 71–79.

(47) Alaerts, L.; Christine, E. A. K.; Maes, M.; Van dar veen, M. A.; Finsy, V.; Depla, A.; Martens, J. A.; Baron, G. V.; Jacobs, P. A.; Denayer, J. F. M.; et al. Selective Adsorption and Separation of Xylene Isomers and Ethylbenzene with the Microporous Vanadium(IV) Terephthalate MIL-47. *Angew. Chemie - Int. Ed.* **2007**, *46*, 4293–4297.

(48) Duerinck, T.; Bueno-Perez, R.; Vermoortele, F.; De Vos, D. E.; Calero, S.; Baron, G. V.; Denayer, J. F. M. Understanding Hydrocarbon Adsorption in the Uio-66 Metal-Organic Framework: Separation of (Un)Saturated Linear, Branched, Cyclic Adsorbates, Including Stereoisomers. *J. Phys. Chem. C* **2013**, *117* (24), 12567–12578.

(49) Wong-Ng, W.; Kaduk, J. A.; Siderius, D. L.; Allen, A. L.; Espinal, L.; Boyerinas, B. M.; Levin, I.; Suchomel, M. R.; Ilavsky, J.; Li, L.; et al. Reference Diffraction Patterns, Microstructure, and Pore-Size Distribution for the Copper (II) Benzene-1,3,5-Tricarboxylate Metal Organic Framework (Cu-BTC) Compounds. *Powder Diffr.* **2015**, *30* (1), 2–13.

(50) Ranjan, R.; Tsapatsis, M. Microporous Metal Organic Framework Membrane on Porous Support Using the Seeded Growth Method. *Chem. Mater.* **2009**, *21* (20), 4920–4924.

(51) Willems, T. F.; Rycroft, C. H.; Kazi, M.; Meza, J. C.; Haranczyk, M. Algorithms and Tools for High-Throughput Geometry- Based Analysis of Crystalline Porous Materials. *Microporous Mesoporous Mater.* **2012**, *149*, 134–141.

CHAPTER 6. ASSESSING THE FREQUENCY OF REPLICATE MATERIALS SYNTHESIS BY LITERATURE META-ANALYSIS[e]

6.1 Introduction

Replicability is a core concept in the scientific method. At a fundamental level, accepting an experimentally-derived observation as factual implies that carefully repeating the experiments under the same conditions would yield the same outcome. From an applied point of view, developing a new material for a practical application cannot occur unless the material's properties are routinely repeatable. Systematic studies in fields including social psychology and biomedicine have raised concerns about repeatability of published studies.[1–5]

Although recommendations for improving repeatability in research have been developed[6–9], it is not clear if they apply in a simple way to all fields. Before attempting to form recommendations appropriate for materials chemistry, or to decide if they are even needed, it is valuable to gather quantitative data related to experimental replicability. Mark Twain reputedly said "Everyone talks about the weather, but no-one does anything about it." The situation for repeatability in materials chemistry may be similar. Any experienced investigator can share "war stories" of days (or weeks or more) spent in futile efforts to repeat reported experiments. Moving beyond this anecdotal level, however, requires a more systematic approach.

[e] The data for this chapter was collected with help from Dr. Rebecca Han in Dr. Sholl's research group as well as undergraduate researchers Dinushka Herath at the Georgia Institute of Technology

The most powerful way to examine repeatability is to systematically repeat experiments.[7,10] An obvious disadvantage of this approach is that is requires substantial resources. A less obvious disadvantage is that reporting results that contradict an earlier study is fraught with challenges. An alternative is to find repeated experiments that have already been performed via literature meta-analysis. In areas of great topical interest, it is not unusual for multiple investigators to study the same or similar materials, even though none of these efforts are performed specifically to study repeatability.

Park et al.[11] used literature meta-analysis to assess repeatability of CO_2 adsorption in metal-organic frameworks (MOFs). This work was only possible because of extensive work at NIST to exhaustively collate reported adsorption isotherms from the open literature.[12] Although thousands of papers related to CO_2 adsorption exist, Park et al.[11] only found a small number of isotherms for which multiple independent experiments have been reported. Among all isotherms of this kind, ~20% were identified as outliers, that is, as inconsistent with other available measurements.

Focusing literature meta-analysis on a highly specific property (e.g. CO_2 uptake) may underestimate what can be learned from published data about how repeatable synthesis of a material is. It is possible, for example, that a series of reports of different but related properties of a single material give useful information regarding the material's reproducibility. This observation motivates the key question addressed in this chapter: after a new material or molecule is synthesized for the first time, how often is the synthesis repeated? Below, we describe a simple power law model for the distribution of repeat syntheses of materials, then compare this model to data from the synthesis of a particular class of materials, MOFs. In addition to studying a large number of example materials from

the literature, we examine the six most widely studied MOFs to comment on the replicability of their material properties.

6.2 A Power Law Model for Repeat Synthesis of Materials

For a well-defined class of materials or chemicals, we define $\theta(n)$ as the fraction of materials whose synthesis has been independently reported exactly *n* times. We hypothesize that this quantity follows a power law:

$$\theta(n) = fn^{-\alpha} \qquad (6.1)$$

Power laws have been found to describe a wide range of phenomena, including the word distributions in many languages, the size of cities, wealth distributions and the number of citations received by academic papers.[13] Eq. (6.1) is a hypothesis, not a result we are attempting to derive or infer from prior reasoning. An interesting property of Eq. (6.1) is that it has only one free parameter because it must satisfy the normalization condition

$$\sum_{n=1}^{\infty} \theta(n) = 1 \qquad (6.2)$$

This implies that $\zeta(\alpha) = 1/f$, where ζ is the Riemann zeta function. Thus, if *f* is estimated or measured, the power law in Eq. (6.1) is fully specified. This is helpful because *f* has a simple physical interpretation: it is the fraction of materials than have been synthesized exactly once. Said differently, *f* is the fraction of materials that have been reported but have never been synthesized again. To give an example of the connection between *f* and α in Eq. (6.1), if *f* = 0.5 (i.e. 50% of materials are only synthesized once),

then α = 1.729 and Eq. (6.1) implies that the probability that a randomly chosen material has been synthesized in 5 independent reports is 0.031.

Using the parameter *f* in Eq. (6.1) focuses attention on materials that have only been synthesized once. There are multiple reasons that synthesis of a material might not be repeated in later reports. At one extreme, it may be that repeat syntheses have been attempted but have failed and that these experiments have not been reported. Another situation that is perhaps more common is that no-one has attempted a repeat synthesis because the first report indicated the material is not "useful" for some reason or simply because of lack of interest. Whatever the root cause, if a material has only been synthesized once then no conclusions can be drawn about the repeatability of any of the material's properties.

Another quantity of interest is the number of times that the most repeated material has been synthesized, which we denote $N_{\max}$. Assuming that only one material has been synthesized $N_{\max}$ times, Eq. (6.1) gives a simple expression for the total number of materials, N_{total}:

$$N_{total} = N_{\max}^{\alpha} / f \qquad (6.3)$$

For example, if *f* = 0.5 and the most popular material has been synthesized 100 times then the power law predicts that the total number of materials in the group described by the power law is 5741.

Testing whether an observed data set can be described by a power law is a nontrivial issue. We use the principled statistical framework recommended by Clauset et al.[13], which uses a Kolmogorov-Smirnov (KS) test to quantify the distance between cumulative distributions of empirical data and a power-law model. In this approach, a power law is fitted to the observed experimental data and then a large number of synthetic datasets corresponding to this power law are generated. The distance, *D*, between a datasets and a power law model is defined by

$$D = \max_{1 \le i \le N} (F^*(n_i) - S(n_i)) \qquad (6.4)$$

where $F^*(n)$ is the cumulative value of the fitted power-law and $S(n)$ is the cumulative value of an empirical dataset. Before *D* is calculated for any synthetic dataset, a power-law model is fitted to that dataset. The KS statistic is calculated for each dataset relative to its own model. In this way the same calculations are performed for each synthetic dataset as for experimental data. The p-value of the power law is defined as the fraction of synthetic data sets that *D* larger than the experimental data. Clauset et al.[13] recommended that the hypothesis of a power-law distribution be rejected if the p-value is less than 0.1.

6.3 Assessing Repeat Synthesis of MOFs Using Literature Meta-Analysis

To determine if Eq. (6.1) has any validity, we studied the synthesis of MOFs. MOFs have several characteristics that are typical of topical areas in materials chemistry: thousands or tens of thousands of distinct materials can be made[14,15], their physical properties create potential applications in multiple different areas, and the potential of creating intellectual property and academic prestige creates strong incentives to introduce new materials. Intense interest in these materials has led to thousands of publications,

dedicated conferences and so on. Because MOFs are crystalline, the concept of synthesizing a new material can be concisely defined as reporting the crystal structure of a previously unknown material. Crucially for our purposes, systematic efforts have been made to catalog the MOFs that have been reported.[14,15] We focused on materials from the CoRE MOF database[15], a collection of >4700 crystal structures from experimental reports.

For this study, we selected 130 materials (~2.7% of the total) from the CoRE MOF database as listed in **Table 6.A.1**. To select these MOFs, we first listed all materials that were first published between 2007 and 2013 and excluded examples in which the original report described more than one CoRE MOF structure. This choice simplified the following literature meta-analysis. The 130 MOFs we analyze below were randomly selected from the resulting list. In cases where the original paper identified an isoreticular family of structures but only a single material was entered into the CoRE MOF database, we looked for citations that re-synthesized any variant reported by the original paper. Restricting our choice to materials reported before 2014 means that opportunities to resynthesize each material have existed for at least 5 years. We examined every paper listed by Google Scholar as citing one of the original reports. Citation statistics for these papers are shown in **Error! Reference source not found.**. The original papers had been cited between 8 and 168 times, with an average of 34 citations. The correlation coefficient between the year of publication and the number of citations for these papers is 0.027, so these two quantities are not correlated (see **Figure 6.A.1**).

Some of the citing papers we examined described synthesis of variations of the original materials, for example, with different metal centers or different linkers. Here, however, we focus on direct replication in which the original and later syntheses produced

the same material. We did not attempt to assess whether any of these syntheses were "successful" or "correct": if a paper states that a specific material was synthesized then we counted this synthesis in our analysis. In addition to counting repeat syntheses, it is interesting to consider who reports each repeat synthesis. If a citing paper and the original paper included one or more common authors, we labeled a repeat synthesis as coming from the original research group.

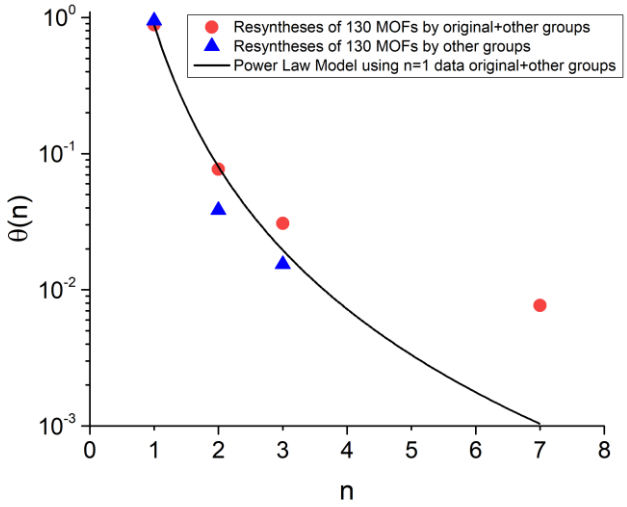

Figure 6.1: Fraction of MOFs whose synthesis has been reported exactly *n* times among the group of 130 MOFs described in the text. Blue (red) symbols show results for all reports (results when only re-synthesis by authors distinct from the original paper are counted). The solid curve shows the power law described in the text with $f = 0.8846$.

The repeat syntheses of the 130 MOFs we considered is described in **Table 6.A.1**. Only one material was synthesized more than 3 times: a Zn-based MOF first produced by An et al. with structure code SAPBIW[16] (common name: Bio-MOF-100) has been synthesized 7 times, including two instances by groups distinct from the original authors. 7 of the 130 MOFs have been re-synthesized by a group distinct from the original authors, and 15 of the MOFs have been synthesized (and reported) more than once by anyone. In

the notation above, f = 115/130 = 0.8846, so if Eq. (6.1) applies then $\alpha = 3.46$. Among the four original papers that have received the most citations (corresponding to the materials SAPBIW,[16] MUVJIX,[17] XUNGUJ[18] and IJOMOJ06[19]), three materials have been synthesized more than once but in one case we did not find any reports of repeat synthesis.

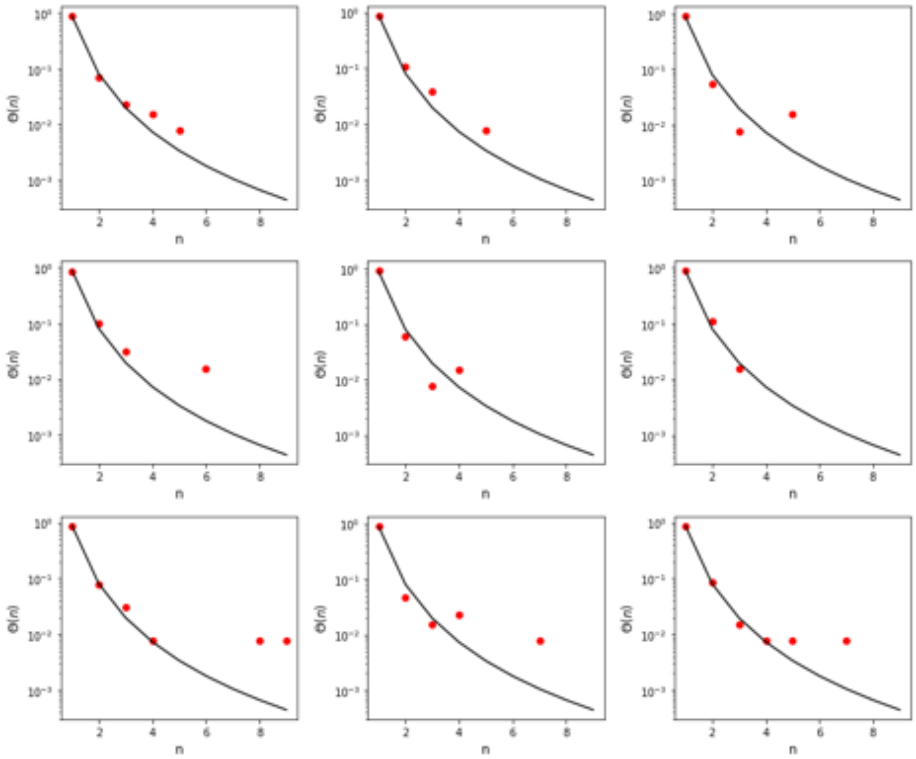

Figure 6.2: An ensemble of 9 examples of synthetic data generated using the fitted power law. The black line shows the power law from which these datasets are generated.

Figure 6.1 compares the power law with f = 0.8846 to the data from our literature meta-analysis. There is some discrepancy between the model and the data for n = 7, but because our data came from 130 materials, accurately resolving values of $\theta(n) < 0.01$ is difficult. To support this argument, **Figure 6.2** shows an ensemble of 9 synthetic datasets generated from the power-law shown in **Figure 6.1** compared with the model. We performed a goodness-of-fit test with the KS statistic using 1000 such synthetic datasets

generated from the power law. This gave a p-value of 0.82, considerably higher than the threshold of 0.1 suggested by Clauset et al.[13] Using 10,000 synthetic data sets gave a p-value of 0.81. A statistical test of this kind cannot prove that the underlying data comes from a power law, but we can conclude that the observed data is not inconsistent with power law behavior.

If only repeat syntheses by groups distinct from the original authors are considered, a power a power law with $f = 0.9461$ and $\alpha = 4.45$. Only two of the 130 materials we examined had been resynthesized more than once by this metric (see

Table 6.A.4). We are not arguing that repeat synthesis by the original authors should be devalued; reports of this kind are surely valuable. Nevertheless, looking at our data in this way highlights the low frequency with which materials synthesis has been repeated by investigators separate from those involved in the original discovery of a material.

The discussion above focuses on direct replicates, that is, work that reports the synthesis synthesis of exactly the same material as a previous report. We also found many examples of modified synthesis in which a new material is made based upon a previously reported material. We examined all papers that cited the original reports of the 130 materials and defined each paper as reporting a modified synthesis if a crystal structure with a different stoichiometry than the original materials or a crystal polymorph was synthesized but no data was given describing (re)synthesis of the original material. Each paper was classified as either replicating the original material or reporting a modified synthesis of a new

material or neither of these options. The numbers of modified syntheses for all 130 materials are given in **Table 6.A.1** and

Table 6.A.5. The prevalence of modified synthesis is very different from direct replication; for 65% of the 130 MOFs we studied modified synthesis was reported at least once. Moreover, 51% of the materials have been synthesized with modifications at least once by a research group distinct from the authors of the original report. It seems likely that in many studies that created a modified material the authors also repeated the synthesis of an original material as part of their work. If this supposition is correct, there are many replications of MOF synthesis that have been performed in laboratories around the world but not reported in the literature. This points to an simple idea that would greatly enhance the materials chemistry community's ability to assess (and enhance) data reproducibility: when an experiment from a previous report is repeated, the outcome should be reported even when this replication was a precursor to the main aim of work that being published.

6.4 Replicability of most synthesized MOFs in the literature

A sensible objection to the analysis above is that the random sampling of materials used above is unlikely to include any of the small number of MOFs that have received the most attention. We used other methods to identify these materials. Specifically, we ranked materials by their frequency of appearance in the NIST Adsorption Database[12], by the frequency of their mention in the abstracts of a recent international conference dedicated to MOFs, and by the number of citations received by the original literature report for each MOF in common between these two rankings (see **Table 6.A.6**). These three approaches gave consistent results, and we selected UiO-66(Zr)[20], ZIF-8(Zn)[21], HKUST-1(Cu)[22] (also

known as Cu-BTC or MOF-199), MIL-101(Cr)[23], IRMOF-1(Zn)[24] (also known as MOF-5) and MOF-177(Zn)[25] for further analysis. For each of these materials, 500 papers that cited the original synthesis report were randomly selected from all citing papers. These 3000 papers were examined in the same way as described above for the materials selected from the CoRE MOF database. The total number of repeat syntheses that have been reported was estimated by scaling the number of replicates found among these 500 reports by the total number of citations a material had received (see **Table 6.A.7**). With this approach, we estimate that the number of times the synthesis of these materials has been reported in the literature varies from 61 (MOF-177) to almost 1000 (Cu-BTC) and that four of the materials (Cu-BTC, UiO-66, ZIF-8, and MIL-101(Cr)) have been synthesized in more than 700 reports.

The existence of MOFs that have been replicated hundreds of times is inconsistent with the power law shown in **Figure 6.1** being valid for large values of *n*. We noted above that Eq. (6.1) immediately predicts the total number of different materials that have been synthesized, N_{total}, if the number of reported syntheses for the most replicated material, N_{max}, is known. If we take N_{max} to be 1000 (the value estimated for Cu-BTC to one significant digit), the power law implies that $N_{total} = 2.7\times10^{10}$. Even using a much lower estimate of $N_{max} = 100$, which is lower than the estimated values for five of the six materials in **Table 6.A.7**, gives $N_{total} = 9.4\times10^{6}$. The CoRE MOF database and related collections of MOF materials[14,15] clearly demonstrate that tens of thousands of distinct MOFs have been made, but not even the most optimistic proponents of the versatility of these materials would claim that millions or billions of different materials have been made. For

comparison, it has been estimated that worldwide, around 6×10^5 new chemical species per year are reported.[26]

Anecdotal descriptions of power law distributions often invoke the Pareto effect (also known as the 80/20 rule or the Matthew effect). In the context of Eq. (6.1), these effects would predict that a small handful of materials would receive a significant majority of all replications. The analysis in **Table 6.A.7**, however, indicates a more extreme situation in which a very small number of materials account for almost all reported replications. If we assume that the actual value of N_{total} for MOFs is 20,000, a reasonable estimate based on efforts to catalog these materials[14,15], and that Eq. (6.1) is only valid for n = 1-10, then Eq. (6.1) predicts that there are ~3600 reported replicate syntheses. Our independent estimates for the six most studied materials in **Table 6.A.7** indicate that ~3600 replicate syntheses of these materials alone have been reported. With these estimates, 0.03% of known MOFs account for ~50% of all replications that have been reported.

The discussion above leads to our tentative conclusion regarding the frequency with which the synthesis of MOFs has been replicated and reported: for most materials this frequency approximately follows a power law, but a small number of "supermaterials" exist that have been replicated many times more than most materials. It would be interesting to know whether similar observations apply to other classes of materials. The description we have just given seems consistent with common perceptions of how research in the materials chemistry community is pursued, but without quantitative analysis of other materials classes extending our conclusions to all materials would be speculative.

It is natural to ask what factors lead to a new material becoming what we have described as a "supermaterial". We cannot offer a definitive answer, and it is likely that issues of timing and the sociology of scientific culture are important. Nevertheless, looking at common factors among the six materials listed in **Table 6.A.7** is interesting. All of these materials can be synthesized using chemicals that are readily available commercially, and all but one (MOF-177), involve only chemicals that are cheap. This suggests that at least in the MOF research community, materials in which chemical synthesis of component chemicals is required before materials synthesis from these components are unlikely to be supermaterials. Our list indicates that it is not necessary to work at an institution at the top of international prestige rankings to discover a supermaterial; most of the materials in **Table 6.A.7** came from institutions that are not "household names" outside their local setting.

All of the results above have examined whether replicate syntheses of MOFs exist but not what can be deduced about reproducibility from these replicates. For the materials shown in **Figure 6.1** it is challenging to discuss reproducibility because the small number of replicates that have been reported did not always report the same quantitative properties as the original synthesis report.[27] Among the materials listed in **Table 6.A.7**, however, there are many replicate measurements of MOF surface areas, a quantity that can readily compared between experiments. We focus below on the BET surface area, since well-established protocols exist for measuring and interpreting the data for this quantity.[28] The BET surface area is strongly correlated with the pore volume, another commonly reported property (see **Figure 6.A.2**). **Figure 6.3** shows the reported BET surface areas for the six MOFs listed above. Among the 528 replicate syntheses listed in **Table 6.A.7**, 355 reported

BET surface areas. The figure also shows the surface area predicted computationally using a defect-free crystal structure using the Zeo++ software with a probe radius size of 1.8 Å to represent N_2 adsorption.[29]

In **Figure 6.3**, HKUST-1 and IRMOF-1 show bimodal distributions of surface area observations. These materials are known to be highly sensitive to moisture[30], so it is likely that this variation is related to differences in materials handling and history among the replicate experiments. UiO-66, ZIF-8 and MIL-101(Cr) are known to be relatively stable towards moisture[30] and they show less variation in surface area among replicates. It is notable that for each material there are examples for which the surface area is much smaller than the theoretical value and examples for which the surface area is larger. In addition to materials degradation, incomplete removal of solvent from materials can lead to reduced surface areas.[31,32] The presence of local defects in MOFs can lead to higher surface areas than in an ideal.[33–36] It is therefore not surprising that each material in **Figure 6.3** shows a range of observed surface areas. This data suggests, however, that there are systematic variations in the materials properties among many replicate syntheses of these materials, implying that efforts to understand the phenomena that lead to these variations and more precisely describe the materials that are made would be useful. Careful comparison of the precise synthesis conditions and experimental details among many replicates would be helpful to begin to address these issues, but this is beyond the scope of our current work.

Because activation of MOFs can be a non-trivial issue,[37,38] it is conceivable that measured surface areas might improve over time as techniques for activating specific materials are improved. To see if there is evidence for this effect, we show in **Figure 6.4** the observed surface areas for each material as a function of years elapsed since their

original synthesis. The same data using the actual date of each report of synthesis is shown in **Figure 6.A.3**. These data offers no support for the idea that the measured surface areas systematically improve over time during many replicate measurements. An caveat in considering this data is that unlike efforts to make high precision measurements of physical constants,[38] the measurement of surface area in the majority of these reports is not the central aim of the work, instead it is a characterization technique used in support of some other scientific goal.

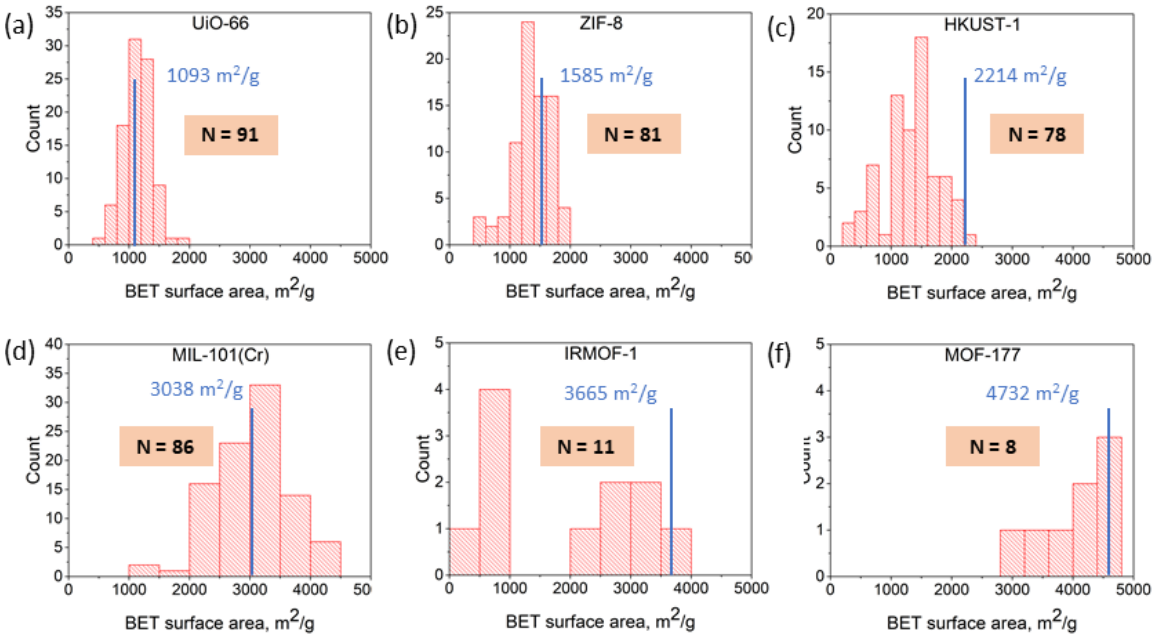

Figure 6.3: Histograms of experimentally reported BET surface areas for (a) UiO-66, (b) ZIF-8, (c) HKUST-1, (d) MIL-101(Cr), (e) IRMOF-1 and (f) MOF-177. The number of reported surface areas (N) for each material is indicated in each figure. Blue text and vertical lines shows the calculated theoretical values from defect-free and solvent-free crystal structures.

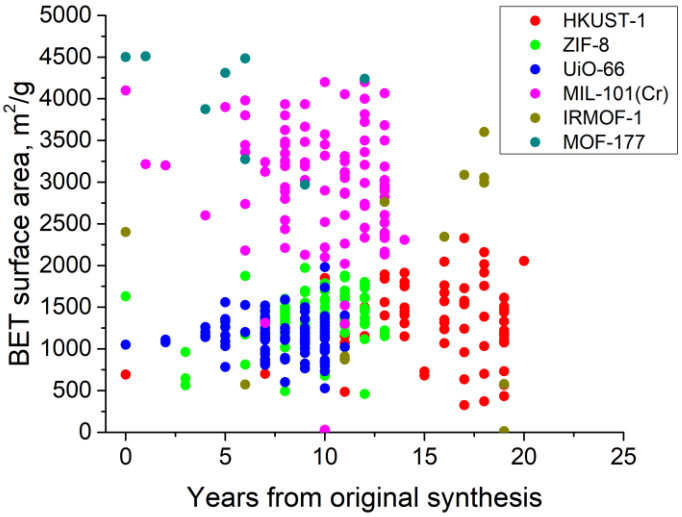

Figure 6.4: Variation in BET surface areas of resynthesized MOFs from the year of their original synthesis

6.5 Summary

We have collected data on how often the synthesis of new materials is replicated by analyzing the > 4,300 papers that cite the original reports of 130 MOFs that were first made between 2007 and 2013. Among these materials, less than 12% have been replicated in a published report, and less than 6% have been replicated by a group of authors distinct from those of the original paper. The synthesis of one of these materials has been reported more than three times; for every other material less information than this is available in published reports. We showed that that the frequency of replications for these 130 materials can be described with a simple power law model. This power law model, however, does not appear to describe the most frequently replicated MOFs in the literature. We identified six MOFs that could be described as "supermaterials" in the sense that they have been far more frequently than a power law model would predict. The synthesis of these materials has been replicated hundreds of times, an observation that creates opportunities to consider

factors underlying experimental reproducibility and variability that cannot be assessed for materials that have only been synthesized a few times.

Although replicate syntheses have been reported for only a small fraction of the 130 materials we studied, we found many instances where later work produced modified versions of these materials. These modified materials have a different chemical composition or crystal structure from the original material. For 65% of the 130 materials, a modified synthesis has been reported without any information being provided about replicate synthesis of the original material. It may be that in many of these studies, a replicate synthesis of the original material was performed but the authors chose not to report the results. If this is correct, this practice means that many opportunities for the scientific community to learn about the repeatability of materials synthesis are being missed.

Our study focused on MOFs, in part because the existence of curated libraries of these materials made it possible to select materials to analyze in an unbiased way. We do not know of any similar analysis for other classes of materials, so any discussion of how directly our findings will extend to other materials is speculative. Our methods, however, could readily be applied to other areas within materials chemistry. We hope that the work described here motivates future efforts of this kind.

APPENDIX 6.A. SUPPORTING INFORMATION FOR CHAPTER 6

Table 6.A.1: Year of publication, reference code, number of citations, number of exact syntheses by same and new authors, and number of modified syntheses by same and new authors, of all 130 materials from CoRE MOF database

Year	CSD Code	Citations	Exact, new authors	Exact, same authors	Modified, new authors	Modified, same authors
2007	CETGOY[39]	49	0	0	0	0
2007	DIXHIC[40]	15	0	0	0	0
2007	GIQZIQ[41]	21	0	0	1	1
2007	HEXNII[42]	20	0	0	1	2
2007	HOMZEP[43]	54	0	0	0	4
2007	IJOMOJ06[19]	77	0	0	7	10
2007	KIFJIT[44]	32	0	0	0	0
2007	PIKBUH[45]	27	0	0	0	0
2007	RIPTAM[46]	26	0	0	0	0
2007	SINXET[47]	19	0	0	0	0
2007	TICPOL[48]	19	0	0	0	1
2007	TIRLIQ[49]	17	0	0	0	0
2007	TISGUY[50]	48	0	0	1	0
2007	TIVYAZ01[51]	41	0	0	1	1
2007	XUBJAF02[52]	8	1	0	0	0
2008	AFOYOK[53]	53	0	0	4	2
2008	COMFAM[54]	32	0	0	0	1
2008	GOGSIF[55]	13	0	0	4	1
2008	KOLWEO[56]	52	0	0	0	0
2008	KONCIA[57]	44	0	0	0	1
2008	LOPZAS[58]	24	0	0	0	0
2008	MOGNAY[59]	14	0	0	0	1
2008	NOHFOG[60]	31	0	0	2	1
2008	RIWSUM[61]	27	0	0	0	0
2008	SODZIV[62]	19	0	0	0	0
2008	TOKDON[63]	44	0	0	0	1
2008	UFOFIF[64]	22	1	0	0	1
2008	WOCJII[65]	21	0	0	4	0
2008	XOJWEZ[66]	47	0	0	0	0
2008	YOMBAE[67]	15	0	0	0	1
2009	COXFOL[68]	29	0	0	0	1
2009	CUGVUW[69]	22	0	0	0	1
2009	GIYSAJ02[70]	47	0	0	0	1
2009	GUKZAO[71]	37	0	0	0	0
2009	LUKLIN[72]	55	0	0	0	5

Table 6.A.1 continued…

2009	MUNPAN[73]	28	0	0	0	0
2009	OHAZAZ[74]	44	0	0	0	5
2009	OHOLIH[75]	15	0	0	0	0
2009	QUFFED[76]	53	0	0	1	3
2009	QUTYOU[77]	42	0	0	1	0
2009	RUCGOM[78]	17	0	0	7	0
2009	UHISOU[79]	49	2	0	1	1
2009	VACFUB01[80]	16	0	0	0	4
2010	CESYEF01[81]	17	0	0	0	1
2010	CURBOH[82]	25	0	0	0	1
2010	DUQSEO[83]	54	0	0	0	3
2010	EKARUE[84]	15	0	0	0	0
2010	GURZID[85]	12	0	0	0	1
2010	ILITUT[86]	46	0	0	0	1
2010	LUPYAX[87]	52	0	0	0	0
2010	MACHIJ[88]	27	0	1	0	0
2010	MUTVUT[89]	40	0	0	0	0
2010	MUVJIX[17]	104	1	0	3	8
2010	NUZCER[90]	43	0	0	0	0
2010	OSOYUR[91]	46	0	0	0	1
2010	OWIZAW[92]	30	0	0	0	0
2010	QUQGAL[93]	46	0	1	1	1
2010	QUQGEP[94]	27	0	0	1	0
2010	RUSSAA[95]	13	0	0	0	2
2010	RUTBUE[96]	16	0	0	4	0
2010	RUVKOJ[97]	14	0	0	1	0
2010	UKUBUY[98]	33	0	0	0	1
2010	VAGKOF[99]	47	0	0	1	0
2010	XUNGUJ[18]	86	1	0	2	5
2010	XUYXAR[100]	32	0	0	1	4
2011	ANEPIT[101]	51	0	0	1	0
2011	AXUBOL[102]	43	0	0	1	5
2011	EBUREA[103]	26	0	0	0	0
2011	EMITUQ[104]	26	0	0	0	0
2011	EPOXAJ[105]	46	0	0	1	2
2011	EZOXEX[106]	23	0	0	0	0
2011	HAWREE[107]	55	0	1	0	2
2011	IBUYAH[108]	22	0	0	1	1
2011	IJEXUR[109]	31	0	0	0	0
2011	IYICUP[110]	20	0	0	2	0
2011	IZUMUM[111]	35	2	0	2	4
2011	NALYEG[112]	28	0	0	1	0
2011	OCIZIL[113]	53	0	0	0	2
2011	OVEXOD[114]	42	0	0	0	1

Table 6.A.1 continued…

2011	OVIWIA[115]	48	0	0	2	1
2011	OXUPUT[116]	26	0	0	4	0
2011	OYUJUO[117]	22	0	0	0	0
2011	PAMHIW[118]	14	0	0	0	2
2011	RAHNOF[119]	54	0	0	1	1
2011	REGYOT[120]	50	0	0	1	2
2011	UBOGAV[121]	46	0	0	6	2
2011	UVEVUN[122]	59	0	0	0	0
2011	UVINAP[123]	45	0	0	0	1
2011	UXUYUI[124]	54	0	0	1	3
2011	UZIJUJ[125]	14	0	0	0	0
2012	ADODAA[126]	45	0	0	0	6
2012	BAXSIE[127]	51	0	0	2	0
2012	FAJYAS[128]	13	0	0	1	2
2012	FAQVEA[129]	34	0	0	1	0
2012	FATLUJ[130]	57	0	0	0	0
2012	GEDLIM[131]	18	1	0	3	0
2012	HARNAR[132]	18	0	0	0	0
2012	HEBJAB[133]	55	0	0	0	3
2012	HEBKEG[134]	28	0	0	1	1
2012	HEKTAU[135]	45	0	0	0	3
2012	KEQJEX[136]	46	0	1	0	2
2012	LASMAV[137]	22	0	0	0	0
2012	LECGIL[138]	29	0	0	0	0
2012	MEFHUC[139]	27	0	0	0	3
2012	NAYXOC[140]	29	2	0	1	2
2012	NEFTOJ[141]	11	0	0	0	3
2012	PEMRIK[142]	64	0	0	0	0
2012	QEGNOH[143]	33	0	1	0	0
2012	SAKNOJ[144]	31	0	0	0	0
2012	SAPBIW[16]	168	5	2	4	5
2012	SESKUY[145]	22	0	0	0	2
2012	VEPDEB[146]	15	0	0	0	0
2012	WIFGOJ[147]	47	0	0	0	0
2012	ZEDZAL[148]	30	0	2	0	5
2013	BETZOR[149]	18	0	0	0	0
2013	DEYLUQ[150]	29	0	0	0	0
2013	DEYNIG[151]	23	0	0	0	0
2013	FEZREJ[152]	15	0	0	0	0
2013	GINDEO[153]	20	0	0	2	0
2013	LELMEW[154]	16	0	0	0	0
2013	NIMWUD[155]	22	0	0	3	0
2013	PETWOC[156]	63	0	0	2	3
2013	QEWDON[157]	23	0	0	1	0

Table 6.A.1 continued…

2013	RIDGIW[158]	37	0	0	0	0
2013	SEQTEP[159]	28	0	0	1	2
2013	SETDUS[160]	18	0	0	0	0
2013	SEVLEM[161]	25	0	0	1	1
2013	VICYUD[162]	20	0	0	0	2
2013	VIDPIJ[163]	20	0	0	0	0
2013	ZETMOC[164]	50	0	0	1	2

Table 6.A.2: Breakdown from 2007 to 2013 of the number of original papers, total number of citations, and average citations per paper for the 130 MOFs investigated (citation analysis was done in January 2019)

Original Publication Year	**Number of Original Papers**	**Total Number of Citations**	**Avg Citations per Paper per Year**
2007	15	473	32
2008	15	458	31
2009	13	454	35
2010	22	825	38
2011	25	933	37
2012	24	938	39
2013	16	427	27

Table 6.A.3: Observations of repeat syntheses of 130 MOFs originally reported from 2007-2013

n	**Repeat synthesis by any group**	**Repeat synthesis by original research group**	**Repeat synthesis by different group(s)**
4+	SAPBIW (n = 7)[16]	SAPBIW (n = 5)[16]	
3	UHISOU[79] IZUMUM[111] NAYXOC[140] ZEDZAL[148]	UHISOU[79] IZUMUM[111] NAYXOC[140]	SAPBIW[16] ZEDZAL[148]
2	MACHIJ[88] QUQGAL[93] HAWREE[107] KEQJEX[136] QEGNOH[143] XUBJAF02[52] UFOFIF[64] MUVJIX[17] XUNGUJ[18] GEDLIM[131]	XUBJAF02[52] UFOFIF[64] MUVJIX[17] XUNGUJ[18] GEDLIM[131]	MACHIJ[88] QUQGAL[93] HAWREE[107] KEQJEX[136] QEGNOH[143]
1	115 MOFs from set in Table S1	121 MOFs from set in Table S1	123 MOFs from set in Table S1

Table 6.A.4: Power-law models for exact repeat syntheses of 130 MOFs

n	**# of MOFs exactly synthesized by any group**	**# of MOFs exactly synthesized by original research group**	**# of MOFs exactly synthesized by different groups**
1	115	121	123
2	10	5	5
3	4	3	2
4+	1 (n=7)	1 (n=5)	0
	f **= 0.8846,** α **= 3.46**	f **= 0.9308,** α **= 4.11**	f **= 0.9461,** α **= 4.45**

Table 6.A.5: Modified syntheses of 130 MOFs

n	# of MOFs modified synthesized by any group	# of MOFs modified synthesized by original research group	# of MOFs modified synthesized by different groups
1	46	64	82
2	27	29	28
3	18	16	8
4+	39	21	12

Table 6.A.6: Most studied MOFs, their frequency in NIST database and the number of citations received by their original literature report

S.No.	MOF	DOI (original paper)	Citations	Frequency in NIST database
1	IRMOF-1 / MOF-5	10.1038/46248	5502	314
2	CuBTC / HKUST-1	10.1126/science.283.5405.1148	4401	334
3	MIL-101	10.1126/science.1116275	3286	85
4	ZIF-8	10.1073/pnas.0602439103	3275	157
5	ZIF-7	10.1073/pnas.0602439103	3275	43
6	ZIF-4	10.1073/pnas.0602439103	3273	2
7	MOF-177	10.1038/nature02311	2516	60
8	UiO-66	10.1021/ja8057953	2420	53
9	Zn-MOF-74	10.1021/ja045123o	1798	26
10	COF-102	10.1126/science.1139915	1376	23
11	MIL-53(Cr)	10.1021/ja0276974	1316	44
12	MCM-41	10.1016/0927-6513(93)80058-3	1200	20
13	NU-100x	10.1038/nchem.834	1124	3
14	[Zn(bdc)(ted)0.5]	10.1002/anie.200460712	1033	8
15	MIL-47	10.1002/1521-3773	861	30
16	PCN-14	10.1021/ja0771639	756	15
17	MIL-100(Cr)	10.1002/ange.200460592	611	15
18	MIL-100(Fe)	10.1039/B704325B	524	25
19	UMCM-1	10.1002/anie.200705020	426	16
20	MOF-74-Ni	10.1039/B515434K	372	24
21	Mg-MOF-74 / CPO-27-Mg	10.1002/ejic.200701284	200	51
22	NU-1000	10.1021/ja4050828	390	3
23	MOF-808	10.1021/ja500330a	710	1
24	MIL-125-NH2	10.1021/ja903726m	510	1

Table 6.A.7: Citation details of six MOFs selected as described in the main text, counts of replicate syntheses and linker costs. Linker costs were obtained from commercial suppliers (e.g. SigmaAldrich).

MOF	Total citations of the original paper[a]	Exact repeated syntheses in 500 randomly selected citations	Total approximated exact syntheses of the MOF	Linker	Commercial Cost	Institute of original synthesis
UiO-66[20]	2535	147	745	BDC	$0.3/g	University of Oslo, Norway
ZIF-8[21]	3356	115	772	Imidazole	$0.25/g	University of California Los Angeles
Cu-BTC[22]	4536	110	998	BTC	$1.2/g	Hong Kong University of Science and Tech
MIL-101(Cr)[23]	3355	118	792	BDC	$0.3/g	Institut Lavoisier, CNRS
IRMOF-1[24]	5661	26	295	BDC	$0.3/g	University of Michigan
MOF-177[25]	2552	12	61	H3BTB	$267/g	University of Michigan

[a]Citation analysis was done in January 2019.

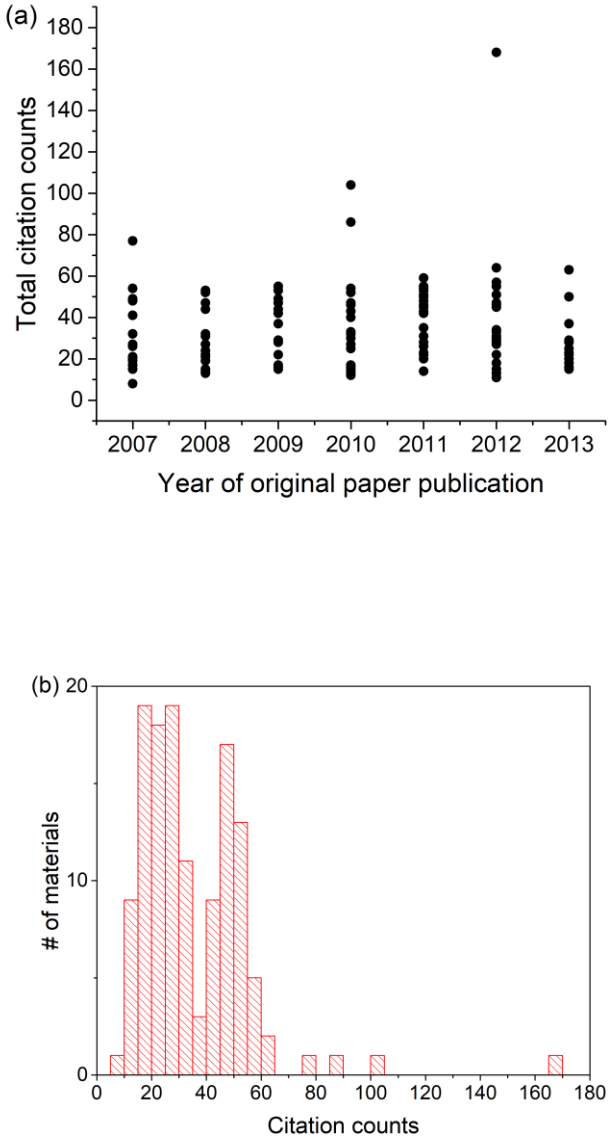

Figure 6.A.1: Citation analysis of all papers performed on Jan 15th 2019 (a) total citations of each paper with the year of publication, (b) histogram of citation counts of all original papers corresponding to synthesis of 130 MOFs from CoRE MOF database

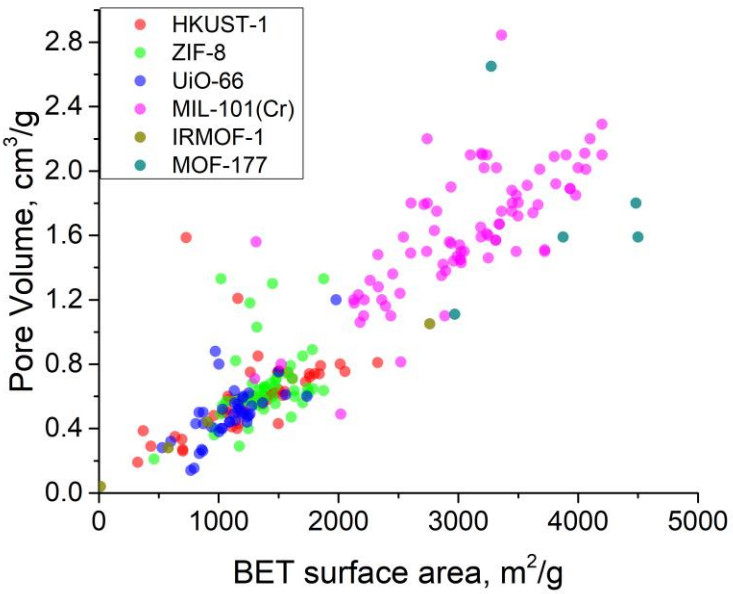

Figure 6.A.2: Correlation between pore volume and BET surface area of syntheses reported in literature for six famous MOFs

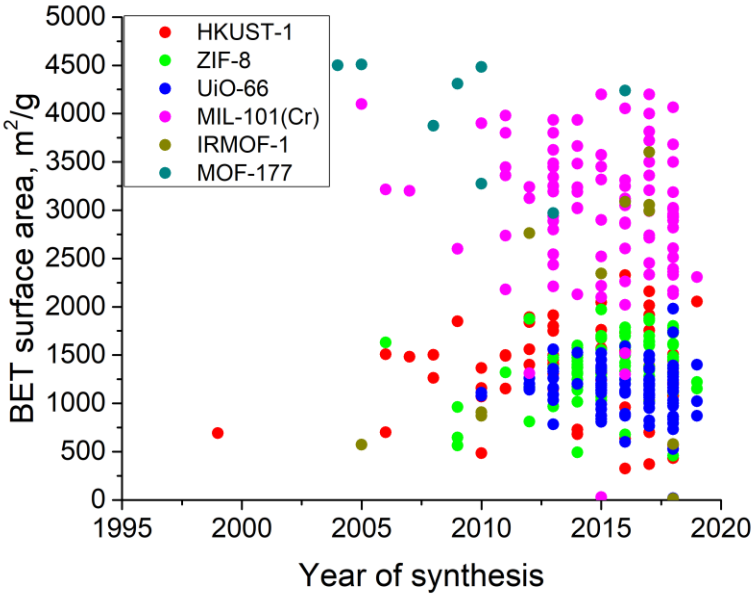

Figure 6.A.3: Variation BET surface area of resynthesized MOFs with the year of synthesis

6.6 References

(1) Prinz, F.; Schlange, T.; Asadullah, K. Believe It or Not: How Much Can We Rely on Published Data on Potential Drug Targets? *Nat. Rev. Drug Discov.* **2011**, *10* (9), 712–713.

(2) Begley, C.; Ellis, L. Drug Development: Raise Standards for Preclinical Cancer Research. *Nature* **2012**, *483*, 531–533.

(3) Klein, R. A.; Ratliff, K. A.; Vianello, M.; Adams, R. B.; Bahník, Š.; Bernstein, M. J.; Bocian, K.; Brandt, M. J.; Brooks, B.; Brumbaugh, C. C.; et al. Investigating Variation in Replicability: A "Many Labs" Replication Project. *Soc. Psychol. Personal. Sci.* **2014**, *45* (3), 142–152.

(4) Garrison, K. E.; Tang, D.; Schmeichel, B. J. Embodying Power: A Preregistered Replication and Extension of the Power Pose Effect. *Soc. Psychol. Personal. Sci.* **2016**, *7*, 623–630.

(5) Ioannidis, J. P. A. Why Most Published Research Findings Are False. *PLoS Med* **2005**, *2* (e124).

(6) Chen, X.; Dallmeier-Tiessen, S.; Dasler, R.; Feger, S.; Fokianos, P.; Gonzalez, J. B.; Hirvonsalo, H.; Kousidis, D.; Lavasa, A.; Mele, S.; et al. Open Is Not Enough. *Nat. Phys.* **2019**, *15* (2), 113–119.

(7) Stark, P. B. No Reproducibility without Preproducibility. *Nature* **2018**, *557* (7707), 613.

(8) Baer, D. R.; Gilmore, I. S. Responding to the Growing Issue of Research Reproducibility. *J. Vac. Sci. Technol. A* **2018**, *36* (6), 068502.

(9) Plant, A. L.; Becker, C. A.; Hanisch, R. J.; Boisvert, R. F.; Possolo, A. M.; Elliott, J. T. How Measurement Science Can Improve Confidence in Research Results. *PLoS Biol.* **2018**, *16* (4), 1–7.

(10) National Academies of Sciences, Engineering, and Medicine, 2019. *Reproducibility and Replicability in Science*; The National Academies Press: Washington DC.

(11) Park, J.; Howe, J. D.; Sholl, D. S. How Reproducible Are Isotherm Measurements in Metal-Organic Frameworks? *Chem. Mater.* **2017**, *29* (24), 10487–10495.

(12) Siderius, D. W.; Shen, V. K.; Johnson III, R. D.; van Zee, R.D., E. NIST/ARPA-E Database of Novel and Emerging Adsorbent Materials. *NIST SRD-205* **2015**.

(13) Clauset, A.; Shalizi, C. R.; Newman, M. E. J. Power-Law Distributions in Empirical Data. *SIAM Rev.* **2009**, *51* (4), 661–703.

(14) Groom, C. R.; Bruno, I. J.; Lightfoot, M. P.; Ward, S. C. The Cambridge Structural Database. *Acta Cryst.* **2016**, *B72*, 171–179.

(15) Chung, Y. G.; Camp, J.; Haranczyk, M.; Sikora, B. J.; Bury, W.; Krungleviciute, V.; Farha, O. K.; Sholl, D. S.; Snurr, R. Q. Computation-Ready, Experimental Metal−Organic Frameworks: A Tool to Enable High-Throughput Screening of Nanoporous Crystals. *Chem. Mater.* **2014**, *26*, 6185–6192.

(16) An, J.; Farha, O. K.; Hupp, J. T.; Pohl, E.; Yeh, J. I.; Rosi, N. L. Metal-Adeninate Vertices for the Construction of an Exceptionally Porous Metal-Organic Framework. *Nat. Commun.* **2012**, *3* (1), 604.

(17) Blake, A. J.; Neil, C. R.; Easum, T. L.; Allan, D. R.; Nowell, H.; George, M. W.; Jia, J.; Sun, X.-Z. Photoreactivity Examined through Incorporation in Metal−organic Frameworks. *Nat. Chem.* **2010**, *2*, 688–694.

(18) Abrahams, B. F.; Grannas, M. J.; Hudson, T. A.; Robson, R. A Simple Lithium(I) Salt with a Microporous Structure and Its Gas Sorption Properties. *Angew. Chemie - Int. Ed.* **2010**, *49* (6), 1087–1089.

(19) Zhang, B.; Wang, Z.; Kurmoo, M.; Gao, S.; Inoue, K.; Kobayashi, H. Guest-Induced Chirality in the Ferrimagnetic Nanoporous Diamond Framework $Mn_3(HCOO)_6$. *Adv. Funct. Mater.* **2007**, *17* (4), 577–584.

(20) Cavka, J. H.; Jakobsen, S.; Olsbye, U.; Guillou, N.; Lamberti, C.; Bordiga, S.; Lillerud, K. P. A New Zirconium Inorganic Building Brick Forming Metal Organic Frameworks with Exceptional Stability. *J. Am. Chem. Soc.* **2008**, *130* (42), 13850–13851.

(21) Park, K. S.; Ni, Z.; Cote, A. P.; Cho, J. Y.; Huang, R.; Uribe-Romo, F. J.; Chae, H. K.; O'Keeffe, M.; Yaghi, O. M. Exceptional Chemical and Thermal Stability of Zeolitic Imidazolate Frameworks. *Proc. Natl. Acad. Sci.* **2006**, *103* (27), 10186–10191.

(22) Chui, S. S. Y.; Lo, S. M. F.; Charmant, J. P. H.; Orpen, A. G.; Williams, I. D. A Chemically Functionalizable Nanoporous Material $[Cu_3(TMA)_2(H_2O)_3]_N$. *Science* **1999**, *283* (5405), 1148–1150.

(23) Férey, C.; Mellot-Draznieks, C.; Serre, C.; Millange, F.; Dutour, J.; Surblé, S.; Margiolaki, I. Chemistry: A Chromium Terephthalate-Based Solid with Unusually Large Pore Volumes and Surface Area. *Science* **2005**, *309* (5743), 2040–2042.

(24) Li, H.; Eddaoudi, M.; O'Keeffe, M.; Yaghi, O. M. Design and Synthesis of an Exceptionally Stable and Highly. *Nature* **1999**, *402*, 276–279.

(25) Chae, H. K.; Siberio-Pérez, D. Y.; Kim, J.; Go, Y.; Eddaoudi, M.; Matzger, A. J.; O'Keeffe, M.; Yaghi, O. M. A Route to High Surface Area, Porosity and Inclusion of Large Molecules in Crystals. *Nature* **2004**, *427* (6974), 523–527.

(26) Llanos, E. J.; Leal, W.; Luu, D. H.; Jost, J.; Stadler, P. F.; Restrepo, G. Exploration of the Chemical Space and Its Three Historical Regimes. *PNAS* **2019**, *116* (26), 12660–12665.

(27) Han, R.; Walton, K. S.; Sholl, D. S. Does Chemical Engineering Research Have a Reproducibility Problem? *Annu. Rev. Chem. Biomol. Eng.* **2019**, *10* (1), 43–57.

(28) Walton, K. S.; Snurr, R. Q. Applicability of the BET Method for Determining Surface Areas of Microporous Metal-Organic Frameworks. *J. Am. Chem. Soc.* **2007**, *129* (27), 8552–8556.

(29) Willems, T. F.; Rycroft, C. H.; Kazi, M.; Meza, J. C.; Haranczyk, M. Algorithms and Tools for High-Throughput Geometry- Based Analysis of Crystalline Porous Materials. *Microporous Mesoporous Mater.* **2012**, *149*, 134–141.

(30) Burtch, N. C.; Jasuja, H.; Walton, K. S. Water Stability and Adsorption in Metal-Organic Frameworks. *Chem. Rev.* **2014**, *114* (20), 10575–10612.

(31) Mondloch, J. E.; Karagiaridi, O.; Farha, O. K.; Hupp, J. T. Activation of Metal-Organic Framework Materials. *CrystEngComm* **2013**, *15* (45), 9258–9264.

(32) Dodson, R. A.; Wong-Foy, A. G.; Matzger, A. J. The Metal-Organic Framework Collapse Continuum: Insights from Two-Dimensional Powder X-Ray Diffraction. *Chem. Mater.* **2018**, *30* (18), 6559–6565.

(33) Fang, Z.; Dürholt, J. P.; Kauer, M.; Zhang, W.; Lochenie, C.; Jee, B.; Albada, B.; Metzler-Nolte, N.; Pöppl, A.; Weber, B.; et al. Structural Complexity in Metal-Organic Frameworks: Simultaneous Modification of Open Metal Sites and Hierarchical Porosity by Systematic Doping with Defective Linkers. *J. Am. Chem. Soc.* **2014**, *136* (27), 9627–9636.

(34) Wu, H.; Chua, Y. S.; Krungleviciute, V.; Tyagi, M.; Chen, P.; Yildirim, T.; Zhou, W. Unusual and Highly Tunable Missing-Linker Defects in Zirconium Metal-Organic Framework UiO-66 and Their Important Effects on Gas Adsorption. *J. Am. Chem. Soc.* **2013**, *135* (28), 10525–10532.

(35) Sholl, D. S.; Lively, R. P. Defects in Metal-Organic Frameworks: Challenge or Opportunity? *J. Phys. Chem. Lett.* **2015**, *6* (17), 3437–3444.

(36) Jiao, Y.; Liu, Y.; Zhu, G.; Hungerford, J. T.; Bhattacharyya, S.; Lively, R. P.; Sholl, D. S.; Walton, K. S. Heat-Treatment of Defective UiO-66 from Modulated Synthesis: Adsorption and Stability Studies. *J. Phys. Chem. C* **2017**, *121* (42), 23471–23479.

(37) Howarth, A. J.; Peters, A. W.; Vermeulen, N. A.; Wang, T. C.; Hupp, J. T.; Farha, O. K. Best Practices for the Synthesis, Activation, and Characterization of Metal−organic Frameworks. *Chem. Mater.* **2017**, *29* (1), 26–39.

(38) Nelson, A. P.; Farha, O. K.; Mulfort, K. L.; Hupp, J. T. Supercritical Processing as a Route to High Internal Surface Areas and Permanent Microporosity in Metal-Organic Framework Materials. *J. Am. Chem. Soc.* **2009**, *131* (2), 458–460.

(39) Chen, Z. F.; Zhang, S. F.; Luo, H. S.; Abrahams, B. F.; Liang, H. $Ni_2(R^*COO)_4(H_2O)(4,4'\text{-Bipy})_2$ - A Robust Homochiral Quartz-like Network with Large Chiral Channels. *CrystEngComm* **2007**, *9* (1), 27–29.

(40) Chang, W. M.; Cheng, M. Y.; Liao, Y. C.; Chang, M. C.; Wang, S. L. Template Effect of Chain-Type Polyamines on Pore Augmentation: Five Open-Framework Zinc Phosphates with 16-Ring Channels. *Chem. Mater.* **2008**, *20* (4), 1660.

(41) Senkovska, I.; Fritsch, J.; Kaskel, S. New Polymorphs of Magnesium-Based Metal-Organic Frameworks $Mg_3(Ndc)_3$ (Ndc = 2,6-Naphthalenedicarboxylate). *Eur. J. Inorg. Chem.* **2007**, *3* (35), 5475–5479.

(42) Cordes, D. B.; Hanton, L. R.; Spicer, M. D. Six-Coordinated Cd(II) Centers as Four- Or Six-Connected Nodes in Coordination Polymer Networks Containing Bis(4-Pyridyl)Amine. *Cryst. Growth Des.* **2007**, *7* (2), 328–336.

(43) Volkringer, C.; Loiseau, T.; Férey, G.; Morais, C. M.; Taulelle, F.; Montouillout, V.; Massiot, D. Synthesis, Crystal Structure and ^{71}Ga Solid State NMR of a MOF-Type Gallium Trimesate (MIL-96) with μ_3-Oxo Bridged Trinuclear Units and a Hexagonal 18-Ring Network. *Microporous Mesoporous Mater.* **2007**, *105* (1–2), 111–117.

(44) Burrows, A. D.; Cassar, K.; Mahon, M. F.; Warren, J. E. The Stepwise Formation of Mixed-Metal Coordination Networks Using Complexes of 3-Cyanoacetylacetonate. *Dalt. Trans.* **2006**, *4* (24), 2499–2509.

(45) Smith, G.; Wermuth, U. D.; Young, D. J.; White, J. M. Polymeric Structures in the Metal Complexes of 5-Sulfosalicylic Acid: The Rubidium(I), Caesium(I) and Lead(II) Analogues. *Polyhedron* **2007**, *26* (14), 3645–3652.

(46) Li, M.; Yuan, L.; Li, H.; Sun, J. A 3D Heterometallic Metal-Organic Framework Constructed from Luminescent Building Blocks, Exhibiting Reversible Dehydration and Rehydration Procedure. *Inorg. Chem. Commun.* **2007**, *10* (11), 1281–1284.

(47) Zhang, H. Y.; Yu, H. J.; Xu, H. X.; Ren, J. S.; Qu, X. G. Structural Diversity of Lanthanide-Amino Acid Complexes under near Physiological PH Conditions and Their Recognition of Single-Stranded DNA. *Polyhedron* **2007**, *26* (18), 5250–5256.

(48) Schull, T. L.; Henley, L.; Deschamps, J. R.; Butcher, R. J.; Maher, D. P.; Klug, C. A.; Swider-Lyons, K.; Dressick, W. J.; Bujoli, B.; Greenwood, A. E.; et al. Organometallic Supramolecular Mixed-Valence Cobalt(I)/Cobalt(II) Aquo Complexes Stabilized with the Water-Soluble Phosphine Ligand p-TPPTP (p-Triphenylphosphine Triphosphonic Acid). *Organometallics* **2007**, *26* (9), 2272–2276.

(49) Luisi, B. S.; Ma, Z.; Moulton, B. Tri-Metal Secondary Building Units: Toward the Design of Thermally Robust Crystalline Coordination Polymers. *J. Chem. Crystallogr.* **2007**, *37* (11), 743–747.

(50) Hu, S.; Zhang, J. P.; Li, H. X.; Tong, M. L.; Chen, X. M.; Kitagawa, S. A Dynamic Microporous Metal-Organic Framework with BCT Zeolite Topology: Construction, Structure, and Adsorption Behavior. *Cryst. Growth Des.* **2007**, *7* (11), 2286–2289.

(51) Luo, F.; Che, Y. X.; Zheng, J. M. A Ternary Metal - Organic Framework Built on Triangular Organic Spacers, Square and Tetrahedral Co_2 Secondary Building Units. *Cryst. Growth Des.* **2008**, *8* (1), 176–178.

(52) Zhang, C. Z.; Mao, H. Y.; Wang, Y. L.; Zhang, H. Y.; Tao, J. C. Syntheses of Two New Hybrid Metal-Organic Polymers Using Flexible Aliphatic Dicarboxylates and Pyrazine: Crystal Structures and Magnetic Studies. *J. Phys. Chem. Solids* **2007**, *68* (2), 236–242.

(53) Bondar, O. A.; Lukashuk, L. V.; Lysenko, A. B.; Krautscheid, H.; Rusanov, E. B.; Chernega, A. N.; Domasevitch, K. V. New Microporous Copper(II) Coordination Polymers Based upon Bifunctional 1,2,4-Triazole/Tetrazolate Bridges. *CrystEngComm* **2008**, *10* (9), 1216–1226.

(54) Han, L.; Zhao, W.; Zhou, Y.; Li, X.; Pan, J. One-Pot Synthesis of Supramolecular Isomers with Two-Dimensional 4^4 Grid and Three-Dimensional $6^4 \cdot 8^2$ NbO Frameworks: Solvothermal in Situ Ligand Formation and Conformational. *Cryst. Growth Des.* **2008**, *8* (10), 3504–3505.

(55) Kiskin, M. A.; Aleksandrov, G. G.; Bogomyakov, A. S.; Novotortsev, V. M.; Eremenko, I. L. Coordination Polymers of Cobalt(II) with Pyrimidine and Pyrazine: Syntheses, Structures and Magnetic Properties. *Inorg. Chem. Commun.* **2008**, *11* (9), 1015–1018.

(56) Heck, R.; Bacsa, J.; Warren, J. E.; Rosseinsky, M. J.; Bradshaw, D. Triply Interpenetrated (3,4)- and (3,5)-Connected Binodal Metal-Organic Networks Prepared from 1,3,5-Benzenetrisbenzoate and 4,4′-Bipyridyl. *CrystEngComm* **2008**, *10* (11), 1687–1692.

(57) Zhang, X. J.; Xing, Y. H.; Han, J.; Zeng, X. Q.; Ge, M. F.; Niu, S. Y. A Series of Novel Ln-Succinate-Oxalate Coordination Polymers: Synthesis, Structure, Thermal Stability, and Fluorescent Properties. *Cryst. Growth Des.* **2008**, *8* (10), 3680–3688.

(58) Liu, Y. J.; Huang, J. S.; Chui, S. S. Y.; Li, C. H.; Zuo, J. L.; Zhu, N.; Che, C. M. A Noncentrosymmetric 3D Coordination Polymer of Metallocalix[4]Arene. *Inorg. Chem.* **2008**, *47* (24), 11514–11518.

(59) Zhou, Y. X.; Shen, X. Q.; Du, C. X.; Wu, B. L.; Zhang, H. Y. 1D, 2D and 3D Coordination Polymers of Aromatic Carboxylate Tb^{III}: Structure, Thermolysis Kinetics and Fluorescence. *Eur. J. Inorg. Chem.* **2008**, *3* (27), 4280–4289.

(60) Kerbellec, N.; Daiguebonne, C.; Bernot, K.; Guillou, O.; Le Guillou, X. New Lanthanide Based Coordination Polymers with High Potential Porosity. *J. Alloys Compd.* **2008**, *451* (1–2), 377–383.

(61) Lee, H. Y.; Park, J.; Lah, M. S.; Hong, J. One-Dimensional Double Helical Structure and 4-Fold Type [2 + 2] Interpenetration of Diamondoid Networks with Helical Fashion. *Cryst. Growth Des.* **2008**, *14*, 2–6.

(62) Lin, Z. J.; Liu, T. F.; Xu, B.; Han, L. W.; Huang, Y. B.; Cao, R. Pore-Size Tuning in Double-Pillared Metal-Organic Frameworks Containing Cadmium Clusters. *CrystEngComm* **2011**, *13* (10), 3321–3324.

(63) Zhu, S.; Zhang, H.; Zhao, Y.; Shao, M.; Wang, Z.; Li, M. Synthesis, Structures and Luminescence of Three Coordination Polymers Constructed from Rigid 1,3,5-Benzenetricarboxylic Acid and Flexible Bis(Imidazol-1-Ylmethyl)-Benzene. *J. Mol. Struct.* **2008**, *892* (1–3), 420–426.

(64) Kosaka, W.; Hashimoto, K.; Ohkoshi, S. I. Three-Dimensional Manganese Octacyanoniobate-Based Pyroelectric Ferrimagnet. *Bull. Chem. Soc. Jpn.* **2008**, *81* (8), 992–994.

(65) The, F.; Duhayon, C.; Venkatakrishnan, T. S.; Sutter, J. Supramolecular Hybrid Architectures Including an Open Framework with Reversible Sorption Properties. *Cryst. Growth Des.* **2008**, *2* (1), 2–9.

(66) Xie, Y. M.; Liu, J. H.; Wu, X. Y.; Zhao, Z. G.; Zhang, Q. S.; Wang, F.; Chen, S. C.; Lu, C. Z. New Ferroelectric and Nonlinear Optical Porous Coordination Polymer Constructed from a Rare $(CuBr)_{\infty}$ Castellated Chain. *Cryst. Growth Des.* **2008**, *8* (11), 3914–3916.

(67) Li, G.; Salim, C.; Hinode, H. Hydrothermal Syntheses and Crystal Structures of Two Hybrid Materials Constructed from Polyoxometalate Clusters and Metal-Dipyridine Complexes. *Solid State Sci.* **2008**, *10* (2), 121–128.

(68) Luo, F.; Zheng, J.; Long, G. J. Unique Anionic Eight-Connected Net with $3^6 4^{18} 5^{36}$ Topology Derived from a Rare $Co_6(\mu_3\text{-}OH)_2(\mu\text{-}H_2O)(CO_2)_{12}$ Building Block. *Cryst. Growth Des.* **2009**, *3*, 1271–1274.

(69) Liu, D.; Li, M.; Li, D. Reversible Solid-Gas Chemical Equilibrium between a 0-Periodic Deformable Molecular Tecton and a 3-Periodic Coordination Architecture. *Chem. Commun.* **2009**, No. 45, 6943–6945.

(70) Gándara, F.; Víctor, A.; Peña-O'Shea, D. La; IIIas, F.; Snejko, N.; Proserpio, D. M.; Gutiérrez-Puebla, E.; Monge, M. A. Three Lanthanum MOF Polymorphs: Insights into Kinetically and Thermodynamically Controlled Phases. *Inorg. Chem.* **2009**, *48* (11), 4707–4713.

(71) He, J.; Yang, C.; Xu, Z.; Zeller, M.; Hunter, A. D.; Lin, J. Building Thiol and Metal-

Thiolate Functions into Coordination Nets: Clues from a Simple Molecule. *J. Solid State Chem.* **2009**, *182* (7), 1821–1826.

(72) Wang, X.-S.; Ma, S.; Yuan, D.; Yoon, J. W.; Hwang, Y. K.; Chang, J. S.; Wang, X.; Jørgensen, M. R.; Chen, Y. S.; Zhou, H. C. A Large-Surface-Area Boracite-Network-Topology Porous MOF Constructed from a Conjugated Ligand Exhibiting a High Hydrogen Uptake Capacity. *Inorg. Chem.* **2009**, *48* (16), 7519–7521.

(73) Nelson, A. P.; Parrish, D. A.; Cambrea, L. R.; Baldwin, L. C.; Trivedi, N. J.; Mulfort, K. L.; Farha, O. K.; Hupp, J. T. Crystal to Crystal Guest Exchange in a Mixed Ligand Metal-Organic Framework. *Cryst. Growth Des.* **2009**, *9* (11), 4588–4591.

(74) Han, Z. B.; Zhang, G. X.; Zeng, M. H.; Ge, C. H.; Zou, X. H.; Han, G. X. Synthesis, Crystal Structure and Magnetic Properties of Two 3-D Gadolinium Complexes. *CrystEngComm* **2009**, *11* (12), 2629–2633.

(75) Seo, J.; Chun, H. Hysteretic Gas Sorption in a Microporous Metal-Organic Framework with Nonintersecting 3d Channels. *Eur. J. Inorg. Chem.* **2009**, No. 33, 4946–4949.

(76) Hunger, J.; Krautscheid, H.; Sieler, J. Hydrothermal Synthesis and Structure of Coordination Polymers by Combination of Bipyrazole and Aromatic Dicarboxylate Ligands. *Cryst. Growth Des.* **2009**, *9* (11), 4613–4625.

(77) Yue, Q.; Sun, Q.; Cheng, A. L.; Gao, E. Q. Metal-Organic Framework Based on $[Zn_4O(COO)_6]$ Clusters: Rare 3D Kagomé Topology and Luminescence. *Cryst. Growth Des.* **2010**, *10* (1), 44–47.

(78) Konno, T.; Yoshinari, N.; Taguchi, M.; Igashira-Kamiyama, A. Drastic Change in Dimensional Structures of D-Penicillaminato $(Au^{I}_2Pt^{II}_2Zn^{II})_n$ Coordination Polymers by Moderate Change in Solution PH. *Chem. Lett.* **2009**, *38* (6), 526–527.

(79) Liu, H. K.; Tsao, T. H.; Zhang, Y. T.; Lin, C. H. Microwave Synthesis and Single-Crystal-to-Single-Crystal Transformation of Magnesium Coordination Polymers Exhibiting Selective Gas Adsorption and Luminescence Properties. *CrystEngComm* **2009**, *11* (7), 1462–1468.

(80) Wu, Y.; Li, D.; Fu, F.; Tang, L.; Wang, J.; Yang, X. G. Microporous 3-D Chiral Metal-Organic Framework with a Quartzlike Topology Based on an Achiral Building Unit. *J. Coord. Chem.* **2009**, *62* (16), 2665–2674.

(81) Kalf, I.; Mathieu, P.; Englert, U. From Crystal to Crystal: A New Polymorph of (4-Carboxylatopyridine) Silver(i) by Topotactic Dehydration of Its Monohydrate. *New J. Chem.* **2010**, *34* (11), 2491–2495.

(82) Ohara, K.; Inokuma, Y.; Fujita, M. The Catalytic Z to E Isomerization of Stilbenes in a Photosensitizing Porous Coordination Network. *Angew. Chemie - Int. Ed.* **2010**, *49* (32), 5507–5509.

(83) Rodríguez-Diéguez, A.; Salinas-Castillo, A.; Sironi, A.; Seco, J. M.; Colacio, E. A Chiral Diamondoid 3D Lanthanum Metal-Organic Framework Displaying Blue-Greenish Long Lifetime Photoluminescence Emission. *CrystEngComm* **2010**, *12* (6), 1876–1879.

(84) Zhang, N.; Li, M. X.; Wang, Z. X.; Shao, M.; Zhu, S. R. Synthesis, Structures and Thermal Stabilities of Five Copper(II) Coordination Polymers Based on 2,4,6-Tris(Pyridyl)-1,3,5-Triazine and 1,2,4,5-Benzenetetracarboxylate Ligands. *Inorganica Chim. Acta* **2010**, *363* (1), 8–14.

(85) Dey, B.; Das, A.; Choudhury, S. R.; Jana, A. D.; Lu, L. P.; Zhu, M. L.; Mukhopadhyay, S. Three Dimensional Metal-Malonate Frameworks with Pillared Layered Architecture: Unusual Role of Metal-Chelate as Pillar. *Inorganica Chim. Acta* **2010**, *363* (5), 981–987.

(86) Barron, P. M.; Wray, C. A.; Hu, C.; Guo, Z.; Choe, W. A Bioinspired Synthetic Approach for Building Metal-Organic Frameworks with Accessible Metal Centers. *Inorg. Chem.* **2010**, *49* (22), 10217–10219.

(87) Xue, M.; Zhang, Z.; Xiang, S.; Jin, Z.; Liang, C.; Zhu, G. S.; Qiu, S. L.; Chen, B. Selective Gas Adsorption within a Five-Connected Porous Metal-Organic Framework. *J. Mater. Chem.* **2010**, *20* (19), 3984–3988.

(88) Yue, Q.; Yan, L.; Zhang, J. Y.; Gao, E. Q. Novel Functionalized Metal-Organic Framework Based on Unique Hexagonal Prismatic Clusters. *Inorg. Chem.* **2010**, *49* (19), 8647–8649.

(89) Huang, X. Y.; Yue, K. F.; Jin, J. C.; Liu, J. Q.; Wang, C. J.; Wang, Y. Y.; Shi, Q. Z. Three-Dimensional Fivefold Interpenetrating Microporous Metal-Organic Framework Based on Mixed Flexible Ligands. *Inorg. Chem. Commun.* **2010**, *13* (3), 338–341.

(90) Yu, Q.; Zeng, Y. F.; Zhao, J. P.; Yang, Q.; Hu, B. W.; Chang, Z.; Bu, X. H. Three-Dimensional Porous Metal-Organic Frameworks Exhibiting Metamagnetic Behaviors: Synthesis, Structure, Adsorption, and Magnetic Properties. *Inorg. Chem.* **2010**, *49* (9), 4301–4306.

(91) Zou, R.; Zhong, R.; Han, S.; Xu, H.; Burrell, A. K.; Henson, N.; Cape, J. L.; Hickmott, D. D.; Timofeeva, T. V.; Larson, T. E.; et al. A Porous Metal-Organic Replica of α-PbO_2 for Capture of Nerve Agent Surrogate. *J. Am. Chem. Soc.* **2010**, *132* (51), 17996–17999.

(92) Liu, D.; Xie, Z.; Ma, L.; Lin, W. Three-Dimensional Metal-Organic Frameworks Based on Tetrahedral and Square-Planar Building Blocks: Hydrogen Sorption and Dye Uptake Studies. *Inorg. Chem.* **2010**, *49* (20), 9107–9109.

(93) Banerjee, D.; Kim, S. J.; Li, W.; Wu, H.; Li, J.; Borkowski, L. A.; Philips, B. L.; Parise, J. B. Synthesis and Structural Characterization of a 3-D Lithium Based

Metal-Organic Framework Showing Dynamic Structural Behavior. *Cryst. Growth Des.* **2010**, *10* (6), 2801–2805.

(94) Hu, B. W.; Zhao, J. P.; Tao, J.; Sun, X. J.; Yang, Q.; Zhang, X. F.; Bu, X. H. A New Azido-Nickel Compound with Three-Dimensional Kagomé Topology. *Cryst. Growth Des.* **2010**, *10* (7), 2829–2831.

(95) Chen, F.; Zheng, F. K.; Liu, G. N.; Wu, A. Q.; Wang, M. S.; Guo, S. P.; Wu, M. F.; Liu, Z. F.; Guo, G. C.; Huang, J. S. Crystal Structure and Magnetic Property of a 3D Heterometallic Coordination Polymer Constructed by 3-Cyanobenzoate and 3-(5H-Tetrazol) Benzoate Ligands. *Inorg. Chem. Commun.* **2010**, *13* (2), 278–281.

(96) Hassanzadeh Fard, Z.; Hołyńska, M.; Dehnen, S. Organotin Chalcogenide Salts: Synthesis, Characterization, and Extended Crystal Structures. *Inorg. Chem.* **2010**, *49* (12), 5748–5752.

(97) Thuéry, P.; Masci, B. Two-and Three-Dimensional Europium-Organic Assemblies with the All-Cis and All-Trans Isomers of 1,2,3,4,5,6-Cyclohexanehexacarboxylic Acid. *Cryst. Growth Des.* **2010**, *10* (8), 3626–3631.

(98) Zhang, J.; Xue, Y. S.; Liang, L. L.; Ren, S. Bin; Li, Y. Z.; Du, H. Bin; You, X. Z. Porous Coordination Polymers of Transition Metal Sulfides with PtS Topology Built on a Semirigid Tetrahedral Linker. *Inorg. Chem.* **2010**, *49* (17), 7685–7691.

(99) Platero-Prats, A. E.; De La Peña-O'shea, V. A.; Snejko, N.; Monge, Á.; Gutiérrez-Puebla, E. Dynamic Calcium Metal-Organic Framework Acts as a Selective Organic Solvent Sponge. *Chem. - A Eur. J.* **2010**, *16* (38), 11632–11640.

(100) Jia, J.; Shao, M.; Jia, T.; Zhu, S.; Zhao, Y.; Xing, F.; Li, M. Coordination Polymers of Biphenyl-2,4,2′,4′-Tetracarboxylic Acid - Synthesis, Structures and Adsorption Properties. *CrystEngComm* **2010**, *12* (5), 1548–1561.

(101) Li, B.; Li, G.; Liu, D.; Peng, Y.; Zhou, X.; Hua, J.; Shi, Z.; Feng, S. Coordination Polymers Constructed by 1,3-Bi(4-Pyridyl)Propane with Four Different Conformations and 2,2′-Dinitro-4,4′-Biphenyldicarboxylate Ligands: The Effects of Metal Ions. *CrystEngComm* **2011**, *13* (5), 1291–1298.

(102) Jiang, G.; Wu, T.; Zheng, S. T.; Zhao, X.; Lin, Q.; Bu, X.; Feng, P. A Nine-Connected Mixed-Ligand Nickel-Organic Framework and Its Gas Sorption Properties. *Cryst. Growth Des.* **2011**, *11* (9), 3713–3716.

(103) Meng, M.; Zhong, D. C.; Lu, T. B. Three Porous Metal-Organic Frameworks Based on an Azobenzenetricarboxylate Ligand: Synthesis, Structures, and Magnetic Properties. *CrystEngComm* **2011**, *13* (22), 6794–6800.

(104) Yamada, T.; Iwakiri, S.; Hara, T.; Kanaizuka, K.; Kurmoo, M.; Kitagawa, H. Porous Interpenetrating Metal-Organic Frameworks with Hierarchical Nodes. *Cryst. Growth Des.* **2011**, *11* (5), 1798–1806.

(105) Lhoste, J.; Henry, N.; Roussel, P.; Loiseau, T.; Abraham, F. An Uranyl Citrate Coordination Polymer with a 3D Open-Framework Involving Uranyl Cation-Cation Interactions. *Dalt. Trans.* **2011**, *40* (11), 2422–2424.

(106) Kanoo, P.; Ghosh, A. C.; Maji, T. K. A Vanadium (VO^{2+}) Metal-Organic Framework: Selective Vapor Adsorption, Magnetic Properties, and Use as a Precursor for a Polyoxovanadate. *Inorg. Chem.* **2011**, *50* (11), 5145–5152.

(107) Han, Z. B.; Lu, R. Y.; Liang, Y. F.; Zhou, Y. L.; Chen, Q.; Zeng, M. H. Mn(II)-Based Porous Metal-Organic Framework Showing Metamagnetic Properties and High Hydrogen Adsorption at Low Pressure. *Inorg. Chem.* **2012**, *51* (1), 674–679.

(108) Wu, H.; Ma, J. F.; Liu, Y. Y.; Yang, J.; Liu, H. Y. Diverse Topologies of Six Coordination Polymers Constructed from a Tris(4-Imidazolylphenyl)Amine Ligand and Different Carboxylates. *CrystEngComm* **2011**, *13* (23), 7121–7128.

(109) Zhao, L. M.; Zhang, Z. J.; Zhang, S. Y.; Cui, P.; Shi, W.; Zhao, B.; Cheng, P.; Liao, D. Z.; Yan, S. P. Metal-Organic Frameworks Based on Transition-Metal Carboxylate Clusters as Secondary Building Units: Synthesis, Structures and Properties. *CrystEngComm* **2011**, *13* (3), 907–913.

(110) Ikobayashi, A.; Suzuki, Y.; Ohba, T.; Noro, S. I.; Chang, H. C.; Kato, M. Ln-Co-Based Rock-Salt-Type Porous Coordination Polymers: Vapor Response Controlled by Changing the Lanthanide Ion. *Inorg. Chem.* **2011**, *50* (6), 2061–2063.

(111) Pérez-Yáñez, S.; Beobide, G.; Castillo, O.; Cepeda, J.; Luque, A.; Aguayo, A. T.; Román, P. Open-Framework Copper Adeninate Compounds with Three-Dimensional Microchannels Tailored by Aliphatic Monocarboxylic Acids. *Inorg. Chem.* **2011**, *50* (12), 5330–5332.

(112) Volkringer, C.; Mihalcea, I.; Vigier, J. F.; Beaurain, A.; Visseaux, M.; Loiseau, T. Metal-Organic-Framework-Type 1D-Channel Open Network of a Tetravalent Uranium Trimesate. *Inorg. Chem.* **2011**, *50* (23), 11865–11867.

(113) Wang, F.; Ke, X.; Zhao, J.; Deng, K.; Leng, X.; Tian, Z.; Wen, L.; Li, D. Six New Metal-Organic Frameworks with Multi-Carboxylic Acids and Imidazole-Based Spacers: Syntheses, Structures and Properties. *Dalt. Trans.* **2011**, *40* (44), 11856–11865.

(114) Li, B.; Yang, F.; Li, G.; Liu, D.; Zhou, Q.; Shi, Z.; Feng, S. Construction of Coordination Polymers Based on Bent 4-Amino-3,5-Bis(3- Carboxyphenyl)-1,2,4-Triazole Ligand: Diverse Structural Topology and Photoluminescent and Magnetic Properties. *Cryst. Growth Des.* **2011**, *11* (5), 1475–1485.

(115) Alsobrook, A. N.; Hauser, B. G.; Hupp, J. T.; Alekseev, E. V.; Depmeier, W.; Albrecht-Schmitt, T. E. From Layered Structures to Cubic Frameworks: Expanding the Structural Diversity of Uranyl Carboxyphosphonates via the Incorporation of Cobalt. *Cryst. Growth Des.* **2011**, *11* (4), 1385–1393.

(116) Adelani, P. O.; Albrecht-Schmitt, T. E. Pillared and Open-Framework Uranyl Diphosphonates. *J. Solid State Chem.* **2011**, *184* (9), 2368–2373.

(117) Ren, G.; Liu, S.; Ma, F.; Wei, F.; Tang, Q.; Yang, Y.; Liang, D.; Li, S.; Chen, Y. A 9-Connected Metal-Organic Framework with Gas Adsorption Properties. *J. Mater. Chem.* **2011**, *21* (40), 15909–15913.

(118) Oh, M.; Lah, M. S. Adsorbate Selectivity of Isoreticular Microporous Metal-Organic Frameworks with Similar Static Pore Dimensions. *Cryst. Growth Des.* **2011**, *11* (11), 5064–5071.

(119) Yan, Y.; Blake, A. J.; Lewis, W.; Barnett, S. A.; Dailly, A.; Champness, N. R.; Schröder, M. Modifying Cage Structures in Metal-Organic Polyhedral Frameworks for H_2 Storage. *Chem. - A Eur. J.* **2011**, *17* (40), 11162–11170.

(120) Gong, Y. N.; Meng, M.; Zhong, D. C.; Huang, Y. L.; Jiang, L.; Lu, T. B. Counter-Cation Modulation of Hydrogen and Methane Storage in a Sodalite-Type Porous Metal-Organic Framework. *Chem. Commun.* **2012**, *48* (98), 12002–12004.

(121) Adelani, P. O.; Albrecht-Schmitt, T. E. Heterobimetallic Copper(II) Uranyl Carboxyphenylphosphonates. *Cryst. Growth Des.* **2011**, *11* (10), 4676–4683.

(122) Zhang, P.; Li, B.; Zhao, Y.; Meng, X.; Zhang, T. A Novel (3,36)-Connected and Self-Interpenetrated Metal-Organic Framework with High Thermal Stability and Gas-Sorption Capabilities. *Chem. Commun.* **2011**, *47* (27), 7722–7724.

(123) Chen, S. S.; Lv, G. C.; Fan, J.; Okamura, T. A.; Chen, M.; Sun, W. Y. Entangled Coordination Frameworks with 1,4-Di(1 H -Imidazol-4-Yl)Benzene. *Cryst. Growth Des.* **2011**, *11* (4), 1082–1090.

(124) Zhao, X.; Wu, T.; Zheng, S. T.; Wang, L.; Bu, X.; Feng, P. A Zeolitic Porous Lithium-Organic Framework Constructed from Cubane Clusters. *Chem. Commun.* **2011**, *47* (19), 5536–5538.

(125) Ma, R.; Chen, C.; Sun, B.; Zhao, X.; Zhang, N. A New 3D Metal-Organic Framework with (4, 8)-Connected A_1B_2 Topology Constructed from Coordinated Evolution of a C_3 Symmetry Ligand. *Inorg. Chem. Commun.* **2011**, *14* (9), 1532–1536.

(126) Su, S.; Zhang, Y.; Zhu, M.; Song, X.; Wang, S.; Zhao, S.; Song, S.; Yang, X.; Zhang, H. An Active-Site-Accessible Porous Metal-Organic Framework Composed of Triangular Building Units: Preparation, Catalytic Activity and Magnetic Property. *Chem. Commun.* **2012**, *48* (90), 11118–11120.

(127) Sen, R.; Saha, D.; Koner, S. Controlled Construction of Metal-Organic Frameworks: Hydrothermal Synthesis, X-Ray Structure, and Heterogeneous Catalytic Study. *Chem. - A Eur. J.* **2012**, *18* (19), 5979–5986.

(128) Zhang, Y.; Wang, Q.; Xiao, Y. J.; Han, J.; Zhao, X. L. Structure Diversity of a Series of New Coordination Polymers Based on a C_3 -Symmetric Tridentate Ligand with Rosette Architecture. *Polyhedron* **2012**, *33* (1), 127–136.

(129) Sun, L.; Ma, L.; Cai, J. B.; Liang, L.; Deng, H. Novel Tetrazole-Based Metal-Organic Frameworks Constructed from in Situ Synthesize Bifunctional Ligands: Syntheses, Structure and Luminescent Properties. *CrystEngComm* **2012**, *14* (3), 890–898.

(130) Lu, Z.; Xing, H.; Sun, R.; Bai, J.; Zheng, B.; Li, Y. Water Stable Metal-Organic Framework Evolutionally Formed from a Flexible Multidentate Ligand with Acylamide Groups for Selective CO_2 Adsorption. *Cryst. Growth Des.* **2012**, *12* (3), 1081–1084.

(131) Lässig, D.; Lincke, J.; Gerhardt, R.; Krautscheid, H. Solid-State Syntheses of Coordination Polymers by Thermal Conversion of Molecular Building Blocks and Polymeric Precursors. *Inorg. Chem.* **2012**, *51* (11), 6180–6189.

(132) Song, X. Z.; Qin, C.; Guan, W.; Song, S. Y.; Zhang, H. J. An Unusual Three-Dimensional Self-Penetrating Network Derived from Cross-Linking of Two-Fold Interpenetrating Nets via Ligand-Unsupported Ag-Ag Bonds: Synthesis, Structure, Luminescence, and Theoretical Study. *New J. Chem.* **2012**, *36* (4), 877–882.

(133) Ahmad, M.; Das, R.; Lama, P.; Poddar, P.; Bharadwaj, P. K. Synthesis, Characterization, and Magnetic Studies of Coordination Polymers with Co(II) and Mn(II) Ions. *Cryst. Growth Des.* **2012**, *12* (9), 4624–4632.

(134) Kundu, T.; Sahoo, S. C.; Banerjee, R. Variable Water Adsorption in Amino Acid Derivative Based Homochiral Metal Organic Frameworks. *Cryst. Growth Des.* **2012**, *12* (9), 4633–4640.

(135) Wen, L.; Ke, X.; Qiu, L.; Zou, Y.; Zhou, L.; Zhao, J.; Li, D. Assembly of Two Porous Cadmium(II) Frameworks: Selective Adsorption and Luminescent Property. *Cryst. Growth Des.* **2012**, *12* (8), 4083–4089.

(136) Stylianou, K. C.; Rabone, J.; Chong, S. Y.; Heck, R.; Armstrong, J.; Wiper, P. V.; Jelfs, K. E.; Zlatogorsky, S.; Bacsa, J.; McLennan, A. G.; et al. Dimensionality Transformation through Paddlewheel Reconfiguration in a Flexible and Porous Zn-Based Metal-Organic Framework. *J. Am. Chem. Soc.* **2012**, *134* (50), 20466–20478.

(137) Chen, Q.; Xue, W.; Wang, B. Y.; Zeng, M. H.; Chen, X. M. Unprecedented Binodal (7,9)-Connected Network Based on Distinct Tricobalt(II) Clusters: Structure, Topology and Cooperative Magnetism. *CrystEngComm* **2012**, *14* (6), 2009–2014.

(138) Ruan, C. Z.; Wen, R.; Liang, M. X.; Kong, X. J.; Ren, Y. P.; Long, L. S.; Huang, R. Bin; Zheng, L. S. Two Triazole-Based Metal-Organic Frameworks Constructed from Nanosized Cu_{20} and Cu_{30} Wheels. *Inorg. Chem.* **2012**, *51* (14), 7587–7591.

(139) Dau, P. V.; Tanabe, K. K.; Cohen, S. M. Functional Group Effects on Metal-Organic Framework Topology. *Chem. Commun.* **2012**, *48* (75), 9370–9372.

(140) Dauth, A.; Love, J. A. Synthesis and Reactivity of 2-Azametallacyclobutanes. *Dalt. Trans.* **2012**, *41* (26), 7782–7791.

(141) Wen, L.; Shi, W.; Chen, X.; Li, H.; Cheng, P. A Porous Metal-Organic Framework Based on Triazoledicarboxylate Ligands - Synthesis, Structure, and Gas-Sorption Studies. *Eur. J. Inorg. Chem.* **2012**, No. 22, 3562–3568.

(142) Gao, W. Y.; Yan, W.; Cai, R.; Williams, K.; Salas, A.; Wojtas, L.; Shi, X.; Ma, S. A Pillared Metal-Organic Framework Incorporated with 1,2,3-Triazole Moieties Exhibiting Remarkable Enhancement of CO_2 Uptake. *Chem. Commun.* **2012**, *48* (71), 8898–8900.

(143) Yang, F.; Li, B.; Xu, W.; Li, G.; Zhou, Q.; Hua, J.; Shi, Z.; Feng, S. Two Metal-Organic Frameworks Constructed from One-Dimensional Cobalt(II) Ferrimagnetic Chains with Alternating Antiferromagnetic/Ferromagnetic and AF/AF/FM Interaction: Synthesis, Structures, and Magnetic Properties. *Inorg. Chem.* **2012**, *51* (12), 6813–6820.

(144) Fang, Q. R.; Yuan, D. Q.; Sculley, J.; Lu, W. G.; Zhou, H. C. A Novel MOF with Mesoporous Cages for Kinetic Trapping of Hydrogen. *Chem. Commun.* **2012**, *48* (2), 254–256.

(145) Majumder, M.; Sheath, P.; Mardel, J. I.; Harvey, T. G.; Thornton, A. W.; Gonzago, A.; Kennedy, D. F.; Madsen, I.; Taylor, J. W.; Turner, D. R.; et al. Aqueous Molecular Sieving and Strong Gas Adsorption in Highly Porous MOFs with a Facile Synthesis. *Chem. Mater.* **2012**, *24* (24), 4647–4652.

(146) Muñoz-Lara, F. J.; Gaspar, A. B.; Muñoz, M. C.; Lysenko, A. B.; Domasevitch, K. V.; Real, J. A. Fast Detection of Water and Organic Molecules by a Change of Color in an Iron(II) Microporous Spin-Crossover Coordination Polymer. *Inorg. Chem.* **2012**, *51* (24), 13078–13080.

(147) Tseng, T. W.; Luo, T. T.; Chen, S. Y.; Su, C. C.; Chi, K. M.; Lu, K. L. Porous Metal-Organic Frameworks with Multiple Cages Based on Tetrazolate Ligands: Synthesis, Structures, Photoluminescence, and Gas Adsorption Properties. *Cryst. Growth Des.* **2013**, *13* (2), 510–517.

(148) Lin, Z.; Zou, R.; Xia, W.; Chen, L.; Wang, X.; Liao, F.; Wang, Y.; Lin, J.; Burrell, A. K. Ultrasensitive Sorption Behavior of Isostructural Lanthanide-Organic Frameworks Induced by Lanthanide Contraction. *J. Mater. Chem.* **2012**, *22* (39), 21076–21084.

(149) Jeong, E.; Lee, W. R.; Ryu, D. W.; Kim, Y.; Phang, W. J.; Koh, E. K.; Hong, C. S. Reversible Structural Transformation and Selective Gas Adsorption in a Unique Aqua-Bridged Mn(II) Metal-Organic Framework. *Chem. Commun.* **2013**, *49* (23),

2329–2331.

(150) Wang, L.; Yan, Z. H.; Xiao, Z.; Guo, D.; Wang, W.; Yang, Y. Reactant Ratio-Modulated Entangled Cd(II) Coordination Polymers Based on Rigid Tripodal Imidazole Ligand and Tetrabromoterephthalic Acid: Interpenetration, Interdigitation and Self-Penetration. *CrystEngComm* **2013**, *15* (27), 5552–5560.

(151) Wen, Z. Z.; Wen, X. L.; Cai, S. L.; Zheng, S. R.; Fan, J.; Zhang, W. G. The Construction of Cu(I)/Cu(II) Coordination Polymers Based on Pyrazine-Carboxylate: Structural Diversity Tuned by in Situ Hydrolysis Reaction. *CrystEngComm* **2013**, *15* (26), 5359–5367.

(152) Huang, Y. Y.; Zhang, X.; Yao, Y. G. Employing Heterometallic Trinuclear Cluster as Building Subunit to Construct a New Coordination Polymer with Rare 3D Inorganic -Cd-O-Ba- Connectivity. *Inorganica Chim. Acta* **2013**, *397*, 38–41.

(153) Chen, L.; Zhang, L.; Li, S. L.; Qiu, Y. Q.; Shao, K. Z.; Wang, X. L.; Su, Z. M. Self-Assembly of Metal-Organic Frameworks Based on N-Donor Ligand and Flexible Tricarboxylic Acids with Different Angular Characters. *CrystEngComm* **2013**, *15* (40), 8214–8221.

(154) Lian, T. T.; Chen, S. M.; Wang, F.; Zhang, J. Metal-Organic Framework Architecture with Polyhedron-in-Polyhedron and Further Polyhedral Assembly. *CrystEngComm* **2013**, *15* (6), 1036–1038.

(155) Li, C. P.; Chen, J.; Liu, P. W.; Du, M. Structural Diversity and Fluorescent Properties of Cd^{II} Coordination Polymers with 5-Halonicotinates Regulated by Solvent and Ligand Halogen-Substituting Effect. *CrystEngComm* **2013**, *15* (45), 9713–9721.

(156) Falaise, C.; Volkringer, C.; Vigier, J. F.; Henry, N.; Beaurain, A.; Loiseau, T. Three-Dimensional MOF-Type Architectures with Tetravalent Uranium Hexanuclear Motifs (U_6O_8). *Chem. - A Eur. J.* **2013**, *19* (17), 5324–5331.

(157) Song, X. Z.; Song, S. Y.; Zhao, S. N.; Hao, Z. M.; Zhu, M.; Meng, X.; Zhang, H. J. Two High-Connected Metal-Organic Frameworks Based on d^{10}-Metal Clusters: Syntheses, Structural Topologies and Luminescent Properties. *Dalt. Trans.* **2013**, *42* (23), 8183–8187.

(158) Zhang, H. X.; Fu, H. R.; Li, H. Y.; Zhang, J.; Bu, X. Porous Ctn-Type Boron Imidazolate Framework for Gas Storage and Separation. *Chem. - A Eur. J.* **2013**, *19* (35), 11527–11530.

(159) Zhan, C.; Zou, C.; Kong, G. Q.; Wu, C. De. Four Honeycomb Metal-Organic Frameworks with a Flexible Tripodal Polyaromatic Acid. *Cryst. Growth Des.* **2013**, *13* (4), 1429–1437.

(160) Murdock, C. R.; Lu, Z.; Jenkins, D. M. Effects of Solvation on the Framework of a

Breathing Copper MOF Employing a Semirigid Linker. *Inorg. Chem.* **2013**, *52* (4), 2182–2187.

(161) Wu, Y.; Zhou, X. P.; Yang, J. R.; Li, D. Gyroidal Metal-Organic Frameworks by Solvothermal Subcomponent Self-Assembly. *Chem. Commun.* **2013**, *49* (33), 3413–3415.

(162) Xing, F.; Jia, J.; Liu, L.; Zhong, L.; Shao, M.; Bai, Y. L.; Zhao, Y.; Zhu, S.; He, X.; Li, M. Synthesis, Structure and Adsorption of Coordination Polymers Constructed from 3,3′,5,5′-Azobenzenetetracarboxylic Acid and Zn Ions. *CrystEngComm* **2013**, *15* (24), 4970–4980.

(163) Zhao, J. P.; Zhao, R.; Song, W. C.; Yang, Q.; Liu, F. C.; Bu, X. H. Azido-Directed Formation of an Unprecedented Mn(II)-Organic Framework with Nanoscale Cubic Cage Units. *Cryst. Growth Des.* **2013**, *13* (2), 437–439.

(164) Ablet, A.; Li, S. M.; Cao, W.; Zheng, X. J.; Wong, W. T.; Jin, L. P. Luminescence Tuning and White-Light Emission of Co-Doped Ln-Cd-Organic Frameworks. *Chem. - An Asian J.* **2013**, *8* (1), 95–100.

CHAPTER 7. CONCLUSIONS

7.1 Dissertation Impact

Adsorptive separation of chemical mixtures using nanoporous materials have shown promise as an energy efficient alternative to traditional methods. MOFs are relatively new materials that have exceptional porosity and wide range of chemical functionality. Due to their high degree of tunability, thousands of MOFs have been synthesized.[1,2] Molecular simulations to study adsorption in MOFs have proven to be useful to reduce the efforts needed to identify material compositions of interest for a particular application. The overall objective of this thesis has been to use computational methods to accurately study adsorption of complex adsorbates in MOFs.

Chapter 2 and chapter 3 focused on studying the effects of flexibility in MOFs on their adsorption properties. Most computational studies to date assume that the structure of MOF is rigid during simulations even though these frameworks can show various kinds of flexibility. In chapter 2, we accounted for the flexibility with $\Delta V=0$ in MOFs in our simulations to assess the impact of their ubiquitous form of flexibility on molecular adsorption. The results showed that while the flexibility with $\Delta V=0$ has a small effect on single component adsorption at non-dilute loadings in most MOFs, it has significant effects on single component adsorption at dilute loadings and multicomponent adsorption at both dilute and non-dilute loadings in many MOFs. Single component adsorption at dilute loadings (Henry constants) were the most affected by the flexibility. For all adsorption properties, the effects of flexibility were the highest for MOFs that have pore diameters comparable to an adsorbate's kinetic diameter. We also found that the effect of flexibility

at dilute loadings is not strongly correlated with the effect at non-dilute loadings, so separate studies need to be done for separation loading conditions. In chapter 3, we studied the effect of flexibility with $\Delta V \neq 0$ in MIL-53 on the adsorption of xylene isomers and concluded that in this example even the single component adsorption at non-dilute loading is influenced significantly by framework flexibility. It was also observed that that MIL-53s with different metal-centers are differently affected by the framework flexibility.

Chapter 4 and chapter 5 explore the adsorption and diffusion properties of chemical warfare agents (CWAs) and their simulants in MOFs. In chapter 4, we performed a detailed comparison between CWAs and their simulants based on their adsorption properties in MOFs to study how accurately simulants are able to mimic the real agent's properties. We found that DMMP and DCP are able to predict sarin's adsorption properties in MOFs with reasonable accuracy while DMNP is the closest simulant to soman. The accuracy of generic force-fields is not known for these complex molecules, so a new force-field was derived using quantum mechanical calculations. This allowed us to conclude that the results are not sensitive to the force-field used in the calculations. In capturing and treatment of CWAs using MOFs, it is not only equilibrium capacity that is important but also kinetics of the process of interest. Diffusion coefficients must be known to estimate kinetics of CWAs capture even at an approximate level. In chapter 5, we determined room temperature diffusion coefficients of CWAs and their simulants using molecular simulations in several prototypical MOFs. We observed that sarin can diffuse 1 micron in MIL-47 or Cu-BTC in less than a millisecond but the same time scale in UiO-66 and ZIF-8 is 3.3 hours and 25 hours, respectively. We also compared the diffusion properties of sarin with several

simulants and concluded that DMMP has diffusion coefficients closest to sarin consistently in all MOFs studied.

In chapter 6, we used literature meta-analysis to gather quantitative data regarding replicability of MOF synthesis research. We selected 130 papers that reported new materials from the CoRE MOF database and went through the citations of each of the 130 papers to determine how frequently these original materials have been re-synthesized. We observed that approximately 88% of the materials reported has not been re-synthesized. Our data suggested that a simple power law could describe the frequency of repeat syntheses for many MOFs but that a small number of "supermaterials" exist that have been replicated many times more than a power law would predict. Our results also hint that there are many repeat syntheses that have been performed but never reported in the literature, which suggests simple steps that could be taken to greatly increase the number of reports of replicate experiments in materials chemistry.

7.2 Suggested Directions for Future Work

There are several interesting future directions in which the work in this thesis can be extended to. Some of them are summarized below:

7.2.1 Developing computational efficient methods to study the flexibility effects in MOFs

We have established that flexibility in MOFs can affect adsorption properties in a significant number of MOFs. However, the study of flexibility in a MOF requires a physically accurate bonded force-field to perform MD simulations to get the snapshots of

the flexible structure, which is not always available. Finding a methodology to generate flexible snapshots of a MOF without using MD simulations would make these kinds of studies much faster. A method that identifies patterns in the atomic displacements in MOFs and similar materials due to flexibility and uses statistical methods to generate plausible snapshots could become an efficient way to study flexibility in these systems. It would be useful to combine work of this kind with recent efforts to describe adsorption of diverse set of molecules in large collection of nanoporous materials.[3,4]

7.2.2 Finding the best material for CWAs capture and degradation

There have been studies that aim to find the best material among CoRE MOF database to capture CWAs based on adsorption properties at dilute loadings.[5] However, as discussed in chapter 5, it is not only the thermodynamic properties such as adsorption but also kinetic properties of the system that play a significant role in real-world processes. The next natural step of our work is to perform calculations in which thermodynamics and kinetics of CWAs capture in MOFs are quantified and the process parameters are determined based on the rate limiting step. For degradation of CWAs in MOFs, combining all steps of the catalysis, namely diffusion inside nanopores, adsorption, reaction and desorption, should all be considered in developing practical device for dealing with CWAs.

7.2.3 Literature meta-analysis for materials chemistry

The last part of this thesis opens up several new directions to assess and improve the replicability of materials synthesis and their properties in chemistry. We performed a literature meta-analysis on replicability of MOFs syntheses and used a simple power law to predict the frequency of the replicate syntheses. It will be very interesting to know if

these observations applicable to other classes of materials. A natural extension from the MOFs we have studied would be zeolites, a class of materials of considerable industrial importance. The methods we have used are quite general, so their use is not restricted to porous materials. As the application of 'big data' approaches within materials chemistry proliferates, developing insight into the reliability of the underlying data will continue to have value.

7.3 References

(1) Groom, C. R.; Bruno, I. J.; Lightfoot, M. P.; Ward, S. C. The Cambridge Structural Database. *Acta Cryst.* **2016**, *B72*, 171–179.

(2) Chung, Y. G.; Camp, J.; Haranczyk, M.; Sikora, B. J.; Bury, W.; Krungleviciute, V.; Farha, O. K.; Sholl, D. S.; Snurr, R. Q. Computation-Ready, Experimental Metal−Organic Frameworks: A tool to enable high-throughput screening of nanoporous crystals. *Chem. Mater.* **2014**, *26*, 6185–6192.

(3) Tang, D.; Kupgan, G.; Colina, C. M.; Sholl, D. S. Rapid Prediction of Adsorption Isotherms of a Diverse Range of Molecules in Hyper-Cross-Linked Polymers. *J. Phys. Chem. C* **2019**, *123* (29), 17884–17893.

(4) Tang, D.; Wu, Y.; Verploegh, R. J.; Sholl, D. S. Efficiently Exploring Adsorption Space to Identify Privileged Adsorbents for Chemical Separations of a Diverse Set of Molecules. *ChemSusChem* **2018**, *11* (9), 1567–1575.

(5) Matito-Martos, I.; Moghadam, P. Z.; Li, A.; Colombo, V.; R Navarro, J. A.; Calero, S.; Fairen-Jimenez, D. Discovery of an Optimal Porous Crystalline Material for the Capture of Chemical Warfare Agents. *Chem. Mater.* **2018**, *30*, 4571–4579.